



ISSN 1343-2230

CNS-REP-69  
November, 2006

# Annual Report 2005

Center for Nuclear Study,  
Graduate School of Science, the University of Tokyo

## Editors

K. Ozawa

Y. Fujiwara

## **Center for Nuclear Study**

CNS Reports are available from:

Wako-Branch at RIKEN

Center for Nuclear Study,

Graduate School of Science, the University of Tokyo

2-1 Hirosawa, Wako

351-0198, Japan

Tel: +81-48-464-4191

Fax: +81-48-464-4554

# Annual Report 2005

Center for Nuclear Study,  
Graduate School of Science, the University of Tokyo



## Preface

This is the annual report of the Center for Nuclear Study (CNS), Graduate School of Science, the University of Tokyo. This report includes activities during the fiscal year 2005 (April 2005 through March 2006). During this period, many fruitful results in various nuclear physics fields have been successfully produced at CNS.

The position-sensitive  $\gamma$ -ray detector array, CNS GRAPE, was operated for in-beam  $\gamma$ -ray spectroscopy experiments of neutron-rich nuclei around  $^{32}\text{Mg}$  and  $^{48}\text{Ca}$  using  $\alpha$  induced reactions in inverse kinematics and fusion-evaporation reaction, respectively. The position sensitivity of the CNS GRAPE was utilized for a lifetime measurement using Recoil Distance method. The array was also used for the  $\beta$ - $\gamma$  spectroscopy combining with Clover Ge detectors. The R&D of the prototype BGO Compton suppressor for GRAPE is in progress. In addition, position sensitivity and energy resolution of CdTe detectors were studied by using digital-pulse-shape analysis.

The research activities of nuclear astrophysics have continued using the CNS low-energy RI beam separator CRIB. They include resonant elastic scattering of  $^7\text{Be}+p$  and  $^{25}\text{Al}+p$  for the solar model test and the astronomical  $^{26}\text{Al}$  nuclear gamma-ray observation, respectively. An intensive  $^{39}\text{Ar}$  beam was also produced to measure the half life precisely. Some new RI beams were developed with CRIB. The first successful experiment was performed at the high resolution spectrograph PA, installed in the experimental hall E2 in the RIKEN accelerator facility. A high resolution mode was established with PA and was used for the measurement of  $^{28}\text{Si}(, ^6\text{He}), ^{26}\text{Si}$  for nuclear astrophysics. As our continuous effort for the field, the international symposium on nuclear astrophysics "Origin of Matter and Evolution of Galaxies 2005" was held in November 2005.

The polarized proton solid target has been established for the use in radioactive nuclear beam experiments. The proton polarization of 20% has been obtained for the beam-experiment setup. In addition, polarization reversal capability has been introduced. The polarized target was used in a high-statistics measurement of the analyzing power for the  $p$ - $^6\text{He}$  elastic scattering. A polarimeter for the GeV-energy polarized deuteron beams has been successfully constructed at the internal target station of Nuclotron at Dubna. The calibration measurements of the polarimeter at  $E_d=880$  MeV and 2.0 GeV have been made under the collaboration between the CNS and the Joint Institute for Nuclear Research.

The experimental study in the PHENIX experiment at Relativistic Heavy Ion Collider (RHIC) at Brookhaven National Laboratory have made a steady progress toward the understanding of hot and dense matter created by colliding gold nuclei at relativistic energies. The CNS group has been playing major roles in the various data analyses, whose subjects include high- $p_T$  hadron and single photon production, single electron production,  $J/\psi$  yields in  $p + p$ ,  $d + \text{Au}$  and  $\text{Au} + \text{Au}$  collisions. The study of basic performances of a new type of gaseous detector, gas electron multiplier (GEM), was made, and development of a UV-photon detector with GEM have been performed.

The Hyper ECR ion source was improved to provide  $\text{Ca}^{11+}$  with 50 e $\mu\text{A}$  by placing the metallic material rod. The design of charge breeding ECR ion source (CBECR) has been finished. The CBECR is under construction and will provide intense and high-charge-state metal ion beams.

An improvement of the power supplies for RIKEN AVF cyclotron has been done. After recent improvements, a main coil and nine pairs of concentric trim coils wound on spiral sectors have generated an isochronous field for acceleration of  $^7\text{Li}$ ,  $^{14}\text{N}$ ,  $^{15}\text{N}$ ,  $^{18}\text{O}$ ,  $^{24}\text{Mg}$ ,  $^{40}\text{Ar}$  for CRIB experiments.

Theoretical studies have been carried out by large-scale nuclear structure calculations in collaboration with RIKEN. Shell-model calculations, in particular, those by the Monte Carlo Shell Model, have produced crucial results to clarify the evolution of shell gaps and its consequences on deformation as well as the precise evaluation of spin-isospin excitations of light and medium-heavy nuclei. Many of such theoretical studies have been made in collaboration with various groups over the world.

The 4th CNS International Summer School (CISS05) has been organized in August 2005 with many

invited lecturers including three foreign distinguished physicists. There were 111 participants from 6 countries mainly from Asia.

The construction of the superconducting quadrupole doublet was started. The RIKEN RI beam facility (RIBF) which is under construction will begin to deliver RI beams in 2007. Matching with the construction, we are currently engaged in the construction of the state-of-the-art high resolution spectrometer SHARAQ.

The SHARAQ project was started as a major activity of the CNS. It aims at the high resolution spectroscopic studies in the RIKEN RI beam facility (RIBF) to be completed in 2007. We determined the detailed specification of the SHARAQ spectrometer and designed the configuration including the high resolution beam line, which will be commissioned in 2009.

Takaharu Otsuka  
Director of CNS



# Table of Contents

## 1a. Experimental Nuclear Physics: Low and Intermediate Energies

Study of the $^{18}\text{F} + \text{p} \rightarrow \alpha + ^{15}\text{O}$ Reaction at Astrophysical Energies .....	1
<i>S. Cherubini, C. Spitaleri, S. Romano, M. Gulino, R.G. Pizzone, A. Tumino, V. Crucillà, M. La Cognata, L. Lamia, L. M. Sergi, S. Kubono, H. Yamaguchi, G. Amadio, H. Fujikawa, J. J. He, A. Saito, Y. Wakabayashi, T. Motobayashi, S. Nishimura, T. Teranishi, A. Chen, J. Pearson, and A. Coc</i>	
Study of Astrophysically Important Resonant States in $^{26}\text{Si}$ by the $^{28}\text{Si}(^4\text{He}, ^6\text{He})^{26}\text{Si}$ Reaction .....	3
<i>Y. K. Kwon, C. S. Lee, J. Y. Moon, J. H. Lee, J. Y. Kim, S. Kubono, N. Iwasa, K. Inafuku, H. Yamaguchi, J. J. He, A. Saito, Y. Wakabayashi, H. Fujikawa, G. Amadio, L. H. Khiem, M. Tanaka, A. Chen, and S. Kato</i>	
Low Energy Implantation of $^{39}\text{Ar}$ at the CRIB Facility .....	5
<i>Zs. Fülöp, H. Yamaguchi, Z. Elekes, S. Kubono, G. Amadio, S. Bishop, H. Fujikawa, J. J. He, L. H. Khiem, Y. K. Kwon, S. Michimasa, M. Niikura, S. Nishimura, A. Saito, T. Teranishi, Y. Wakabayashi and Y. Yanagisawa</i>	
Study of High-Spin States in Nuclei near $^{40}\text{Ar}$ .....	6
<i>M.L. Liu, E. Ideguchi, H. Baba, T. Fukuchi, N. Hokoïwa, C. Ishida, N. Iwasaki, T. Komatsubara, T. Kubo, M. Kurokawa, S. Michimasa, K. Morimoto, K. Miyakawa, M. Niikura, T. Ohnishi, S. Ota, A. Ozawa, S. Shimoura, T. Suda, M. Tamaki, I. Tanihata, Y. Wakabayashi and K. Yoshida</i>	
Measurement of $^{25}\text{Al}+p$ Resonances through Elastic Scattering with CRIB .....	8
<i>J. Pearson, A. A. Chen, S. Kubono, H. Yamaguchi, T. Teranishi, J. J. He, L. H. Khiem, A. Saito, G. Amadio, H. Fujikawa, M. Niikura, Y. Wakabayashi, S. Nishimura, Y. Togano, A. Odahara, J. Y. Moon, Y. K. Kwon, S. Cherubini, R. Pizzone and M. La Cognata</i>	
Low-Lying Resonance Levels in $^{14}\text{O}$ .....	10
<i>T. Teranishi, S. Kubono, H. Yamaguchi, J. J. He, A. Saito, H. Fujikawa, G. Amadio, M. Niikura, S. Shimoura, Y. Wakabayashi, S. Nishimura, M. Nishimura, J. Y. Moon, C. S. Lee, A. Odahara, D. Sohler, L. H. Khiem, Z. H. Li, G. Lian, and W. P. Liu</i>	
Excitation Function Measurement by using $^{19}\text{F}+^{96}\text{Zr}$ Reaction .....	12
<i>Y. Zheng, E. Ideguchi, M. Niikura, M. Liu, H. Baba, T. Fukuchi, T. Morikawa, S. Michimasa, S. Mitarai, S. Ota, S. Shimoura, Y. Wakabayashi, and H. Yamaguchi</i>	
Proton Resonance Scattering of $^7\text{Be}$ .....	14
<i>H. Yamaguchi, A. Saito, J. J. He, Y. Wakabayashi, G. Amadio, H. Fujikawa, S. Kubono, T. Teranishi, S. Nishimura, Y. Togano, Y. K. Kwon, L. H. Khiem, M. Niikura, N. Iwasa and K. Inafuku</i>	
Study of Three Nucleon Force Effects via the $nd$ Elastic Scattering .....	17
<i>Y. Maeda, K. Fujita, M. B. Greenfield, Y. Hagiwara, K. Hatanaka, M. Hatano, K. Itoh, H. Kamada, J. Kamiya, T. Kawabata, H. Kuboki, T. Kudoh, Y. Nagasue, H. Okamura, T. Saito, H. Sakai, Y. Sakemi, M. Sasano, K. Sekiguchi, Y. Shimizu, K. Suda, A. Tamii, T. Uesaka, T. Wakasa and K. Yako</i>	
High Resolution In-beam Gamma Spectroscopy of $N \sim 20$ Neutron-rich Nuclei .....	19
<i>T. Fukui, S. Ota, S. Shimoura, N. Aoi, E. Takeshita, S. Takeuchi, H. Suzuki, H. Baba, T. Fukuchi, Y. Hashimoto, E. Ideguchi, K. Ieki, N. Iwasa, H. Iwasaki, S. Kanno, Y. Kondo, T. Kubo, K. Kurita, T. Minemura, S. Mitimasa, T. Motobayashi, T. Murakami, T. Nakabayashi, T. Nakamura, M. Niikura, T. Okumura, T. K. Onishi, H. Sakurai, M. Shinohara, D. Suzuki, M. K. Suzuki, M. Tamaki, K. Tanaka, Y. Togano, Y. Wakabayashi, and K. Yamada</i>	
Exotic Cluster States in $^{12}\text{Be}$ via $\alpha$ -Inelastic Scattering .....	21
<i>A. Saito, S. Shimoura, T. Minemura, Y. U. Matsuyama, H. Baba, N. Aoi, T. Gomi, Y. Higurashi, K. Ieki, N. Imai, N. Iwasa, H. Iwasaki, S. Kanno, S. Kubono, M. Kunibu, S. Michimasa, T. Motobayashi, T. Nakamura, H. Ryuto, H. Sakurai, M. Serata, E. Takeshita, S. Takeuchi, T. Teranishi<sup>†</sup>, K. Ue, K. Yamada and Y. Yanagisawa</i>	
Proton Single-Particle States in the Neutron-Rich $^{23}\text{F}$ Nucleus .....	23

<i>S. Michimasa, S. Shimoura, H. Iwasaki, M. Tamaki, S. Ota, N. Aoi, H. Baba, N. Iwasa, S. Kanno, S. Kubono, K. Kurita, M. Kurokawa, T. Minemura, T. Motobayashi, M. Notani, H.J. Ong, A. Saito, H. Sakurai, E. Takeshita, S. Takeuchi, Y. Yanagisawa and A. Yoshida</i>	
High-Spin States of $^{93}\text{Nb}$ .....	25
<i>Y. Wakabayashi, T. Fukuchi, Y. Gono, A. Odahara, S. Tanaka, M. Inoue, T. Sasaki, M. Kibe, N. Hokoiiwa, T. Shinozuka, M. Fujita, A. Yamazaki, T. Sonoda, C. S. Lee, Y. K. Kwon, J. Y. Moon, and J. H. Lee</i>	
Analyzing Power Measurement for the $\vec{p}+^6\text{He}$ Elastic Scattering at 71 MeV/u .....	27
<i>S. Sakaguchi, T. Uesaka, T. Wakui, T. Kawabata, N. Aoi, Y. Hashimoto, M. Ichikawa, Y. Ichikawa, K. Itoh, M. Itoh, H. Iwasaki, T. Kawahara, H. Kuboki, Y. Maeda, R. Matsuo, T. Nakao, H. Okamura, H. Sakai, N. Sakamoto, Y. Sasamoto, M. Sasano, Y. Satou, K. Sekiguchi, M. Shinohara, K. Suda, D. Suzuki, Y. Takahashi, A. Tamii, K. Yako, and M. Yamaguchi</i>	
In-beam Gamma-ray Measurement of the $^{46}\text{Ar} + ^9\text{Be}$ Reaction .....	29
<i>M. Niikura, E. Ideguchi, N. Aoi, H. Baba, T. Fukuchi, Y. Ichikawa, H. Iwasaki, T. Kubo, M. Kurokawa, M. Liu, S. Michimasa, T. Ohnishi, T. K. Onishi, S. Ota, S. Shimoura, H. Suzuki, D. Suzuki, Y. Wakabayashi, K. Yoshida and Y. Zheng</i>	
Study of Inelastic Contribution in the $^7\text{Be} + p$ Scattering Experiment at CRIB .....	31
<i>G. Amadio, H. Yamaguchi, J. J. He, A. Saito, Y. Wakabayashi, H. Fujikawa, S. Kubono, L. H. Khiem, Y. K. Kwon, T. Teranishi, S. Nishimura, M. Niikura, Y. Togano, N. Iwasa, and S. Inafuku</i>	
Study of Cluster States in $^{11}\text{B}$ and $^{13}\text{C}$ via $(\alpha, \alpha')$ Reaction .....	33
<i>Y. Sasamoto, T. Kawabata, T. Uesaka, K. Suda, Y. Maeda, S. Sakaguchi, K. Itoh, K. Hatanaka, M. Fujiwara, A. Tamii, Y. Shimizu, K. Nakanishi, K. Kawase, H. Hashimoto, Y. Tameshige, H. Matsubara, M. Itoh, H. P. Yoshida, and M. Uchida</i>	
Lifetime Measurement of $^{32}\text{Mg}$ First $2^+$ State .....	35
<i>M. K. Suzuki, H. Sakurai, H. Iwasaki, A. Dewald, T. Fukuchi, T. Fukui, Y. Ichikawa, E. Ideguchi, M. Liu, T. Nakao, M. Niikura, H. J. Ong, T. K. Onishi, H. Otsu, T. Sumikama, D. Suzuki, H. Suzuki, Y. Zheng, and S. Shimoura</i>	
Development of a High-Efficiency Method for $\alpha$ Resonant Scattering with the Thick Target Method .....	37
<i>H. Fujikawa, S. Kubono, A. Saito, H. Yamaguchi, G. Amadio, J. J. He, L. H. Khiem, S. Nishimura, H. Ohta, A. Ozawa, Y. Tagishi, Y. Wakabayashi, M. Yamaguchi and T. Yasuno</i>	
Beta Decay Study of C, N, O Isotopes Close to the Neutron-Drip Line .....	39
<i>T. K. Onishi, H. Sakurai, N. Aoi, T. Fukuchi, T. Fukui, A. Gelberg, Y. Ichikawa, E. Ideguchi, H. Iwasaki, T. Kishida, M. Liu, T. Nakao, M. Niikura, S. Nishimura, H. J. Ong, H. Otsu, S. Shimoura, T. Sumikama, D. Suzuki, H. Suzuki, M. K. Suzuki, N. Yamada and Y. Zheng</i>	

## 1b. Experimental Nuclear Physics: PHENIX Experiment at BNL-RHIC

Progress of the PHENIX Experiment in the Year 2005 .....	41
<i>H. Hamagaki, K. Ozawa, K. Kino, F. Kajihara, T. Gunji, T. Isobe, N. Kurihara, S. X. Oda, Y. Morino, S. Saito, Y. Aramaki, Y. L. Yamaguchi, J. Kikuchi, S. Sano, Y. Tanaka, and T. Fusayasu</i>	
Measurements of Low-Mass Vector Mesons in Au+Au Collisions at RHIC-PHENIX .....	43
<i>K. Ozawa, H. Hamagaki, F. Kajihara, T. Gunji, T. Isobe, S. X. Oda, Y. Morino, S. Saito, Y. Aramaki, and Y. L. Yamaguchi, for the PHENIX collaboration</i>	
Measurement of Single Electrons in the $\sqrt{s_{NN}} = 200$ GeV Au+Au Collisions .....	45
<i>F. Kajihara, Y. Akiba, R. Averbeck, A. Dion, T. Gunji, H. Hamagaki, and K. Ozawa, for the PHENIX Collaboration</i>	
Measurement of Vector Mesons via Di-Electron Decay in Cu+Cu Collisions at RHIC-PHENIX .....	47

<i>S. X. Oda, H. Hamagaki, K. Ozawa, K. Das, A. D. Frawley, A. Lebedev, and W. Xie, for the PHENIX collaboration</i>	
Measurement of $J/\psi \rightarrow e^+e^-$ in Au+Au Collisions at $\sqrt{s_{NN}} = 200$ GeV by PHENIX at RHIC	49
<i>T. Gunji, H. Hamagaki, K. Ozawa, F. Kajihara, Y. Akiba, A. Lebedev, and C. L. Silva, for the PHENIX collaboration</i>	
Direct Photon Measurement in $\sqrt{s_{NN}} = 200$ GeV Au+Au Collisions at RHIC-PHENIX	51
<i>T. Isobe, H. Hamagaki, T. Sakaguchi, G. David, and B. Sahlmueller for the PHENIX Collaboration</i>	
Measurement of Neutral Pion in $\sqrt{s_{NN}} = 200$ GeV Au+Au Collisions at RHIC-PHENIX	53
<i>T. Isobe, H. Hamagaki, T. Sakaguchi, G. David, S. Mioduszewski, M. L. Porschke, D. Winter, B. Sahlmueller, and J. Imrek, for the PHENIX Collaboration</i>	
<b>2. Accelerator and Instrumentation</b>	
Improvement of Magnet Power Supply for RIKEN AVF Cyclotron	55
<i>S. Watanabe, Y. Ohshiro, S. Kubono, M. Fukuda, M. Nagase, A. Goto, and M. Kase</i>	
Design of a CNS Charge Breeder ECR Ion Source	57
<i>Y. Ohshiro, S. Yamaka, S. Watanabe, T. Nakagawa, T. Hattori, M. Oyaizu, H. Miyatake, and S. Kubono</i>	
Production of High Intensity $^{40}\text{Ca}^{11+}$ Ion Beam	59
<i>Y. Ohshiro, S. Yamaka, S. Watanabe, Y. Higurashi, T. Kageyama, and S. Kubono</i>	
High Resolution SHARAQ Spectrometer	61
<i>T. Uesaka, S. Shimoura, T. Kawabata, H. Sakai, S. Kubono, E. Ideguchi, H. Yamaguchi, T. Kubo, and G. P. Berg</i>	
High Resolution Beam Line for the SHARAQ Spectrometer	63
<i>T. Kawabata, T. Kubo, H. Sakai, S. Shimoura, and T. Uesaka</i>	
Design of D2 Dipole Magnet for the SHARAQ Spectrometer	65
<i>T. Uesaka, G. P. Berg, S. Shimoura, T. Kawabata, and H. Sakai</i>	
Status of CNS GRAPE	67
<i>E. Ideguchi, S. Shimoura, H. Baba, T. Fukuchi, M. Kurokawa, M. Liu, S. Michimasa, M. Niikura, S. Ota, Y. Zheng, and H. Sakai</i>	
Gamma-Ray Imaging Analysis by Using CNS GRAPE	69
<i>Y. Zheng, E. Ideguchi, H. Baba, T. Fukuchi, M. Kurokawa, M. Liu, S. Michimasa, M. Niikura, S. Ota, and S. Shimoura</i>	
Development of Liquid Nitrogen-Cooled Gas Target System	71
<i>H. Yamaguchi, S. Kubono, G. Amadio, Y. Wakabayashi, A. Saito, J. J. He, and H. Fujikawa</i>	
$d$ - $p$ Elastic Scattering Measurement at Internal Target Station of Nuclotron	73
<i>K. Suda, T. Uesaka, V. P. Ladygin, T. Kawabata, Y. Maeda, K. Itoh, S. Sakaguchi, Y. Sasamoto, H. Sakai, K. Sekiguchi, P. K. Kurilkin, Yu. V. Gurchin, A. Yu. Isupov, M. Janek, J. T. Karachuk, A. N. Khrenov, A. S. Kiselev, V. A. Kizka, J. Kliman, V. A. Krasnov, A. N. Livanov, A. I. Malakhov, V. Matoucek, M. Morhac, S. M. Piyadin, S. G. Reznikov, I. Turzo, and T. A. Vasiliev</i>	
Digital Pulse Shape Analysis of Thick CdTe Detectors	75
<i>T. Moriguchi, T. Hoya, M. Niikura, S. Ota, H. Baba, T. Fukuchi, E. Ideguchi, and S. Shimoura</i>	
Polarized Proton Target Performance During Scattering Experiment	77

<i>T. Wakui, S. Sakaguchi, T. Kawahara, M. Hatano, T. Uesaka, and H. Sakai</i>	
Polarization Relaxation Time of Polarized $^3\text{He}$ in Target Cell with Ti Windows .....	79
<i>K. Itoh and T. Uesaka</i>	
New Method of Polarization Reversal by means of 180-Degree Pulse Nuclear Magnetic Resonance .....	81
<i>T. Kawahara, T. Wakui, T. Uesaka, and S. Sakaguchi</i>	
Performance of Gas Electron Multiplier (GEM) Developed at CNS .....	83
<i>Y. L. Yamaguchi, H. Hamagaki, K. Ozawa, S. X. Oda, Y. Aramaki and S. Sano</i>	
Development of a CsI-coated Gas Electron Multiplier .....	85
<i>Y. Aramaki, H. Hamagaki, K. Ozawa, S. Yokkaichi, S. X. Oda, Y. Morino, Y. L. Yamaguchi, M. Inuzuka, S. Sano, and S. Maki</i>	
Simulation Study of Gas Electron Multiplier .....	87
<i>S. Sano, H. Hamagaki, K. Ozawa, S. Yokkaichi, T. Isobe, S. X. Oda, and Y. L. Yamaguchi</i>	
Measurements of Ion Feedback in the Gas Electron Multiplier (GEM) .....	89
<i>S. Maki, H. Hamagaki, K. Ozawa, S.X. Oda, Y. Morino, Y. Aramaki, Y.L. Yamaguchi, S. Sano, S. Yokkaichi, and J. Chiba</i>	
Electron Identification Capability of Real Size, Six Layer Transition Radiation Detector for ALICE .....	91
<i>Y. Morino, S. Saito, T. Gunji, H. Hamagaki, and K. Ozawa, for the ALICE TRD Collaboration</i>	
<b>3. Theoretical Nuclear Physics</b>	
Large Scale Nuclear Structure Calculations in CNS .....	93
<i>N. Shimizu, T. Otsuka, N. Itagaki, T. Mizusaki, M. Honma and Y. Utsuno</i>	
Large-Scale Shell-Model Description of $^{16}\text{C}$ with Microscopic Effective Interactions .....	95
<i>S. Fujii, T. Mizusaki, T. Otsuka, T. Sebe, and A. Arima</i>	
<b>4. Other Activities</b>	
The Fourth CNS International Summer School (CISS05) .....	97
<i>S. Shimoura, T. Otsuka, T. Mizusaki, and H. Sakai</i>	
Nuclear Scattering Experiments for Education of Undergraduate Students .....	98
<i>T. Kawabata, K. Yako, Y. Sasamoto, H. Sakai, and S. Shimoura</i>	
<b>Appendices</b>	
Symposium, Workshop, Seminar, Colloquium, and PAC .....	99
CNS Reports .....	103
Publication List .....	104
Talks and Presentations .....	112
Personnel .....	120

# **Experimental Nuclear Physics: Low and Intermediate Energies**



# Study of the $^{18}\text{F} + \text{p} \rightarrow \alpha + ^{15}\text{O}$ Reaction at Astrophysical Energies

S. Cherubini<sup>a</sup>, C. Spitaleri<sup>a</sup>, S. Romano<sup>a</sup>, M. Gulino<sup>a</sup>, R. G. Pizzone<sup>a</sup>, A. Tumino<sup>a</sup>, V. Crucillà<sup>a</sup>,  
M. La Cognata<sup>a</sup>, L. Lamia<sup>a</sup>, L. M. Sergi<sup>a</sup>, S. Kubono, H. Yamaguchi, G. Amadio, H. Fujikawa,  
J. J. He, A. Saito, Y. Wakabayashi, T. Motobayashi<sup>b</sup>, S. Nishimura<sup>b</sup>, T. Teranishi<sup>c</sup>, A. Chen<sup>d</sup>,  
J. Pearson<sup>d</sup>, and A. Coc<sup>e</sup>

<sup>a</sup>University of Catania and INFN-LNS, Catania, Italy

Center for Nuclear Study, Graduate School of Science, University of Tokyo

<sup>b</sup>RIKEN (The Institute of Physical and Chemical Research), Wako, Japan

<sup>c</sup>Kyushu University, Kyushu, Japan

<sup>d</sup>McMaster University, Hamilton, Canada

<sup>e</sup>CSNSM, Orsay, France

Observations suggest that nova explosions and x-ray bursts occur in close binaries in which the hydrogen-rich material from the outer layers of an extended star is filling its Roche lobe and accreting onto the surface of its companion, a white dwarf or a neutron star, respectively. In such explosive events, the temperatures and densities involved are sufficiently high so that proton and alpha-particle induced nuclear reactions can be fast enough to by-pass beta-decay processes. These nuclear reactions involving radioactive nuclei can greatly increase both the rate of energy generation and the total amount of energy produced and can have a dramatic impact on both the isotopic and elemental abundances produced. It has been shown in [1] that classical novae emit  $\gamma$ -ray at and below 511 keV soon after the explosion. The positrons which give rise to this electron-positron  $\gamma$ -ray emission in the expanding envelope mainly come from  $^{18}\text{F}$   $\beta$ -decay, because its life-time ( $\tau=158$  min) is such that positrons are emitted when the nova-envelope begins to be transparent to gamma radiation.

Thus the radiation intensity strongly depends on the  $^{18}\text{F}$  abundance; for this reason it is necessary the study of processes that produce and destroy this isotope in novae. Among these reactions the  $^{18}\text{F}(p, \alpha)^{15}\text{O}$  stands as one of the main  $^{18}\text{F}$  destruction channels. Consequently, its study at astrophysically relevant energy regions is strongly required. From these observations it follows that the reaction  $^{18}\text{F}(p, \alpha)^{15}\text{O}$  has to be studied in the energy range 100-500 keV (center of mass) roughly. In particular, the contribution on the cross section of the resonance at 330 keV has to be investigated together with the interferences between several levels occurring in the region of interest.

We plan to study the  $^{18}\text{F}(p, \alpha)^{15}\text{O}$  reaction using a  $^{18}\text{F}$  beam produced at CRIB.

We intend to study the excitation function on the full range of astrophysical interest. To this end, we will implement two different experimental approaches. We will make a direct measurement for the higher (i.e. greater than roughly 400 keV) energy region. Owing to the expected extremely small values of the cross section of the reaction in the low energy region (200 keV - 400 keV roughly), we will use the Trojan Horse method [2-5] in order to explore this part of the excitation function. [6]

$^{18}\text{O}$ intensity (nA)	$^{18}\text{F}$ intensity (pps)	Purity (%)	Primary target gas pressure (Torr)
1	90	98	540
5	340	98	539
11	1500	97	539
55	8000	99	539
100	13000	98	539
410	50000	95	540
440	43000	96	533
1400	105000	98	537
2000	150000	98	538

Table 1.  $^{18}\text{F}$  beam intensity obtained during the test at different experimental conditions.

In beginning of November 2005 a test run was performed in order to characterize the  $^{18}\text{F}$  beam produced at CRIB. The usual CRIB setup was used.

A primary  $^{18}\text{O}$  beam of 3.97 MeV/u and intensity over 2  $\mu\text{A}$  produced by the AVF cyclotron bombarded a  $\text{H}_2$  production target 0.42 mg/cm<sup>2</sup> thick.

The secondary particles produced in the  $\text{H}_2$  target were separated along the CRIB line using the dipole pair and the Wien filter so that an almost pure (see table 1)  $^{18}\text{F}$  beam could be driven downstream to the secondary target position.

A careful check of the secondary beam was performed at each critical point in the apparatus with a special attention devoted to the beam contaminants. After the determination and optimization of the magnetic elements, an intensity check of the produced  $^{18}\text{F}$  beam was performed. The result of this study is reported in the Table I. In particular a peak intensity of  $1.5 \times 10^5$  particles per second was obtained.

It must be stressed that the full AVF beam intensity was not used in the test for security reasons. In principle 4  $\mu\text{A}$  could be used. Also the production target used in the test was not the most recent version: a cooling system can be added and this will allow for a higher pressure of the gas in the target. Taking into account these remarks, a final goal of a  $^{18}\text{F}$  beam with an intensity greater than  $5 \times 10^5$  pps is well

within the capabilities of the CRIB setup.

### References

- [1] A. Coc *et al.*, *A.&A.*, 357 (2000) **561** and references therein.
- [2] G. Baur, *Phys. Lett. B* **178** (1986) 135.
- [3] C. Spitaleri, Proceedings of the 5th Winter School on Hadronic Physics, Folgaria, Italy, 1990.
- [4] S. Cherubini, V. N. Kondratyev, M. Lattuada , *et al.*, *ApJ* **457** (1996) 855
- [5] R. G. Pizzone, C. Spitaleri, S. Cherubini, *et al.*, *Phys. Rev. C* **71** (2005) 058801 and references therein
- [6] Proposal of this experiment, accepted by the CNS PA Committee

# Study of Astrophysically Important Resonant States in $^{26}\text{Si}$ by the $^{28}\text{Si}(^4\text{He}, ^6\text{He})^{26}\text{Si}$ Reaction

Y. K. Kwon, C. S. Lee, J. Y. Moon, J. H. Lee, J. Y. Kim, S. Kubono<sup>a</sup>, N. Iwasa<sup>b</sup>, K. Inafuku<sup>b</sup>, H. Yamaguchi<sup>a</sup>, J. J. He<sup>a</sup>, A. Saito<sup>a</sup>, Y. Wakabayashi<sup>a</sup>, H. Fujikawa<sup>a</sup>, G. Amadio<sup>a</sup>, L. H. Khieu<sup>c</sup>, M. Tanaka<sup>d</sup>, A. Chen<sup>e</sup>, and S. Kato<sup>f</sup>

*Department of Physics, Chung-Ang University, Korea*

<sup>a</sup>*Center for Nuclear Study, Graduate School of Science, University of Tokyo*

<sup>b</sup>*Department of Physics, Tohoku University*

<sup>c</sup>*Institute of Physics and Electronics, Vietnam*

<sup>d</sup>*KEK (The High Energy Accelerator Organization)*

<sup>e</sup>*Department of Physics and Astronomy, McMaster University, Canada*

<sup>f</sup>*Department of Physics, Yamagata University*

## 1. Introduction

$^{26}\text{Al}$  is the first cosmic radioactivity ever detected through its characteristic 1.809 MeV  $\gamma$ -ray line. It could be emitted from the first excited state of  $^{26}\text{Mg}$  followed by  $\beta$ -decay of  $^{26}\text{Al}$  in its ground state ( $^{26}\text{Al}_{g.s.}$ ). Since the  $\beta$ -decay life time of  $^{26}\text{Al}$  ( $t_{1/2} = 7.17 \times 10^5$  yr) is much shorter than the time scale of galactic chemical evolution ( $\approx 10^{10}$  year), the observation of large amounts ( $\sim 3 M_{\odot}$ ) of  $^{26}\text{Al}$  in the Galaxy [1] is strong evidence that the process of nucleosynthesis is currently active. To resolve controversy over the possible sources of the observational 1.809 MeV  $\gamma$ -rays, one needs accurate knowledge of the production rate of  $^{26}\text{Al}$ . The  $^{25}\text{Al}(p, \gamma)^{26}\text{Si}$  reaction which is the competitor against production of  $^{26}\text{Al}_{g.s.}$  is one of the key reactions to be investigated. Illiadis *et al.* [2] suggested that the  $^{25}\text{Al}(p, \gamma)^{26}\text{Si}$  reaction should be dominated by the  $3^+$  unnatural parity state ( $E_x=5970(100)$  keV) under explosive hydrogen burning process in novae. Recent studies of  $^{28}\text{Si}(p, t)^{26}\text{Si}$  [3],  $^{24}\text{Mg}(^3\text{He}, n\gamma)^{26}\text{Si}$  [4], and  $^{29}\text{Si}(^3\text{He}, ^6\text{He})^{26}\text{Si}$  [5] reduced the uncertainties of level energies in  $^{26}\text{Si}$  above the proton threshold and identified new states as candidates for the unnatural parity states. However, for such candidates, they could not make any spin assignment directly using the angular distribution measurement. In this work, we decided to study the astrophysically important resonant states in  $^{26}\text{Si}$  via the  $^{28}\text{Si}(^4\text{He}, ^6\text{He})^{26}\text{Si}$  reaction which could excite unnatural parity state directly, in contrast with the  $(p, t)$  reaction that cannot excite unnatural parity state.

## 2. Experiment

The  $^{28}\text{Si}(^4\text{He}, ^6\text{He})^{26}\text{Si}$  reaction was studied using the high resolution QDD (quadrupole-dipole-dipole) magnetic spectrograph (PA) at Center for Nuclear Study (CNS), University of Tokyo. A beam of  $^4\text{He}$  at 120 MeV was extracted from RIKEN linear accelerator (RILAC) + RIKEN ring cyclotron (RRC). Beam intensity was typically 70 nA at the target position. A self-supporting natural silicon target (thickness  $\sim 1$  mg/cm<sup>2</sup>) was used to populate states in  $^{26}\text{Si}$ . The magnetic parameters of the PA were set to bend the elastically scattered  $^4\text{He}$  beam off the effective region of the focal plane detection system. Consequently the

spectra were free from the contamination of elastically and inelastically scattered  $^4\text{He}$ . The focal plane detection sys-

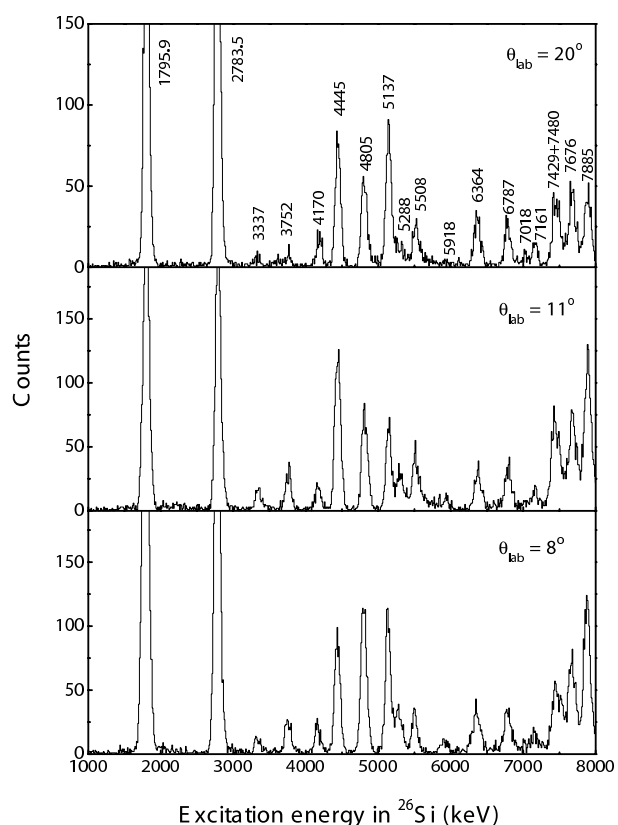


Figure 1. Calibrated  $^{26}\text{Si}$  excitation energy spectra are shown. The position information at focal plane was calibrated by the well-known peaks.

tem consisted of a hybrid gas counter and plastic scintillators. Four proportional gas counters, which were two position counters (X1 and X2) and two energy loss counters ( $\Delta E1$  and  $\Delta E2$ ) were installed in the hybrid drift chamber. The position information was derived by the charge division of signals from both ends of position counters. The plastic scintillators consisted of thin (0.5 mm) and thick (10 mm) scintillators as  $\Delta E$  and E detectors, respectively. For the particle identification, we used six  $\Delta E$ -E information:

8°	11°	15°	20°	adopted
1795.9 <sup>a</sup>				
2783.5 <sup>a</sup>				
3337(4)	3338(4)	3346(7)	3328(13)	3337(6)
3750(4)	3754(4)	3753(8)	3752(4)	3752(5)
4166(4)	4164(3)	4170(4)	4181(4)	4170(4)
4445 <sup>a</sup>				
4805 <sup>a</sup>				

<sup>a</sup> Used for the energy calibration.

Table 1. <sup>26</sup>Si levels with 1 MeV ≤ E<sub>x</sub> ≤ 5 MeV observed in <sup>28</sup>Si(<sup>4</sup>He, <sup>6</sup>He)<sup>26</sup>Si reaction. The excitation energies have been determined using the weighted average value method.

ΔE1-E, ΔE2-E, ΔE-E, (L1+H1, sum of lower and higher momentum side signals for X1)-E, and (L2+H2)-E. Also we used time-of-flight (TOF) information with RF signal from accelerator and vertical position information. Using these information, we clearly identified <sup>6</sup>He. Focal plane was inclined to 35° about the incident particles at the central position. The effective length of the detection system along the focal plane was 40 cm.

### 3. Results

To get the information for the level structure in <sup>26</sup>Si, we have measured the angular distribution at  $\theta_{lab} = 8^\circ, 11^\circ, 15^\circ,$  and  $20^\circ$ . The overall energy resolution was 100 keV (FWHM). Figure 2 shows the calibrated excitation energy spectra. The well-known states that were populated and observed in the <sup>28</sup>Si(<sup>4</sup>He, <sup>6</sup>He)<sup>26</sup>Si reaction were used for energy calibration with a polynomial function of the focal plane detector position representing the linear momentum. Using the calibration function, we converted focal plane position into excitation energies in <sup>26</sup>Si at each angle. Finally we determined excitation energies using the weighted average value method (Table 1). The states used for calibration were the ground state and excited states in <sup>26</sup>Si at 0, 1795.9(0.2), 2783.5(0.4), 4445(3), and 4805(2) keV [6]. The uncertainties of excitation energies were determined mainly by uncertainty in determining the <sup>6</sup>He peak channels. The excitation energies in <sup>26</sup>Si are given in Table 2. Our excitation energies agree well with those from previous experimental results [3,5,7,8]. 7018(6) keV state which was only observed by (p,t) reaction [3] was confirmed. For E<sub>x</sub> = 7687 and 7885 keV, our result significantly reduces the uncertainties in the excitation energies. Also we observed several candidates for unnatural parity states at 5612, 5825, 5918(8) and 6107(8) keV. To clarify the level information, spin-parity assignment by the distorted-wave Born approximation (DWBA) calculation is in progress. To determine the optical potential parameters of <sup>28</sup>Si+<sup>4</sup>He channel, we also performed the angular distribution measurement for <sup>28</sup>Si(<sup>4</sup>He, <sup>4</sup>He)<sup>28</sup>Si. Further data analysis will be performed to find out the 3<sup>+</sup> resonant states above proton threshold level.

Ref [7] ( <sup>3</sup> He, n)	Ref [8] (p, t)	Ref [5] ( <sup>3</sup> He, <sup>6</sup> He)	Ref [3] (p, t)	This work ( <sup>4</sup> He, <sup>6</sup> He)
0.0	0.0	0.0	0.0	<sup>a</sup>
1795(11)	1800(30)	1795.9	1795.9	<sup>a</sup>
2790(12)	2780(30)	2783.5	2783.5	<sup>a</sup>
3339(19)	3330(30)		3332.5	3337(6)
	3760(30)	3756(2)		3752(5)
	4140(30)	4144(8)	4155(2)	4170(4) <sup>b</sup>
4183(11)		4211(16)	4155(2)	4170(4) <sup>b</sup>
4457(13)	4450(30)	4445	4445	<sup>a</sup>
4821(13)	4810(30)	4805	4805	<sup>a</sup>
5229(12)		5140(10)	5145(2)	5137(2)
	5310(30)	5291	5291(3)	5288(10)
5562(28)		5526(8)	5515(5)	5508(3)
				5612 <sup>c</sup>
				5825 <sup>c</sup>
		5678(8)		
5960(22)	5910(30)		5916(2)	5918(8) <sup>c</sup>
			5945(8)	
				6107(8) <sup>c</sup>
6381(20)	6320(30)		6300(4)	6364(4) <sup>b</sup>
			6380(4)	6364(4) <sup>b</sup>
	6470(30)			
6786(20)	6780(30)		6787(4)	6787(4)
	6880(30)			
7019(10)				7018(6)
7150(15)	7150(30)		7160(5)	7161(6)
	7390(30)		7425(7)	7429(7)
7476(20)	7480(30)		7498(4)	7480(30)
7695(31)			7687(22)	7676(4)
7902(21)	7900(30)		7900(22)	7885(4)

<sup>a</sup> This level was used for energy calibration.

<sup>b</sup> Average centroid of doublet peak.

<sup>c</sup> Candidates for unnatural parity state.

Table 2. The excitation energies (units in keV) in <sup>26</sup>Si from our measurement with the previous results.

### References

- [1] R. Diehl *et al.*, *Astron. Astrophysics* **97** (1993) 181.
- [2] C. Illiadis *et al.*, *Phys. Rev. C* **53** (1996) 475.
- [3] D. Bardayan *et al.*, *Phys. Rev. C* **65** (2002) 032801(R).
- [4] Y. Parpottas *et al.*, *Phys. Rev. C* **70** (2004) 065805.
- [5] J. A. Caggiano *et al.*, *Phys. Rev. C* **65** (2002) 055801.
- [6] R. A. I. Bell *et al.*, *Nucl. Phys. A* **133** (1969) 337.
- [7] W. Bohne *et al.*, *Nucl. Phys. A* **378** (1982) 525.
- [8] R. A. Paddock, *Phys. Rev. C* **5** (1972) 485.

# Low Energy Implantation of $^{39}\text{Ar}$ at the CRIB Facility

Zs. Fülöp<sup>a</sup>, H. Yamaguchi, Z. Elekes<sup>a</sup>, S. Kubono, G. Amadio, S. Bishop<sup>b</sup>, H. Fujikawa, J. J. He, L. H. Khiem, Y. K. Kwon, S. Michimasa<sup>b</sup>, M. Niikura, S. Nishimura<sup>b</sup>, A. Saito, T. Teranishi<sup>c</sup>, Y. Wakabayashi<sup>c</sup> and Y. Yanagisawa<sup>b</sup>

Center for Nuclear Study, Graduate School of Science, University of Tokyo

<sup>a</sup>ATOMKI, Debrecen, Hungary

<sup>b</sup>RIKEN, Wako, Japan

<sup>c</sup>Kyushu University, Fukuoka, Japan

Implanted  $^{39}\text{Ar}$  samples with weak activity have been prepared at the CRIB facility to study the feasibility of determination of half-life of  $^{39}\text{Ar}$  [1].

$^{39}\text{Ar}$  is a 100% beta-decaying isotope with a half-life of 269 years. It can be produced by the  $^{39}\text{K}(n,p)^{39}\text{Ar}$  reaction underground [2] and by cosmic-ray-induced spallation reactions [3]. The determination of the  $^{39}\text{Ar}$  concentration in rocks and groundwater gives valuable data for geochemical studies. By comparing the concentration of  $^{37}\text{Ar}$  ( $T_{1/2} = 35$  d) with that of  $^{39}\text{Ar}$  in meteorites, the cosmic ray distribution in the solar system can be estimated [3].

The well-established methods of half-life determination are not suitable for the case of  $^{39}\text{Ar}$ . The half-life of  $^{39}\text{Ar}$  is too long to obtain its decay curve. In addition, since argon is a noble gas, the Accelerator Mass Spectrometry (AMS) technique is also difficult to apply, because a negative ion source is needed [4, 5]. The implantation method [6, 7], however, is suitable for the  $^{39}\text{Ar}$  half-life measurement, because it is not necessary to determine the decay curve, only the detection of the activity of the implanted isotopes is required. For the implantation method a known amount of radioactive isotopes is implanted into a substrate, and its absolute activity is determined off-line.

As a first step towards the investigation of  $^{39}\text{Ar}$  half-life, the production of  $^{39}\text{Ar}$  was tested [1] at the CNS low-energy in-flight type RI beam separator, CRIB.

During the present experiment  $^{39}\text{Ar}$  particles were produced by  $^{40}\text{Ar}(^3\text{He}, ^4\text{He})^{39}\text{Ar}$  reaction in inverse kinematics using a 4.5 MeV/nucleon  $^{40}\text{Ar}$  beam bombarding an 80 mm long  $^3\text{He}$  gas target with a pressure of 1 atm. The primary beam intensity was limited because of the stability of the 2.2  $\mu\text{m}$  Havar windows of the gas target. Due to the high deposited energy of the primary beam, a local density loss in the primary gas target cell was observed, supporting the results of a previous study [8].

The  $^{39}\text{Ar}$  products were separated at a charge state of  $15^+$  by the CRIB separator, and further separation was provided by a Wien filter. Two PPACs and a silicon detector were used for particle identification and position determination. The  $^{39}\text{Ar}$  particles were well separated (See Fig.1) from  $^{40}\text{Ar}$  with a total beam intensity of  $5 \times 10^4/\text{s}$  and a secondary beam purity of 0.59%. The host material for the implantation was 50  $\mu\text{m}$  Al to match the expected 10  $\mu\text{m}$  range of the  $^{39}\text{Ar}$  particles of 2 MeV/nucleon incident energy. In addition, Al already proved to be stable host material for low energy Ar implantation [9]. In summary, two implanted

$^{39}\text{Ar}$  samples have been prepared with very low expected activities of  $10^{-3}\text{Bq}$ .

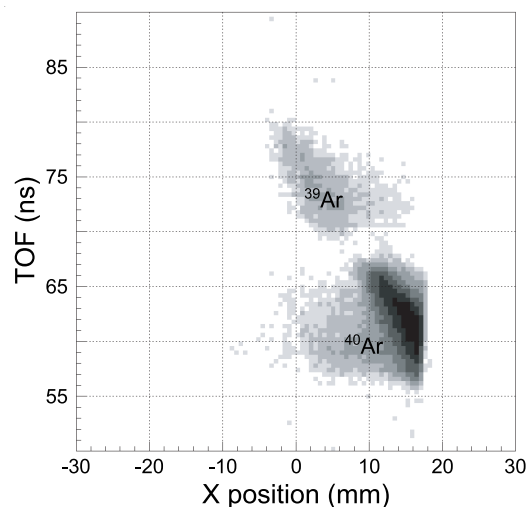


Figure 1. Particle identification diagram of the implanted isotopes based on the Time-of-Flight between the PPAC detectors and the position information from the downstream PPAC.

## References

- [1] Zs. Fülöp *et al.*, CNS Annual Report 2004 (2005) 8.
- [2] T. Florkowski: *J. Phys. G* **17** (1991) S513.
- [3] R. C. Reedy *et al.*, *Science* **219** (1983) 127.
- [4] W. Kutschera, *Annu. Rev. Nucl. Part. Sci.* **40** (1990) 411.
- [5] I. Ahmad *et al.*, ANL Annual Report 2001 **ANL-02/15** (2002) 79.
- [6] Zs. Fülöp *et al.*, in *Proceedings Nuclei in the Cosmos V*, edited by N. Prantzos and S. Harissopulos (1998) 281.
- [7] T. Hashimoto *et al.*, *Nucl. Phys. A* **686** (2001) 591.
- [8] J. Görres *et al.*, *Nucl. Instrum. Methods A* **177** (1980) 295.
- [9] I. Goeminne *et al.*, *Nucl. Instrum. Methods A* **489** (2002) 577.

# Study of High-Spin States in Nuclei near $^{40}\text{Ar}$

M. L. Liu, E. Ideguchi, H. Baba<sup>a</sup>, T. Fukuchi<sup>b</sup>, N. Hokoïwa<sup>c</sup>, C. Ishida<sup>d</sup>, N. Iwasaki<sup>e</sup>,  
T. Komatsubara<sup>f</sup>, T. Kubo<sup>a</sup>, M. Kurokawa<sup>a</sup>, S. Michimasa<sup>a</sup>, K. Morimoto<sup>a</sup>, K. Miyakawa<sup>f</sup>,  
M. Niikura, T. Ohnishi<sup>a</sup>, S. Ota<sup>g</sup>, A. Ozawa<sup>f</sup>, S. Shimoura, T. Suda<sup>a</sup>, M. Tamaki, I. Tanihata<sup>h</sup>,  
Y. Wakabayashi<sup>c</sup> and K. Yoshida<sup>a</sup>

*Center for Nuclear Study, Graduate School of Science, University of Tokyo*

<sup>a</sup>*RIKEN (The Institute of Physical and Chemical Research)*

<sup>b</sup>*Department of Physics, Rikkyo University*

<sup>c</sup>*Department of Physics, Kyushu University*

<sup>e</sup>*Department of Physics, Graduate School of Science, University of Tokyo*

<sup>f</sup>*Institute of Physics, University of Tsukuba*

<sup>g</sup>*Department of Physics, Faculty of Science, Kyoto University*

<sup>h</sup>*Physics Division, Argonne National Laboratory, USA*

## 1. Introduction

The phenomenon of nuclear shape coexistence manifests itself in the presence of close-lying nuclear states with different shapes. A particular instance is the coexistence of spherical ground state and deformed excited states in nuclei near the closed shells, where the high- $j$  orbits intrude across the energy gaps and therefore can give rise to the presence of the many-particle many-hole deformed states. The coexistence of spherical yrast states up to  $6^+$  and deformed rotational states up to  $(8^+)$  has been discovered in  $^{40}\text{Ar}$  [1]. This work will investigate the high-spin states based on different intrinsic shapes in  $^{40}\text{Ar}$  and its neighboring nuclei [1].

## 2. Experiment

In order to quest for high-spin states in nuclei  $^{40}\text{Ar}$ ,  $^{42}\text{K}$  and  $^{43}\text{K}$ , a test experiment was performed. A neutron-rich secondary beam  $^{38}\text{S}$  was produced at the RIPS (RIKEN Projectile-fragment Separator) facility by the fragmentation reaction [2]. A primary beam  $^{40}\text{Ar}$ , provided by the RIKEN Ring cyclotron at an energy of 63 MeV/A and with an intensity of 60 pnA, was utilized to bombard a  $^9\text{Be}$  target of 1.5 mm thickness. An aluminum wedge with a mean thickness of 221 mg/cm<sup>2</sup> was placed at the momentum-dispersive focal plane (F1) to get a clean isotope separation and to lower the energy of the fragments. The energy of the  $^{38}\text{S}$  beam was further lowered by another rotatable degrader of 0.425 mm thickness at the achromatic focal plane (F2). Particles of the secondary beam were identified by TOF- $\Delta E$  method.  $\Delta E$  (Energy loss) was measured by a silicon detector at F2 with a thickness of 0.5 mm; TOF (time of flight) information was obtained from the timing of a plastic scintillator at F2 relative to the cyclotron RF signal. By operating RIPS at the maximum values of momentum acceptance and solid angle, a typical intensity of  $\sim 1.0 \times 10^5$  particles per second for the  $^{38}\text{S}$  beam was obtained at F2. The low-energy  $^{38}\text{S}$  beam was transmitted to the final focal plane (F3) to impinge on a  $^9\text{Be}$  target of 1.8 mg/cm<sup>2</sup> to induce the fusion-evaporation reactions. Two PPAC (Parallel Plate Avalanche Counter) counters were placed at the upstream of the sec-

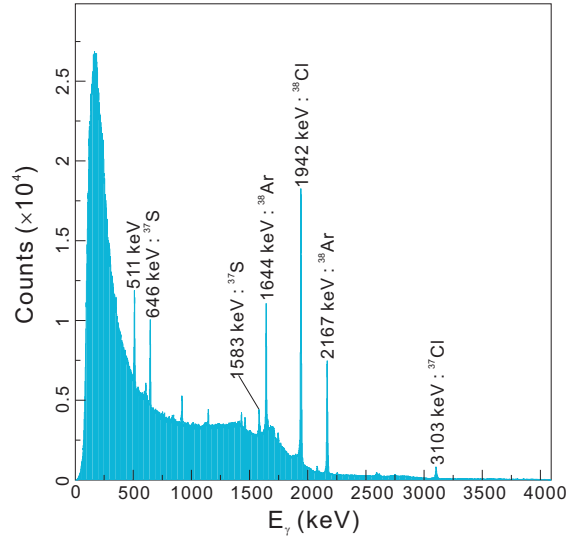


Figure 1. Gamma rays after the beta decay of  $^{38}\text{S}$ ,  $^{37}\text{P}$  and their daughter nuclei.

ondary target at F3 to profile the image and monitor the incident angle of the beam on the target; the beam energy before the secondary target was deduced to be 5.45 MeV/A from the time of flight between the upper-stream PPAC and the plastic scintillator at F2, with the energy loss in PPAC's being taken into account. Figure 1 shows  $\gamma$  rays after the beta decay of the secondary beam particles and their daughter nuclei. From the spectrum, we can see that the main components of the secondary beam particles were  $^{38}\text{S}$  and  $^{37}\text{P}$  at the final focal plane.

## 3. Analysis and Results

The recoil velocity of the compound nucleus  $^{47}\text{Ca}$  is deduced to be  $\sim 8.42\%$  of the light velocity. The large recoil velocity will lead to large Doppler shift of the emitted  $\gamma$  ray. In order to observe the de-excitation  $\gamma$  ray and do the Doppler correction, the GRAPE (Gamma-Ray detector Array with Position and Energy sensitivity) system was used for the experiment [3]. The array was composed

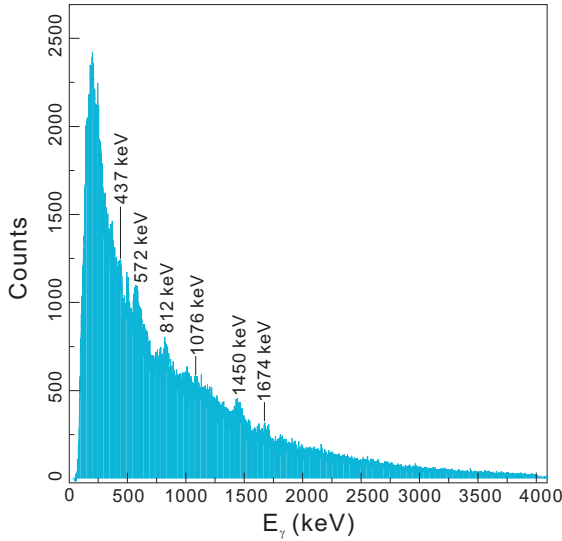


Figure 2. Doppler-corrected gamma-ray spectrum observed in the reaction  $^{38}\text{S}+^9\text{Be}$ .

of 14 Ge detectors surrounding the secondary target. Each detector contains two planar crystals that share a common anode and the cathode sides are divided into nine segments. The crystal has a thickness of 2.0 cm and diameter of 6.0 cm. The detectors were aligned so that their side surfaces face the target. From the velocity of the reaction product and the emission angle of the  $\gamma$  ray, the energy of Doppler-shifted  $\gamma$  ray can be corrected; the former is derived from the TOF and the position information of the beam detected by PPAC's, while the latter is extracted from the  $\gamma$  ray hit position in the detector relative to the direction of the reaction product. Here we took the center of each segment as the interaction points of the incident  $\gamma$  rays. Figure 2 shows the spectrum obtained from current analysis in the reaction of  $^{38}\text{S}$  bombarding  $^9\text{Be}$ .  $\gamma$  rays emitted from  $\alpha 3n$  channel  $^{40}\text{Ar}$  [1],  $5n$  channel  $^{42}\text{Ca}$  [4] and  $4n$  channel  $^{43}\text{Ca}$  [5] can be seen in the spectrum. The 437-keV line comes from the  $6^+ \rightarrow 4^+$  transition in  $^{42}\text{Ca}$ , while the nonobservation of the 1525-keV  $2^+ \rightarrow 0^+$  and 1228-keV  $4^+ \rightarrow 2^+$  lines is most probably due to the low efficiency of the detector in the 1.2-1.5 MeV region [4]. It should be noted that the peak at around 812 keV from  $^{42}\text{Ca}$  is the doublet of 810- and 815-keV transitions [4]. The components of the doublet 1450-keV line are the 1431-keV  $2^+ \rightarrow 0^+$  and 1460-keV  $4^+ \rightarrow 2^+$  transitions in  $^{40}\text{Ar}$  [1]. The strong 572-keV  $\gamma$  ray is the de-excitation transition of yrast  $6^+$  state in  $^{40}\text{Ar}$  [1], whereas the weak 1674- and 1076-keV lines are the corresponding first and second yrast transitions in  $^{43}\text{Ca}$  [5]. It is believed that the above-mentioned  $2^+$ ,  $4^+$  and  $6^+$  are low-lying spherical states in the nucleus  $^{40}\text{Ar}$  [1]. However, due to lack of statistics, we did not observe the  $K^\pi=0^+$  inband transitions and the transitions between different shapes in  $^{40}\text{Ar}$  [1], and the transitions from  $p3n$  channel  $^{43}\text{K}$  and  $p4n$  channel  $^{42}\text{K}$  [6]. To observe these transitions and study high-spin states based on different shapes more in  $^{40}\text{Ar}$ ,  $^{42}\text{K}$ ,  $^{43}\text{K}$ , etc., further experimental investigations are necessary.

## References

- [1] E. Bitterwolf *et al.*, Z. Phys. A **313** (1983) 123.
- [2] T. Kubo *et al.*, Nucl. Instrum. Methods B **461** (1992) 309.
- [3] S. Shimoura *et al.*, CNS Annual Report 2003 (2004) 87.
- [4] M. Lach *et al.*, Eur. Phys. J. A **16** (2003) 309.
- [5] P. Bednarczyk *et al.*, Eur. Phys. J. A **2** (1998) 157.
- [6] M. Morales *et al.*, Phys. Rev. C **58** (2003) 739.

# Measurement of $^{25}\text{Al}+p$ Resonances through Elastic Scattering with CRIB

J. Pearson<sup>a</sup>, A. A. Chen<sup>a</sup>, S. Kubono<sup>b</sup>, H. Yamaguchi<sup>b</sup>, T. Teranishi<sup>c</sup>, J. J. He<sup>b</sup>, L. H. Khiem<sup>b</sup>, A. Saito<sup>b</sup>, G. Amadio<sup>b</sup>, H. Fujikawa<sup>b</sup>, M. Niikura<sup>b</sup>, Y. Wakabayashi<sup>b</sup>, S. Nishimura<sup>d</sup>, Y. Togano<sup>e</sup>, A. Odahara<sup>f</sup>, J. Y. Moon<sup>g</sup>, Y. K. Kwon<sup>g</sup>, S. Cherubini<sup>h</sup>, R. Pizzone<sup>h</sup> and M. La Cognata<sup>h</sup>

<sup>a</sup>Department of Physics and Astronomy, McMaster University (Canada)

<sup>b</sup>Centre for Nuclear Study, University of Tokyo (Japan)

<sup>c</sup>Department of Physics, Kyushu University (Japan)

<sup>d</sup>RIKEN (Japan)

<sup>e</sup>Department of Physics, Rikkyo University, Tokyo (Japan)

<sup>f</sup>Department of Physics, Osaka University (Japan)

<sup>g</sup>Department of Physics, Chung-Ang University (Korea)

<sup>h</sup>University of Catania (Italy)

The origin of galactic  $^{26}\text{Al}$  remains a long-standing question in nuclear astrophysics. Within the context of explosive hydrogen burning, the  $^{25}\text{Al}(p,\gamma)^{26}\text{Si}$  reaction bypasses the production of  $^{26}\text{Al}$  at lower temperatures found in novae, while the same reaction contributes indirectly to  $^{26}\text{Al}$  production at higher temperatures. The present rate of the  $^{25}\text{Al}(p,\gamma)^{26}\text{Si}$  reaction suffers from significant uncertainties due to the lack of relevant structure information in the compound nucleus  $^{26}\text{Si}$ .

The recent detection of decaying  $^{26g}\text{Al}$  ( $t_{1/2} = (7.1 \pm 0.2) \times 10^5$  yr) via its characteristic 1.809 MeV  $\gamma$ -ray by the RHESSI and INTEGRAL satellites has furthered understanding of the production sites of this radioisotope [1, 2]. The COMPTEL all-sky map of the 1.809 MeV line [3] points to young, high-mass progenitors such as core collapse supernovae (CCSN) and Wolf-Rayet stars [4]. Though previous studies suggested that the measured  $2.8 \pm 0.8 M_{\odot}$  [5] of  $^{26g}\text{Al}$  in the Galaxy could have been entirely produced in CCSN [6], these new results have suggested that CCSN may be a much less dominant component, and that other sources, likely Wolf-Rayet stars, must contribute [7].

Due to the long lifetime of  $^{26g}\text{Al}$ , space-based  $\gamma$ -ray observatories such as INTEGRAL are unable to detect it from individual sources. Therefore, the likely primary progenitors can only be inferred from the Galactic  $^{26g}\text{Al}$  distribution. However, with a firm understanding of the  $^{26g}\text{Al}(p,\gamma)^{27}\text{Si}$  and  $^{25}\text{Al}(p,\gamma)^{26}\text{Si}$  rate we can infer solid upper limits for the nova contribution to Galactic  $^{26g}\text{Al}$  as a secondary source.

Classical novae are one potential source of  $^{26g}\text{Al}$  and it has been shown that up to  $0.4 M_{\odot}$  of the Galactic abundance could have been produced in these sites [8]. Of particular importance to the calculation of nova-synthesized  $^{26g}\text{Al}$  abundances are the  $^{25}\text{Al}(p,\gamma)^{26}\text{Si}$  and  $^{26g}\text{Al}(p,\gamma)^{27}\text{Si}$  reaction rates, the former being the most uncertain.

At the highest temperatures in explosive hydrogen burning (e.g. in supernovae), s-wave resonances in the energy range  $E_x(^{26}\text{Si}) \sim 6\text{--}8$  MeV will dominate the reaction rate (see Figure 1). While some states in this energy region have been found, their level parameters are largely unknown. Furthermore, a comparison between the relevant energy re-

gions in  $^{26}\text{Si}$  and in  $^{26}\text{Mg}$  reveals the presence of missing states in the former, some of which could be s-wave resonances in the  $^{25}\text{Al}+p$  system and therefore important for the stellar reaction rate.

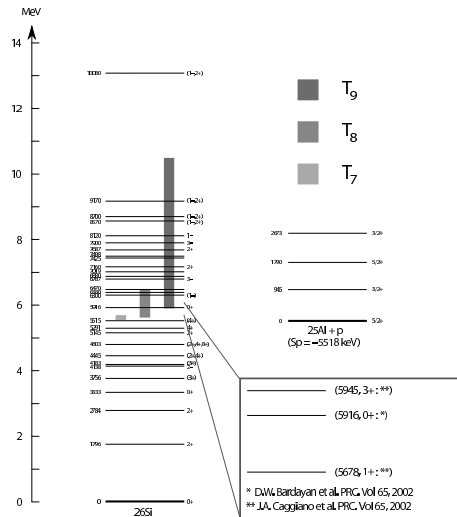


Figure 1. Astrophysically important energy levels in  $^{26}\text{Si}$  and the  $^{25}\text{Al}+p$  threshold [9, 10].

To address the uncertainties in the  $^{25}\text{Al}(p,\gamma)^{26}\text{Si}$  reaction rate and obtain spectroscopic information on  $^{26}\text{Si}$ , a  $^{25}\text{Al}+p$  elastic-scattering experiment in inverse kinematics was performed recently, using the CNS radioactive ion beam separator (CRIB) facility at RIKEN. The experiment aims to improve upon a similar previous experiment performed using CRIB by having a purer  $^{25}\text{Al}$  beam using a Wien filter and a higher beam intensity to increase the counting rate [11].

A  $^{24}\text{Mg}^{8+}$  primary beam with an intensity of  $1.6 \times 10^{11}$  pps, produced by an ECR ion source, was accelerated by the RIKEN AVF cyclotron to an energy of 7.49 MeV/u. The shape of the  $^{24}\text{Mg}$  beam was checked using a ZnS scintillator target at the F0 position and found to be well-contained within a  $3 \times 3$  mm spot. The beam bombarded a  $^2\text{H}$  gas target which was kept at a constant pressure of 760 Torr throughout the experiment. A primary beam reaction of  $^2\text{H}(^{24}\text{Mg},n)^{25}\text{Al}$  produced the desired secondary  $^{25}\text{Al}^{13+}$  beam with an intensity of  $2 - 5 \times 10^5$  pps. The cur-

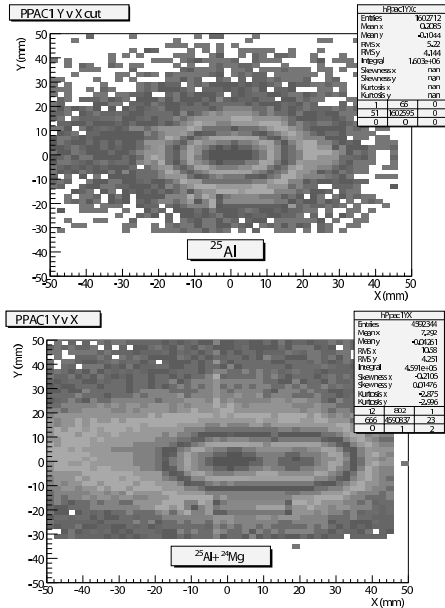


Figure 2. Ion species selection using a cut on RF timing.

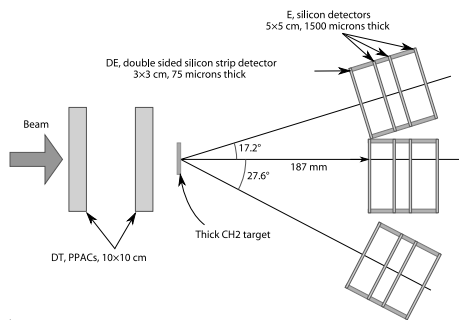


Figure 3. Detector configuration for the  $^{25}\text{Al}(p,p')^{25}\text{Al}$  reaction. The PPACs were used for beam identification, the  $E\Delta E$  telescopes for scattering product identification.

rent intensity was limited by the event-handling rate of the parallel-plate avalanche counters (PPACs) used for beam identification. The secondary beam was identified by using time-of-flight (TOF) (between the two PPACs on an achromatic focal plane at the F2 position), beam energy and TOF between the production target and a PPAC on the F2 plane (an example of secondary beam identification is shown in Figure 2).

The secondary beam impinged upon a thick polyethylene ( $\text{CH}_2$ ) target of  $6.5 \text{ mg/cm}^2$  in the F3 scattering chamber, where it was stopped. Three sets of silicon  $E\Delta E$  telescopes were used to detect elastically scattered protons from  $^1\text{H}(^{25}\text{Al},p)^{25}\text{Al}$ . The telescopes consisted of a  $75 \mu\text{m}$  thick position-sensitive silicon detector (PSD) backed by two  $1500 \mu\text{m}$  surface-barrier silicon detectors (SSD), installed at  $0.0$ ,  $17.2$  and  $27.6^\circ$ . The second SSD was added to each telescope to aid the background rejection of high-energy protons. Figure 3 shows the experimental configuration around the secondary target. An example  $E\Delta E$  spectrum is shown in Figure 4.

The  $^{25}\text{Al}$  beam had an energy of  $3.43 \text{ MeV/u}$ , allowing a scan up to  $\sim E_x = 8.5 \text{ MeV}$  in  $^{26}\text{Si}$ . A  $^{12}\text{C}$  target was used to obtain data for a background subtraction (due to a

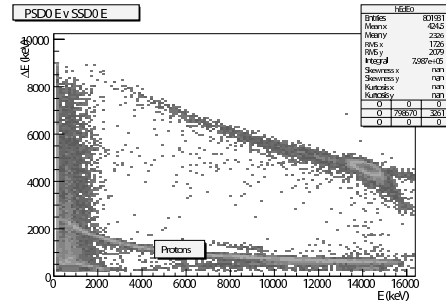


Figure 4. Example  $E\Delta E$  spectrum. Protons are clearly separated from other ion species.

contribution by carbon contained in the  $\text{CH}_2$  target) from the proton spectrum obtained with the  $\text{CH}_2$  target. An array of 10 NaI scintillator detectors were used to monitor the inelastic contribution to the yield. These were positioned slightly upstream of and above the target position. Energy calibration was made with a proton beam at energies of 5, 9 and 14 MeV (as determined by the CRIB magnet settings). Analysis of the data is ongoing.

## References

- [1] D. M. Smith, *Astrophys. J.* **589** (2003) L55.
- [2] J. Knödlseider, *New Astron. Rev.* **48** (2004) 189.
- [3] R. Diehl *et al.*, *Astron. Astrophys.* **298** (1995) 445.
- [4] N. Prantzos and R. Diehl, *Physics Reports* 267 (1996) 1.
- [5] R. Diehl *et al.*, *Nature* **439** (2006) 54.
- [6] F. X. Timmes *et al.*, *Astrophys. J.* **449** (1995) 204.
- [7] N. Prantzos, *Astron. Astrophys.* **420** (2004) 1033.
- [8] J. José, M. Hernanz and A. Coc, *Astrophys. J.* **479** (1997) L55 9.
- [9] D. W. Bardayan *et al.*, *Phys. Rev. C* **65** (2002) 032801.
- [10] J. A. Caggiano *et al.*, *Phys. Rev. C* **65** (2002) 055801.
- [11] J. Y. Moon, C. S. Lee, J. H. Lee *et al.*, *Nucl. Phys. A* **758** (2005) 158.

# Low-Lying Resonance Levels in $^{14}\text{O}$

T. Teranishi<sup>a</sup>, S. Kubono, H. Yamaguchi, J. J. He, A. Saito, H. Fujikawa, G. Amadio, M. Niikura, S. Shimoura, Y. Wakabayashi, S. Nishimura<sup>b</sup>, M. Nishimura<sup>b</sup>, J. Y. Moon<sup>c</sup>, C. S. Lee<sup>c</sup>, A. Odahara<sup>d</sup>, D. Sohler<sup>e</sup>, L. H. Khiem<sup>f</sup>, Z. H. Li<sup>g</sup>, G. Lian<sup>g</sup>, and W. P. Liu<sup>g</sup>

Center for Nuclear Study, Graduate School of Science, University of Tokyo

<sup>a</sup>Department of Physics, Kyushu University

<sup>b</sup>The Institute of Physical and Chemical Research (RIKEN)

<sup>c</sup>Chung-Ang University, Republic of Korea

<sup>d</sup>Department of Physics, Osaka University

<sup>e</sup>ATOMKI, Hungary

<sup>f</sup>Institute of Physics and Electronics, Vietnamese Academy for Science and Technology, Vietnam

<sup>g</sup>China Institute of Atomic Energy (CIAE), P.R. China

## 1. Introduction

Energy systematics of isobaric analog multiplets gives interesting information in a nuclear structure in conjunction with the charge-independence of nuclear force and the effects of Coulomb force. A set of  $T = 1$  triplets in  $A = 14$  nuclei ( $^{14}\text{C}$ ,  $^{14}\text{N}$ , and  $^{14}\text{O}$ ) is a good example of isobaric analog multiplets that has been studied for many years. However, knowledge of the  $^{14}\text{O}$  levels is still poor compared to that of  $^{14}\text{C}$  and  $^{14}\text{N}$ . The latest compilation of the  $^{14}\text{O}$  levels is found in ref. [1], but new experimental results [2, 3, 4] have been reported after the compilation. The  $J^\pi$  value of the 6.8-MeV level has yet to be determined. Its width has been recently determined to be 107(40) keV [4]. The  $0^-$  level, which is supposed to be several hundreds keV above the  $1^-$  level at 5.2 MeV (see Fig. 1), has yet to be identified. The  $E_x$ ,  $\Gamma$ , and  $J^\pi$  for the low-lying  $^{14}\text{O}$  levels should be further investigated in order to study the wave functions and to determine their relations to the analog levels. In the present study, we have investigated resonance levels in  $^{14}\text{O}$  populated as intermediate states in the  $^{13}\text{N}+p$  elastic scattering, which was measured in inverse kinematics with a secondary beam of  $^{13}\text{N}$  and a proton target.

## 2. Experiment

The experiment was performed at CRIB [5] of CNS in the RIKEN facility. The secondary  $^{13}\text{N}$  beam was produced by the  $p(^{13}\text{C}, ^{13}\text{N})n$  reaction with a primary  $^{13}\text{C}$  beam and a hydrogen gas target. The primary  $^{13}\text{C}$  beam was accelerated by the Upgraded AVF cyclotron up to 6.0 MeV per nucleon and had an intensity of about 400 pA. The hydrogen gas target with a thickness of  $0.3 \text{ mg/cm}^2$  was confined in a cell by two Havar window foils, each of which was  $2.2 \text{ }\mu\text{m}$  thick. The secondary  $^{13}\text{N}$  particles were selected by the CRIB separator. To improve the beam purity, a  $3\text{-}\mu\text{m}$  thick mylar energy degrader was inserted at the intermediate momentum-dispersive focal plane of CRIB.

The detection system for the  $^{13}\text{N}+p$  elastic scattering was set inside a vacuum chamber at the final focal plane of CRIB. The  $^{13}\text{N}$  beam particles went through two parallel-plate avalanche counters (PPACs) before reaching the secondary proton target. The timing and position information

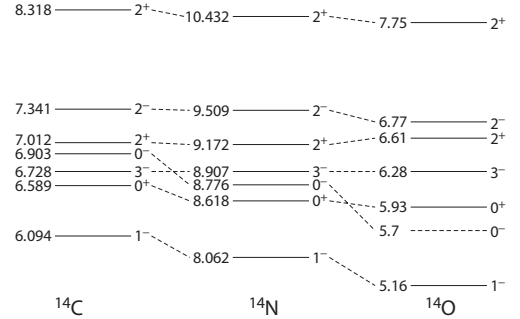


Figure 1. Diagram for the first seven excited  $T = 1$  levels in  $^{14}\text{C}$ ,  $^{14}\text{N}$ , and  $^{14}\text{O}$ . The  $E_x$  and  $J^\pi$  values for  $^{14}\text{C}$  and  $^{14}\text{N}$  are from ref. [1], while those for  $^{14}\text{O}$  are based on the present work and ref. [4]. The vertical positions of the levels are shifted to align the  $3^-$ .

from the two PPACs were used to determine the target hit point and the beam velocity vector on an event-by-event basis. The secondary  $^{13}\text{N}$  beam energy before the target was 48.6 MeV with a width of 1.6 MeV (FWHM). The  $^{13}\text{N}$  intensity was about  $2 \times 10^5$  particles/sec, which was about 98 % of the total secondary beam intensity. We utilized the thick target method [6, 7] to efficiently measure the excitation functions of  $^{13}\text{N}+p$  elastic scattering without changing the  $^{13}\text{N}$  energy before the proton target, which was a sheet of  $(\text{CH}_2)_n$  with a thickness of  $8.3 \text{ mg/cm}^2$  and a diameter of 3 cm. Recoil protons emitted from the proton target were detected by a silicon-detector telescope, which consisted of two layers with the same sensitive area of  $50 \times 50 \text{ mm}^2$ . The first ( $\Delta E$ ) and second ( $E$ ) layers had thicknesses of  $75 \text{ }\mu\text{m}$  and  $1500 \text{ }\mu\text{m}$ , respectively. The telescope was set with its center at a laboratory angle of  $\theta_{\text{LAB}} = 0^\circ$ .

Protons were identified using the  $\Delta E$ ,  $E$ , and time-of-flight information. The proton energy was deduced from the energy sum of  $\Delta E$  and  $E$ . The  $\Delta E$  layer had double-sided 32 (= 16 + 16) stripes, which enabled the proton scattering angle to be determined. The center-of-mass energy ( $E_{\text{CM}}$ ) was deduced from the proton energy and scattering angle on an event-by-event basis by assuming the kinematics of elastic scattering and by considering the energy losses of

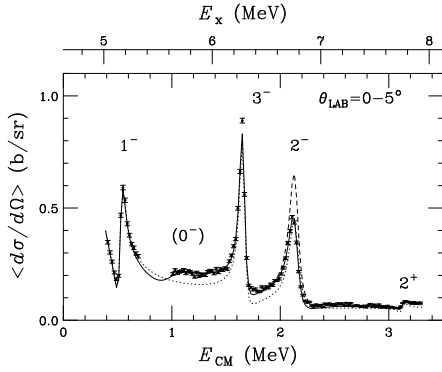


Figure 2. Experimental excitation function for the  $^{13}\text{N}+p$  scattering measured at around  $\theta_{\text{LAB}} = 0^\circ$ . The solid line shows the result of the fitting calculation. The dashed line represents the result when  $J^\pi$  for the 6.8-MeV is changed to  $3^-$ . The dotted line shows the result without a contribution of the  $0^-$  level at  $E_x \sim 5.7$  MeV.

beam and proton in the target.

### 3. Results and discussion

Figure 2 shows the  $^{13}\text{N}+p$  excitation function measured by the silicon detector telescope at  $\theta_{\text{LAB}} = 0^\circ$ . The spectrum covers  $E_{\text{CM}} = 0.4\text{--}3.3$  MeV ( $E_x = 5.0\text{--}7.9$  MeV). The spectrum has a gap at  $E_{\text{CM}} \sim 0.8$  MeV due to the removed events corresponding to the detector dead layers between the  $\Delta E$  and  $E$  sensitive layers. Four resonance-like signatures are clearly seen at  $E_{\text{CM}} \sim 0.5, 1.6, 2.1,$  and  $3.1$  MeV in the spectrum. These may be attributed to known  $^{14}\text{O}$  levels at  $E_x = 5.2, 6.3, 6.8,$  and  $7.7$  MeV with  $J^\pi = 1^-, 3^-$ , (unknown), and  $2^+$ , respectively. The peak of 6.8-MeV level ( $J^\pi = \text{unknown}$ ) has a very similar shape with the 6.3-MeV peak, which is dominated by a  $d$ -wave ( $l = 2$ ) resonance. Thus,  $J^\pi$  for the 6.8-MeV level is probably  $2^-$  or  $3^-$  in the case of  $l = 2$ . In order to determine  $J^\pi$  for the 6.8-MeV level, the experimental spectrum was fitted with an R-matrix based calculation, which used essentially the same method as that used in ref. [8]. The result for the  $J^\pi = 2^-$  case is shown by the solid line in Fig. 2 and is consistent with the experimental spectrum. However, when  $J^\pi = 3^-$  is assumed for the 6.8-MeV level in the calculation, the 6.8-MeV peak becomes higher as shown by the dashed line in Fig. 2, which is inconsistent with the experimental data. Therefore, we assigned  $J^\pi = 2^-$  to the 6.8-MeV level.

The  $0^-$  level, which should be above the  $1^-$  level, is not clearly identified in the present spectrum. However, we included the  $0^-$  level in the fitting calculation to improve the fit with the data. We estimated  $E_x \sim 5.7$  MeV and  $\Gamma \sim 0.5$  MeV for the  $0^-$  level by calculating the resonance phase shift in a proton scattering model with a Woods-Saxon potential [9, 10]. A result of calculation without the  $0^-$  level is shown by the dotted line in Fig. 2. The agreement of the fit

without the  $0^-$  level (dotted line) is much worse than that with the  $0^-$  level (solid line).

The widths of the  $1^-$ ,  $3^-$ , and  $2^-$  level were determined to be 42, 42, and, 92 keV (preliminary results), respectively, by the fitting procedure. These widths are comparable to the single-particle widths estimated by the Woods-Saxon potential model. This indicates that the wave functions of these low-lying negative parity levels in  $^{14}\text{O}$  can be well described by a  $^{13}\text{N}_{g.s.}+p$  component where the proton is in the  $2s_{1/2}$  orbit for the  $1^-$  level or in the  $1d_{5/2}$  orbit for the  $3^-$  and  $2^-$  levels. These results are consistent with the large spectroscopic factors for the mirror levels in  $^{14}\text{C}$  populated by the  $^{13}\text{C}(d,p)^{14}\text{C}$  reaction [11]. Therefore, significant breaking of charge independence was not found for these  $^{14}\text{O}$  levels in the present experimental information. The energies of the low-lying  $^{14}\text{O}$  resonances were also updated by the present experiment. These energies are also important for studying the wave functions of these levels and the astrophysical  $^{13}\text{N}(p,\gamma)^{14}\text{O}$  reaction rates. Lowering of the  $0^-$  and  $1^-$  energies in  $^{14}\text{O}$  as shown in Fig. 1 may be mainly due to Thomas-Ehrman shifts [12, 13, 14]. Proton elastic resonance scattering with a thick target adopted here is a useful spectroscopic tool for investigating single-particle resonance levels in unstable nuclei.

### References

- [1] F. Ajzenberg-Selove, Nucl. Phys. A **523** (1991) 1.
- [2] P. Decroock *et al.*, Phys. Lett. B **304** (1993) 50.
- [3] P. V. Magnus *et al.*, Phys. Rev. C **49** (1994) R1755.
- [4] A. Negret *et al.*, Phys. Rev. C **71** (2005) 047303.
- [5] Y. Yanagisawa *et al.*, Nucl. Instrum. and Methods **A539** (2005) 74.
- [6] K. P. Artemov *et al.*, Sov. J. Nucl. Phys. **52** (1990) 408.
- [7] S. Kubono, Nucl. Phys. A **693** (2001) 221, and references therein.
- [8] T. Teranishi *et al.*, Phys. Lett. B **556** (2003) 27.
- [9] T. A. Tombrello, Phys. Lett. **23** (1966) 134.
- [10] R. Sherr, Phys. Rev. C **73** (2006) 037310, and references therein.
- [11] R. J. Peterson *et al.*, Nucl. Phys. A **425** (1984) 469.
- [12] R. G. Thomas, Phys. Rev. **81** (1951) 148.
- [13] J. B. Ehrman, Phys. Rev. **81** (1951) 412.
- [14] R. G. Thomas, Phys. Rev. **88** (1952) 1109.

# Excitation Function Measurement by using $^{19}\text{F}+^{96}\text{Zr}$ Reaction

Y. Zheng, E. Ideguchi, M. Niikura, M. Liu, H. Baba<sup>a</sup>, T. Fukuchi<sup>b</sup>, T. Morikawa<sup>c</sup>, S. Michimasa<sup>a</sup>, S. Mitarai<sup>c</sup>, S. Ota, S. Shimoura, Y. Wakabayashi, and H. Yamaguchi

Center for Nuclear Study, Graduate School of Science, the University of Tokyo

<sup>a</sup>The Institute of Physical and Chemical Research (RIKEN)

<sup>b</sup>Department of Physics, Rikkyo University

<sup>c</sup>Department of Physics, Kyushu University

The excited states of  $A\sim 100$  nuclei with  $Z\sim 50$  are expected to be of single particle character due to the spherical shell gap for protons. However, other excitation mechanisms such as magnetic rotation (M1 band) [1] and collective rotation exhibiting smooth band termination [2, 3] also play a role in generating angular momentum. At high-spin states, a presence of superdeformed (SD) band is also reported in  $^{108}\text{Cd}$  [4] and it is suggested to have the most deformed structure identified in any nucleus. The wealth of excitation modes in these nuclei make them particularly interesting system to study. In this region  $^{109}\text{In}$  is expected to have M1 band, smooth band termination, and SD band at high-spin states. In order to identify these excitation modes, we have investigated high-spin states in  $^{109}\text{In}$ . In this report in-beam gamma-ray measurement of nuclei in  $A\sim 100$  region by using  $^{19}\text{F}+^{96}\text{Zr}$  reaction is presented.

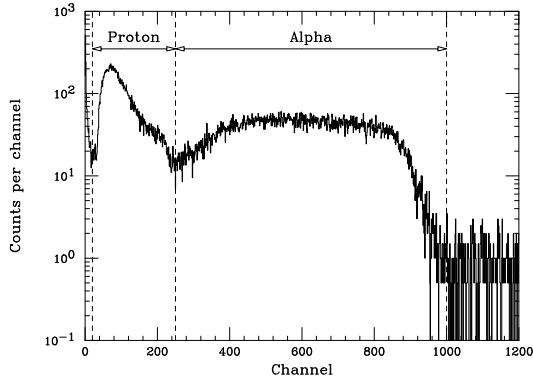


Figure 1. Energy spectrum of Si detector.

The experiment was performed at RIKEN accelerator research facility. The  $^{19}\text{F}$  ions accelerated by AVF cyclotron to an energy of 6 MeV/A was used to bombard a  $^{96}\text{Zr}$  target with a thickness of 1 mg/cm<sup>2</sup>. High-spin states of  $A\sim 100$  nuclei were populated by the  $^{19}\text{F}+^{96}\text{Zr}$  reaction. Beam energy was chosen so that the cross section to produce  $^{109}\text{In}$  becomes dominant, which is neighboring nucleus of  $^{108}\text{Cd}$ . In order to take two energy points for the excitation function measurement, an Al degrader of 0.01 mm was used to lower the energy to 5.45 MeV/A. Gamma rays from fusion evaporation residues were measured by using 2 segmented-planar Ge detectors [5] placed at 120° and a coaxial Ge detector at 90° relative to the beam direction. Evaporated charged particles were simultaneously detected by using a Si Ball, a 4π array of 11 Si detectors [6]. Figure 1 shows an energy spectrum of the Si detector at forward angle. Protons and α particles were identified by gating different energy region

in the spectrum.

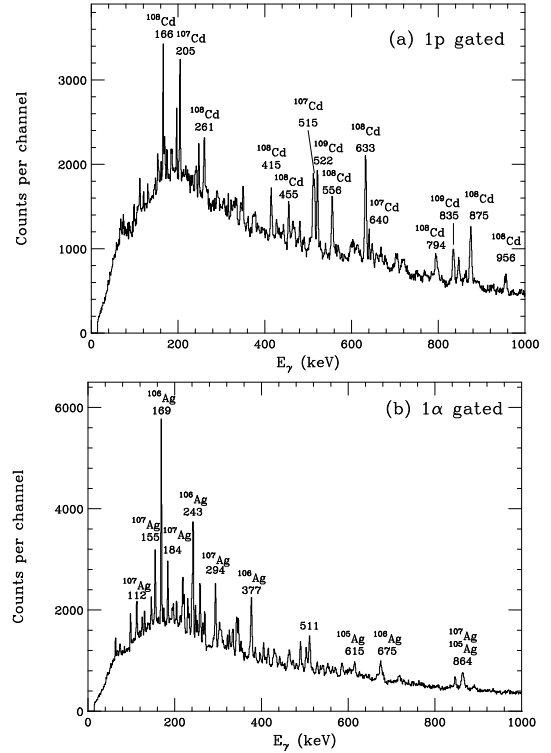


Figure 2. Gamma-ray energy spectra at 6 MeV/A with a proton gate (a) and an α gate (b).

Production cross-sections of evaporation residues as a function of beam energies in the  $^{19}\text{F}+^{96}\text{Zr}$  reaction were estimated by using the statistical model code, CASCADE [7]. In the measured energy region, nuclei in the evaporation channels of 5–7n ( $^{108-110}\text{In}$ ), 1p4n–1p6n ( $^{107-109}\text{Cd}$ ), and 1α4n–1α6n ( $^{105-107}\text{Ag}$ ) are expected to be mainly produced.

Figure 2 shows the gamma-ray energy spectra obtained in the 6 MeV/A data with a proton gate (a) and an α gate (b). Low-lying states of these nuclei were previously studied [8,9,10,11,12,13,14,15]. Gamma-ray assignments were performed by using previously reported peak energies. In Fig.2(a), gamma peaks at 633, 875, 556, 794, and 956 keV appeared strongly which are yrast cascade transitions of  $^{108}\text{Cd}$ . The 205, 640 and 515 keV peaks of  $^{107}\text{Cd}$  as well as 522 and 835 keV peaks of  $^{109}\text{Cd}$  also appeared clearly. In Fig.2(b), strong peaks at 169, 243, 377, and 675 keV are dipole transitions in  $^{106}\text{Ag}$ . In the low energy region several gamma peaks of  $^{107}\text{Ag}$  appeared at 112, 155, 184, and

294 keV. The 864 keV peak is a doublet of transitions in  $^{105}\text{Ag}$  and  $^{107}\text{Ag}$ . At 615 keV  $11/2^+ \rightarrow 9/2^+$  transition of  $^{105}\text{Ag}$  was also observed.

In order to perform excitation-function analysis,  $\gamma$ -ray peak intensities at lowest-lying transitions of each evaporation residues normalized by that of the  $2^+ \rightarrow 0^+$  transition in  $^{108}\text{Cd}$  were plotted at two energy points, 5.45 and 6.0 MeV/A in Fig. 3(a). In this plot proton and  $\alpha$ -particle detection efficiency of Si Ball was not included.

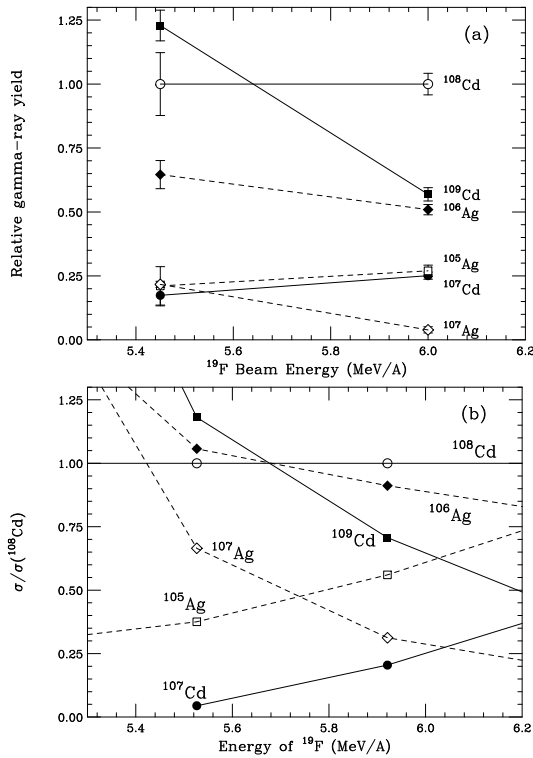


Figure 3. (a) Relative  $\gamma$ -ray yield of lowest lying transitions in  $^{107-109}\text{Cd}$  and  $^{105-107}\text{Ag}$  normalized by that of  $^{108}\text{Cd}$ . (b) Relative cross sections of  $^{107-109}\text{Cd}$  and  $^{105-107}\text{Ag}$  normalized by that of  $^{108}\text{Cd}$  calculated by CASCADE code.

For the comparison, relative cross-sections of  $^{107-109}\text{Cd}$  and  $^{105-107}\text{Ag}$  normalized by that of  $^{108}\text{Cd}$  calculated by the CASCADE code were plotted as a function of beam energies in Fig. 3(b). Relative  $\gamma$ -ray yield of  $^{107}\text{Cd}$  is increasing while that of  $^{109}\text{Cd}$  is decreasing as  $^{19}\text{F}$  beam energy increases. This trend as well as relative intensities of  $^{107}\text{Cd}$  and  $^{109}\text{Cd}$  were reproduced by the CASCADE calculation. In Fig. 3(a) the  $\gamma$ -ray yield curves for  $^{108}\text{Cd}$  and  $^{109}\text{Cd}$  cross each other around 5.7 MeV/A. This crossing point was almost reproduced by the calculation. In  $^{106,107}\text{Ag}$ , relative  $\gamma$ -ray yield is decreasing but that of  $^{105}\text{Ag}$  is increasing. This trend was also reproduced by the calculation.

Further analysis of the experimental data is still in progress.

## References

- [1] A. Gadea *et al.*, Phys. Rev. C **55**(1997) R1.
- [2] I. Ragnarsson *et al.*, Phys. Rev. Lett. **74** (1995) 3935.

- [3] R. Wadsworth *et al.*, Phys. Rev. C **53** (1996) 2763.
- [4] R. M. Clark *et al.*, Phys. Rev. Lett. **87** (2001) 202502.
- [5] S. Shimoura, Nucl. Instrum. Methods A **525** (2004) 188.
- [6] T. Kuroyanagi *et al.*, Nucl. Instrum. Methods A **316** (1992) 289.
- [7] F. Fühlhofer, Nucl. Phys. A **280** (1977) 267.
- [8] C. J. Chiara *et al.*, Phys. Rev. C **64** (2001) 054314.
- [9] J. Kownacki *et al.*, Nucl. Phys. A **627** (1997) 239.
- [10] D. Jerrestam *et al.*, Nucl. Phys. A **545** (1992) 835.
- [11] N. S. Kelsall *et al.* Phys. Rev. C **61** (2000) 011301(R).
- [12] C. J. Chiara *et al.*, Phys. Rev. C **61** (2000) 034318.
- [13] D. Jerrestam *et al.*, Phys. Rev. C **52** (1995) 2448.
- [14] P. Joshi *et al.*, J. Phys. (London) G **31** (2005) S1895.
- [15] F. R. Espinoza-Quiñones *et al.*, Phys. Rev. C **55** (1997) 1548.

# Proton Resonance Scattering of ${}^7\text{Be}$

H. Yamaguchi, A. Saito, J. J. He, Y. Wakabayashi, G. Amadio, H. Fujikawa, S. Kubono, T. Teranishi<sup>a</sup>, S. Nishimura<sup>b</sup>, Y. Togano<sup>c</sup>, Y. K. Kwon<sup>d</sup>, L. H. Khiem<sup>e</sup>, M. Niikura, N. Iwasa<sup>f</sup> and K. Inafuku<sup>f</sup>

*Center for Nuclear Study, Graduate School of Science, University of Tokyo*

<sup>a</sup>*Department of Physics, Kyushu University*

<sup>b</sup>*RIKEN (The Institute of Physical and Chemical Research)*

<sup>c</sup>*Department of Physics, Rikkyo University*

<sup>d</sup>*Department of Physics, Chung-Ang University*

<sup>e</sup>*Department of Physics and Electronics, Vietnam Academy of Science and Technology*

<sup>f</sup>*Department of Physics, Tohoku University*

## 1. Introduction

The astrophysical S-factor  $S_{17}(E)$  is one of the most important parameters in the standard solar model, and is defined as

$$S_{17}(E) = E\sigma_{17}(E) \exp(2\pi\eta), \quad (1)$$

where  $\sigma_{17}(E)$  is the cross section of the  ${}^7\text{Be}(p,\gamma){}^8\text{B}$  reaction, and  $\eta$  is the Sommerfeld parameter. This  $S_{17}$  value at the solar energy is directly related to the flux of the  ${}^8\text{B}$  neutrino observed on the earth.  ${}^8\text{B}$  neutrinos are only less than 0.01 % of the total neutrinos emitted from the sun, but they are the majority of the detected neutrinos in most of the neutrino detectors such as Super-Kamiokande and Sudbury Neutrino Observatory (SNO). Due to this reason,  $S_{17}(E)$  is regarded as an important factor for the solar neutrino problem in the standard solar model. Although great efforts were spent by many experimental groups [1], the experimental precision remains still around 10 %, because of the small reaction cross section. It is claimed that the determination of the  $S_{17}$  below 300 keV with a precision better than 5% may make a major contribution to our knowledge for the solar model [2].

The existence of excited levels of  ${}^8\text{B}$  may affect the determination of  $S_{17}$ . However, we do not have sufficient knowledge of the nuclear structure of  ${}^8\text{B}$ . Only the lowest two states at 0.77 MeV and 2.32 MeV were clearly observed in past experiments. Another excited state around 3 MeV was observed as an unexpectedly wide resonance, and this was explained as a low-lying 2s state [3]. The reason why a 2s state appeared at such a low energy is also an interesting topic, and there are theoretical investigations [4, 5, 6]. This kind of wide states may affect the measurement of  ${}^7\text{Be}(p,\gamma){}^8\text{B}$  cross section even at very low energies (much less than 1 MeV). In the same measurement, an indication of  $1^+$  state at 2.8 MeV was also reported. In another recent experiment [7], on the other hand, they could not observe the  $1^+$  state at 2.8 MeV nor yet another  $1^+$  state at 1.5 MeV, the latter of which was theoretically proposed in [8]. The wide state was not directly observed, but they concluded that their spectrum is consistent if it is located at 3.5 MeV with a width of 4 MeV or more. Thus we intended to measure the resonances of  ${}^8\text{B}$ , to evidently observe the 3.5 MeV resonance reported in the past measurements, and

to explore the totally unknown region  $E > 3.5$  MeV, where we may find new resonances. The “thick target method”, by which we can measure proton elastic resonance scatterings, was suitable for our purpose.

The  ${}^7\text{Be}(p,\gamma){}^8\text{B}$  reaction and  ${}^8\text{B}$  structure are important topics also in the nuclear synthesis. In a standard nuclear synthesis theory, the triple- $\alpha$  process is considered as the dominant process to pass over the stability gap at  $A=8$ . However, in special environments such as very metal-poor, high temperature stars, the proton- or  $\alpha$ -capture process of  ${}^7\text{Be}$  might play a significant role, and thus how they compete each other is an interesting problem. We are able to obtain information about these processes by measuring the  ${}^7\text{Be}(p,p){}^7\text{Be}$  elastic scatterings.

## 2. Method

The measurement was performed at CRIB [9, 10]. CRIB can produce RI beams with the in-flight method, using primary heavy-ion beams from the AVF cyclotron of RIKEN ( $K=70$ ). The primary beam used in this measurement was  ${}^7\text{Li}^{3+}$  of 8.76 MeV/u, with the beam current of about 100 pA. The RI-beam production target was pure hydrogen gas, which was enclosed in an 8 cm-long cell, at 760 Torr and room temperature ( $\sim 300$  K). The  ${}^7\text{Be}$  beam energy used in this measurement was 53.8 MeV, which enabled us to measure events with the center-of-mass energy up to 6.7 MeV.

We used a standard experimental method for the proton elastic resonance scattering, well-established at CRIB [11]. A main feature of this method is the thick target, which makes it possible to measure the cross section of various excitation energies at the same time, and so is suitable for the elastic resonance scattering.

The targets and detectors for the scattering experiment were in a vacuum chamber located at the downstream of the Wien filter. Figure 1 shows a schematic setup in the experimental chamber. Two PPACs (Parallel-Plate Avalanche Counters [12]) measured the timing and position of the incoming  ${}^7\text{Be}$  beam. The timing information was used for making event triggers, and also for the particle identification by the time-of-flight (TOF) method. The beam position and its incident angle at the target were determined by extrapolating the positions measured by the PPACs. The

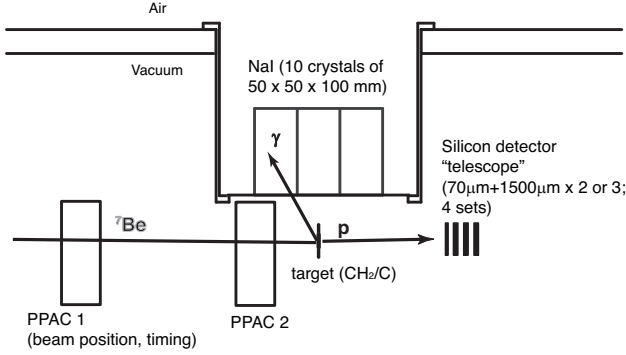


Figure 1. Setup at the experimental chamber (schematic).

targets were foils of 39 mg/cm<sup>2</sup>-thick polyethylene (CH<sub>2</sub>), and 54 mg/cm<sup>2</sup>-thick carbon. Carbon foils were used for evaluating backgrounds by carbon in the polyethylene target. These target foils were thick enough to stop all the <sup>7</sup>Be beam. Multi-layered silicon detector sets (called  $\Delta E$ -E telescopes) were used for measuring the energy and angular distribution of the recoil protons. They were placed  $\sim 23$  cm distant from the target, and they covered scattering angle of up to 45 degrees in the laboratory frame. Each  $\Delta E$ -E telescope consisted of a  $\Delta E$  counter and two or three E counters, all of which had an area of 50 mm x 50 mm. Each of the  $\Delta E$  counters was 60–75  $\mu\text{m}$  thick and divided into 16 strips for both sides. The E counters were 1.5 mm thick and were put in rear of the  $\Delta E$  counters. The recoil proton energy was 23 MeV at maximum, and a proton having this energy could not penetrate all the E counters. With these  $\Delta E$ -E telescopes, we identified recoil protons from other particles. NaI detectors were used for measuring 429 keV gamma rays from inelastic scatterings,  $p(^7\text{Be}, ^7\text{Be}^*)p$ . Each NaI crystal has a geometry of 50 mm x 50 mm x 100 mm, and ten crystals were used to cover  $\sim 20\%$  of the total solid angle.

Compared to the past measurements with similar methods [3, 7], this measurement has three major advantages. The first one is the energy range. We used a high-energy <sup>7</sup>Be beam, and we could measure up to 6.8 MeV in the excitation energy of <sup>8</sup>B. The second is the covered scattering angle. We measured data with almost full coverage between 0 and 45 degrees in laboratory frame, and thus we obtained complete information about the angular distribution. The final advantage is that we used the NaI detectors to evaluate the inelastic scattering events. The contribution of the inelastic scattering events should be taken into account for the excitation function.

### 3. Result

#### 3.1. Beam production

We used full-stripped lithium (<sup>7</sup>Li<sup>3+</sup>) beam from AVF cyclotron to obtain a high energy secondary beam. Although this was the first trial of <sup>7</sup>Li<sup>3+</sup> beam in RIKEN, it was successfully operated and used in this measurement. Figure 2 shows the time of flight and energy of the secondary beams detected at near the F2 focal plane. The time of flight was determined by the timing of PPAC signal against the RF signal of the AVF cyclotron. <sup>7</sup>Be<sup>4+</sup> had

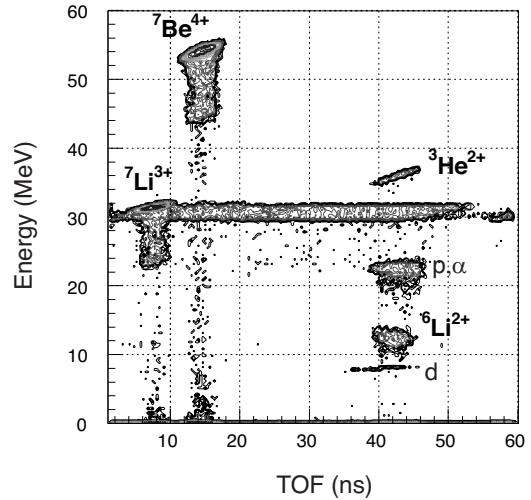


Figure 2. Secondary beams detected at the F2 focal plane.

the highest energy among the other beams, and the beam purity (the number ratio of <sup>7</sup>Be<sup>4+</sup> to total) was 56%. The largest background was from the primary beam, <sup>7</sup>Li<sup>3+</sup>. The other particles, such as proton, deuteron,  $\alpha$ , and <sup>6</sup>Li, are also seen in this figure, of which positions agree well with our calculations. The intensity of the produced <sup>7</sup>Be<sup>4+</sup> beam was  $5 \times 10^5$  particles per second at F2. For low-energy and relatively light ions as in this experiment, the Wien filter worked efficiently. The Wien filter was operated at high voltages of  $\pm 39$  kV with the corresponding magnetic field of 0.025 T. With these conditions, we had a beam purity of almost 100% at the experimental target.

#### 3.2. Measured recoil protons

Figure 3 shows the relation of the energy deposit in the first layer and the total energy, for the particles measured with one of the silicon  $\Delta E$ -E telescopes. Comparing these with energy-loss calculations, we performed a clear particle identification, as indicated in the figure. Proton was the most frequently detected particle, but we also detected considerable amount of <sup>3</sup>He and <sup>4</sup>He, which should be originated from <sup>7</sup>Be. Using these data, we were able to select proton events from other particles clearly.

The proton energy at the reaction point can be calculated from the measured proton energy, by considering the energy loss in the target. Then the proton energy  $E_p$  can be converted into the center-of-mass energy  $E_{\text{cm}}$ , with the following formula,

$$E_{\text{cm}} = E_p \frac{m_1 + m_7}{4m_7 \cos^2 \theta}, \quad (2)$$

where  $m_1$  and  $m_7$  are the masses of proton and <sup>7</sup>Be,  $\theta$  is the scattering angle. The excitation energy is the sum of center-of-mass energy of the elastic resonance scattering and the proton threshold energy (0.1375 MeV in this case),

$$E_{\text{ex}} = E_{\text{cm}} + E_{\text{th}}. \quad (3)$$

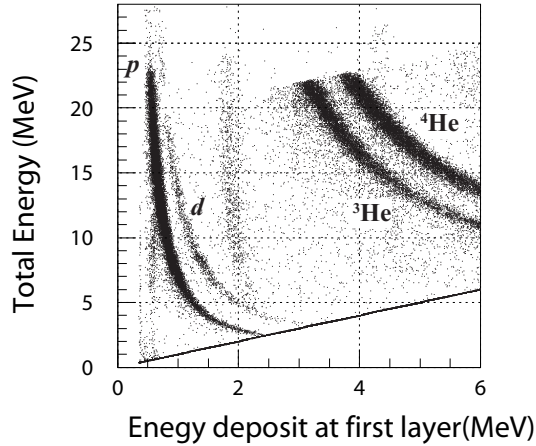


Figure 3.  $\Delta E$ - $E$  relationship of the detected particles with a silicon telescope.

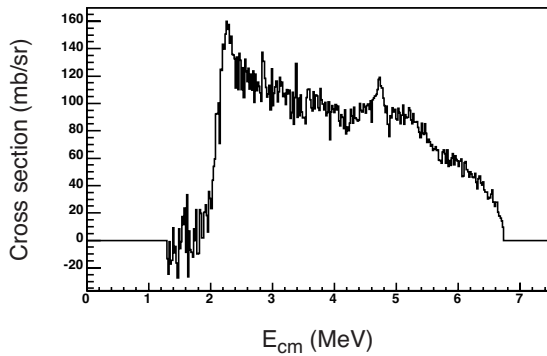


Figure 4. Excitation function measured at 0 degrees (preliminary). The excitation energy of  ${}^8\text{B}$ ,  $E_{\text{ex}}$  equals to  $E_{\text{cm}}+0.1375$  MeV.

By calculating the cross section from the counted numbers of the proton events, excitation functions were obtained. Figure 4 shows an excitation function at zero degree. The analysis is still going on, and this spectrum should be regarded as a preliminary one. The cross section agree well with the past measurements [3, 7] in the energy region around the known 2.2 MeV resonance. The 3.5 MeV resonance, which was reported as a wide resonance, is not seen in this preliminary spectrum. Some part of the continuum spectrum is considered as contributions from inelastic scatterings and three-body decays of  ${}^8\text{B}$ . In a near future, we will make a more detailed analysis including these effects. The excited states of  ${}^8\text{B}$  higher than 3.5 MeV were not explored by the past measurements, but we found an indication of a new resonance near 4.6 MeV.

## References

- [1] C. Angulo, *et al.*, Nucl. Phys. A **656** (1999) 3.
- [2] E. Adelberger, *et al.*, Rev. of Mod. Phys. **70** (1998) 1265.
- [3] V. Gol'dberg *et al.*, *JETP Lett.* **67**, (1998) 1013.
- [4] A. van Hees and P. Glaudemans, Z. Phys. A **314** (1983) 323.
- [5] A. van Hees and P. Glaudemans, Z. Phys. A **315** (1984) 223.
- [6] F. Barker, and A. Mukhamedzhanov, Nucl. Phys. A **673** (2000) 526.
- [7] G. Rogachev *et al.*, Phys. Rev. C **64** (2001) 061601(R).
- [8] A. Csóto *et al.*, Phys. Rev. C **61** (2000) 024311.
- [9] S. Kubono *et al.*, Eur. Phys. J. A **13** (2002) 217.
- [10] Y. Yanagisawa *et al.*, Nucl. Instrum. Methods Phys. Res., Sect. A **539** (2005) 74.
- [11] T. Teranishi *et al.*, Phys. Lett. B **556** (2003) 27.
- [12] H. Kumagai *et al.*, Nucl. Instrum. Methods A **470** (2001) 562.

We are grateful to RIKEN accelerator staff for their help. This work was supported by the Grant-in-Aid for Young Scientists (B) (Grant No. 17740135) of JSPS.

# Study of Three Nucleon Force Effects via the $nd$ Elastic Scattering

Y. Maeda, K. Fujita<sup>b</sup>, M. B. Greenfield<sup>g</sup>, Y. Hagiwara<sup>d</sup>, K. Hatanaka<sup>b</sup>, M. Hatano<sup>a</sup>, K. Itoh<sup>f</sup>, H. Kamada<sup>h</sup>, J. Kamiya<sup>b</sup>, T. Kawabata, H. Kuboki<sup>a</sup>, T. Kudoh<sup>d</sup>, Y. Nagasue<sup>d</sup>, H. Okamura<sup>c</sup>, T. Saito<sup>a</sup>, H. Sakai<sup>a</sup>, Y. Sakemi<sup>b</sup>, M. Sasano<sup>a</sup>, K. Sekiguchi<sup>e</sup>, Y. Shimizu<sup>b</sup>, K. Suda, A. Tamii<sup>b</sup>, T. Uesaka, T. Wakasa<sup>d</sup> and K. Yako<sup>a</sup>

Center for Nuclear Study, Graduate School of Science, University of Tokyo

<sup>a</sup>Department of Physics, University of Tokyo

<sup>b</sup>Research Center for Nuclear Physics, Osaka University

<sup>c</sup>CYRIC, Tohoku University

<sup>d</sup>Department of Physics, Kyushu University

<sup>e</sup>RIKEN (The Institute of Physical and Chemical Research)

<sup>f</sup>Department of Physics, Saitama University

<sup>g</sup>International Christian University

<sup>h</sup>Department of Physics, Kyushu Institute of Technology

The study of three-nucleon force (3NF) effects in the few-nucleon system is one of the most interesting topics. The modern NN potentials reproduce the experimental NN data up to a laboratory energy of 350 MeV very accurately. When applied to many body ( $> 2N$ ) systems, however, the NN potentials fail to predict the experimental data. The three-nucleon force (3NF) was introduced into the theoretical calculations to reproduce the data. Recently, highly precise measurements of the  $dp$  elastic scattering have been performed [1]. The calculations with NN forces only fail to reproduce the data of cross sections and vector analyzing powers, but these discrepancies are filled by adding the  $2\pi$  exchange 3NFs. These results support the prediction that the  $Nd$  elastic scattering at intermediate energy is a good probe to study the 3NF effects. However, there is a caveat, since such discussions are made by the comparison between the precise  $pd$  data and the rigorous  $nd$  Faddeev calculations because performing the three-body calculation with the long-range Coulomb repulsion is extremely difficult.

To study the 3NF effects in a Coulomb-free system, we have carried out the  $\vec{n}d$  elastic scattering at 250 MeV at the Research Center for Nuclear Physics (RCNP). We measured the differential cross sections and vector analyzing powers for  $\theta_{cm} = 10^\circ - 180^\circ$ . To cover such a wide angular region, we used two different techniques to perform the forward and the backward measurements, respectively [2]. The measurements in the backward angular region ( $\theta_{cm} \geq 60^\circ$ ) were carried out at the  $(n, p)$  facility [3] at RCNP with the polarized neutron beam which was produced by the  ${}^7\text{Li}(\vec{p}, \vec{n}){}^7\text{Be}(\text{g.s.}+0.4 \text{ MeV})$  reaction at 250 MeV. We used the self-supporting deuterated polyethylene ( $\text{CD}_2$ ) sheets [4] as the deuteron targets. The measurements in the forward angular region ( $\theta_{cm} \leq 60^\circ$ ) were carried out at the neutron time-of flight (NTOF) facility [5] at RCNP. The polarized neutron beam was also produced by the  ${}^7\text{Li}(\vec{p}, \vec{n})$  reaction and the deuterated liquid scintillator BC537 was used as the deuteron target.

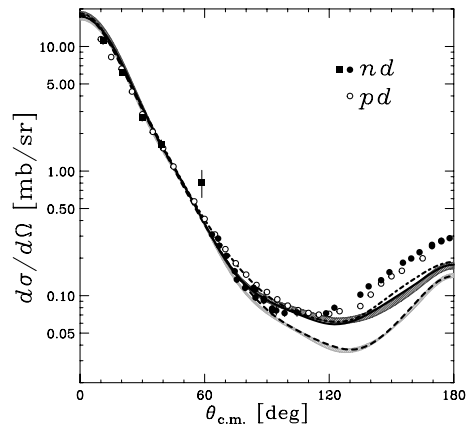


Figure 1. The differential cross section for the  $Nd$  elastic scattering at 250 MeV. The error bars show the statistical errors only. See text for the details of the theoretical predictions in this figure.

The results of the differential cross sections are shown in Fig.1. The solid circles and the solid squares represent the  $nd$  elastic scattering cross sections obtained with the  $(n, p)$  and the NTOF facility, respectively. The error bars show the statistical errors only. The open circles are the data taken at the same energy for the  $pd$  elastic scattering [6]. The light band represents the predictions with realistic NN potentials. The dark band results when these potentials are combined with the TM99 3NF [7]. The solid line is prediction obtained with AV18+Urbana IX combination. From the comparison of the data and these theoretical results, it can be seen that the calculations including 3NF better reproduce the data but still underestimate largely at backward region. These discrepancies may be considered as an indication of the relativistic effects [8] which are not taken into account in these calculations. However, it is shown that the effect of relativistic corrections is kinematically restricted to  $\theta_{cm} \geq 160^\circ$  and it can not fill the gap between the data and the theoretical results [9]. Another possible solution to fill the gap may be to take into account the contributions from other types of 3NFs than  $2\pi$  exchange 3NFs.

The dot-dashed and dashed lines are predictions of the coupled channel approach of Hannover group based on CD-Bonn potential with and without  $\Delta$ -isobar excitations, respectively [10]. It is claimed that the effective 3NF arising from this coupled channel potential presumably includes  $\pi, \rho, \omega$  and  $\sigma$  exchange contributions. However, one can see that this coupled channel approach is also unable to improve the fit to the data.

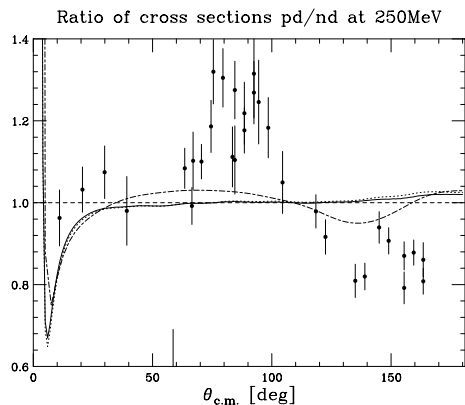


Figure 2. The angular dependence of the ratio between the  $pd$  and  $nd$  elastic scattering cross sections. The circles show the results deduced from the  $nd$  data and  $pd$  data of Ref. [6]. The solid, dots, and dot-dashed curves show the theoretical prediction obtained by including the Coulomb interaction in  $pd$  calculations (see text).

We have also carried out the  $\vec{p}d$  measurements at 250 MeV [6] and these results are shown by open circles. This allows us to compare the  $nd$  and  $pd$  data directly. In Fig. 2, the ratio of the cross sections are plotted with open circles. The curves in the figure represents the theoretical prediction at 250 MeV which is based on the CDBonn. The solid and dotted curves show the prediction calculated by Hannover group with and without  $\Delta$ -isobar 3NF, respectively. In the calculations, the screening and renormalization approach were performed to include Coulomb potential [11]. The dot-dashed curve shows the prediction calculated by Kamada [12]. In this calculation, the Coulomb force was included in an approximate way using approach of Ref. [13]. As can be seen, a similar oscillating structure, though the amplitude is very different, is present in both experimental data and dot-dashed curve. The angle where the experimental value crosses unity is around  $\theta_{cm} = 110^\circ$ , which is well reproduced by dot-dashed curve with an approximate treatment of the Coulomb interaction. However, theoretical curves with the screened Coulomb potential do not show such oscillating structure.

In the study of 3NF effect at higher energy region, which is our next step, the breakup reactions are expected to be more important, because the total cross sections of the breakup reactions are predicted to become larger than that of the elastic reactions [14]. However the three-nucleon final state of the breakup reaction is kinematically much more complicated than that of the elastic reaction. Recently, theoretical survey was made for the configurations which exhibit large 3NF effects in some observables. On the basis

of the theoretical results, we are going to measure the vector analyzing powers in the so-called final state interaction (FSI) geometry,

$$\vec{p} + d \rightarrow (p_1 n)_{FSI} + p_2.$$

We performed the test experiment at RCNP with polarized proton beam at 250 MeV. We used deuterated polyethylene ( $CD_2$ ) as the deuteron target. Momentum of the scattered protons ( $p_2$ ) and recoiled protons in FSI ( $p_1$ ) were analyzed by Grand Raiden (GR) and LAS, respectively. Fig.3 shows the missing mass spectrum of  $CD_2(p,pp)$  reaction. The peak around 940 MeV represents the neutrons from  $pd$  breakup reactions. To subtract the contribution from the carbons in  $CD_2$ , we also used polyethylene ( $CH_2$ ) as the carbon target. The analysis is still in progress.

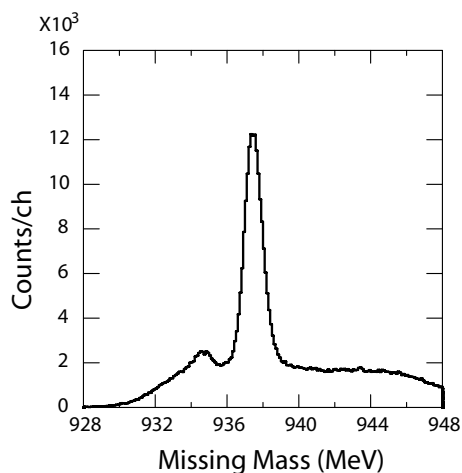


Figure 3. The missing mass spectra obtained by  $CD_2(p,pp)$  measurements.

## References

- [1] K. Sekiguchi *et al.*, Phys. Rev. C **65** (2002) 034003.
- [2] Y. Maeda *et al.*, CNS Annual Report 2004 (2005) 38.
- [3] K. Yako *et al.*, Nucl. Phys. A **684** (2001) 563c.
- [4] Y. Maeda *et al.*, Nucl. Instrum. Methods A **490** (2002) 518.
- [5] H. Sakai *et al.*, Nucl. Instrum. Methods A **369** (1996) 120.
- [6] K. Hatanaka *et al.*, Phys. Rev. C **66** (2002) 044002.
- [7] S. A. Coon *et al.*, Nucl. Phys. A **317** (1979) 242.
- [8] H. Witała *et al.*, Phys. Rev. C **57** 2111 (1998)
- [9] H. Witała, *et al.*, Phys. Rev. C **71** (2002) 054001.
- [10] A. Deltuva *et al.*, Phys. Rev. C **67** (2003) 034001.
- [11] A. Deltuva *et al.*, Phys. Rev. C **71** (2005) 054005.
- [12] H. Kamada, private communication.
- [13] P. Doleschall *et al.*, Nucl. Phys. A **380** (1982) 72.
- [14] J. Kuroś-Żołnierczuk *et al.*, Phys. Rev. C **66** (2002) 024003.

# High Resolution In-beam Gamma Spectroscopy of $N \sim 20$ Neutron-rich Nuclei

T. Fukui<sup>a</sup>, S. Ota, S. Shimoura, N. Aoi<sup>b</sup>, E. Takeshita<sup>b</sup>, S. Takeuchi<sup>b</sup>, H. Suzuki<sup>c</sup>, H. Baba<sup>b</sup>,  
T. Fukuchi<sup>d</sup>, Y. Hashimoto<sup>e</sup>, E. Ideguchi, K. Ieki<sup>f</sup>, N. Iwasa<sup>g</sup>, H. Iwasaki<sup>h</sup>, S. Kanno<sup>b</sup>, Y. Kondo<sup>e</sup>,  
T. Kubo<sup>b</sup>, K. Kurita<sup>f</sup>, T. Minemura<sup>b</sup>, S. Mitimasa<sup>b</sup>, T. Motobayashi<sup>b</sup>, T. Murakami<sup>a</sup>,  
T. Nakabayashi<sup>e</sup>, T. Nakamura<sup>e</sup>, M. Niikura, T. Okumura<sup>e</sup>, T. K. Onishi<sup>c</sup>, H. Sakurai<sup>b</sup>,  
M. Shinohara<sup>e</sup>, D. Suzuki<sup>c</sup>, M. K. Suzuki<sup>c</sup>, M. Tamaki, K. Tanaka<sup>b</sup>, Y. Togano<sup>f</sup>, Y. Wakabayashi<sup>i</sup>,  
and K. Yamada<sup>b</sup>

*Center for Nuclear Study, Graduate School of Science, University of Tokyo*

<sup>a</sup>*Department of Physics, Kyoto University*

<sup>b</sup>*RIKEN (The Institute of Physical and Chemical Research)*

<sup>c</sup>*Department of Physics, University of Tokyo*

<sup>d</sup>*Department of Physics, Osaka University*

<sup>e</sup>*Department of Physics, Tokyo Institute Technology*

<sup>f</sup>*Department of Physics, Rikkyo University*

<sup>g</sup>*Department of Physics, Tohoku University*

<sup>h</sup>*Institut de Physique Nucléaire, IN2P3-CNRS, 91406 Orsay, France*

<sup>i</sup>*Department of Physics, Kyushu University*

The high resolution in-beam gamma-ray spectroscopy was performed in the region so called “island of inversion”. In this region, a picture of the evolution of the shell structure is being obtained related to magicity loss in the  $N=20$  neutron-rich nuclei. A large quadrupole deformation has been found in the  $^{32}\text{Mg}$  nucleus based on the experimental result such as low excitation energy of the first  $2^+$  state and large transition probability ( $B(E2\uparrow)$ ) [1], which suggest the vanishing of the  $N=20$  magicity. On the other hand, in the  $^{34}\text{Si}$  nucleus its ground state is believed to be spherical which suggest the existence of  $N=20$  shell closure. The ground state of  $^{33}\text{Al}$  is also believed to be spherical [2], and only one excited state is known [3]. This situation is similar to the  $^{13}\text{B}$  case [4], in which the ground state is spherical but a low-lying excited state of 4.83 MeV exciting energy may be deformed, so that the low-lying deformed excited state is expected to be in  $^{33}\text{Al}$  nucleus. In addition, there still remain excited states whose spins and parities are not determined in the nuclei nearby “island of inversion”. We aim at investigating new gamma-ray transitions, and at discussing the changing of shell structure as a function of neutron and proton number by extracting the information of spin and parity of each state from the angular distribution of the differential cross sections and by comparing the populations in various reactions.

For this purpose, the high energy resolution gamma-ray measurement is a powerful tool. However, in in-beam experiments, we need correcting the Doppler shift up to about 30% of gamma-ray energy, since the de-excited gamma-ray is emitted from the moving source at  $\beta \sim 0.3$ . The total energy resolution consists of the resolution of the particle velocity, the angular resolution, and the intrinsic energy resolution. The angular resolution mainly depends on the resolution of interaction point in the crystal of Germanium. In the present work, we aim at extracting more precise infor-

mation of interaction point by using Pulse Shape Analysis (PSA).

In this paper, preliminary gamma-ray energy spectra and observed gamma-ray transitions are shown.

The experiment was performed at RIKEN Accelerator Facility with RIKEN Projectile-fragment Separator (RIPS) [5]. The primary beam of  $^{40}\text{Ar}$  at 63 MeV/nucleon bombarded the primary target of 1 mm-thick carbon and beryllium. As products of projectile-fragmentation reaction, many isotopes including mainly  $^{28-31}\text{Na}$ ,  $^{30-33}\text{Mg}$ ,  $^{32-35}\text{Al}$ ,  $^{34-36}\text{Si}$ ,  $^{36,37}\text{P}$  were obtained and analyzed by using RIPS. These isotopes were identified event-by-event based on the energy loss and time-of-flight information measured by using a Si detector and couple of plastic scintillator, respectively. The secondary beam bombarded a liquid helium target [6] of about 150mg/cm<sup>2</sup> thick with average bombarding energy of 40 MeV/nucleon. Outgoing particles were identified event-by-event based on the energy loss, kinetic energy and time-of-flight information measured by using a Si detector, a NaI calorimeter and a couple of plastic scintillator, respectively. The positions and directions of incident and outgoing particles were measured by using PPACs [7]. De-excited gamma-rays emitted from outgoing particle moving at  $\beta \sim 0.3$  were detected by GRAPE [8] surrounding the liquid helium target. The details of experimental setup is described in ref. [9].

Figure 1 shows the gamma-ray energy spectra after Doppler correction. To obtain these spectra, only outgoing particles were identified so that the excited states could be populated by any allowed reactions. In order to achieve high energy resolution a pulse shape analysis (PSA) was applied to determine the interaction position of the gamma-ray in the crystal of Germanium. A typical energy resolution is 24 keV (FWHM) for the 885-keV gamma-ray corresponding to the transition from  $2^+_1$  to  $0^+_1$  of the  $^{32}\text{Mg}$  with

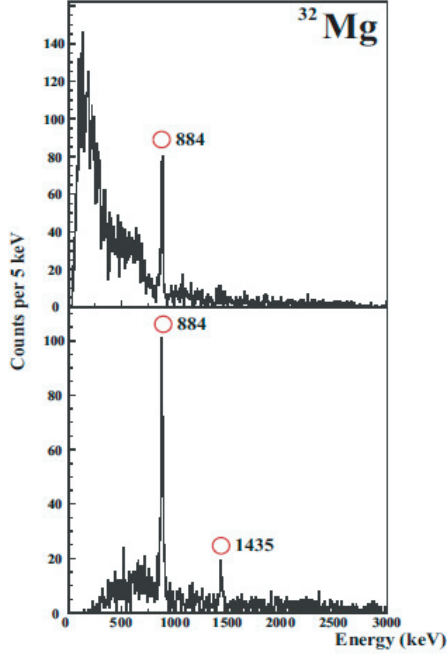


Figure 1. Doppler corrected gamma-ray energy spectra for  $^{32}\text{Mg}$ . In upper panel, the gamma-ray energy spectrum under the condition of single segment hit in a detector is shown. In lower panel, the gamma-ray energy spectrum under the condition of more than two hits in a detector is shown.

PSA, whereas 36 keV without PSA. Table 1 lists the transition energies of the observed gamma-rays for each isotope. Each error in present work is only statistical one. The candidates of new transitions in each isotopes are preliminarily obtained.

Data analysis is in progress.

## References

- [1] T. Motobayashi *et al.*, Phys. Lett. B **346** (1995) 9.  
 [2] A. C. Morton *et al.* Phys. Lett. B **544** (2002) 274.  
 [3] W. Mittig *et al.* Eur. Phys. J. A **15** (2002) 157160.  
 [4] S. Ota *et al.*, CNS Annual Report 2003, p13, 2nd Joint Meeting of the Nuclear Physics Divisions of the APS and The Physical Society of Japan, Maui (2005) DC.00004.  
 [5] T. Kubo *et al.*, Nucl. Instrum. Methods B **70** (1992) 309.  
 [6] H. Ryuto *et al.*, Nucl. Intsrum. Methods A **555** (2005) 1.  
 [7] H. Kumagai *et al.*, Nucl. Instrum. Methods A **470** (2001) 562.  
 [8] S. Shimoura, Nucl. Instrum. Methods A **525** (2004) 188.  
 [9] S. Ota *et al.*, CNS Annual Rep. 2004, p24.  
 [10] Z. Elekes *et al.* Phys. Rev. C **73** (2006) 044314.  
 [11] Vandana Tripathi *et al.*, Phys. Rev. Lett. **94** (2005) 162501.  
 [12] D. Guillemaud-Mueller *et al.*, Nucl. Phys. A **426** (1984) 37.  
 [13] S. Nummela *et al.*, Phys. Rev. C **64** (2001) 054313  
 [14] S. Gréby *et al.*, Nucl. Phys. A **734** (2004) 369.

Table 1. Transition energies of the observed gamma-ray with statistical errors. The previously observed de-excitation gamma-ray energies are also listed with those references. The symbol of '\*' indicates a candidate of new gamma-ray transition observed in present work.

Nucleus	present work	previous work
$^{28}\text{Na}$	$278.2 \pm 0.6$	*
	$405.7 \pm 1.0$	*
	$635.9 \pm 0.4$	*
	$861.2 \pm 1.2$	863 [11]
	$1302.7 \pm 2.3$	*
$^{29}\text{Na}$	$1732.8 \pm 4.1$	*
$^{30}\text{Na}$	$338.7 \pm 0.7$	*
	$423.6 \pm 0.8$	$433 \pm 16$ [11]
$^{31}\text{Na}$	$375.1 \pm 0.7$	$370 \pm 12$ [10]
	$787.8 \pm 0.7$	*
$^{30}\text{Mg}$	$984.2 \pm 1.3$	$985.4 \pm 0.9$ [12]
	$1483.1 \pm 0.5$	$1482.8 \pm 0.5$ [12]
	$1819.3 \pm 0.9$	$1820.7 \pm 0.9$ [12]
	$1893.5 \pm 1.9$	*
$^{31}\text{Mg}$	$169.6 \pm 1.5$	$171.2 \pm 0.8$ [12]
	$221.9 \pm 0.8$	$221.7 \pm 0.9$ [12]
$^{32}\text{Mg}$	$892.7 \pm 0.6$	$894.7 \pm 1.2$ [12]
	$883.9 \pm 0.3$	$885.5 \pm 0.7$ [12]
	$1434.9 \pm 1.3$	$1436.1 \pm 1.0$ [12]
$^{33}\text{Mg}$	$299.4 \pm 1.1$	$297.9 \pm 1$ [13]
	$483.6 \pm 1.0$	$484.1 \pm 1$ [13]
$^{32}\text{Al}$	$219.4 \pm 0.5$	222 [14]
	$280.4 \pm 0.8$	*
	$530.2 \pm 1.1$	*
	566	566 [14]
	$735.5 \pm 0.6$	735 [14]
	786	565 [14]
$^{33}\text{Al}$	$747.5 \pm 1.0$	$730 \pm 50$ [3]
	$1838.6 \pm 1.7$	*
$^{34}\text{Al}$	$383.7 \pm 1.2$	*
	$425.3 \pm 1.1$	*
$^{35}\text{Al}$	$760.1 \pm 2.1$	*

# Exotic Cluster States in $^{12}\text{Be}$ via $\alpha$ -Inelastic Scattering

A. Saito, S. Shimoura, T. Minemura<sup>a</sup>, Y. U. Matsuyama<sup>b</sup>, H. Baba<sup>a</sup>, N. Aoi<sup>a</sup>, T. Gomi<sup>c</sup>, Y. Higurashi<sup>a</sup>, K. Ieki<sup>b</sup>, N. Imai<sup>d</sup>, N. Iwasa<sup>e</sup>, H. Iwasaki<sup>f</sup>, S. Kanno<sup>b</sup>, S. Kubono, M. Kunibu<sup>b</sup>, S. Michimasa<sup>a</sup>, T. Motobayashi<sup>a</sup>, T. Nakamura<sup>g</sup>, H. Ryuto<sup>a</sup>, H. Sakurai<sup>a</sup>, M. Serata<sup>b</sup>, E. Takeshita<sup>b</sup>, S. Takeuchi<sup>a</sup>, T. Teranishi<sup>h</sup>, K. Ue<sup>f</sup>, K. Yamada<sup>a</sup> and Y. Yanagisawa<sup>a</sup>

Center for Nuclear Study, Graduate School of Science, University of Tokyo

<sup>a</sup>RIKEN (The Institute of Physical and Chemical Research)

<sup>b</sup>Department of Physics, Rikkyo University

<sup>c</sup>National Institute of Radiological Sciences

<sup>d</sup>Institute of Particle and Nuclear Studies, KEK

<sup>e</sup>Department of Physics, Tohoku University

<sup>f</sup>Department of Physics, University of Tokyo

<sup>g</sup>Department of Physics, Tokyo Institute of Technology

<sup>h</sup>Department of Physics, Kyushu University

Cluster structure in neutron-rich beryllium isotopes is one of the most interesting phenomena in unstable nuclei. For  $^{12}\text{Be}$ , recently observed highly excited states with  $J^\pi=4^+$  to  $8^+$  above  $^6\text{He}+^6\text{He}$  threshold are considered to form a rotational band with a developed  $^6\text{He}+^6\text{He}$  cluster structure [1]. These excited states have been reasonably reproduced by several theoretical calculations. The microscopic coupled-channels calculation predicts that several rotational bands with different couplings, such as  $0^+\otimes 2^+$ , appear at high-excitation energy region [2]. Strong mixing between  $^6\text{He}+^6\text{He}$  and  $\alpha+^8\text{He}$  is predicted by the microscopic cluster model calculation [3]. The Antisymmetrized Molecular Dynamics reproduces the experimentally observed rotational band [4]. The deduced density distribution shows a developed cluster structure in highly excited states. Therefore several excited states with developed cluster structure are expected to overlap each other above the  $^6\text{He}+^6\text{He}$  or  $\alpha+^8\text{He}$  thresholds.

We aim at searching for excited states with low spins such as  $0^+$  and  $2^+$ , which may lie just above the  $^6\text{He}+^6\text{He}$  decay threshold. The  $\alpha$ -inelastic scattering at 60A MeV in inverse kinematics using a liquid helium target [5] was used to populate these excited states. Since the  $(\alpha,\alpha')$  reaction has the advantage of well-known reaction mechanism, it is possible to determine spins by angular distributions of the inelastic scattering by comparing with distorted wave Born approximation (DWBA) calculations. In the present work, the angular correlations between decay particles are also compared with DWBA predictions. Since the level density is rather high in the region of interest, the multipole decomposition analysis (MDA) based on the angular distributions obtained with DWBA was used to discriminate contributions from different  $J^\pi$  states. The experimental details are described in Ref. [6].

The MDA based on DWBA calculations has been used by including angular correlations of decay particles as well as the angular distribution of the inelastic scattering. In this analysis, the DWBA calculations for  $\alpha$ -inelastic scattering were performed using the computer code TWOFNR

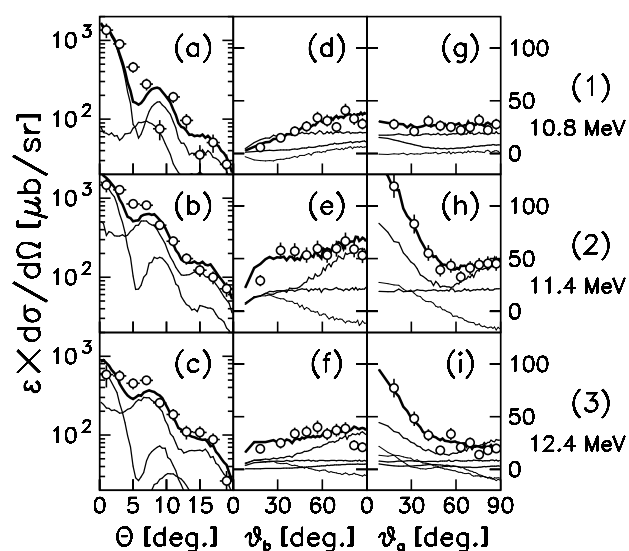


Figure 1. Angular distributions of the differential cross section of the inelastic scattering, the correlation between breakup products respect to the beam axis, and the one respect to the momentum transfer.

[7]. A single-folding model with density-dependent effective nucleon- $\alpha$  interactions was used in the DWBA calculations [8]. The details of the transition densities are described in Ref. [9]. Figure 1 shows angular distributions of (a-c) the differential cross section of the inelastic scattering, (d-f) the angular correlation between breakup products with respect to the beam axis, and (g-i) the one with respect to the momentum transfer, corresponding to  $E_x=(1)$  10.8, (2) 11.4, and (3) 12.4 MeV. The solid curves correspond to contributions of the  $\Delta L=0, 2, 4$ . The thin ones are interferences of  $0\otimes 2$ ,  $0\otimes 4$ , and  $2\otimes 4$ . The thick curves are sums of all the contributions. Contributions with negligibly small magnitudes are not shown. The calculated angular correlations show good agreements with the data when the contributions of the interference between different multipoles

are taken into account. The 10.8-MeV data has characteristics of the forward peaking in the angular distribution and flat structures in both of the angular correlations. On the other hand, the 11.4-MeV data shows rather flat structure at forward angles in Fig. 1 (b) and an anisotropic shape especially in Fig. 1 (h). It is clear that the angular correlation with respect to the momentum transfer is quite sensitive to the multipolarity. The 12.4-MeV data include certain contributions of all the multipoles.

Excitation energy spectra of  $J^\pi=0^+$ ,  $2^+$ , and  $4^+$  are shown in Figs. 2 (a), (b), and (c), respectively, which were deduced by the MDA. The spectra except for  $4^+$  were fitted by several Gaussians with continuums assumed by

$$\frac{d\sigma_L^c}{dE_d} = \frac{P_L(E_d)}{c_0 + c_1 E_d + c_2 E_d^2}, \quad (1)$$

where  $P_L(E_d)$  is the penetrability. The deduced energy ( $E_R$ ), cross section ( $\sigma_R$ ), and width ( $\Gamma_R$ ) are listed in Table 1. The confidence levels for all peaks are larger than 99.7%. Each peak was also statistically tested based on the significance level.

Table 1. Results of the fit to excitation energy spectra.

$J^\pi$	$E_R$ [MeV]	$\sigma_R$ [ $\mu\text{b}$ ]	$\Gamma_R$ [MeV]
$0^+$	10.41(4)	2.2(7)	0.0090(28)
	10.82(3)	16(4)	0.18(12)
	11.27(3)	21(5)	0.12(25)
	11.91(10)	20(6)	0.72(16)
	13.83(9)	14(5)	0.63(33)
$2^+$	10.60(5)	3.9(1.0)	0.20(4)
	11.26(6)	43(9)	0.51(5)
	11.82(12)	47(10)	0.75(9)
	13.01(12)	52(9)	1.29(14)
	14.71(7)	14(3)	<0.37 <sup>†</sup>
	15.93(10)	10(3)	<0.65 <sup>†</sup>

<sup>†</sup>C.L. 68%

The energy-spin systematics is shown in Fig. 3. Closed circles are new levels observed in the present work. Cross symbols and closed triangles are data taken from Refs. [1] and [10], respectively. The moment of inertia of the solid lines correspond to  $\hbar^2/2I=139$  keV, which is close to that of  ${}^6\text{He}$  touching each other with radii given by  $r = 1.5 \times A^{1/3}$  [fm]. The first and the second lowest  $0^+$  and  $2^+$  levels may be members of the rotational band with a developed  ${}^6\text{He}+{}^6\text{He}$  cluster structure in  ${}^{12}\text{Be}$  [1]. By assuming each rotational band has moment of inertia closed to each other, the third lowest  $0^+$  and  $2^+$  states may be connected to previously observed  $6^+$  state at 18.6 MeV [1]. The possible existence of several molecular bands is qualitatively consistent with the coupled-channels calculation by Ito and Sakuragi [2]. The wave functions of the band members may consist of the contribution from the configurations of  ${}^6\text{He}(0^+)+{}^6\text{He}(0^+)$ ,  ${}^6\text{He}(0^+)+{}^6\text{He}(2^+)$ ,  $\alpha+{}^8\text{He}(0^+)$ ,  $\alpha+{}^8\text{He}(2^+)$ , etc., with different spectroscopic amplitudes. The  $0^+$  states are the candidates of the exotic

cluster states with a novel molecular-orbital structure of valence neutrons predicted in Ref. [4].

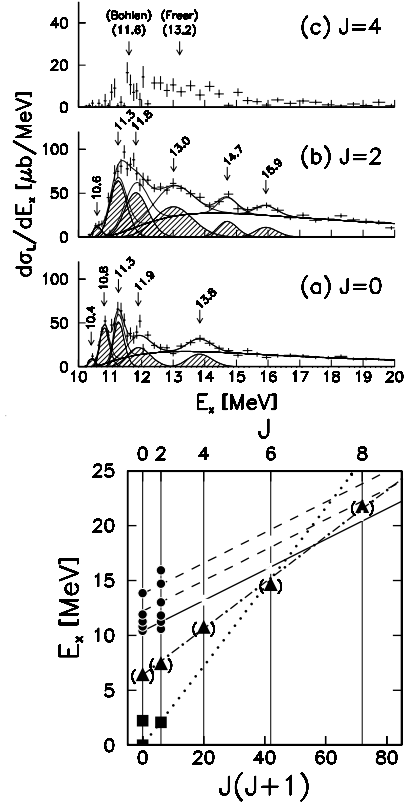


Figure 2. Decay energy spectra of  $J^\pi=0^+$ ,  $2^+$ , and  $4^+$ . The  $0^+$  and  $2^+$  spectra were fitted by several Gaussians with continuum structures.

Figure 3. Energy-spin systematics for  ${}^{12}\text{Be}$ . Closed circles are levels observed in the present work. Cross symbols and closed triangles are data of Refs. [1] and [10], respectively.

In summary, the  $\alpha$ -inelastic scattering of  ${}^{12}\text{Be}$  with the inverse kinematics was measured using the liquid helium target. The multipole decomposition analysis was performed using the angular distributions of the inelastic scattering and the angular correlations of decay particles. Newly observed excited states with  $0^+$  and  $2^+$  may be members of rotational bands with large moments of inertia corresponding to the developed  ${}^6\text{He}+{}^6\text{He}$  cluster structure in  ${}^{12}\text{Be}$ .

## References

- [1] M. Freer *et al.*, Phys. Rev. Lett. **82** (1999) 1383.
- [2] M. Ito and Y. Sakuragi, Phys. Rev. **C62** (2000) 064310.
- [3] P. Descouvemont and D. Baye, Phys. Lett. B **505** (2001) 71.
- [4] Y. Kanada-En'yo and H. Horiuchi, Phys. Rev. C **68** (2003) 014319.
- [5] H. Ryuto *et al.*, Nucl. Instrum. Methods B **555** (2005) 1.
- [6] A. Saito *et al.*, CNS Annual Repprt 2004 (2005) 30.
- [7] M. Igarashi, DWBA code TWOFNR, unpublished.
- [8] A. Kolomiets *et al.*, Phys. Rev. C **61** (2000) 34312.
- [9] G. R. Satchler *et al.*, Nucl. Phys. A **472** (1987) 215.
- [10] H. G. Bohlen *et al.*, Nucl. Phys. A **722** (2003) 3c.

# Proton Single-Particle States in the Neutron-Rich $^{23}\text{F}$ Nucleus

S. Michimasa, S. Shimoura<sup>a</sup>, H. Iwasaki<sup>b</sup>, M. Tamaki<sup>a</sup>, S. Ota<sup>a</sup>, N. Aoi, H. Baba, N. Iwasa<sup>c</sup>, S. Kanno, S. Kubono<sup>a</sup>, K. Kurita<sup>d</sup>, M. Kurokawa, T. Minemura, T. Motobayashi, M. Notani<sup>e</sup>, H. J. Ong<sup>b</sup>, A. Saito<sup>a</sup>, H. Sakurai, E. Takeshita, S. Takeuchi, Y. Yanagisawa and A. Yoshida

*RIKEN (The Institute of Physical and Chemical Research)*

<sup>a</sup>*Center for Nuclear Study, Graduate School of Science, University of Tokyo*

<sup>b</sup>*Department of Physics, University of Tokyo*

<sup>c</sup>*Department of Physics, Tohoku University*

<sup>d</sup>*Department of Physics, Rikkyo University*

<sup>e</sup>*Argonne National Laboratory, USA*

## 1. Introduction

Neutron-rich oxygen isotopes attract much attention since the conventional magic number  $N = 20$  disappears [1] and an alternative new magic number  $N = 16$  appears [2]. A shell model describes this change of the magic numbers as an evolution of neutron effective single particle energies as decrease of the proton number by the effect of the two-body attractive force between  $\pi d_{5/2}$  and  $\nu d_{3/2}$  which is absent in oxygen [3]. The same effect between  $\pi d_{3/2}$  and  $\nu d_{5/2}$  is expected in the effective proton single particle energies in fluorine isotopes and can be investigated quantitatively by measuring the excitation energies of  $\pi d_{3/2}$  single-particle states between  $^{17}\text{F}$  (empty in  $\nu d_{5/2}$ ) and  $^{23}\text{F}$  (full in  $\nu d_{5/2}$ ). In the present work, we have studied excited states in  $^{23}\text{F}$  by  $\gamma$ -ray spectroscopy with the one-proton transfer reaction. The one-proton transfer reaction is a good probe for investigation on proton shell structure, because this reaction selectively populates single-particle states. Furthermore, we have measured an  $\alpha$  inelastic scattering, a neutron knockout and two-nucleon knockout reactions to research excited state in  $^{23}\text{F}$ . Comparison of population strengths in the different reactions demonstrates the feature of an observed state. In the report, we discuss the excitation energies of the proton single-particle states in  $^{23}\text{F}$  comparing the experimental result and shell-model predictions.

## 2. Experiment

The experiment was performed at the secondary beam line RIPS [4] in RIKEN Accelerator Research Facility. The secondary beam was a cocktail of unstable  $^{22}\text{O}$ ,  $^{23}\text{F}$  and  $^{24}\text{F}$  nuclei, which were produced by a projectile-fragmentation reaction of  $^{40}\text{Ar}$  with a  $^9\text{Be}$  target. The secondary beam bombarded a liquid helium target [5]. The products of secondary reactions were detected by a telescope consisting of 9 SSDs and 36 NaI(Tl) detectors [6] and de-excited  $\gamma$  rays from the reaction product were detected by an array of 150 NaI(Tl) scintillators DALI2 [7] surrounding the secondary target. In order to measure scattering angles of the reaction products, three PPACs [8] were located on the beam line. The two PPACs were placed before the secondary target and the other PPAC was placed after the target. Further details about the present experiment were written in Ref. [9].

## 3. Results and Discussions

We have obtained  $\gamma$ -ray spectra in  $^{23}\text{F}$  from the proton transfer reaction  $^4\text{He}(^{22}\text{O}, ^{23}\text{F}\gamma)$ , the inelastic scattering  $^4\text{He}(^{23}\text{F}, ^{23}\text{F}\gamma)$ , the neutron knockout reaction  $^4\text{He}(^{24}\text{F}, ^{23}\text{F}\gamma)$  and the two-nucleon knockout reaction  $^4\text{He}(^{25}\text{Ne}, ^{23}\text{F}\gamma)$ . We assigned the proton-single particle states on basis of the population strengths of these reactions. When we treat a nucleus as a simple one-particle structure, the proton transfer reaction is easy to populate proton single-particle states; the alpha inelastic scattering induces core excitations and possibly populate single-particle states through non-spin-flip excitation; the neutron-knockout reaction favors states to have a neutron-hole configuration; the two-nucleon knockout reaction has a large cross section for high-spin states because it can transfer a large angular momentum.

Among the observed excited states, the 2268- and 4059-keV states were strongly populated by the transfer reaction, but were not seen significantly in the neutron-knockout reaction. Since the ground state has  $5/2^+$ , it is reasonable that these states were deduced to be proton single-particle states in the  $s_{1/2}$  or  $d_{3/2}$  orbitals. The angular distributions for the 2268- and 4056-keV states in the transfer reaction were consistent with  $L = 0$  and  $L = 2$ , and therefore we identified the 2268- and 4059-keV states were the single-particle states for the  $\pi s_{1/2}$  and  $\pi d_{3/2}$  orbitals, respectively.

The level scheme proposed in present experiment was compared with the shell-model prediction based on the USD effective interaction [10], as shown in Fig. 1. The spin assignments for the other states will be discussed elsewhere. In the figure, the single-particle states predicted by the USD are located lower than the present results by 500 keV, while the other states, which have configuration of neutron excitation, are reproduced well. The same tendency was also seen in the SDPF-M effective interaction [11, 12], and a strong spin-isospin monopole interaction [3] caused that the  $3/2_1^+$  state was located at lower excitation energy.

We attempted to reproduce the measured excitation energies in  $^{23}\text{F}$  by the USD shell-model calculation with changing the spin-orbit splitting of proton  $d$  shell, because the spin-orbit splitting are considered to be sensitive to the excitation energies of the proton single-particle states and to

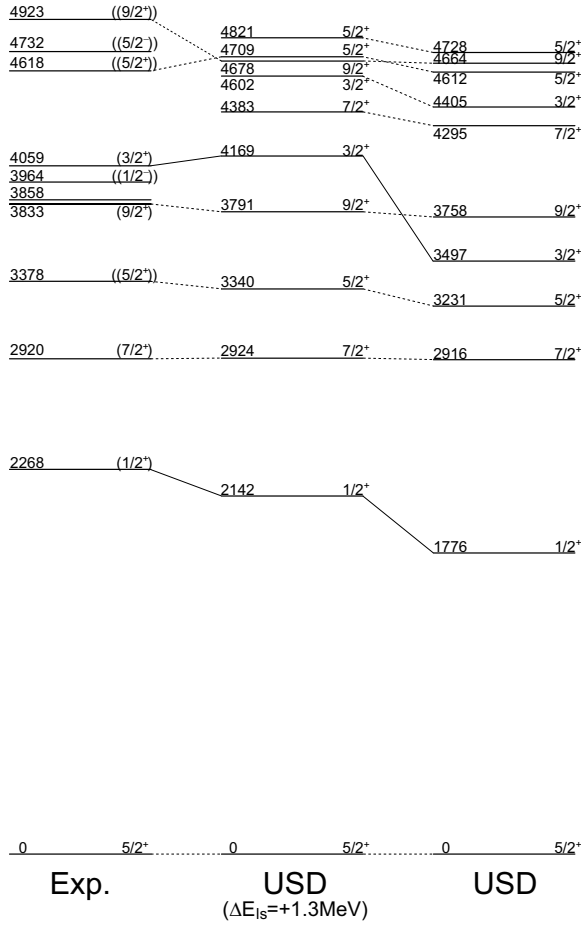


Figure 1. Shell-model prediction in  $^{23}\text{F}$  improved by tuning the proton spin-orbit splitting (middle), together with the experimental result (left) and the original USD prediction (right). The spin-orbital splitting is widened by 1.3 MeV for the best prediction.

be insensitive to those of purely neutron collective states. The level scheme obtained when the  $d_{5/2}$  orbital energy was decreased by 0.52 MeV and the  $d_{3/2}$  orbital energy was increased by 0.78 MeV, which corresponded to an increase of the spin-orbit splitting by 1.3 MeV, is shown in the middle of Fig. 1. The calculation reproduced well the excitation energies of the single-particle states in  $^{23}\text{F}$  and also improved those of the other states. Since the single-particle energy gaps used in the original USD and SDPF-M interactions were determined to reproduce the single-particle states in  $^{17}\text{F}$ , this may indicate that the spin-orbit splitting between  $\pi d_{5/2}$  and  $\pi d_{3/2}$  in  $^{23}\text{F}$  is wider than that in  $^{17}\text{F}$ .

The spin-orbit interaction is a nuclear surface effect, and is affected by the differential of the nuclear potential. Therefore the spin-orbit splitting is naively considered to be determined by the depth of the potential, and to sensitive to the binding energy of the valence proton. In the present case, the valence proton in  $^{23}\text{F}$  is much more deeply bound (13.24 MeV) than in  $^{17}\text{F}$  (0.60 MeV). Therefore, this difference in binding energy may cause the wider spin-orbit splitting in  $^{23}\text{F}$ .

## References

- [1] E. K. Warburton *et al.*, Phys. Rev. C **41** (1990) 1147.
- [2] A. Ozawa *et al.*, Phys. Rev. Lett. **84** (2000) 5493.
- [3] T. Otsuka *et al.*, Phys. Rev. Lett. **87** (2001) 082502.
- [4] T. Kubo *et al.*, Nucl. Instrum. Methods B **70** (1992) 309.
- [5] H. Ryuto *et al.*, Nucl. Instrum. Methods A **555** (2005) 1.
- [6] M. Tamaki *et al.*, CNS-REP-59, 76 (2003).
- [7] S. Takeuchi *et al.*, RIKEN Accel. Prog. Rep. **36** (2003) 148.
- [8] H. Kumagai *et al.*, Nucl. Instrum. Methods A **470** (2001) 562.
- [9] S. Michimasa *et al.*, Phys. Lett. B **638** (2006) 146.
- [10] B. H. Wildenthal, Prog. Part. Nucl. Phys. **11** (1984) 5.
- [11] Y. Utsuno *et al.*, Phys. Rev. C **64** (1999) 011301.
- [12] T. Otsuka and Y. Utsuno, *private communication*.

# High-Spin States of $^{93}\text{Nb}$

Y. Wakabayashi<sup>a</sup>, T. Fukuchi<sup>b</sup>, Y. Gono<sup>c</sup>, A. Odahara<sup>b</sup>, S. Tanaka<sup>d</sup>, M. Inoue<sup>d</sup>, T. Sasaki<sup>d</sup>,  
M. Kibe<sup>d</sup>, N. Hokoïwa<sup>d</sup>, T. Shinozuka<sup>e</sup>, M. Fujita<sup>e</sup>, A. Yamazaki<sup>e</sup>, T. Sonoda<sup>e</sup>, C. S. Lee<sup>f</sup>,  
Y. K. Kwon<sup>f</sup>, J. Y. Moon<sup>f</sup>, and J. H. Lee<sup>f</sup>

<sup>a</sup>Center for Nuclear Study, Graduate School of Science, University of Tokyo

<sup>b</sup>Department of Physics, Osaka University

<sup>c</sup>RIKEN (The Institute of Physical and Chemical Research)

<sup>d</sup>Department of Physics, Kyushu University

<sup>e</sup>Cyclotron and Radioisotope Center, Tohoku University

<sup>f</sup>Department of Physics, Chung-Ang University

High-spin isomers are known to exist in  $N = 83$  isotones [1], systematically, with  $60 \leq Z \leq 68$  at almost constant excitation energies ( $E_x = 8.5 \sim 9.0$  MeV), except for  $^{151}\text{Er}$ . The decay schemes and characteristics of these isomers were studied well experimentally [1] and theoretically [2]. According to these results, they are considered to be shape isomers caused by sudden shape changes from near spherical to oblate shapes.

High-spin isomers were also known in  $N = 84$  isotones of  $64 \leq Z \leq 68$  [3]. They are much different from those of  $N = 83$  isotones in excitation energies and spin values as well as half lives. The half lives of them are considerably shorter than those of  $N = 83$  isotones.

In order to study the existence of the same kind of high-spin shape isomers in other mass region, the  $^{90}\text{Zr}$  region was selected. Comparing the spherical single particle orbits near Fermi surfaces of nuclei in these two regions, there are similarities both for protons and neutrons. Then in case of  $N = 51, 52$  isotones there may be isomers originated from the same mechanism as those of  $N = 83$  isotones.

Recently, a high-spin isomer was found in  $^{93}\text{Mo}$  of an  $N = 51$  isotone, at about 9.7 MeV in excitation energy and having a half life of 1.1  $\mu\text{s}$  [4]. A population of this isomer in the reaction  $^{82}\text{Se}(^{16}\text{O}, 5n)^{93}\text{Mo}$  was only 2% of the total  $^{93}\text{Mo}$  yield which was much different from the cases of  $N = 83$  isotones. To clarify the differences as well as the similarities of the isomers of  $N = 83, 84$  isotones and those of  $N = 51, 52$  isotones, high-spin states of  $^{93}\text{Nb}$  of an  $N = 52$  isotone were studied.

High-spin states in  $^{93}\text{Nb}$  were populated via the  $^{82}\text{Se}(^{16}\text{O}, p4n)^{93}\text{Nb}$  reaction at a bombarding energy of 100 MeV. Two experiments were performed at Cyclotron and Radioisotope Center (CYRIC) of Tohoku University. The  $^{82}\text{Se}$  target of 5.2 mg/cm<sup>2</sup> was enriched to 90%. A target foil was supported by 500  $\mu\text{g}/\text{cm}^2$  of gold. Measurements of  $\gamma$ -t,  $\gamma$ - $\gamma$ -t coincidence,  $\gamma$ -ray angular distributions and  $\gamma$ -ray linear polarizations were performed. For the  $\gamma$ -ray detection, 2 BGO anti-Compton shielded and 2 unshielded clover Ge detectors, and 1 LEPS Ge detectors were used in the first experiment. In the second experiment, 2 BGO anti-Compton shielded and 1 unshielded clover Ge detectors, 2 co-axial and 1 LEPS Ge detectors were used. In the data analysis, the clover Ge detectors were treated in the add-back mode except for angular distributions. About 1.2

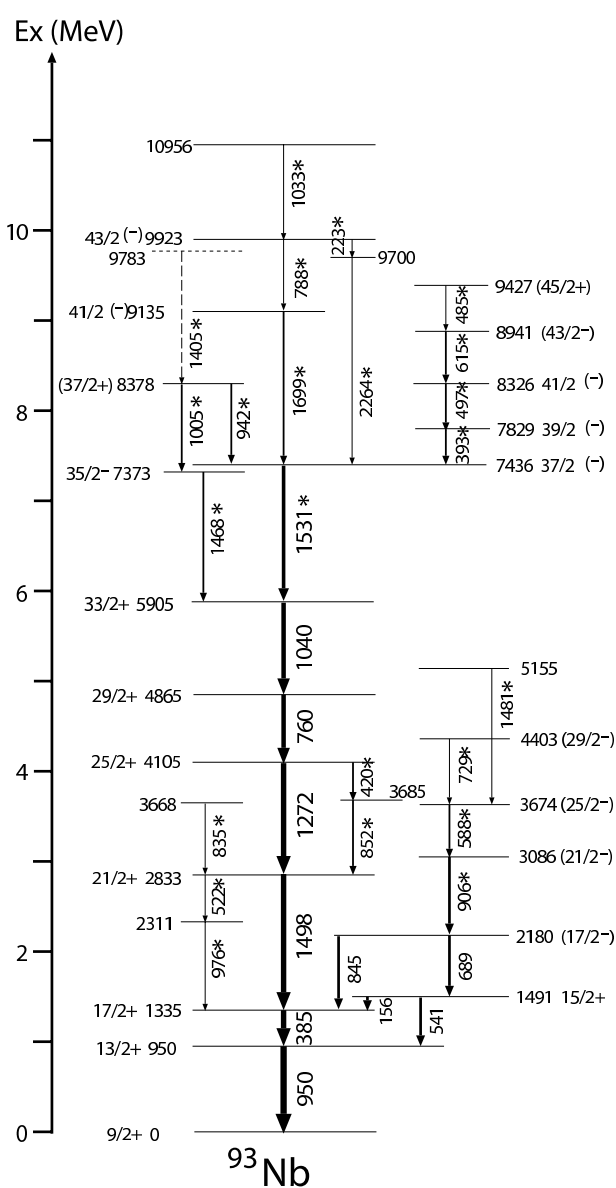


Figure 1. A proposed level scheme of  $^{93}\text{Nb}$ . The widths of the arrows follow the  $\gamma$ -ray intensities. The energies are given in keV units.

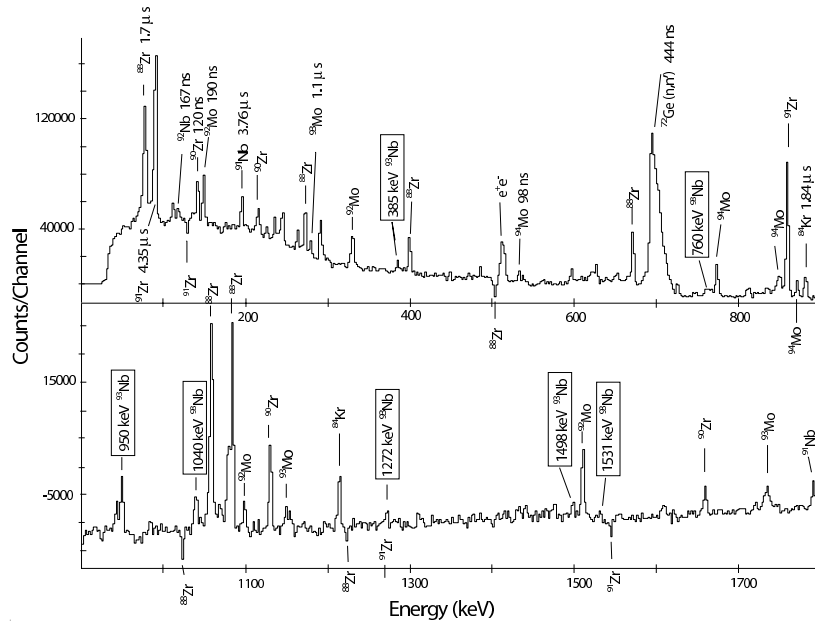


Figure 2. A difference spectrum made by subtracting a spectrum gated on pre-prompt from that gated on post-prompt.

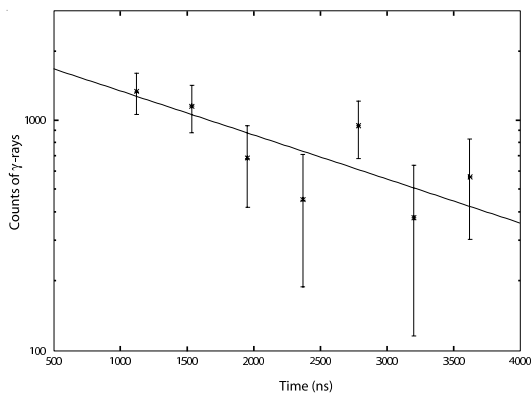


Figure 3. Decay curve of the high-spin isomer in  $^{93}\text{Nb}$ .

$\times 10^9$  coincident events in total were recorded for off-line analysis.

The level scheme of  $^{93}\text{Nb}$  up to the  $(33/2)$  state at 5905 keV were studied previously [5]. Figure 1 shows the proposed level scheme of  $^{93}\text{Nb}$  constructed in this work using the  $\gamma$ - $\gamma$ -t coincidences, angular distributions, linear polarization measurements, and the analysis of directional correlations of  $\gamma$ -rays deexciting oriented states (DCO). The transitions marked by asterisks are new ones. The widths of the arrows follow the  $\gamma$ -ray intensities. Twenty three new  $\gamma$ -rays and 19 new levels were identified.

A dipole rotational-like sequence was found just above 7436 keV level as seen in Fig. 1. The energies of intraband transitions are 393, 497 and 615 keV. Such a dipole band of  $^{93}\text{Nb}$  have not been reported in  $A \sim 90$  region.

To search for relatively long lived isomers, a  $\gamma$ - $\gamma$ -t delayed coincidence measurements were performed as well as the prompt coincidences. Figure 2 shows a delayed  $\gamma$ - $\gamma$  projection spectrum made by subtracting a pre-prompt spectrum from a post-prompt spectrum. The delayed time

conditions for this spectrum were set in range from 1 to 3  $\mu\text{s}$  in both sides of the prompt peak. The  $\gamma$ -rays de-exciting and feeding isomers are observed as positive and negative peaks, respectively. The names of the isotopes to which each isomer belongs are indicated in the figure. The known half life of each isomer is also given. Several transitions of  $^{93}\text{Nb}$  were observed as positive peaks in this spectrum. A  $\gamma$ -ray of 1531 keV deexciting  $37/2^{(-)}$  state at 7436 keV in  $^{93}\text{Nb}$  is seen in Fig. 2. This means that a relatively long lived isomer exists above the  $37/2^{(-)}$  state. Figure 3 shows the time distribution obtained in this work. From this decay curve, a half life of the high-spin isomer of  $^{93}\text{Nb}$  was determined to be  $T_{1/2} = 1.5(5) \mu\text{s}$ . By using the half life information, a population of this high-spin isomer was extracted to be 0.4(2) %.

These detailed results and discussions are given in another paper.

## References

- [1] Y. Gono *et al.*, Eur. Phys. J. A **13** (2002) 5 and references therein.
- [2] T. Dwssing *et al.*, Phys. Scr. **24** (1981) 258.
- [3] H. Watanabe *et al.*, Eur. Phys. J. A **19** (2004) 163; Y. Wakabayashi, Master thesis (2002) and references therein.
- [4] T. Fukuchi *et al.*, Eur. Phys. J. A **24** (2005) 249.
- [5] E. A. Zobov *et al.*, Program and Theses, Proc. Ann. Conf. Nucl. Spectrosc. Struct. At. Nuclei, Almata, (1992) 54.

# Analyzing Power Measurement for the $\vec{p}+{}^6\text{He}$ Elastic Scattering at 71 MeV/u

S. Sakaguchi, T. Uesaka, T. Wakui<sup>a</sup>, T. Kawabata, N. Aoi<sup>b</sup>, Y. Hashimoto<sup>c</sup>, M. Ichikawa<sup>d</sup>, Y. Ichikawa<sup>e</sup>, K. Itoh<sup>f</sup>, M. Itoh<sup>a</sup>, H. Iwasaki<sup>e</sup>, T. Kawahara<sup>g</sup>, H. Kuboki<sup>e</sup>, Y. Maeda, R. Matsuo<sup>d</sup>, T. Nakao<sup>e</sup>, H. Okamura<sup>a</sup>, H. Sakai<sup>e</sup>, N. Sakamoto<sup>b</sup>, Y. Sasamoto, M. Sasano<sup>e</sup>, Y. Satou<sup>c</sup>, K. Sekiguchi<sup>b</sup>, M. Shinohara<sup>c</sup>, K. Suda, D. Suzuki<sup>e</sup>, Y. Takahashi<sup>e</sup>, A. Tamii<sup>h</sup>, K. Yako<sup>e</sup>, and M. Yamaguchi<sup>b</sup>

Center for Nuclear Study, Graduate School of Science, University of Tokyo

<sup>a</sup>Cyclotron and Radioisotope Center, Tohoku University

<sup>b</sup>RIKEN (The Institute of Physical and Chemical Research)

<sup>c</sup>Department of Physics, Tokyo Institute of Technology

<sup>d</sup>Department of Physics, Tohoku University

<sup>e</sup>Department of Physics, University of Tokyo

<sup>f</sup>Department of Physics, Saitama University

<sup>g</sup>Department of Physics, Toho University

<sup>h</sup>Research Center for Nuclear Physics, Osaka University

## 1. Introduction

Direct reactions induced by polarized protons have revealed various aspects of nuclear structure and reaction mechanisms in the study of stable nuclei. However, there has been no scattering experiment of unstable nuclei and polarized protons until 2003 [1] due to the lack of polarized proton target that can be used in RI beam experiments. In this situation, a solid polarized proton target has been constructed at CNS [2,3]. Applicability of the target in RI beam experiments was realized, for the first time, by its modest operating condition of  $B = 0.1$  T and  $T = 100$  K.

Making use of the polarized solid proton target, vector analyzing power was measured for the  $\vec{p}+{}^6\text{He}$  elastic scattering at 71 MeV/u. Aims of the measurement are (a) to determine the spin-orbit potential between a proton and a  ${}^6\text{He}$  particle and then (b) to discuss the effectiveness of microscopic theories from the viewpoint of polarization phenomena in weakly bound systems. It is also expected that polarization observables provide new information on the neutron skin structure of a  ${}^6\text{He}$  particle because the spin-orbit interaction is sensitive to the surface structure of nuclei.

## 2. Experiment

The experiment was carried out at RIKEN Accelerator Research Facility (RARF) using RIKEN Projectile-fragment Separator (RIPS). A  ${}^6\text{He}$  beam was produced through the projectile fragmentation of a  ${}^{12}\text{C}$  beam with an energy of 92 MeV/u bombarded on to a Be target. The energy and the typical intensity of the  ${}^6\text{He}$  beam were 71 MeV/u and 250 kcps, respectively. The purity of the beam was 95%. The spot size on the secondary target was 10 mm FWHM in diameter.

Experimental setup is schematically illustrated in Fig. 1. The material of the solid polarized proton target was a single naphthalene crystal doped with 0.005 mol% of pentacene. The diameter and the thickness of the crystal were 14 mm and 1 mm, respectively. The number of protons in the target was  $4.29 \pm 0.17 \times 10^{21} \text{ cm}^{-2}$ . Polarizing direc-

tion was reversed three times during the experiment by 180° pulse NMR method [4]. The average and the maximum polarization were 13.8% and 20.4%, respectively.

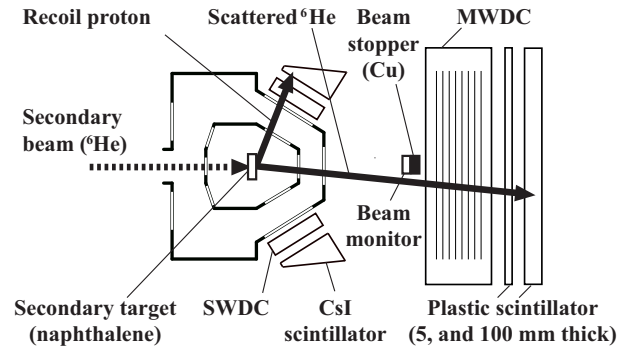


Figure 1. Experimental setup is illustrated. A secondary  ${}^6\text{He}$  beam from RIPS bombarded the solid polarized proton target. Both leading and recoil particles were detected.

Leading particles were detected by a multi-wire drift chamber (MWDC) and plastic scintillators. Scattering angle was determined by the MWDC. The energy deposit  $\Delta E$  and the total energy  $E$  were measured by two layers of plastic scintillators. Recoil particle detectors, consisting of a single-wire drift chamber (SWDC) and a CsI scintillator, were placed at left and right side of the beam line. The SWDCs were used to determine recoil angles. Total energy of the recoil particles was measured by CsI scintillators.

## 3. Results and Discussions

Identification of  ${}^6\text{He}$  particles was carried out by the  $\Delta E - E$  method. Protons were identified by making use of the correlation between the scattering angle and the total energy. The  $\vec{p}+{}^6\text{He}$  elastic scattering events were selected by requiring kinematical consistency to identified particles. Figure 2 shows the polar angle correlation between leading and recoil particles. Yields were obtained in each  $5^\circ$  bin in the CM angle by integrating the peaks corresponding to the

elastic scattering as shown in the right panel of Fig. 2.

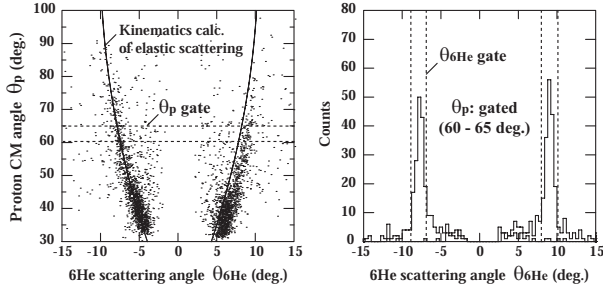


Figure 2. The left panel shows the polar angle correlation of protons and  ${}^6\text{He}$  particles. The right panel is a histogram of  $\theta_{6\text{He}}$  where  $\theta_p = 60 - 65^\circ$ .

Analyzing power was then deduced, canceling spurious asymmetry, as

$$A_y = \frac{1}{\overline{P}_y} \frac{\sqrt{N_L^\uparrow N_R^\downarrow} - \sqrt{N_R^\uparrow N_L^\downarrow}}{\sqrt{N_L^\uparrow N_R^\downarrow} + \sqrt{N_R^\uparrow N_L^\downarrow}}. \quad (1)$$

Here,  $\overline{P}_y$  is the average polarization of the target.  $N_i^j$  is the yield where the subscript ( $i=L/R$ ) and the superscript ( $j=\uparrow/\downarrow$ ) denote a scattering direction and a polarizing direction, respectively. Preliminary results of the differential cross section and the analyzing power are shown in Fig. 3.

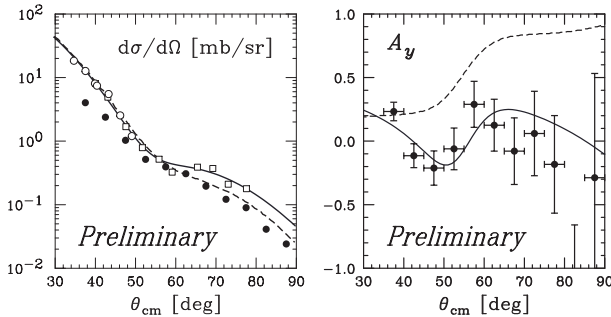


Figure 3. Measured differential cross section and analyzing power are plotted by closed circles. Previously obtained differential cross section data are also plotted by open circles [1] and open squares [5]. The solid and dashed lines show the calculation of a phenomenological optical potential analysis and a prediction of a microscopic model [6], respectively.

The measured analyzing power was compared with predictions of microscopic models based on the  $g$ -matrix theory. The data exhibit a significant discrepancy with the calculation [6] shown by a dashed line in Fig. 3. This indicates an inadequacy of the conventional microscopic models in the description of polarization phenomena involving light unstable nuclei which have weakly bound neutrons.

For quantitative discussions, we carried out an optical model analysis using a phenomenological optical potential of Woods-Saxon type. Solid lines in Fig. 3 show fitting results giving the best agreement with the data. As for the differential cross section, the data of previous measurements

were used for the fitting because the present data is underestimated due to a severe selection of leading particles. Preliminary obtained parameters of the spin-orbit potential are summarized in Table 1, together with those of neighboring stable nuclei and a global optical potential. Radial shapes of them are shown in Fig. 4.

Parameter	$\vec{p}+{}^6\text{He}$	$\vec{p}+{}^4\text{He}$	$\vec{p}+{}^6\text{Li}$	Global OP
		[7]	[8]	[9]
$V_{ls}$ (MeV)	-2.70	-3.92	-3.36	-5.94
$r_{ls}$ (fm)	1.21	0.86	0.90	0.83
$a_{ls}$ (fm)	1.06	0.49	0.94	0.59

Table 1. Depth, radius, and diffuseness parameters of spin-orbit potentials are listed.

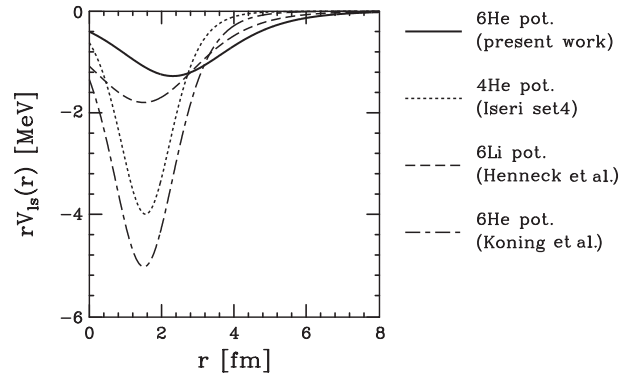


Figure 4. Radial shapes of the spin-orbit potentials are shown.

It was indicated through the comparison that the  ${}^6\text{He}$  has a relatively shallow and widely extended spin-orbit potential. This unexpected shape may contain important information on the surface structure of the  ${}^6\text{He}$  particle, since the spin-orbit interaction is a surface effect. To extract more detailed information, further investigations such as the evaluation of channel coupling effects will be required. Data analysis and theoretical calculations are now in progress.

## References

- [1] M. Hatano *et al.*, *Eur. Phys. J. A* **25** (2005) 255.
- [2] T. Wakui *et al.*, *Nucl. Instrum. and Methods A* **550** (2005) 521.
- [3] T. Uesaka *et al.*, *Nucl. Instrum. and Methods A* **526** (2004) 186.
- [4] T. Kawahara *et al.*, *CNS Annual Report 2005* (2006) 81.
- [5] A. Korshennikov *et al.*, *Nucl. Phys. A* **617** (1997) 45.
- [6] K. Amos, private communication.
- [7] Y. Iseri, private communication.
- [8] R. Henneck *et al.*, *Nucl. Phys. A* **571** (1994) 541.
- [9] A. Koning *et al.*, *Nucl. Phys. A* **713** (2003) 231.

# In-beam Gamma-ray Measurement of the $^{46}\text{Ar} + ^9\text{Be}$ Reaction

M. Niikura, E. Ideguchi, N. Aoi<sup>a</sup>, H. Baba<sup>a</sup>, T. Fukuchi<sup>b</sup>, Y. Ichikawa<sup>c</sup>, H. Iwasaki<sup>c</sup>, T. Kubo<sup>a</sup>, M. Kurokawa<sup>a</sup>, M. Liu, S. Michimasa<sup>a</sup>, T. Ohnishi<sup>a</sup>, T. K. Onishi<sup>c</sup>, S. Ota, S. Shimoura, H. Suzuki<sup>c</sup>, D. Suzuki<sup>c</sup>, Y. Wakabayashi, K. Yoshida<sup>a</sup> and Y. Zheng

Center for Nuclear Study, Graduate School of Science, University of Tokyo

<sup>a</sup>RIKEN (The Institute of Physical and Chemical Research)

<sup>b</sup>Research Center for Nuclear Physics, Osaka University

<sup>c</sup>Department of Physics, Graduate School of Science, University of Tokyo

In-beam gamma-ray spectroscopy by fusion-evaporation reactions is one of the most efficient methods for the study of nuclear structure at high spin, since large amounts of angular momentum can be brought into the system. However, nuclei produced via fusion-evaporation reactions using stable isotope beams are limited, in many cases, to the proton-rich side relative to the  $\beta$ -stability line. In order to investigate high-spin states of neutron-rich nuclei by the fusion-evaporation reaction, it is necessary to use neutron-rich secondary beams. In the doubly magic nuclei  $^{40}\text{Ca}$  [1] and  $^{48}\text{Ca}$ , the onset of deformed collective states due to the presence of deformed shell gaps in  $Z = 20, 22$  and  $N = 28$  are expected at high-spin. In this report, in-beam  $\gamma$ -ray measurements in  $^{48}\text{Ca}$  region by secondary fusion reaction,  $^{46}\text{Ar} + ^9\text{Be}$ , is described.

The experiment was performed at RIKEN Projectile-fragment Separator (RIPS) [2] in RIKEN Accelerator Research Facility. Figure 1 shows a schematic view of the experimental setup. A neutron-rich  $^{46}\text{Ar}$  beam was produced by projectile fragmentation of a primary beam of  $^{48}\text{Ca}$  at 64 MeV/nucleon bombarding the primary target of 1.625 mm-thick  $^9\text{Be}$  and separated by RIPS. An aluminum curved degrader with thickness of 0.6 mm placed at the momentum dispersive focal plane (F1) was used to achieve a clear isotope separation as well as to lower the energy of the secondary beam to  $\sim 24$  MeV/nucleon. The particle identification of the fragments was performed by measuring time-of-flight (TOF) and energy loss ( $\Delta E$ ). The TOF was obtained from the timing information between plastic scintillator of 0.1-mm thickness placed at the achromatic focal plane (F2) and two PPACs (Parallel-Plate Avalanche Counter) [3] at the third focal plane (F3). A purity of  $^{46}\text{Ar}$  was 99%.

The  $^{46}\text{Ar}$  beam was further lowered in energy using a rotatable aluminum degrader of 0.3-mm thickness placed at F2. The energy of the secondary beam was adjusted by changing the rotation angle of the degrader relative to the beam direction and the TOF between F2 and F3 was measured on an event by event level. Figure 2 shows an energy spectrum of the secondary beam at F3. The energy was optimized to produce  $^{50}\text{Ti}$  at the maximum cross section by a measured and calculated excitation function reported in Ref. [4]. The low-energy beam was transported to F3, where a thin  $^9\text{Be}$  of 10- $\mu\text{m}$  thick secondary target was placed for the fusion-evaporation reaction. A typical intensity of  $1.0 \times 10^6$  particle per second was obtained at the secondary target.

RIPS experimental room at RIKEN

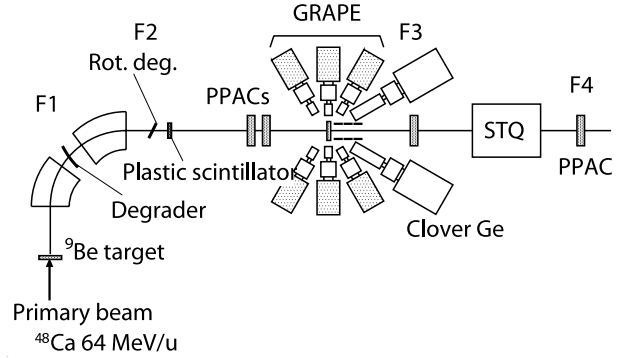


Figure 1. Schematic view of the experimental setup.

Gamma rays emitted from the high-spin states of evaporation residues were detected by the CNS GRAPE (Gamma-Ray detector Array with Position and Energy sensitivity) [5] as well as two clover and one coaxial germanium detectors. The CNS GRAPE was composed of 18 Ge detectors and each detector has two cylindrical-shaped planar crystals that share a common anode. The cathode sides are divided into nine segments. The segmentation makes it possible to determine interaction points of the detected  $\gamma$  rays using analogue pulse-shape analysis [6] for an accurate Doppler-shift correction. These  $\gamma$ -ray detectors were placed around the secondary target to cover the angular range between  $30^\circ$  and  $120^\circ$  relative to the beam direction.

Ti, Sc and Ca isotopes were produced by  $xn$ ,  $pxn$  and  $\alpha xn$  channels in the  $^{46}\text{Ar} + ^9\text{Be}$  fusion reaction, respectively. In order to identify the reaction exit channels, Si-barrel was placed downstream from the target for the collection of the evaporated protons and alphas. The Si-barrel was composed of three pentagonal rings of Si detectors. In each rings, 5 Si detectors was located, which had  $450 \mu\text{m}$  thickness and  $480 \times 480$  mm active area.

A Super-conducting Triplet Quadrupole magnets (STQ) was placed after the secondary target in order to focus the outgoing particles and one PPAC was placed at the final focal plane after the STQ (F4). The beam and evaporation residues were distinguished based on the velocity shift after the fusion-evaporation reaction, which was measured by the

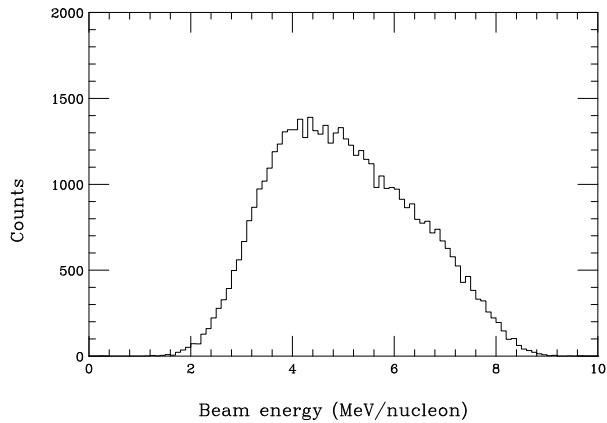


Figure 2. An energy spectrum of the  $^{46}\text{Ar}$  beam at the secondary target deduced from TOF information.

TOF between F3 and F4.

With a trigger condition of two or more Ge detectors firing in coincidence with the plastic at F2 and the PPACs at F3, a total amount of  $1 \times 10^8$  events were collected.

Data analysis is in progress.

## References

- [1] E. Ideguchi *et al.*, Phys. Rev. Lett. **87** (2001) 222501.
- [2] T. Kubo *et al.*, Nucl. Instrum. Methods B **70** (1992) 309.
- [3] H. Kumagai *et al.*, Nucl. Instrum. Methods A **470** (2001) 562.
- [4] M. Niikura *et al.*, RIKEN Prog. Rep. **38** (2005) 67.
- [5] S. Shimoura, Nucl. Instrum. Methods A **525** (2004) 188.
- [6] M. Kurokawa *et al.*, IEEE Trans. Nucl. Sci. **50** (2003) 1309.
- [7] N. Aoi *et al.*, RIKEN Accel. Prog. Rep. **38** (2005) 176.

# Study of Inelastic Contribution in the ${}^7\text{Be} + p$ Scattering Experiment at CRIB

G. Amadio, H. Yamaguchi, J. J. He, A. Saito, Y. Wakabayashi, H. Fujikawa, S. Kubono,  
L. H. Khiem, Y.=K. Kwon, T. Teranishi<sup>a</sup>, S. Nishimura<sup>b</sup>, M. Niikura<sup>c</sup>, Y. Togano<sup>b</sup>, N. Iwasa<sup>d</sup>,  
S. Inafuku<sup>d</sup>

*CNS, University of Tokyo, Japan, Saitama, Wako, Hirosawa, 2-1, Zip Code 351-0198*

<sup>a</sup>*Kyushu University, Japan*

<sup>b</sup>*RIKEN, Japan*

<sup>c</sup>*Kyoto University, Japan*

<sup>d</sup>*Tohoku University, Japan*

## Introduction

The solution of the solar neutrino problem depends on the knowledge of several experimental inputs that are used in the calculation of the neutrino production rates [1]. The astrophysical factor for the  ${}^7\text{Be}(p,\gamma){}^8\text{B}$  reaction ( $S_{17}(0)$ ), despite its importance in the prediction of the high-energy neutrino production rates, still remains one of the most uncertain [3] parameters in the solar model. Although it has been measured many times in the last decades [2], the challenges in performing the measurement have limited the accuracy of existing experimental values, preventing it to reach the desirable accuracy of  $\sim 5\%$ . In addition, recent experimental studies [4, 5, 6] have opened to discussion what kind of influence the suggested low-lying  $2^-$  broad state in  ${}^8\text{B}$  might produce in the extrapolations of  $S_{17}(0)$ .

The need for improvement being evident, a study of the  ${}^7\text{Be} + p$  scattering was performed to both improve the current knowledge of the  ${}^8\text{B}$  nuclear structure and to give us some experience on how to produce a high-current pure  ${}^7\text{Be}$  beam and how to set the final arrangement for the measurement of the cross section of the  ${}^7\text{Be}(p,\gamma){}^8\text{B}$  capture reaction, our ultimate goal. This was the first time in which  $\gamma$ -rays from inelastic scattering were simultaneously measured, providing us with extra information.

## Experiment

The experiment was performed at the CRIB facility, of University of Tokyo. We have used the inverse kinematics technique by bombarding a thick polyethylene target with a  ${}^7\text{Be}$  beam at a laboratory energy of 7.69 MeV/u. The secondary beam was produced through the reaction  ${}^7\text{Li}(p,n){}^7\text{Be}$  by bombarding an 8 cm thick, 1 atm pressure hydrogen gas target with a  ${}^7\text{Li}$  primary beam from RIKEN's AVF cyclotron, at 8.76 MeV/u. The energy spread of the secondary beam was set to 0.8%. After the production target, the secondary beam passed through a double achromatic system and a velocity filter, leading to a virtually pure beam at the end. The setup at the scattering chamber (F3 chamber) consisted of two PPACs that measured the beam position and angle of incidence into the target, as well as time of flight between them; a set of four silicon detector telescopes, composed by a position-sensitive 70  $\mu\text{m}$  detector backed by two or three 1.5 mm detectors, that measured the recoiled protons; and an array of ten NaI detectors that

measured the  $\gamma$ -rays from inelastic scattering. The array of NaI detectors was set at a distance of 7 cm above the target position. An aluminum plate separated these detectors from vacuum. It was as thin as 2 mm, to avoid absorption. The angular range covered by the silicon telescopes was  $0 \leq \theta_{lab} \leq \pi/4$ , with a solid angle of about 60 msr per detector. The NaI detectors covered a total solid angle of  $\Delta\Omega \sim 4\pi/5$ , with a resolution of 61 keV at 429 keV (FWHM).

## Preliminary analysis

In the thick target method, that was adopted in this experiment, the beam has its energy set to the maximum value to be measured and the target is chosen thick enough to cover the energy range of interest. Because of the energy loss of the beam inside the target, it is possible to measure the excitation function all at once. Notwithstanding, an adequate treatment using the kinematics and energy loss of the recoiled proton inside the target is required in the analysis. The development of the code to treat the data with all these considerations is now under development. In order to be able to subtract the background contribution due to carbon in the polyethylene target, carbon foil runs were also performed. These data also require similar treatment, since the target thickness seen by the beam is different, according to the reaction point and density of the target. The inelastic contribution can be distinguished by taking coincidence between the proton and the  $\gamma$ -ray (spectrum shown in Fig. 1) from the deexcitation of  ${}^7\text{Be}$  to its ground state ( $E_\gamma = 429$  keV). The background contribution from the  $\beta$ -decay of the implanted  ${}^7\text{Be}$  to  ${}^7\text{Li}^*$ , that decays to the ground state emitting a  $\gamma$ -ray ( $E_\gamma = 470$  keV) was found to be very low (less than 7%), as expected. The similarities between the raw proton spectra (top of Fig. 2) and the raw proton spectra in coincidence with a  $\gamma$ -ray gated around the 429 keV peak and the timing peak (bottom of Fig. 2) indicate that some of the resonances in  ${}^8\text{B}$  might have a significant branching to the first excited state in  ${}^7\text{Be}$  as well. In addition, we may be able to confirm the now uncertain existence of a  $2^-$  state at around 3 MeV [4, 5], since our data covers a wide range up to  $E_{cm} = 7$  MeV.

A detailed analysis is though necessary before we make a conclusion.

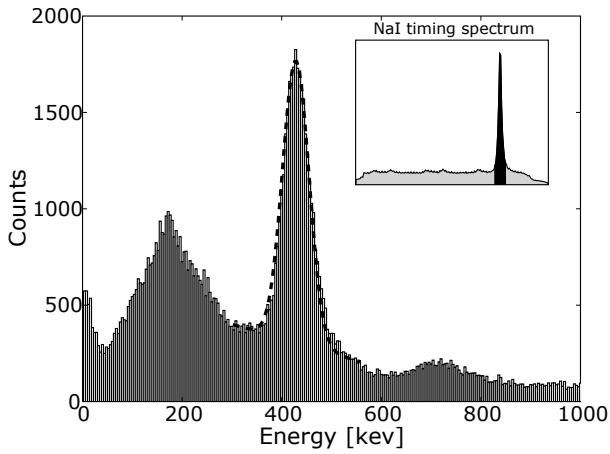


Figure 1. The  $\gamma$ -ray spectrum for the polyethylene target runs. The inset shows the timing spectrum for the detectors and the region where the gate is set.

## References

- [1] J. N. Bahcall and C. Peña-Garay, *New J. Phys.* **6** (2004) 63.
- [2] A. R. Junghans *et al.*, *Phys. Rev. C* **68** (2003) 065803.
- [3] E. G. Adelberger, *Rev. Mod. Phys.* **70** (1998) 1265-1291.
- [4] V. Z. Gol'dberg *et al.*, *JETP Lett.* **67** (1998) 1013.
- [5] G. V. Rogachev *et al.*, *Phys. Rev. C* **64** (2001) 061601.
- [6] C. Angulo *et al.*, *Nucl. Phys. A* **716** (2003) 211-229.
- [7] F. C. Barker and A.M. Mukhamedzhanov, *Nucl. Phys. A* **673** (2000) 526-532.

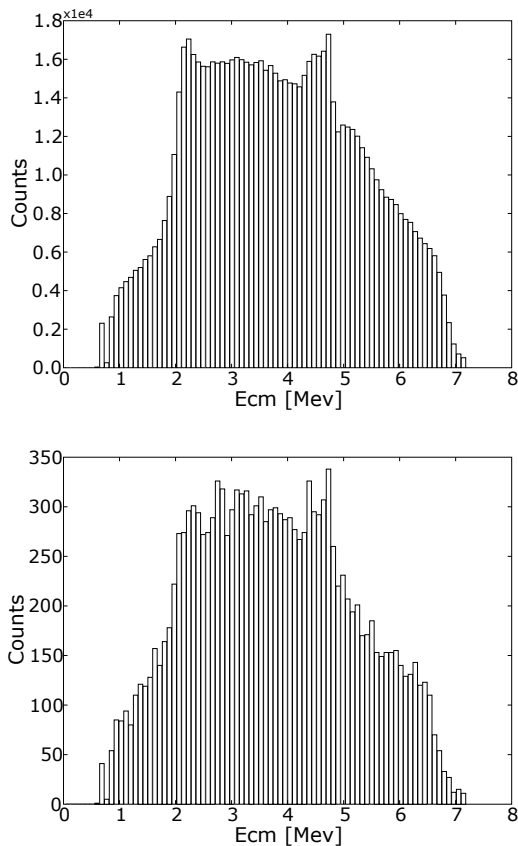


Figure 2. Raw proton spectra in coincidence with  $\gamma$ -rays measured by the NaI detector array (bottom) and events not in coincidence (top). The timing gate is shown in the inset of Fig. 1, the energy gate covers the region of the 429 keV peak.

# Study of Cluster States in $^{11}\text{B}$ and $^{13}\text{C}$ via $(\alpha, \alpha')$ Reaction

Y. Sasamoto, T. Kawabata, T. Uesaka, K. Suda, Y. Maeda, S. Sakaguchi, K. Itoh<sup>a</sup>, K. Hatanaka<sup>b</sup>, M. Fujiwara<sup>b</sup>, A. Tamii<sup>b</sup>, Y. Shimizu<sup>b</sup>, K. Nakanishi<sup>b</sup>, K. Kawase<sup>b</sup>, H. Hashimoto<sup>b</sup>, Y. Tameshige<sup>b</sup>, H. Matsubara<sup>b</sup>, M. Itoh<sup>c</sup>, H. P. Yoshida<sup>d</sup> and M. Uchida<sup>e</sup>

Center for Nuclear Study, Graduate School of Science, University of Tokyo

<sup>a</sup>Department of Physics, Saitama University

<sup>b</sup>Research Center for Nuclear Physics (RCNP), Osaka University

<sup>c</sup>Cyclotron and Radioisotope Center (CYRIC), Tohoku University

<sup>d</sup>Department of Physics, Kyusyu University

<sup>e</sup>Department of Physics, Tokyo Institute of Technology

Alpha cluster is one of the important concepts in the nuclear structure. Alpha cluster states in self-conjugate 4N nuclei are expected to emerge near  $\alpha$ -decay thresholds as shown in the Ikeda diagram [1]. For example, it has been suggested that the 7.65-MeV  $0_2^+$  state in  $^{12}\text{C}$  has a  $3\alpha$  configuration [2]. This state locates at 0.39 MeV above the  $3\alpha$ -decay threshold energy.

Recently, it was found through the measurement of the Gamow-Teller and spin-flip  $M1$  strength that the  $3/2_3^-$  state in  $^{11}\text{B}$  at  $E_x = 8.56$  MeV is not well described by shell-model (SM) calculations [3]. The  $3/2_3^-$  state, which locates just 100-keV below the  $\alpha$ -decay threshold, is considered to be a cluster state where a proton hole in the  $p_{3/2}$  orbit couples to the  $0_2^+$  state in  $^{12}\text{C}$ . On the other hand, Milin and Oertzen proposed that the  $1/2_2^-$  state ( $E_x = 8.86$  MeV) and the  $1/2_2^+$  state ( $E_x = 10.996$  MeV) in  $^{13}\text{C}$  are  $3\alpha$  cluster states with one excess neutron which acts as a covalent particle [4]. The influence of such excess particles and holes in the cluster states can be examined by comparing of the cluster state in  $^{12}\text{C}$  with those in  $^{13}\text{C}$  and  $^{11}\text{B}$ .

In order to investigate their structure, a measurement of the isoscalar transition strengths is useful since most cluster states in nuclei are excited by the isoscalar transitions. In the present work, we measured the angular distribution of the  $\alpha$ -inelastic scattering from  $^{11}\text{B}$ ,  $^{13}\text{C}$ , and  $^{nat}\text{C}$  at forward angles of  $\theta = 0^\circ - 19.4^\circ$  to obtain the isoscalar transition strengths. Generally, both the isoscalar and isovector transitions contribute to the transition strengths in  $N \neq Z$  nuclei. Therefore, isoscalar probes like the  $\alpha$ -inelastic scattering should be used to extract the isoscalar strengths.

The experiment was performed by using a 400-MeV alpha beam at the Research Center for Nuclear Physics, Osaka University. The alpha particles scattered from the target were momentum analyzed by the magnetic spectrometer Grand Raiden (GR). In the measurement at forward angles, hydrogen in the target causes severe backgrounds since the cross section for the  $\alpha + p$  elastic scattering is much larger than that for the inelastic scattering. To eliminate the background, we developed a recoil proton counter (RPC) and installed it in the scattering chamber of GR. The RPC detected recoil protons from the  $\alpha + p$  scattering. Therefore, the background from hydrogen can be separated from  $\alpha$ -inelastic scattering events by requiring or imposing the con-

dition that the recoil protons are detected by the RPC.

In the  $0^\circ$  measurement, we changed the experimental setup from the standard one to a special one in order to measure the low-lying states with  $E_x \leq 6$  MeV. Those low excited states have never been measured at  $0^\circ$  due to a geometrical limitation in the experimental setup. In the usual experimental setup at  $0^\circ$ , the beam duct was placed at the high momentum side of the focal plane detectors of GR to lead the beam to a Faraday cup. The primary beam passed through the GR and was stopped in the Faraday cup placed 12-m downstream from the focal plane. Since the distance between the beam duct and the effective area of the focal plane detectors was fixed at 12 cm, the momentum acceptance was geometrically restricted to  $E_x \geq 6$  MeV. In the special setup used in the present experiment, a beam stopper was installed in front of the focal plane detectors in order to overcome this restriction. Fig.1 shows the excitation energy

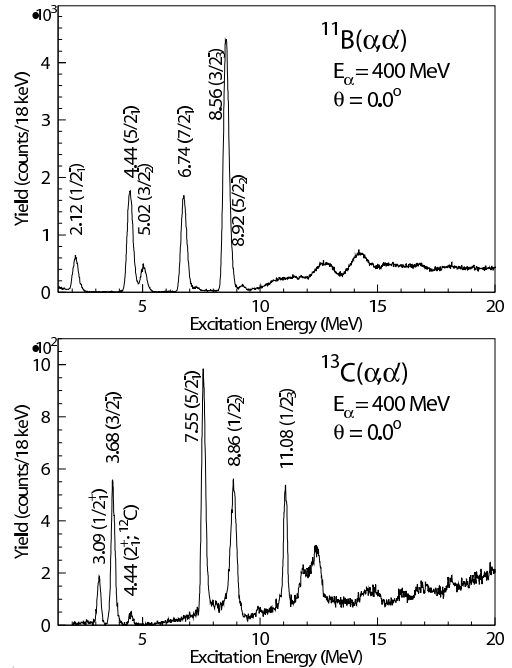


Figure 1. Energy spectra for  $^{11}\text{B}(\alpha, \alpha')$  and  $^{13}\text{C}(\alpha, \alpha')$  reactions at  $0^\circ$ .

spectra for the  $^{11}\text{B}(\alpha, \alpha')$  and  $^{13}\text{C}(\alpha, \alpha')$  reactions measured at  $0^\circ$  with the beam stopper. The first excited state in  $^{11}\text{B}$

Table 1. Measured isoscalar monopole and quadrupole strengths for the excited states in  $^{11}\text{B}$  compared with the theoretical predictions by the SM and AMD (VAP) calculations.

$J^\pi$	$E_x$ (MeV)	Experiment		Shell-model		AMD (VAP)	
		$B(E0; IS)$ (fm $^4$ )	$B(E2; IS)$ (fm $^4$ )	$B(E0; IS)$ (fm $^4$ )	$B(E2; IS)$ (fm $^4$ )	$B(E0; IS)$ (fm $^4$ )	$B(E2; IS)$ (fm $^4$ )
$1/2_1^-$	2.12		$11.6 \pm 0.6$		12.0		12.3
$5/2_1^-$	4.44		$39.2 \pm 2.0$		49.5		66.5
$3/2_2^-$	5.02	$1.7 \pm 0.6$	$6.4 \pm 0.3$	$\sim 0$	14.2	7	2.3
$7/2_1^-$	6.74		$34.6 \pm 1.8$		42.9		34.4
$3/2_3^-$	8.56	$72 \pm 6$	$4.4 \pm 1.7$	$\sim 0$	0.012	94	5.3

at the very low excitation energy of 2.12 MeV was successfully measured.

Angular differential cross sections for several low-lying states of  $^{11}\text{B}$  excited via  $(\alpha, \alpha')$  reactions are shown in Fig. 2. Since the ground state of  $^{11}\text{B}$  has non-zero spin, the cross sections for the  $^{11}\text{B}(\alpha, \alpha')$  reaction are described by an incoherent sum over the cross section of the different multipole contributions. The  $^{11}\text{B}(\alpha, \alpha')$  cross sections are, therefore, analyzed by summing up the cross sections calculated with a few multipole transitions. The cross section for each multipole transition was calculated by using the macroscopic model [5]. Since the angular distribution of the cross section is characterized by the transferred angular momentum  $L$ , it is possible to decompose the cross section into each multipole component by fitting the measured angular distribution as shown in Fig. 2.

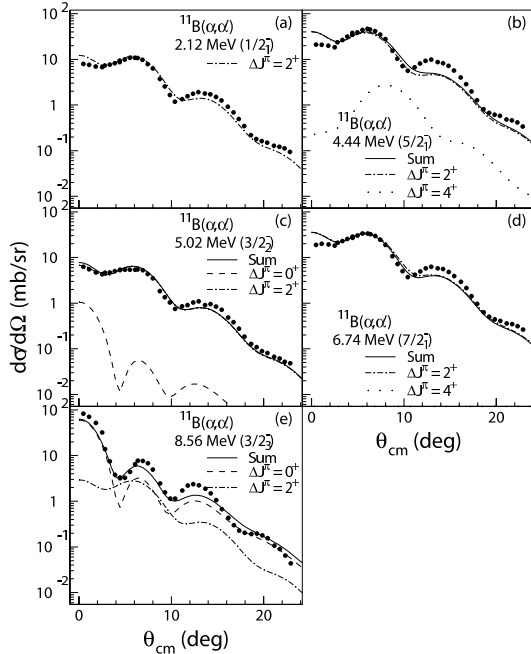


Figure 2. Cross sections for the  $^{11}\text{B}(\alpha, \alpha')$  reaction at  $E_\alpha=400$  MeV. The dashed, dash-dotted and dotted curves shows the  $\Delta J^\pi=0^+, 2^+$  and  $4^+$  contributions.

By the multipole decomposition analysis, isoscalar monopole [ $B(E0; IS)$ ] and quadrupole [ $B(E2; IS)$ ] strengths were deduced. Table 1 lists the obtained  $B(E0; IS)$  and  $B(E2; IS)$  values together with theoretical predictions.

The shell-model (SM) calculation are performed by using the SFO interactions [6] within the  $0-2\hbar\omega$  configuration space. In this SM calculation, the effective charges of  $e_p^{eff}=1.24$  and  $e_n^{eff}=0.22$  are used to reproduce the experimental values. The SM calculation reasonably well explains the experimental  $B(E2; IS)$  for all the excited states in Table 1 except for the  $3/2_3^-$  state. For the  $3/2_3^-$  state, almost no monopole excitation strength is predicted by the SM calculations while the large monopole strength is observed in the present work.

To examine cluster nature of the excited states in  $^{11}\text{B}$ , the experimental results are compared with the antisymmetrized molecular dynamics (AMD) calculation. In the AMD calculation, the method of the variational calculation after the spin-parity projection (VAP) [7] [8] was used. The level structure predicted by the AMD calculations is slightly different from the experimental level scheme of  $^{11}\text{B}$ . However, the excitation strength are reasonably well explained without any effective charges. The large monopole strength for the  $3/2_3^-$  state, which is not well described in the SM calculation, is successfully predicted by the AMD calculation. According to the AMD calculation, the  $3/2_3^-$  state has a spatially well-developed cluster structure with a loosely bound  $2\alpha+t$  configuration. The present result suggests that the  $3/2_3^-$  state has a  $2\alpha+t$  cluster structure.

The angular distribution of cross sections for  $^{13}\text{C}(\alpha, \alpha')$  will also be analyzed. The results will be reported elsewhere soon.

## References

- [1] K. Ikeda *et al.* Prog. Theor. Phys. Suppl. Extra Number p. (1968) 464.
- [2] H. Morinaga, Phys. Rev. **101** (1956) 254.
- [3] T. Kawabata *et al.*, Phys. Rev. C **70** (2004) 034318.
- [4] M. Milin *et al.*, Eur. Phys. J. A **14** (2002) 295.
- [5] M. N. Harakeh *et al.* Giant Resonances. Clarendon Press, Oxford, (2001).
- [6] T. Suzuki *et al.* Phys. Rev. C **67** (2003) 044302.
- [7] Y. Kaneda-En'yo, Phys. Rev. Lett. **81** (1998) 5291.
- [8] Y. Kaneda-En'yo *et al.* Phys. Rev. C **60** (1999) 064304.

## Lifetime Measurement of $^{32}\text{Mg}$ First $2^+$ State

M. K. Suzuki<sup>a</sup>, H. Sakurai<sup>b</sup>, H. Iwasaki<sup>a</sup>, A. Dewald<sup>c</sup>, T. Fukuchi<sup>d</sup>, T. Fukui<sup>e</sup>, Y. Ichikawa<sup>a</sup>, E. Ideguchi<sup>f</sup>, M. Liu<sup>f</sup>, T. Nakao<sup>a</sup>, M. Niikura<sup>f</sup>, H. J. Ong<sup>a</sup>, T. K. Onishi<sup>a</sup>, H. Otsu<sup>b</sup>, T. Sumikama<sup>b</sup>, D. Suzuki<sup>a</sup>, H. Suzuki<sup>a</sup>, Y. Zheng<sup>f</sup>, and S. Shimoura<sup>f</sup>

<sup>a</sup>Department of Physics, University of Tokyo

<sup>b</sup>RIKEN (The Institute of Physical and Chemical Research)

<sup>c</sup>Institut für Kernphysik Universität zu Köln

<sup>d</sup>Department of Physics, Osaka University

<sup>e</sup>Department of Physics, Kyoto University

<sup>f</sup>Center for Nuclear Study, Graduate School of Science, University of Tokyo

Lifetime of excited states of nuclei provides us with important information of the nuclear structure. Direct lifetime measurements in the range of greater than 1 ps are usually applied to unstable nuclei using slow-down or stopped RI beams. To extend the measurement to nuclei far from stability, it is necessary to develop new methods fit for unstable nuclei by fragmentation reactions at intermediate energies. So far, two methods have been used for lifetime measurements with intermediate-energy RI beams. The Doppler-Shift Attenuation Method [1] was applied to measure lifetime in the order of 1 ps, while relatively long lifetimes in the 100-ps range can be measured with the Recoil Shadow Method [2]. We improved the Recoil Distance Method (RDM) [3] and expanded the lifetime measurements to the 10ps range.

In the RDM, RI beams excited by any reactions at the secondary target fly to the plunger at  $\sim 1$  mm downstream of the target, and then they are decelerated by the plunger. De-excitation  $\gamma$  rays emitted before and after deceleration will have different energies, because their Doppler coefficients are different. The lifetime of the excited state is deduced by comparing the counts of the two peaks.

The RDM with intermediate-energy beams has more advantages than with slow beams [4] [5]. The distance between the secondary target and the plunger can be longer, thus the uncertainty of distance becomes relatively small. Moreover, intermediate-energy beams allow us to use thick secondary target for efficient measurements. We applied the RDM to intermediate-energy RI beams of  $^{32}\text{Mg}$  for the first time.

$^{32}\text{Mg}$  is a typical nucleus of the ‘Island of Inversion’. The energy of the first excited state and the value of  $B(E2; 2_1^+ \rightarrow 0^+)$  implies the break of closed shell structures. The  $B(E2)$  values of  $^{32}\text{Mg}$  were obtained from the intermediate Coulomb scattering of  $^{32}\text{Mg}$  and the  $\beta$ - $\gamma$  decay of  $^{32}\text{Na}$ . The value of  $B(E2)$  has been reported to be  $454 \pm 78 e^2 \text{fm}^4$  [6],  $333 \pm 70 e^2 \text{fm}^4$  [7] and  $622 \pm 90 e^2 \text{fm}^4$  [8] by the intermediate Coulomb scattering,  $325^{+109}_{-65} e^2 \text{fm}^4$  [9] by the  $\beta$ - $\gamma$  spectroscopy, as shown Fig.1. All the results are not consistent with each other. Thus, high precision measurement of  $B(E2)$  with an accuracy of 10% should be desired. In this experiment, the advantages described before expected to achieve the necessary accuracy.

The experiment was performed in the RIKEN Acceler-

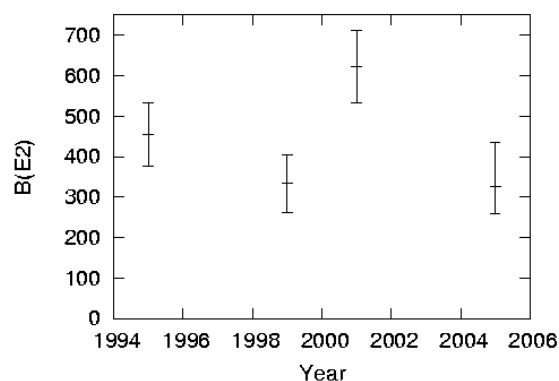


Figure 1. Experimental values of  $^{32}\text{Mg}$   $B(E2; 2_1^+ \rightarrow 0^+)$

ator Facility. A radioactive beam of  $^{32}\text{Mg}$  was produced via fragmentation of a 95-MeV/nucleon  $^{40}\text{Ar}$  beam with a 277-mg/cm<sup>2</sup>-thick  $^9\text{Be}$  target. The secondary beam was separated by the RIPS with the  $B\rho$ - $\Delta E$ - $B\rho$  method. The beam particles were identified event-by-event by the time-of-flight(TOF)- $\Delta E$  method. The TOF was defined as the time between a 0.1-mm-thick plastic scintillator and PPACs placed 5.3 m apart along the beam line. The number of PPACs were two to determine the incidence angle of the particles, so the timing of PPACs was defined as average of the two PPACs with a distance correction. The  $\Delta E$  information was obtained by a 0.1-mm-thick Si detector placed at the first achromatic focal plane of RIPS. The  $^{32}\text{Mg}$  beam had a average intensity of 1 k counts per second and a purity of about 21%. The major contaminants were  $^{33,34}\text{Al}$  and  $^{35}\text{Si}$ . A reaction target system composed of a secondary target and plunger was placed at the final focal plane of RIPS. We used two different systems. One had a 1353-mg/cm<sup>2</sup>-thick Au target and a 98.4-mg/cm<sup>2</sup> Au plunger placed at 1200  $\mu\text{m}$  downstream (target system-1). The other had a 1339-mg/cm<sup>2</sup>-thick Au target and a 98.8-mg/cm<sup>2</sup> Au plunger placed at 5000  $\mu\text{m}$  downstream (target system-2). The mean energies of  $^{32}\text{Mg}$  nuclei between the target and plunger were calculated to be 26.1 MeV/nucleon for both systems.

Scattered particles were detected by a 100mm $\times$ 100mm PPAC and a 150mm $\times$ 150mm PPAC located 200 mm and 383 mm downstream from the target, respectively, to mea-

measure the emission angle of the scattered particles. Moreover, the scattered particles were identified by the  $\Delta E$ - $E$  method using a Si-detector telescope located 458-mm downstream from the target. The telescope was comprised of three layers of silicon detectors with thickness of  $200\mu\text{m}$ ,  $500\mu\text{m}$ , and  $500\mu\text{m}$ , respectively. The telescope covered  $150\text{mm}\times 150\text{mm}$  area, corresponding to the laboratory scattering angles up to 12 degrees.

De-excitation  $\gamma$  rays were detected by the position sensitive Ge detector array GRAPE [11] [12] which composed of 12 Ge crystals surrounding the target around 120 degrees with respect to the beam axis. Each crystal was placed at a distance of 135 mm from the target. Energy and efficiency calibrations of each Ge were made using the standard  $\gamma$  sources,  $^{152}\text{Eu}$ ,  $^{133}\text{Ba}$  and  $^{88}\text{Y}$ . The energy resolution of each crystal was  $5.27(2)$  keV FWHM and the total efficiency was  $7.50(1) \times 10^{-3}$  for 898-keV  $\gamma$  rays as measured with the  $^{88}\text{Y}$  source.

To decrease backgrounds originated from environmental  $\gamma$  rays and neutrons, seven BGO crystals with a size of  $80 \times 250 \times 25 \text{ mm}^3$  were arranged at the upstream and downstream of the GRAPE. Energy and efficiency calibrations of each BGO were made using the standard  $\gamma$  source  $^{22}\text{Na}$ . The energy resolution was 200keV FWHM for the 1275-keV  $\gamma$  rays.

Fig. 2 shows Doppler-corrected  $\gamma$ -ray energy spectra using the target system-2, which was obtained in coincidence with inelastically scattered  $^{32}\text{Mg}$  isotopes. The solid line shows a spectrum without any conditions about BGO and the hatched area shows a spectrum with the condition that any BGO crystals did not have signals. The signal to background ratio advanced from 0.2 to 1. As seen in Fig. 2, a  $\gamma$ -ray peak is evident at 895(10) keV, which is attributed to  $2_1^+ \rightarrow 0_{g.s.}^+$  transition in  $^{32}\text{Mg}$ .

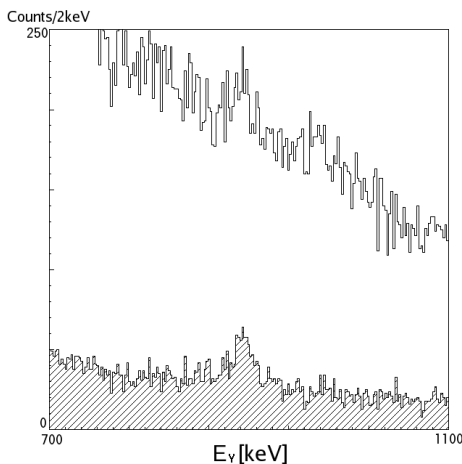


Figure 2. Doppler-corrected  $\gamma$ -ray energy spectra using the target system with the distance of  $5000 \mu\text{m}$ .

Fig. 3 shows a Doppler-corrected  $\gamma$ -ray energy spectrum using the target system-1 with no-BGO-signal condition. As expected, it really has a double-peaked structure.

The analysis of the lifetime is in progress.

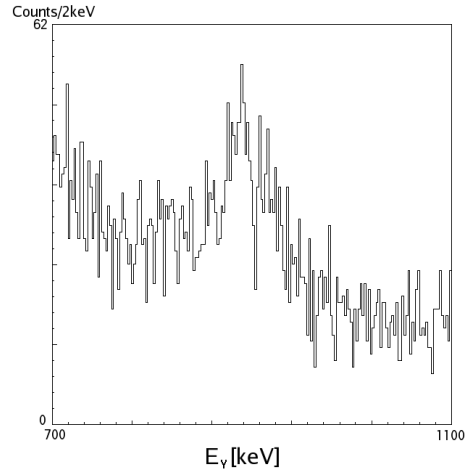


Figure 3. Doppler-corrected  $\gamma$ -ray energy spectrum using the target system with the distance of  $1200 \mu\text{m}$  with no-BGO-signals condition

## References

- [1] N. Imai *et al.*, RIKEN Accel. Prog. Rep. **38** (2005) 41.
- [2] N. Imai *et al.*, Phys. Rev. Lett. **92** (2004) 062501.
- [3] C. Broude *et al.*, Nucl. Phys. A **216** (1973) 603.
- [4] G. Kemper *et al.*, Eur. Phys. J. A **11**. (2001) 121.
- [5] J. R. Cooper *et al.*, Phys. Rev. Lett. **87** (2001) 132503.
- [6] T. Motobayashi *et al.*, Phys. Lett. B **346** (1995) 9.
- [7] B. V. Pritychenko *et al.*, Phys. Lett. B **461** (1999) 322.
- [8] V. Chisté *et al.*, Phys. Lett. B **514** (2001) 233.
- [9] H. Mach *et al.*, J. Phys. G: Nucl. Part. Phys. **31** (2005).
- [10] T. Kubo *et al.*, Nucl. Instrum. Methods B **70** (1992) 309.
- [11] S. Shimoura, Nucl. Instrum. Methods A **470** (2004) 188.
- [12] M. Kurokawa *et al.*, IEEE Trans. Nucl. Sci. **50** (2003) 1309.

# Development of a High-Efficiency Method for $\alpha$ Resonant Scattering with the Thick Target Method

H. Fujikawa, S. Kubono, A. Saito, H. Yamaguchi, G. Amadio, J. J. He, L. H. Khieu<sup>a</sup>,  
S. Nishimura<sup>b</sup>, H. Ohta<sup>c</sup>, A. Ozawa<sup>c</sup>, Y. Tagishi<sup>c</sup>, Y. Wakabayashi<sup>d</sup>, M. Yamaguchi<sup>c</sup> and  
T. Yasuno<sup>c</sup>

Center for Nuclear Study, Graduate School of Science, University of Tokyo

<sup>a</sup>Institute of Physics and Electronics, Vietnam

<sup>b</sup>RIKEN (The Institute of Physical and Chemical Research)

<sup>c</sup>Institute of Physics, University of Tsukuba

<sup>d</sup>Department of Physics, Kyushu University

The  $\alpha$ -induced reactions such as  $(\alpha,p)$ ,  $(\alpha,n)$  are important in astrophysical nucleosynthesis. For instance, in novae and X-ray bursts, the rapid proton-capture (rp-) process is considered to start with the breakout reactions from the hot-CNO cycle. One of the breakout reactions for X-ray bursts is the  $^{14}\text{O}(\alpha,p)^{17}\text{F}$  reaction [1]. This is partly because the hydrogen burning of  $^{14}\text{O}$  is inhibited since  $^{15}\text{F}$  is proton unbound. Another example is the  $^8\text{Li}(\alpha,n)^{11}\text{B}$  reaction [2], recognized as an important reaction to pass through the valley of  $A=8$  in the primordial nucleosynthesis. Thus, properties of  $\alpha$  resonances especially in unstable nuclei are important for nuclear astrophysics.

We have been working to establish an experimental method to determine properties of such  $\alpha$  resonances with high precision. Once established, the method should be useful for studies of astrophysical  $(\alpha,p)$  reaction and  $\alpha$ -clustering aspects in nuclear structures. In our previous experiment [1], a gaseous helium target cooled down to 30 K confined in Havar windows was used. However the cooled target trapped materials which made the energy losses of the incident and outgoing particles uncertain. The uncertainty of the absolute cross section is increased by the materials. In the present study, a helium gas target at room temperature is used for the  $\alpha$  resonant scattering with the thick target method [3]. Silicon detectors for recoiled particles are set in the gas to minimize the energy loss and the multiple scattering of the incident and recoiled particles in confining foils. We aim at measuring the energy and the scattering angle of recoiled  $\alpha$  particles.

In order to establish the experimental method to measure the  $\alpha$  resonant scattering, we performed an experiment of  $\alpha+^{16}\text{O}$  elastic scattering at the University of Tsukuba Tandem Accelerator Center (UTTAC). Figure 1 shows a schematic view of the experimental setup. An  $^{16}\text{O}$  beam at 40 MeV was supplied by the 12UD Pelletron tandem accelerator. In the beam-monitoring section, the beam was collimated by a double-collimator system. A carbon foil was set after the collimators. A silicon detector was set at 12 degrees with respect to the beam direction in order to monitor the beam current using the  $^{16}\text{O}+^{12}\text{C}$  elastic scattering. The setup for measuring the  $\alpha$  resonant scattering is shown in the target section in Fig. 1. Helium gas at room temperature was used as a target. The target gas region was separated from the vacuum of the transport line by a 2.2-

$\mu\text{m}$ -thick Havar foil. The pressure of helium gas was adjusted so as to stop the beam particles before the telescope in the gas. The energy of the  $^{16}\text{O}$  beam decreased down to 32.5 MeV after the Havar foil. A telescope consisting of two position sensitive silicon detectors (PSD1 and PSD2) and a pad silicon detector (SSD) was set on rotatable table to cover a certain range of scattering angle inside the gas. The recoiled  $\alpha$  particles were identified by the  $\Delta E$ - $E$  method.

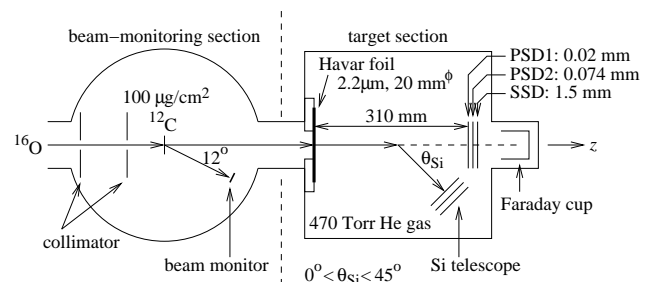


Figure 1. Schematic view of the experimental setup.

We performed an analysis to compare the experimental data with the  $R$ -matrix calculation. Figure 2 shows an energy spectrum of  $\alpha$  particles measured by the strip at 0 degree. The closed circles show the experimental data. The solid curve corresponds to the  $R$ -matrix calculation including the experimental resolution. Several peaks were observed which correspond to known levels in  $^{20}\text{Ne}$  [4].

Figure 3 shows the correlation between the energy and the scattering angle of the recoiled  $\alpha$  particles. The vertical axis is the energy of the recoiled  $\alpha$  particles at the telescope, whereas the horizontal axis is the scattering angle in the center-of-mass system. The scattering angle was determined by taking the kinematics and the energy losses of the incident and the recoiled particles into account. The solid curves are the calculations which well reproduce the experimental data.

Figure 4 shows an example of the angular distribution of the recoiled  $\alpha$  particles for the 10.55 MeV  $4^+$  state in  $^{20}\text{Ne}$ . The solid curve is a square of the Legendre polynomial  $P_4(\cos \theta_{\alpha}^{\text{c.m.}})$  which is the characteristic of  $J^{\pi}=4^+$  state. The data has a good agreement with the calculation, which shows the kinematic correction worked properly.

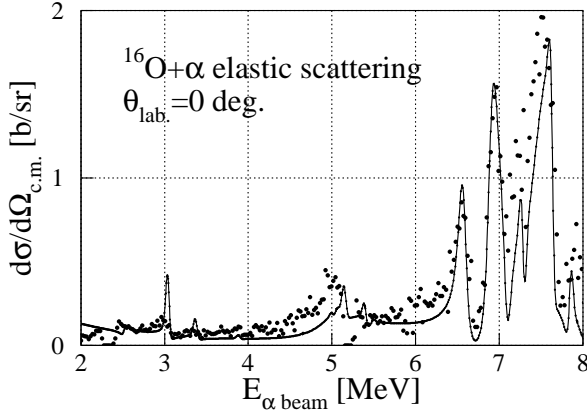


Figure 2. The  $R$ -matrix fit to the data at  $\theta_{\text{lab.}}=0$  deg.

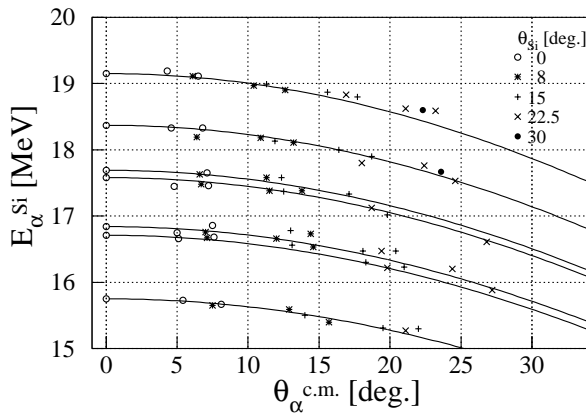


Figure 3. Correlation between the energy and the scattering angle of the recoiled  $\alpha$  particles.

In the present study, the experimental method for the  $\alpha$  resonant scattering was developed using the room-temperature helium gas target and the inverse kinematics. The  $R$ -matrix analysis of the data showed good agreements with the resonance parameters known for the excited states in  $^{20}\text{Ne}$ . The kinematic shifts of energies and scattering angles were well reproduced by the calculation including the kinematics and the energy losses. This method will be applied to  $\alpha$  resonant scattering experiment using RI beams.

## References

- [1] M. Notani *et al.*, Nucl. Phys. A **738** (2004) 411.
- [2] M. Kurata-Nishimura *et al.*, CNS Annual Report 2003 (2004) 42.
- [3] S. Kubono, Nucl. Phys. A **693** (2001) 221.
- [4] D. R. Tilley *et al.*, Nucl. Phys. A **636** (1998) 249.

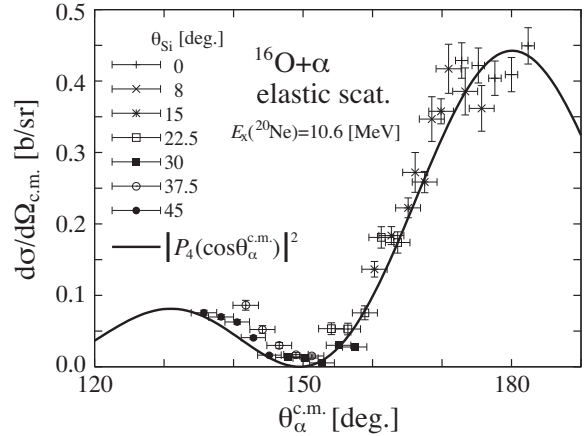


Figure 4. Angular distribution of the 10.6 MeV  $4^+$  state in  $^{20}\text{Ne}$ .

# Beta Decay Study of C, N, O Isotopes Close to the Neutron-Drip Line

T. K. Onishi, H. Sakurai<sup>a</sup>, N. Aoi<sup>a</sup>, T. Fukuchi<sup>b</sup>, T. Fukui<sup>c</sup>, A. Gelberg<sup>d</sup>, Y. Ichikawa, E. Ideguchi<sup>e</sup>, H. Iwasaki, T. Kishida<sup>a</sup>, M. Liu<sup>e</sup>, T. Nakao, M. Niikura<sup>e</sup>, S. Nishimura<sup>a</sup>, H. J. Ong, H. Otsu<sup>a</sup>, S. Shimoura<sup>e</sup>, T. Sumikama<sup>a</sup>, D. Suzuki, H. Suzuki, M. K. Suzuki, N. Yamada<sup>a</sup> and Y. Zheng<sup>e</sup>

*Department of Physics, University of Tokyo*

<sup>a</sup>*RIKEN (The Institute of Physical and Chemical Research)*

<sup>b</sup>*Department of Physics, Osaka University*

<sup>c</sup>*Department of Physics, Kyoto University*

<sup>d</sup>*Institut für Kernphysik der Universität zu Köln*

<sup>e</sup>*Center for Nuclear Study, Graduate School of Science, University of Tokyo*

## 1. Introduction

One of the most interesting phenomena in nuclei far from the line of stability is a variation of the magic numbers. The magic number  $N = 20$  is broken in the region of the island of inversion [1] and the new magic number  $N = 16$  is suggested in the oxygen isotopes [2]. In this region, the proton-neutron ratio becomes imbalance and residual interactions are modified from that in the stable nuclei. This causes the modification of the shell structure.

The nuclei with  $Z \approx 8$  provide an opportunity to investigate the effects of neutron excess on the  $p$ - $sd$  shell gap of the proton side. In particular, the  $\beta$ -decay of the neutron-rich C, N isotopes is an excellent probe. In these nuclei, the valence neutrons belong to the  $sd$  shell, while the valence protons belong to the  $p$  shell. Therefore, intruder states are populated selectively through the  $\beta$ -decay because of the selectivity of the  $\beta$ -decay.

## 2. Experiment

The present study was performed at RIKEN Projectile Fragment Separator (RIPS) in the RIKEN accelerator research facility. Radioactive ions were produced by projectile fragmentation of a 63 MeV/nucleon  $^{40}\text{Ar}$  primary beam with a beam intensity of 500 pA. The production target was Ta with a thickness of 333 mg/cm<sup>2</sup>. The reaction fragments were collected and analyzed by RIPS and transported to the final focal plane (F3) of RIPS. There were three settings of RIPS, depending on the nuclei of interest. Table 1 shows the rates of the obtained fragments in each setting. The beam was pulsed for measuring the half-lives of the nuclei. The durations of the beam-on and beam-off periods were also shown in Table 1. In the setting of  $^{20}\text{C}$  and  $^{22}\text{N}$ , the beam was not pulsed. Because the half-lives of these nuclei are short (a few ms) and the rate is relatively low (a few pps). In this situation, a  $\beta$ -decay event can be related to a parent nucleus. Therefore, the half-lives were measured by the difference of the times between a beam and a  $\beta$ -decay.

The radioactive ions were implanted into a plastic scintillator with a thickness of 5 mm at F3. This active stopper enables us to count the number of the implanted ions.

The active stopper also was used as a  $\beta$ -ray detector. This stopper had two photomultiplier tubes at both ends, in order to reject a single photon noise for the efficient detection of  $\beta$ -rays.

Table 1. Rates of the obtained nuclei, the pulsing periods and the momentum acceptances in each setting are shown.

setting No.	pulsing periods on-off (ms)	momentum acceptance (%)	obtained nucleus	rate (pps)
1	330-330	$\pm 3$	$^{20}\text{N}$	2.1 k
2	170-170	$\pm 2$	$^{17}\text{B}$	36
			$^{19}\text{C}$	52
			$^{21}\text{N}$	300
			$^{23}\text{O}$	23
3	—	$\pm 2$	$^{20}\text{C}$	7.8
			$^{22}\text{N}$	9.4
			$^{24}\text{O}$	2.0

The  $\gamma$ -ray detection system consisted of two clover-type Ge detectors and the CNS Ge array (GRAPE). The photopeak efficiency of this system was 4.3 % for 1 MeV  $\gamma$ -rays. Each clover-type Ge detectors was surrounded by anti-Compton shield, which consisted of eight BGO scintillators. Each BGO scintillator had a size of  $80 \times 250 \times 25$  mm<sup>3</sup>. For a veto of a  $\beta$ -ray to the Ge detectors, each Ge detector had an plastic scintillator at the front end. The plastic scintillators with a thickness of 1 mm were used for the clover-type Ge detectors and a plastic scintillators with the thickness of 5 mm for GRAPE.

## 3. Summary

We have carried out an experiment of  $\beta$ - $\gamma$  measurements for  $^{19-20}\text{C}$ ,  $^{20-22}\text{N}$ ,  $^{24}\text{O}$ . We observed  $\beta$ -delayed  $\gamma$ -rays originated from these nuclei. The data analysis is now in progress.

## References

- [1] E. K. Warburton *et al.*, Phys. Rev. C **41** (1990) 1147.
- [2] B. A. Brown and W. A. Richier, Phys. Rev. C **72** (2005) 057301.



**Experimental Nuclear Physics:  
PHENIX Experiment at BNL-RHIC**



# Progress of the PHENIX Experiment in the Year 2005

H. Hamagaki, K. Ozawa, K. Kino, F. Kajihara, T. Gunji, T. Isobe, N. Kurihara, S. X. Oda, Y. Morino, S. Saito, Y. Aramaki, Y. L. Yamaguchi, J. Kikuchi<sup>a</sup>, S. Sano<sup>a</sup>, Y. Tanaka<sup>b</sup>, and T. Fusayasu<sup>b</sup>

*Center for Nuclear Study, Graduate School of Science, University of Tokyo*

<sup>a</sup> *Advanced Research Institute for Science and Engineering, Waseda University*

<sup>b</sup> *Nagasaki Institute of Advanced Science*

## 1. Introduction

Experimental studies at the Relativistic Heavy Ion Collider (RHIC) of Brookhaven National Laboratory, USA, has been producing many new results since the first successful collisions between Au nuclei in June 2000. The physics goal of the studies at RHIC is to find evidence of the quantum chromodynamical (QCD) phase transition from normal nuclear matter to deconfined quark matter, called quark-gluon plasma (QGP), and to study the properties of the hot QCD matter.

The CNS group has been participating in the PHENIX experiment with financial support from the Japan-US cooperation in the field of high energy physics sponsored by MEXT. The PHENIX experiment is one of the major experiments at RHIC, which consists of two central arms (East and West), two muon arms (North and South) and inner detectors for event trigger and event characterization. The PHENIX experiment was designed so as to address as many signatures as possible for QGP formation, by having a very unique capability to measure photons, electrons and muons as well as hadrons.

In this report, major topics of the PHENIX experiment and the activities of the CNS group in the Japanese fiscal year (JFY) 2005 are summarized.

## 2. RHIC Runs; Run 5 and 6

In the JFY 2005, PHENIX has successfully performed the latter half of Run 5, which started in the beginning of January 2005 and lasted until May 2005, and the first part of Run 6, which started in February 2006 and will continue until the end of June 2006. In Run 5, after a long run of Cu-Cu collisions at  $\sqrt{s_{NN}} = 200$  GeV, a short run at lower energy,  $\sqrt{s_{NN}} = 63$  GeV was performed. PHENIX collected  $1.08 \times 10^9$  events of Cu-Cu collisions at  $\sqrt{s_{NN}} = 200$  GeV ( $3.06 \text{ nb}^{-1}$  recorded), and  $4.25 \times 10^8$  events at  $\sqrt{s_{NN}} = 63$  GeV ( $190.2 \mu\text{b}^{-1}$  recorded). Run 6 is totally devoted to polarized p-p collisions. PHENIX accumulated  $10.7 \text{ pb}^{-1}$  of p-p collisions at  $\sqrt{s} = 200$  GeV, and run with a lower energy remains to be executed.

The CNS group has been responsible for maintenance, operation during the run, and calibration for data analysis of the RICH (Ring Imaging Cherenkov) subsystem, which is a gaseous Cherenkov counter using CO<sub>2</sub> gas as a Cherenkov radiator. RICH is a primary device for electron identification in the PHENIX experiment. The RICH subsystem worked without serious problems throughout Run 5, and has been working fine during Run 6.

## 3. Data analysis and results

Fourteen physics papers were published in refereed journals in JFY 2005 by the PHENIX collaboration, as listed in the publication list of this annual report. Several others have been submitted for publication and are in different stages before final publication. A paper internally called as 'white paper', which summarizes the physics achievement in the first few years of RHIC runs, was published in a special issue of Nuclear Physics A [1], together with the papers from the other three collaborations at RHIC.

The CNS group had several distinct data analysis activities in the JFY 2005. Brief introduction is intended in this article as an overview, and detailed descriptions will be provided in the following separate articles. Major efforts of the CNS group has been on the physics with photons and leptons, and various achievements are being made.

Photons are emitted at various stages of collision process and they mostly escape from the sources without scattering or absorption. Therefore, they can provide unique information from the interim of the hot and dense matter. The PHENIX succeeded in measuring direct photons from pQCD hard process in Au + Au collisions. The result clearly demonstrates that  $N_{\text{coll}}$  scaling holds well for pQCD photon production in the initial stage of the collisions, which indicates that initial state effects such as nuclear shadowing and Cronin effect are minor. This result is a powerful backup to the claim that yield suppression of high- $p_T$  hadrons are mainly due to Jet quenching effect. Excess of the photon yield over background was clearly demonstrated recently in the  $p_T$  region between 1 and 3 GeV/c, where thermal radiation from QGP phase is expected to have a large share. Recent progress on the photon analysis is described in Ref. [2].

Systematic studies of Jet quenching effect is in progress which should help understanding better the energy loss mechanism and properties of dense matter. Extension to a higher momentum was aimed for  $\pi^0$ , with Run 4 high statistical data for Au + Au collisions at  $\sqrt{s_{NN}} = 200$  GeV, as described in Ref. [3].

Big progress has been made for energy loss of heavy quarks, that is, charm quarks seem to undergo large energy loss comparable to the light quarks. The results were deduced from single electron measurements. Sources of single electrons are categorized into two items; 'photonic' and 'non-photonic'. Main 'non-photonic' sources at the RHIC energies are leptonic decay of charm and bottom mesons. 'Photonic' electrons, majority of which come from Dalitz decay of neutral mesons and external conversion of pho-

tons, are major and severe background sources for measuring ‘non-photonic’ electrons. The two methods, cocktail method and the converter method, were employed to estimate the photonic background contributions and to reduce ambiguity. Since energy loss of charm and bottom quarks due to gluon bremsstrahlung are estimated to be small because of their heavy mass, large yield suppression of single electron yield is demanding us to re-examine the mechanism of energy loss. Current status is described in Ref. [4].

The  $J/\psi$  yield suppression has been considered to be a key probe of deconfinement of hadronic matter. Enhancement of the  $J/\psi$  yield has been proposed at RHIC energies, which is due to coalescence process from charm and anti-charm quarks in QGP phase or in the hadronization stage. It is noted here that idea of coalescence production of  $J/\psi$  is not a new one, but has been neglected until recently since it should become effective only at high energy collisions [5]. The CNS group has been taking a leading role in the analysis of  $J/\psi$  productions. Preliminary results of the  $J/\psi$  yield and  $p_T$  distribution for a few centrality bins in Au-Au and Cu-Cu collisions has been obtained from the Run 4 [6] and Run 5 [7], respectively.

One of the research subjects at RHIC, which has critical importance but is not well developed, is low-mass vector mesons and low-mass lepton-pair continuum. Low-mass vector mesons should provide information relevant to chiral symmetry restoration. Importance of measuring low-mass lepton-pair continuum originated from thermal sources cannot be over-emphasized. Huge combinatorial background has prevented from extracting clean signals. Current status of analysis of low-mass electron-pairs in Au-Au and Cu-Cu collisions is presented in Ref. [8] and Ref. [7], respectively.

#### 4. R & D efforts

Development and application of GEM (gas electron multiplier) has been a central subject of R & D efforts of our group in the last few years. GEM, originally developed at CERN, has very simple structure having regularly arrayed holes pierced through a polyimide sheet with typical thickness of  $50\mu\text{m}$  with both sides coated by copper foils with thickness of  $\sim 5\mu\text{m}$  which serve as electrodes.

A new GEM (CNS-GEM) was developed which uses a different method for making holes [9], and extensive study of basic performance has been performed. As an effort, long-term gain stability was investigated, and the CNS-GEM was found to have better stability [10]. Another effort was to make systematic study of ion feedback. To have quantitative understanding of ion feedback is often crucial in order to make design specifications of a detector system such as time projection chamber [11]. In order to investigate electron multiplication processes, simulation study of GEM was made. MAXWELL3D was used to calculate the 3D electric field map using the finite-element analysis, and the field map was fed to GARFIELD, with which simulations on gas multiplication, diffusion, absorption etc have been made [12].

As an application of GEM, development of Cherenkov counter with CsI photo-cathode has been started. A spe-

cial GEM was developed with additional Ni and Au layers coated on the Cu electrode, which is needed to prevent Chemical reaction between CsI and Cu. Current status is reported in Ref. [13]

#### 4.1. R & D of ALICE TRD

The CNS group has been involved in the development of TRD (transition radiation detector) in the ALICE experiment at CERN-LHC, which is planned to start operation in 2008. The TRD should provide unique capability of electron identification to the ALICE experiment.

The CNS group participated in the test of TRD production-scale prototypes using secondary beams from CERN-PS in the fall of 2004. TRD performance was investigated [14].

#### 5. Summary

In the year 2005, the PHENIX experiment completed Run 5 with Cu + Cu collisions at  $\sqrt{s_{NN}} = 200$  GeV and  $\sqrt{s_{NN}} = 63$  GeV, and have been executing the first half of Run 6 which is dedicated to p + p collisions.

The major activities of the CNS groups are presented, which includes data analysis efforts, R & D efforts related to GEM, and ALICE TRD.

#### References

- [1] K. Adcox, T. Gunji, H. Hamagaki, M. Inuzuka, T. Isobe, F. Kajihara, S. Kametani, N. Kurihara, T. Kawabata, T. Matsumoto, S. Nishimura, K. Oyama, K. Ozawa, T. Sakaguchi *et al.* [PHENIX Collaboration]: Nucl. Phys. A **757** (2005) 184–283.
- [2] T. Isobe *et al.*, CNS Annual Report 2005 (2006) 51.
- [3] T. Isobe *et al.*, CNS Annual Report 2005 (2006) 53.
- [4] F. Kajihara *et al.*, CNS Annual Report 2005 (2006) 45.
- [5] T. Matsui: Proceedings of the Second Workshop on Experiments and Detectors for a Relativistic Heavy Ion Collider (RHIC), LBL, May 25–29, 1987.p251–255, LBL-24604, and private communications.
- [6] T. Gunji *et al.*, CNS Annual Report 2005 (2006) 49.
- [7] S. X. Oda *et al.*, CNS Annual Report 2005 (2006) 47.
- [8] K. Ozawa *et al.*, CNS Annual Report 2005 (2006) 43.
- [9] M. Inuzuka *et al.*, Nucl. Instrum. and Methods A **525** (2004) 529–534.
- [10] Y. L. Yamaguchi *et al.*, CNS Annual Report 2005 (2006) 83.
- [11] S. Maki *et al.*, CNS Annual Report 2005 (2006) 89.
- [12] S. Sano *et al.*, CNS Annual Report 2005 (2006) 87.
- [13] Y. Aramaki *et al.*, CNS Annual Report 2005 (2006) 85.
- [14] Y. Morino *et al.*, CNS Annual Report 2005 (2006) 91.

# Measurements of Low-Mass Vector Mesons in Au+Au Collisions at RHIC-PHENIX

K. Ozawa, H. Hamagaki, F. Kajihara, T. Gunji, T. Isobe, S. X. Oda, Y. Morino, S. Saito, Y. Aramaki, and Y. L. Yamaguchi, for the PHENIX collaboration

*Center for Nuclear Study, Graduate School of Science, University of Tokyo*

## 1. Introduction

In 6 years operation of Relativistic Heavy Ion Collider (RHIC) at Brookhaven National Laboratory (BNL), many new phenomena related to hot and dense nuclear matter have been discovered. The PHENIX experiment produced many new results on a wide range of physics subjects, including charged and neutral hadron production, single electron production, event isotropy, and many other topics [1].

In spite of these fruitful results, there are still remaining questions to be answered to further characterize the state of matter formed at RHIC. In particular, chiral properties of the dense matter produced has not been obtained, and should be provided. For the study of the chiral properties,  $\phi(1020)$  is an interesting meson because the restoration of approximate chiral symmetry at high temperature may modify its mass and width [2]. These modifications can be shown directly in the line shape of the  $\phi \rightarrow e^+e^-$  peak. Here, the measurements with lepton decays are essential, since leptons do not interact with the medium and carry direct information about conditions and properties of the medium. In addition to line shape measurements, the branching fraction of  $\phi \rightarrow K^+K^-$  and  $\phi \rightarrow e^+e^-$  could change when the  $\phi$  decays in medium [3]. Results on  $\phi \rightarrow K^+K^-$  in Au-Au collisions are quoted from Ref. [4].

In this paper, the current results on  $\phi \rightarrow e^+e^-$  in Au-Au collisions are reported. Also, an upgrade plan for the PHENIX detector is briefly discussed.

## 2. $\phi$ meson measurements at PHENIX

The PHENIX experiment is specifically designed to measure low-mass lepton pairs. The current PHENIX detector consists of two central spectrometer arms for detecting electrons. Each central arm covers pseudo-rapidity of  $|\eta| < 0.35$ , transverse momentum of  $p_T > 0.2$  GeV/c, and azimuthal angle of  $\delta\phi = \pi/2$ . Further details of the detector design and performance are given in Ref. [5].

During the fourth running period (Run4), RHIC delivered a luminosity of approximately  $1400 \mu\text{b}^{-1}$  to the PHENIX intersection region within a vertex  $z$  range ( $|z| < 45$  cm). PHENIX successfully recorded Au-Au events on order of 1.5 billion at  $\sqrt{s_{NN}} = 200$  GeV after a vertex selection of  $|z| < 30$  cm.

PHENIX has an excellent electron identification capability that is necessary to separate electrons from the much more abundant charged pions. The RICH provides a threshold selection for electrons and the EMC confirms the matching of the tracked momentum and electromagnetic energy ( $E/p$ ). Since electrons deposit all of their energy in the

EMC,  $E/p$  for electrons should be approximately unity. Fig. 1 shows  $(E-p)/p/\sigma$  distribution. Here the  $\sigma$  stands for the standard deviation of  $(E-p)/p$ . A background of less than 10%, caused by accidental association of tracks with RICH hits, still remains in electron identification. In the analysis, the background is evaluated and subtracted as a combinatorial background.

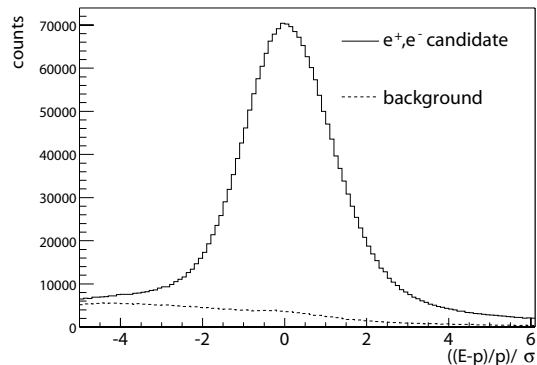


Figure 1.  $(E-p)/p/\sigma$  distribution. A background of less than 10%, caused by accidental association of tracks with RICH hits, still remains.

Analysis of Run4 data is underway and the first results is appeared using a part of data. Figure 2 shows the  $e^+e^-$  invariant mass distribution after the combinatorial background subtraction. The combinatorial background is estimated by an event mixing method and the invariant mass distribution of like sign pair is well produce by the method. There is a peak around the  $\phi$  mass with a signal strength of  $691 \pm 174(\text{stat})$  and a signal to background ratio of 1/44. Within relatively large errors, the mass peak and width values agree with the values from the Particle Data Group and experimental mass resolution.

Figure 3 shows  $\phi$  yield in  $e^+e^-$  and  $K^+K^-$  decays as a function of the number of participant. Here, the number of participant is the total number of protons and neutrons which are participate in a collision. Without medium effects, the  $\phi$  yield is expected to be propotional to the number of participant in this collision energy. As a result, the  $\phi$  yiled is propotional to the number of participant within a large statistical and systematic error. The significant deviation from the results of  $K^+K^-$  decay mode is not observed.

To figure out hot nuclear matter effects on  $\phi$  meson production, the significant improvement of the statistics or the suppression of the combinatorial background is needed. For

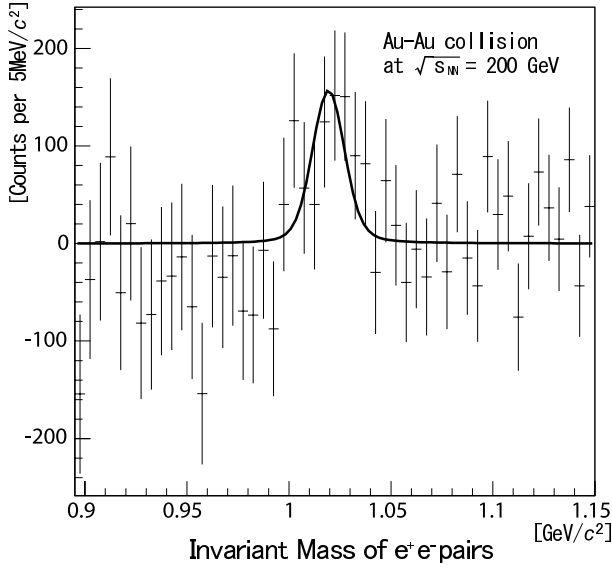


Figure 2.  $e^+e^-$  invariant mass distribution after mixed event subtraction for minimum bias (0-90% central) Au-Au collisions at  $\sqrt{s_{NN}} = 200$  GeV in Run4.

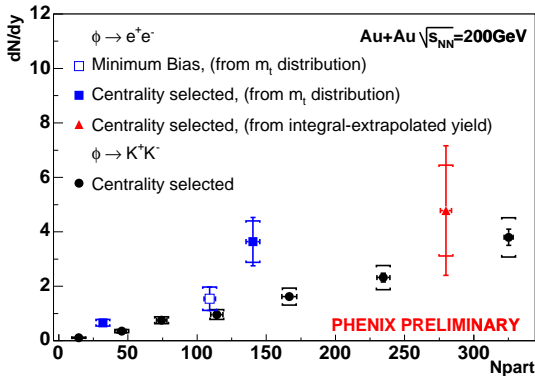


Figure 3.  $dN_\phi/dy$  in  $e^+e^-$  and  $K^+K^-$  decays as a function of number of participant in Au-Au collisions at  $\sqrt{s_{NN}} = 200$  GeV in Run4.

the statistics, we will have a long Au-Au data acquisition period from 2006 to 2007. In this coming run, we will have four times larger statistics. For the suppression of the combinatorial background, we will install a new detector soon, as described in the next section.

### 3. Hadron Blind Detector

To extend the capability of the measurement of lepton pairs, several upgrade projects of the detector are currently underway. The difficulty of the measurement of low mass dileptons comes from the large combinatorial background, which is mainly contributed to by  $\pi^0$  Dalitz decays and external conversion of photons. Thus, for this measurement, a Dalitz rejector with a large rejection power covering a large solid angle is needed.

The proposed Dalitz rejector is composed of two essential elements; zero magnetic field, and improved electron identification. Electron positron pairs from Dalitz decays

and gamma conversions have a very small angle. Thus, these pairs produce very close hits in the electron identification detector under zero field conditions. The zero magnetic field is realized by canceling the magnetic field produced by the outer coils of the PHENIX central magnet with the reverse magnetic field produced by a set of inner coils.

To realize electron identification near the vertex region, a hadron blind detector (HBD), which is a threshold-type Čerenkov counter using  $\text{CF}_4$  as a radiator gas [6], is proposed. The detector consists of a 50 cm long radiator, directly coupled in a windowless configuration to a triple GEM detector which has CsI photocathode evaporated on the top face of the first GEM foil, and pad readout at the bottom of the GEM stack [7].

The R&D phase to demonstrate the validity of the HBD concept is complete. A test of a prototype detector was performed at PHENIX using electrons from p-p collisions. The preliminary result of the test showed that electrons produce enough number of photoelectrons. Construction of the final detector will start soon and the detector is expected to be installed in PHENIX in 2006.

### 4. Summary

The yield of  $\phi$  mesons are measured for the first time using  $e^+e^-$  decay mode in Au-Au collisions at  $\sqrt{s_{NN}} = 200$  GeV. The mass peak and width values agree with the values from the Particle Data Group and experimental resolution. The significant difference from the results of  $K^+K^-$  decay mode is not observed.

In the future, a Hadron Blind Detector will be installed in PHENIX that will enhance our capabilities of rejecting external photon conversion and Dalitz pairs, and will result in a significant reduction of the large combinatorial background. This will open up the possibility of studying chiral symmetry restoration as well as thermal di-electrons.

### References

- [1] K. Adcox *et al.* [PHENIXCollaboration], Nucl. Phys. A **757** (2005) 184–283.
- [2] V. Koch, Int. J. Mod. Phys. **E6**, (1997) 203. R. Rapp, Nucl. Phys. **A661**, (1999) 238c
- [3] D. Lissauer and E. V. Shuryak, Phys. Lett. B253, 15 (1991).
- [4] S. S. Adler *et al.*, Phys. Rev. C72, (2005) 014903.
- [5] K. Adcox *et al.*, Nucl. Instrum. Methods A **499**, (2003) 469.
- [6] Z. Fraenkel *et al.*, Proposal for a Hadron Blind detector for PHENIX, PHENIX Technical Note **391** (2001).
- [7] A. Kozlov *et al.*, Nucl. Instrum. Methods A **523** (2004) 345.

# Measurement of Single Electrons in the $\sqrt{s_{NN}} = 200$ GeV Au+Au Collisions

F. Kajihara, Y. Akiba<sup>a</sup>, R. Averbeck<sup>b</sup>, A. Dion<sup>b</sup>, T. Gunji, H. Hamagaki, and K. Ozawa,  
for the PHENIX Collaboration

Center for Nuclear Study, Graduate School of Science, the University of Tokyo

<sup>a</sup>RIKEN (The Institute of Physical and Chemical Research), Wako, Saitama

<sup>b</sup>Department of Physics and Astronomy, Stony Brook University, SUNY, Stony Brook, NY, USA

## 1. Introduction

A strong suppression of light flavor mesons at a high transverse momentum ( $p_T$ ) was observed [1, 2] in high-energy heavy-ion collisions at RHIC. This suppression is ascribed to a jet quenching effect, where high- $p_T$ -scattered partons suffer a significant energy loss in an extremely hot and dense QCD matter [3]. This effect reveals a very high dense matter is created, which is not the conventional hadronic matter. Heavy quarks (charm/bottom) are also important probes. They can interact with the medium in different ways from light quarks due to their heavy mass. The energy loss for heavy quarks was predicted to be smaller than that of light quarks [4, 5]. There are other important issues on heavy quark productions at RHIC. Open charm production is a crucial input for the recombination models of the  $J/\psi$  production. Open charm/bottom can be produced in the initial hard processes of the hot dense matter. The difference of open charm/bottom at central and forward rapidity can be an important signature of the formation of Color-Glass Condensate (CGC). It would be also very interesting to learn about possible transitions and their locations in  $p_T$  from thermal to coalescence or perturbative QCD energy loss, similar to what appears to be emerging from light hadrons. The heavy quark measurement will extend our knowledge of underlying QCD properties.

## 2. Experiment and Analysis

The PHENIX experiment took significant amount of data for Au+Au collisions at  $\sqrt{s_{NN}} = 200$  GeV in RHIC RUN-4 (2004). Since a large fraction of electrons ( $e^+/e^-$ ) in high- $p_T$  ( $> 1$  GeV/c) comes from semileptonic decays of open charm/bottom, heavy quark productions can be studied by single electron measurement. In the PHENIX experiment, electrons were detected by two central arms, each covering azimuthal angle  $\Delta\phi = \pi/2$  and pseudo-rapidity  $|\eta| < 0.35$  [6]. Reconstruction of charged tracks required the hit information of Drift Chamber (DC) and Pad Chamber (PC). Electrons were identified with Ring Imaging Čerenkov counter (RICH) and ElectroMagnetic Calorimeter (EMCal) in  $p_T > 0.4$  GeV/c.

All measured electrons can be categorized into two groups. The first group consists of "photonic" electrons which mainly come from (1) Dalitz decays of mesons ( $\pi^0, \eta$ , etc) and (2) photon conversion ( $\pi^0 \rightarrow 2\gamma, \gamma \rightarrow e^+e^-$ , etc). They are background electrons. The second group is termed as "nonphotonic" electrons. The decays of open charm/bottom are the dominant sources of the second group.

We can apply two methods to extract *nonphotonic* electrons by subtracting the *photonic* electrons from all inclusive electrons. The both methods check the consistency of each other result. The first one is the so-called "cocktail subtraction" method. This method is used to reconstruct all possible *photonic* electron components, that is cocktail, using a hadron-decay simulator on the basis of published pion spectra [2, 3] and to subtract them from the inclusive electron spectrum. This method is effective to count signal electrons at high- $p_T$ , where the signal to background ratio is quite large. The second one is "converter subtraction" method. In the experiment, special runs were performed with a photon converter, a brass sheet (1.68 % radiation length) around the beam pipe. The photon converter enhances *photonic* electron yield  $P(p_T)$  by a certain amount. The ratio of *photonic* electron yield with/without the converter is defined as  $R_\gamma$ , which can be evaluated within 3% systematic error by a GEANT-based simulation which includes branching ratios, form factors, conversion probabilities, and the amount of materials in the PHENIX environment. The measured inclusive electron yield  $I(p_T)$  is given as  $I(p_T) = P(p_T) + N(p_T)$  without the converter and  $I'(p_T) = R_\gamma P(p_T) + N(p_T)$  with the converter. Here,  $N(p_T)$  is *nonphotonic* electron yield.  $N(p_T)$  is obtained by solving these two equations. Converter subtraction method has small systematic error by direct measurement of *photonic* electron components, but the statistics error is dominated by the amount of data with converter.

The background of *nonphotonic* electrons comes from di-electron decays and semileptonic decays from the other mesons. But they are small, especially negligible at high- $p_T$  region. The largest contributions to this background are electrons from semileptonic decays of Kaon, which are 15% of *nonphotonic* electron yield at  $p_T \sim 1$  GeV/c. Since Kaon spectra have been already measured by the PHENIX experiment, the yield of background electrons can be evaluated with simulation and subtracted from *nonphotonic* electrons. We usually consider and call "nonphotonic" electron as *nonphotonic* electron after these subtractions.

## 3. Results

Figure 1 shows the *nonphotonic* electron invariant yield for each centrality, scaled with the corresponding number of binary collisions,  $N_{col}$ . The spectra was extracted with the cocktail subtraction method. The brackets and bars indicate the systematical and statistical errors, respectively. The curves are the best fit curves for RHIC RUN-3 p+p *nonphotonic* electron spectrum [7]. In central collisions,

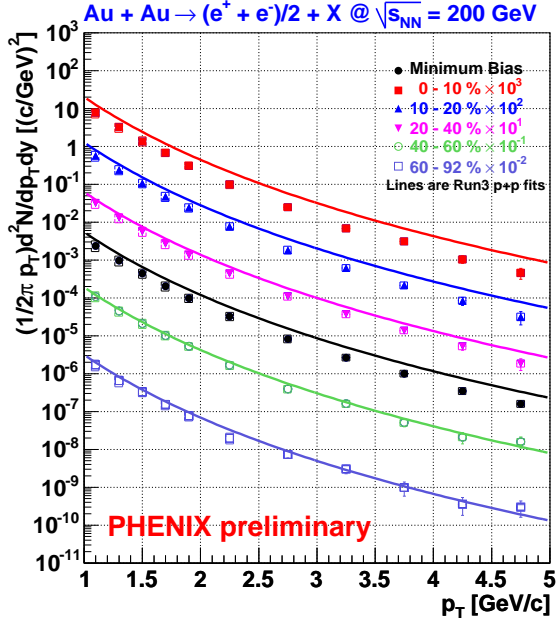


Figure 1.  $p_T$  distribution of *nonphotonic* electron invariant yield for each centrality in RHIC RUN-4 Au+Au compared with RUN-3  $p + p$  best fit, scaled by  $N_{col}$ .

strong suppression is observed in the high- $p_T$  region. To quantify the suppression, the nuclear modification factors,  $R_{AuAu}(p_T)$  is used:

$$R_{AuAu}(p_T) = \frac{dN^{AuAu}/dp_T}{T_{AuAu} d\sigma_{in}^{pp}/dp_T} = \frac{dN^{AuAu}/dp_T}{N_{col} dN^{pp}/dp_T}. \quad (1)$$

Here,  $\sigma_{in}^{pp}$  is the inelastic scattering cross section of RUN-3  $p+p$  *nonphotonic* electron,  $T_{AuAu}(b)$  is the nuclear thickness function for Au+Au at an impact parameter ( $b$ ) and  $N_{col}(b) = T_{AuAu}(b) \cdot \sigma_{in}^{pp}$ .  $R_{AuAu}(p_T)$  for each centrality are shown in Fig. 2. The large systematic errors consist of contributions from  $T_{AuAu}$  (a horizontal band around  $R_{AuAu}(p_T) = 1.0$ ), RUN-3  $p+p$  data (vertical bands for each data point), and RUN-4 Au+Au data (brackets for each data point). The statistical errors are shown as vertical bars for each data point. Suppression is clearly seen for *nonphotonic* electrons from the most central to the mid central collisions, comparable to the suppression observed for  $\pi^0$  and  $\eta$ . This is in strong contradiction to the original expectations. This phenomenon suggests the existence of another energy-loss-mechanism for heavy quarks in the high dense matter.

#### 4. Summary and Outlook

The *nonphotonic* electron spectra from the central to the peripheral events were measured for Au+Au collisions at  $\sqrt{s_{NN}} = 200$  GeV in RHIC RUN-4. The nuclear modification factor ( $R_{AuAu}$ ) shows a very strong suppressive effect. The result suggests that unusual high dense matter is created, which is unlike hadronic matter. To understand it systematically, we need to separate the contributions from charm or bottom in the future experiment. The mass differ-

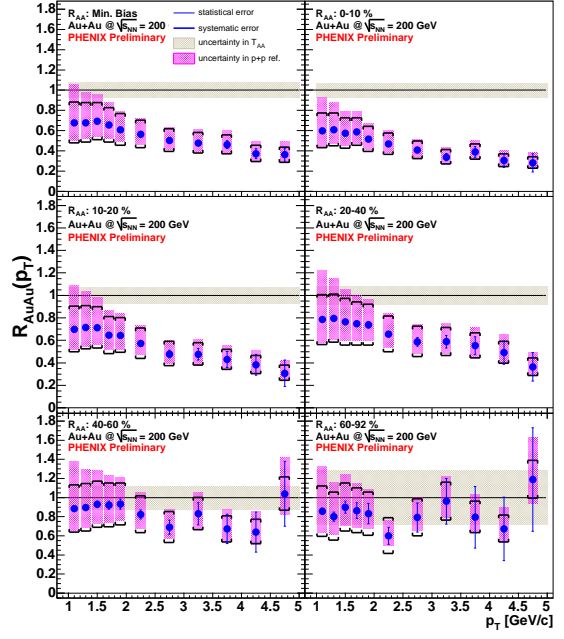


Figure 2.  $p_T$  distribution of nuclear modification factor ( $R_{AuAu}$ ) for each centrality in RHIC RUN-4 Au+Au.

ence of these heavy quarks will provide us the information of the energy-loss mechanism in high dense matter.

The presented figures were created by the cocktail method to subtract *photonic* electron background. Currently, we are analyzing data with the converter subtraction method which allows to measure *nonphotonic* electron spectra in the low- $p_T$  region ( $< 1$  GeV/ $c$ ). We are working to improve the error calculations. Extension of the spectra toward high- $p_T$  region ( $\geq 5$  GeV/ $c$ ) is intended, where a large  $b$  quark decay contribution is expected.

#### References

- [1] S. S. Adler *et al.*, Phys. Rev. Lett. **91** (2003) 072301.
- [2] M. Gyulassy and X. N. Wang, Nucl. Phys. B **420** (1994) 583.
- [3] K. Adcox *et al.*, Phys. Rev. Lett. **88** (2002) 022301.
- [4] Y. L. Dokshitzer *et al.*, Phys. Lett. B **519** (2001) 199.
- [5] N. Armesto *et al.*, Phys. Rev. D **71** (2005) 054027.
- [6] K. Adcox *et al.*, Nucl. Instrum. Methods A **499**(2003) 460.
- [7] M. Togawa *et al.*, RIKEN Accel. Prog. Rep. **39** (2005).

# Measurement of Vector Mesons via Di-Electron Decay in Cu+Cu Collisions at RHIC-PHENIX

S. X. Oda, H. Hamagaki, K. Ozawa, K. Das<sup>a</sup>, A. D. Frawley<sup>a</sup>, A. Lebedev<sup>b</sup>, and W. Xie<sup>c</sup>, for the PHENIX collaboration

Center for Nuclear Study, Graduate School of Science, University of Tokyo

<sup>a</sup>Florida State University

<sup>b</sup>Iowa State University

<sup>c</sup>RIKEN BNL Research Center, Brookhaven National Laboratory

## 1. Introduction

Vector mesons, such as  $\rho$ ,  $\omega$ ,  $\phi$ ,  $J/\psi$  and  $\Upsilon$ , have di-lepton ( $e^+e^-$ ,  $\mu^+\mu^-$ ) decay channels. Since the leptons do not couple to the strong interaction, they are transparent probes for the early hot dense stage of high energy heavy ion collisions. The leptons also have the advantage that they are easily identified.

Especially,  $J/\psi$  has been considered to be one of the most promising probes for the hot and dense matter consisting of quarks and gluons, because it dissociates in the deconfined matter by the color Debye screening and its yield is suppressed [1]. However, the yield will be modified by other competing processes such as cold nuclear matter effect, comover scatterings, recombination and feed down effect. About 40% of  $J/\psi$ 's come from the excited charmonium states  $\psi'$  and  $\chi_c$  and these heavy quarkonia are expected to dissociate at lower temperatures than  $J/\psi$  [2]. However, except for  $J/\psi$ , measurements of the heavy quarkonia are difficult at the PHENIX experiment at RHIC due to the current small statistics and large background. Therefore, systematic study of  $J/\psi$  production with several system sizes and energy densities is necessary to understand the behavior of  $J/\psi$  in the hot and dense matter.

The light vector mesons are expected to be sensitive to possible in-medium modifications by chiral symmetry restoration which coincides with the deconfinement phase transition, and those yields, masses and/or mass widths will be modified [3].

## 2. Cu+Cu collisions at RHIC in 2005

The PHENIX experiment had collected data for  $p+p$ ,  $d+Au$  and  $Au+Au$  collisions at  $\sqrt{s_{NN}}=200$  GeV by 2004. In 2005, the PHENIX experiment recorded  $\sqrt{s_{NN}}=200$  GeV and  $\sqrt{s_{NN}}=62.4$  GeV Cu+Cu collisions (the integrated luminosities are  $3.06 \text{ nb}^{-1}$  and  $0.19 \text{ nb}^{-1}$ , respectively) to study the dependence on the collision species and energies.

The collision vertex and centrality of an event are determined by beam-beam counters in Cu+Cu collisions. Created particles at mid rapidity are tracked by drift chambers and pad chambers. Ring imaging Cherenkov counters and electromagnetic calorimeters are used for electron identification and Level-1 (hardware) electron triggering. Additionally, in the Cu+Cu 200 GeV data taking, a Level-2 (software) di-electron trigger is used to reduce the data size to be analyzed.

The results of Cu+Cu 200 GeV data are reported in this

report.

## 3. Results

### 3.1. $J/\psi$ meson

Figure 1 shows the invariant mass distribution of di-electrons. The mass window of 2.9–3.3  $\text{GeV}/c^2$  is used to count the number of  $J/\psi$ (3097) mesons and the number of like-sign pairs ( $e^+e^+$  and  $e^-e^-$ ) is used to estimate combinatorial background,  $N_{J/\psi} = N_{+-} - (N_{++} + N_{--})$ .

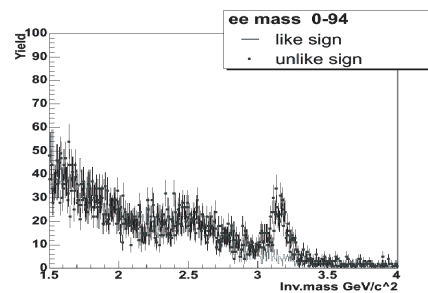


Figure 1. The invariant mass distribution of di-electrons.

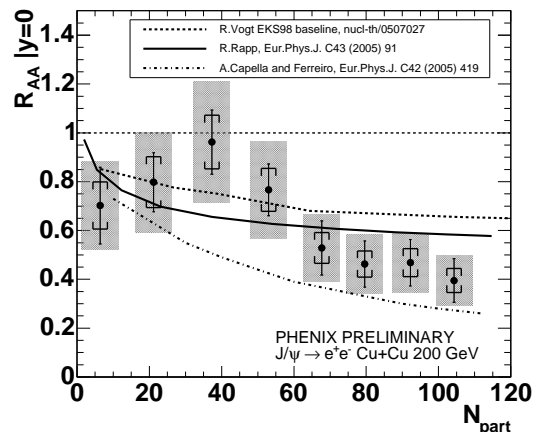


Figure 2. The nuclear modification factor of  $J/\psi$  as a function of the number of participants,  $N_{part}$ .

The yield modification between the superposition of nucleon-nucleon collisions and a nucleus-nucleus collision is quantified by the nuclear modification factor defined as follows,  $R_{AA} = (Y_{AA}/N_{coll})/Y_{pp}$ , where  $Y_{AA}$  is the  $J/\psi$  yield in a nucleus-nucleus collision and  $Y_{pp}$  is the  $J/\psi$  yield in a  $p+p$  collision. The number of nucleon-nucleon col-

lisions,  $N_{coll}$ , in a nucleus-nucleus collision is calculated within a Glauber model. The nuclear modification factor of  $J/\psi$  is shown in Fig. 2 as a function of the number of participants,  $N_{part}$ . The solid lines, brackets and boxes associated with the data points represent the statistical, point systematic and overall systematic errors, respectively. Strong suppression is observed in central collisions. Some predicted lines from model calculations are also shown in the figure. The cold nuclear matter model (dashed line) [4] seems to underpredict the observed data. The comover model (dot-dashed line) [5], which was successful in describing the SPS data, seems to overpredict the suppression at RHIC. The recombination model (solid line) [6] also seems to underpredict the suppression.

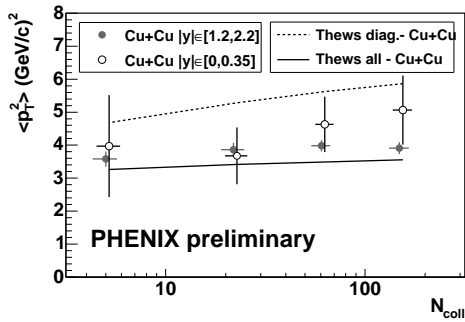


Figure 3. The mean square of the transverse momentum ( $\langle p_T^2 \rangle$ ) of  $J/\psi$  as a function of the number of collisions,  $N_{coll}$ .

Figure 3 shows the mean square of the transverse momentum,  $\langle p_T^2 \rangle$ , as a function of the number of collisions,  $N_{coll}$ . Data points at the forward and backward rapidity are measured using the PHENIX spectrometers via di-muon decay. Theoretical predictions with recombination (solid line) and without recombination (dashed line) [7] are also shown in the figure. There is no significant centrality dependence of  $\langle p_T^2 \rangle$ .

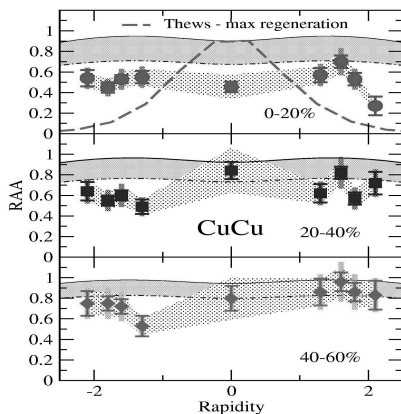


Figure 4. The rapidity distribution of  $J/\psi$  in centrality regions of 0-20% (top), 20-40% (center) and 40-60% (bottom).

Figure 4 shows the rapidity distribution of  $J/\psi$ . Although a recombination model expects the rapidity shape to become narrower as  $N_{part}$  increases [7], no significant change is observed.

### 3.2. $\phi$ and $\Upsilon$ mesons

The invariant mass plots in the  $\phi$  and  $\Upsilon(1S, 2S$  and  $3S)$  mass regions ( $1.019 \text{ GeV}/c^2$  and  $9.46\text{--}10.36 \text{ GeV}/c^2$ , respectively) with a part of collected data are shown in Fig. 5 and the candidates of those mesons are seen. The backgrounds are subtracted using the event-mixing technique for the  $\phi$  mass region and estimated from the counts of like-sign pairs for the  $\Upsilon$  mass region. About 1000  $\phi$  and  $\sim 10$   $\Upsilon$  mesons are expected with the whole Cu+Cu 200 GeV data which will be available by the summer of 2006.

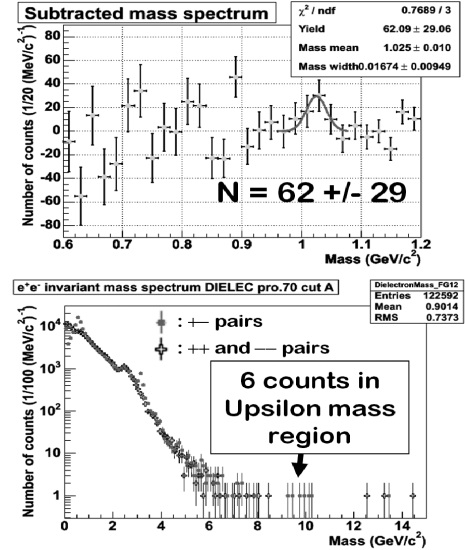


Figure 5. The invariant mass distribution in the  $\phi$  (top) and  $\Upsilon$  (bottom) mass regions.

### 4. Summary

Vector mesons are good probes for the hot and dense medium created by high energy heavy ion collisions. The centrality dependence of the yield of  $J/\psi$  in Cu+Cu collisions was measured using di-electron decay at RHIC-PHENIX. Strong suppression beyond cold nuclear matter effect is observed and the suppression pattern seems to be different from model calculations.

### References

- [1] N. Brambilla, *et al.*, CERN Yellow Report, CERN-2005-005 (2005).
- [2] H. Satz, J.Phys. G **32** (2006) R25.
- [3] H. van Hees and R. Rapp, hep-ph/0604269 (2006).
- [4] R. Vogt, nucl-th/0507027 (2005).
- [5] A. Capella and E. G. Ferreiro, Eur. Phys. J. C **42** (2005) 419.
- [6] R. Rapp, Eur. Phys. J. C **43** (2005) 91.
- [7] R. L. Thews and M. L. Mangano, Phys. Rev. C **73** (2006) 014904, and private communication.

# Measurement of $J/\psi \rightarrow e^+e^-$ in Au+Au Collisions at $\sqrt{s_{NN}} = 200$ GeV by PHENIX at RHIC

T. Gunji, H. Hamagaki, K. Ozawa, F. Kajihara, Y. Akiba<sup>a</sup>, A. Lebedev<sup>b</sup>, and C. L. Silva<sup>c</sup>, for the PHENIX collaboration

Center for Nuclear Study, Graduate School of Science, University of Tokyo, Japan

<sup>a</sup>RIKEN (The Institute of Physics and Chemical Research), Japan

<sup>b</sup>Iowa State University, USA

<sup>c</sup>Universidade de São Paulo, Instituto de Física, Brazil

## 1. Introduction

Ultra-relativistic heavy ion collision is a unique tool to realize in the laboratory the QCD phase transition from ordinary hadronic matter to a plasma of de-confined quarks and gluons, called Quark-Gluon-Plasma (QGP). Relativistic Heavy Ion Collider (RHIC) at Brookhaven National Laboratory is a dedicated facility to realize such a phase transition and study the properties of QGP.

$J/\psi$  has long been considered as one of the most promising probes to study the formation of QGP. Since the mass of charm quark is large, creation of charm quarks takes place only at the initial stage of the collisions at RHIC energy.  $J/\psi$  or the pre-resonance  $c\bar{c}$  state would enter the hot and dense de-confined medium and they could be dissolved due to the color Debye screening effect. This leads to the suppression of  $J/\psi$  yield, which was originally proposed by T. Matsui and H. Satz [1].

Recent lattice QCD calculations suggest that the dissociation temperature of  $J/\psi$  is higher than the temperature which might be achieved at collisions at RHIC, and that  $J/\psi$  would survive at RHIC [2]. The other interesting theoretical prediction is that the  $J/\psi$  yield could be enhanced due to the recombination of uncorrelated  $c\bar{c}$  pairs [3].

Recent HERA-B experiments show that 40% of  $J/\psi$  come from the feed down of  $\chi_c$  and  $\psi'$  [4]. Since the  $\chi_c$  and  $\psi'$  are expected to be dissolved at RHIC energy, it is important to take into account feed down effect at RHIC.

PHENIX [5] measured  $J/\psi$  yield in  $p+p$ ,  $d+Au$ , Au+Au and Cu+Cu collisions to extract the cold matter effect and hot and dense medium effect on the  $J/\psi$  production and study its modification in the medium.

## 2. Data analysis

Au+Au collisions at  $\sqrt{s_{NN}} = 200$  GeV were performed at RHIC in 2004. During the period, PHENIX recorded the integrated luminosity of  $\sim 240 \mu\text{b}^{-1}$ . 75% of the data was reconstructed and used in this analysis.  $J/\psi$  event is reconstructed via  $e^+e^-$  decay mode and the number of  $J/\psi$  are  $\sim 600$   $J/\psi$  in the analyzed data.

### 2.1. Invariant Yield Extraction

The formula of  $J/\psi$  invariant yield is written as follows:

$$B \frac{dN}{dy} = \frac{N_{J/\psi}}{N_{evt}} \frac{1}{\Delta y \epsilon_{acc} \epsilon_{embed}}, \quad (1)$$

where  $B$  is the branching ratio of  $e^+e^-$  decay mode (5.93% from PDG [6]),  $N_{J/\psi}$  and  $N_{evt}$  stand for the number of  $J/\psi$  counts and the number of analyzed event, respectively.  $\Delta y$  in Eq.( 1) is the rapidity coverage. The correction factor,  $\epsilon_{acc}$ , is the acceptance for  $e^-$  and  $e^+$  pair from  $J/\psi$ , where detection efficiency of  $e^+$  and  $e^-$  pairs and run-by-run fluctuation of the detector acceptance are taken into account. The correction factor,  $\epsilon_{embed}$ , is the embedding efficiency, which has a centrality dependence. In more central collisions, probability of track mis-reconstruction becomes higher due to higher hit occupancy. These correction factors were obtained from the simulation study of  $J/\psi$  and reported in Ref. [7].

## 3. Results

Nuclear modification factor ( $R_{AA}$ ) is a variable widely used to quantify the medium effects in A+A collisions.  $R_{AA}$  of  $J/\psi$  is the ratio of the  $J/\psi$  yield in Au+Au collisions to that in  $p+p$  collisions scaled by the average number of binary nucleon-nucleon collisions.  $R_{AA}$  of  $J/\psi$  is expected to be 1 in the absence of medium effects.

Figure 1 shows the  $R_{AA}$  of  $J/\psi$  as a function of the number of participants and the comparison to the various suppression models [9].

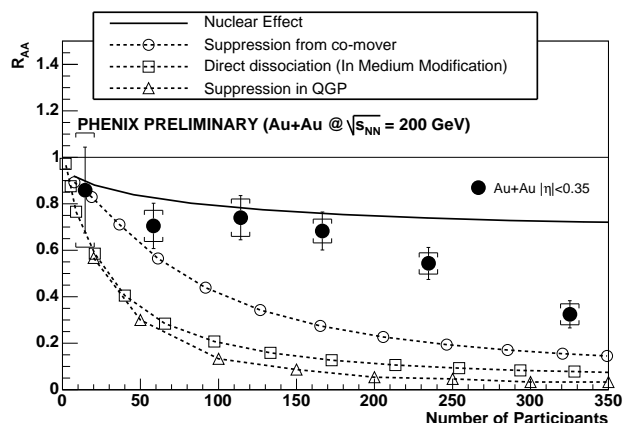


Figure 1. Nuclear modification factor of  $J/\psi$  as a function of the number of participants. Solid line is the prediction from the models taking into account the cold matter effects. Open symbols and dot-lines are the predictions from suppression models extrapolated from SPS energy

Solid line is the prediction of the models taking into ac-

count the cold matter effects such as nuclear absorption and gluon shadowing, where the absorption cross section (1 mb) and the gluon distribution function in nuclei were evaluated from PHENIX d+Au results [8]. A suppression by a factor of 3 is seen at the most central collisions, which is beyond the cold matter effect. Open circles is the results of the comover suppression model, which takes into account the dissociation of  $J/\psi$  in the hadronic phase via the break up interaction with secondary charged particles. Open triangles and squares are the results of the suppression models, where dissociation of  $J/\psi$  in QGP due to color screening and comover interactions in the hadronic phase are took into account. These models over-estimated the  $J/\psi$  suppression observed at RHIC.

Figure 2 shows the comparison of  $R_{AA}$  to the predictions from suppression + recombination models (open triangles, circles and squares) [9]. The differences between

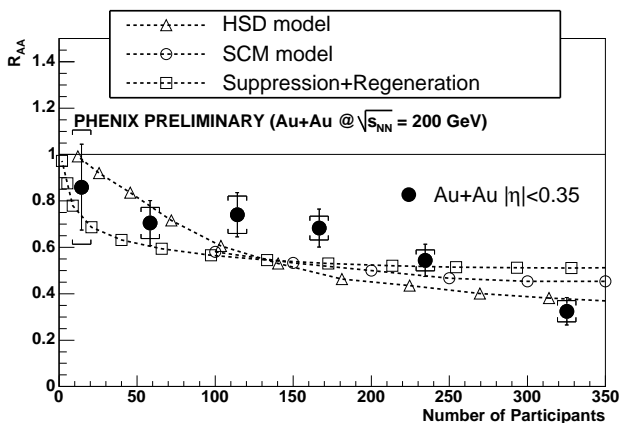


Figure 2. Nuclear modification factor of  $J/\psi$  as a function of the number of participants. Open symbols and dot-lines are the predictions from suppression + recombination models.

them are the nuclear absorption cross section, production cross section of  $c\bar{c}$  pairs participating in the recombination of  $J/\psi$  and the way to dissolve the  $J/\psi$  in QGP. The predictions with recombination match better to the data points. Therefore, the recombination process seems to compensate the strong suppression at RHIC energy.

Figure 3 shows the  $\langle p_T^2 \rangle$  of  $J/\psi$  as a function of the number of collisions in  $p+p$ ,  $d+Au$  and  $Au+Au$  collisions. Theoretical predictions with and without recombination are also shown in Fig. 3 [9]. Recombination model matches better to the data points.

#### 4. Summary and Outlook

The PHENIX experiment measured the  $J/\psi$  yield at  $\sqrt{s_{NN}} = 200$  GeV in  $Au+Au$  collisions and extracted the nuclear modification factor ( $R_{AA}$ ) of  $J/\psi$  for various collision centralities. Suppression by a factor of 3 is seen at the most central collisions and it is beyond the cold matter effects. Suppression models extrapolated from SPS energy over-predict the observed suppression at RHIC. Models with suppression and recombination can describe the observed suppression and  $\langle p_T^2 \rangle$  better.

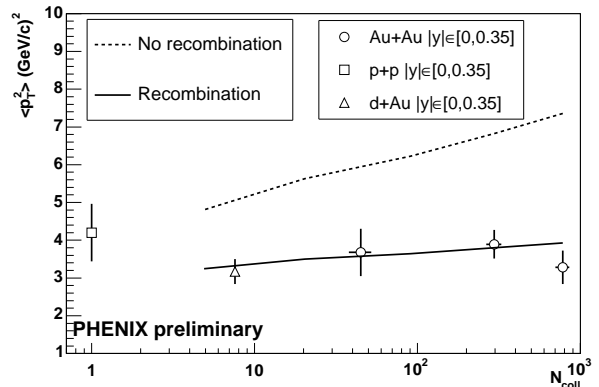


Figure 3.  $\langle p_T^2 \rangle$  as a function of the number of collisions in  $p+p$ ,  $d+Au$  and  $Au+Au$  collisions. Solid and dashed line is the predictions with and without recombination, respectively

Since the recombination of  $J/\psi$  would occur at hadronization stage and the charm quark could interact with medium strongly [10], it is necessary to understand the charm production and its modification in the medium such as charm cross section as a function of  $p_T$ , rapidity and centrality and the magnitude of the radial and longitudinal charm flow, in conjunction with recombination of  $J/\psi$ , which have not been understood at RHIC energy.

To take into account the feed down effect in describing the  $J/\psi$  suppression at RHIC, the fraction of the feed down from  $\chi_c$  and  $\psi'$  at RHIC energy has to be determined experimentally. Analysis of  $\chi_c$  production in  $p+p$  collisions is underway and it will clarify the situation.

Since the systematic error from current  $p+p$  reference is one of the dominant ones (10%) in  $R_{AA}$  calculation, high statistic  $p+p$  data taken in 2005 will improve the systematic error coming from the  $p+p$  reference.

#### References

- [1] T. Matsui and H. Satz, Phys. Lett. B **178** (1986) 416.
- [2] M. Asakawa and T. Hatsuda, Phys. Rev. Lett. **92** (2004) 012001.
- [3] L. Grandchamp *et al.*, Phys. Rev. Lett. **92** (2004) 212301.
- [4] L. Abt, *et al.*, (HERA-B Collaboration), Phys. Lett. B **561** (2003) 61-72.
- [5] K. Adcox, *et al.* [PHENIX Collaboration], Nucl. Instrum. Methods A **499** (2003) 469.
- [6] K. Hagiwara *et al.*, Phys. Rev. D **66** (2002) 010001.
- [7] T. Gunji *et al.*, CNS Annual Report 2004 (2005) 53,
- [8] S. S. Adler *et al.* [PHENIX Collaboration], Phys. Rev. Lett. **96** (2006) 012304.
- [9] H. Pereira Da Costa *et al.*, [PHENIX Collaboration] nucl-ex/0510051.
- [10] F. Kajihara *et al.*, CNS Annual Report 2005 (2006) 45.

# Direct Photon Measurement in $\sqrt{s_{NN}} = 200$ GeV Au+Au Collisions at RHIC-PHENIX

T. Isobe, H. Hamagaki, T. Sakaguchi<sup>a</sup>, G. David<sup>a</sup>, and B. Sahlmueller<sup>b</sup> for the PHENIX Collaboration

Center for Nuclear Study, Graduate School of Science, University of Tokyo

<sup>a</sup>Brookhaven National Laboratory, USA

<sup>b</sup>University of Muenster, German

## 1. Introduction

It is predicted from lattice QCD calculations that a phase transition from hadronic matter to a plasma of deconfined quarks and gluons may occur at ultimate high energy density. The new phase of matter is called as Quark Gluon Plasma (QGP), which is believed to have existed in the early universe for a few micro seconds after the Big Bang.

One of the main observables in the PHENIX experiment [1] is direct photon. Since photons do not interact strongly and thus can directly carry out information of these states of matter, direct photon is a powerful probe to study the bulk matter produced in the relativistic heavy ion collisions at the Relativistic Heavy Ion Collider (RHIC). They are emitted from all the stages of the collision process such as the initial state, the Quark-Gluon Plasma (QGP), and the final hadron gas phase.

## 2. Direct photon measurement at PHENIX Year-4 Run

Measurement of direct photons is challenging because there is a large amount of background from decay of neutral mesons such as  $\pi^0$  and  $\eta$ . It is estimated that the  $\gamma/\gamma_{bg}$  would be  $\sim 10\%$  at the transverse momentum ( $p_T$ ) range of 2-4 GeV/c, where thermal photon is expected to be dominant. In order to extract direct photon signal, conventional cocktail method has been used. In this method, the inclusive photon spectra are measured at first. Then, the background is estimated based on the actual measurement of neutral mesons, and subtracted. The remained signals are direct photon. The hadrons which are taken into account in the background estimation are summarized in Table 1.

PHENIX-EMCal [3] is used to measure inclusive photons. A lead-scintillator sampling-type calorimeter (PbSc), and a lead-glass Cherenkov calorimeter (PbGl) are used. In RHIC Year-4 run, PHENIX recorded the integrated luminosity of  $0.24 \text{ nb}^{-1}$  in  $\sqrt{s_{NN}}=200$  GeV Au+Au collisions. It allows us to extend the measurement of  $\pi^0$  up to high  $p_T \sim 20$  GeV/c. To estimate the background photons from other hadronic sources, the  $m_T$  scaled function ( $p_T \rightarrow \sqrt{p_T^2 - m_{\pi^0}^2 + m_{hadron}^2}$ ) to  $\pi^0$  spectrum is employed to produce a spectrum of hadrons. During the scaling the normalization factor  $R_{h/\pi^0}$  is applied to the spectra. The factor for  $\eta$  is measured at PHENIX and agrees within 5% [4].

## 3. Result of direct photon measurement

Direct photon excess ratio can be represented as  $(\gamma/\pi^0)_{measured}/(\gamma/\pi^0)_{background}$ , where the numerator is

State	Mass (MeV)	$R_{h/\pi^0}$	Decay mode	Branching ratio
$\pi^0$	134.98	-	$\gamma\gamma$	98.798 %
			$e^+e^-\gamma$	1.198 %
$\eta$	547.8	0.45	$\gamma\gamma$	39.43 %
			$\pi^+\pi^-\gamma$	4.68 %
			$e^+e^-\gamma$	$6.0 \cdot 10^{-3}$
			$\pi^0\gamma\gamma$	$7.2 \cdot 10^{-4}$
			$\mu^+\mu^-\gamma$	$3.1 \cdot 10^{-4}$
$\rho^0$	769.0	1.0	$\pi^+\pi^-\gamma$	$9.9 \cdot 10^{-3}$
			$\pi^0\gamma$	$6.0 \cdot 10^{-4}$
			$\eta\gamma$	$3.0 \cdot 10^{-4}$
$\omega$	782.6	1.0	$\pi^0\gamma$	8.92 %
			$\eta\gamma$	$4.9 \cdot 10^{-4}$
$\eta'$	957.8	1.0	$\rho^0\gamma$	29.5 %
			$\omega\gamma$	3.0 %
			$\gamma\gamma$	2.12 %
			$\mu^+\mu^-\gamma$	$1.0 \cdot 10^{-4}$
$K_S^0$	497.65	1.0	$\pi^0\pi^0$	31.05 %

Table 1. Dominant sources of background photons from hadronic decays and the employed  $m_T$  scaling factors relative to the  $\pi^0$  measurement  $R_{h/\pi^0}$ . The listed masses, decay branches, and branching ratios are taken from [2].

the ratio of the measured inclusive photon and the measured  $\pi^0$  and the denominator is the estimated ratio of hadronic photon and expected  $\pi^0$  obtained from fitting of measured  $\pi^0$ . The main source of the systematic error for photon measurement is uncertainty of energy scale. The part of the systematic error, such as the error from overall scale of energy correction can be canceled out for the ratio of  $(\gamma/\pi^0)_{measured}$ . Figure 1 shows the direct photon excess ratio as a function of  $p_T$  for each centrality. The strong suppression of neutral hadrons in central collision allows to extract direct photons at the momentum region of  $p_T > 5$  GeV/c.

Figure 2 shows the fully corrected direct photon invariant yield as a function of  $p_T$  for each centrality. The spectra are combined results of PbSc measurement and PbGl measurement. The yields are in good agreement with a NLO pQCD calculation [5] scaled by the number of binary nucleon collisions. This result implies that the initial-hard-scattering probability is not suppressed. It supports that the suppression of high  $p_T$  hadrons is attributed to final state interaction.

It is hard to observe significant direct photons at the mid- $p_T$  region where thermal emission is expected to be dom-



# Measurement of Neutral Pion in $\sqrt{s_{NN}} = 200$ GeV Au+Au Collisions at RHIC-PHENIX

T. Isobe, H. Hamagaki, T. Sakaguchi<sup>a</sup>, G. David<sup>a</sup>, S. Mioduszewski<sup>b</sup>, M. L. Porschke<sup>a</sup>, D. Winter<sup>c</sup>, B. Sahlmueller<sup>d</sup>, and J. Imrek<sup>e</sup>, for the PHENIX Collaboration

Center for Nuclear Study, Graduate School of Science, University of Tokyo

<sup>a</sup>Brookhaven National Laboratory, USA

<sup>b</sup>Texas A&M University, USA

<sup>c</sup>Columbia University, USA

<sup>d</sup>University of Muenster, German

<sup>e</sup>University of Debrecen, Hungary

## 1. Introduction

The PHENIX experiment [1] has been carried out at the Relativistic Heavy Ion Collider (RHIC) at Brookhaven National Laboratory (BNL) to find an evidence of phase transition from normal nuclear matter to Quark Gluon Plasma (QGP). QGP is a new phase of matter consisting of deconfined quarks and gluons. According to the Lattice QCD calculation, a phase transformation to QGP occurs at a temperature of  $T \sim 170$  MeV [2]. This transition temperature corresponds to an energy density of  $\epsilon \sim 1$  GeV/fm<sup>3</sup>.

One of the most intriguing observations at RHIC is that the yield of  $\pi^0$  at high transverse momentum ( $p_T$ ) in the central  $\sqrt{s_{NN}}=200$  GeV Au+Au collisions is suppressed compared with the yield of p+p collision scaled by the number of underlying nucleon-nucleon collisions [3]. The suppression is ascribed to a final state effect since it is absent in d+Au collisions and it indicates the suppression is not due to the cold nuclear effect [4]. Another strong confirmation came from direct photon measurement. The direct photon yield is not suppressed in the Au+Au collisions [5], implying that the initial hard scattering yield in Au+Au is well reproduced as the  $N_{coll}$  scaled yield in p+p. The observed suppression is interpreted as a consequence of the jet-quenching effect, that is, hard-scattered partons produced in the initial stage suffer a large energy loss while traversing the hot and dense matter.

## 2. Systematic study of jet-quenching effect

The amount of suppression can be quantified using a nuclear modification factor ( $R_{AA}$ ).  $R_{AA}$  is the ratio between the measured yield and the expected yield from the p+p result, and is defined as

$$R_{AA}(p_T) = \frac{d^2 N_{AA}/dp_T d\eta}{T_{AA}(b) d^2 \sigma_{NN}/dp_T d\eta}, \quad (1)$$

where the numerator is the invariant  $\pi^0$  yield in unit rapidity and the denominator is the expected yield in the p+p collisions scaled with the number of underlying nucleon-nucleon collisions ( $T_{AA}(b)$ ) in Au+Au.  $T_{AA}(b)$  is defined as

$$T_{AA}(b) = N_{coll}(b)/\sigma_{NN}, \quad (2)$$

where  $N_{coll}(b)$  is the average number of binary nucleon-nucleon collisions at an impact parameter  $b$  with an inelastic

cross section  $\sigma_{NN}$ . If a hard-scattered parton penetrates the bulk matter without any nuclear effects, the  $R_{AA}$  is unity.

There are several models that provide quantitative predictions of the amount of suppression. Each model has various effects: initial state effects, Cronin effect [6] and nuclear shadowing, or strong hadronic final state effects, and energy loss in a dense matter. The systematic study of  $\pi^0$  production is important to clarify the parton energy loss mechanism in the dense matter.

The measurement of neutral pions is also essential for the measurement of direct photons since the decay photons from neutral pions constitute the main source of background photons.

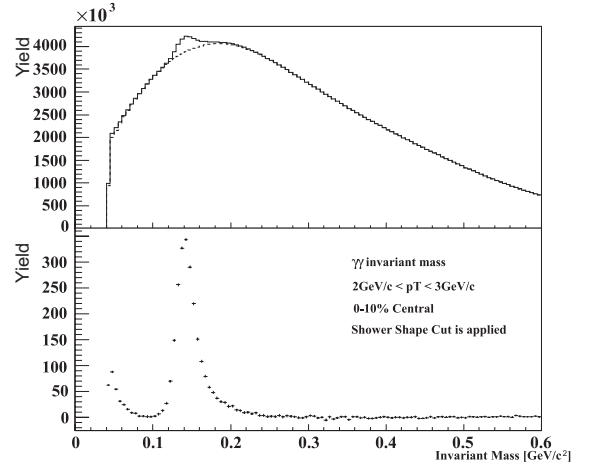


Figure 1. Invariant mass spectra of  $\gamma + \gamma$ . Upper figure shows the raw spectra. Large combinatorial background is seen and estimated with event mixing technique. Bottom figure shows the spectra after combinatorial back ground is subtracted.

## 3. $\pi^0$ measurement in PHENIX Year-4 Run

In RHIC Year-4 run, PHENIX recorded the integrated luminosity of  $0.24 \text{ nb}^{-1}$  in the  $\sqrt{s_{NN}}=200$  GeV Au+Au collisions. Using the PHENIX electromagnetic calorimeter (EMCal) [7],  $\pi^0$ s were detected via the two-photon decay mode ( $\pi^0 \rightarrow 2\gamma$ ). Position and energy of individual photons are measured with EMCal. There are two types of calorimeters at PHENIX. One is a lead-scintillator

sampling-type calorimeter, and the other is a lead-glass Cherenkov calorimeter. The lead-scintillator calorimeter is used in this analysis. Figure 1 shows the invariant mass spectra of  $2\gamma$ . A large combinatorial back ground is seen and is estimated with an event mixing method. To obtain  $\pi^0$  yield, corrections for geometrical acceptance, particle identification efficiency, and overlapping effect in high multiplicity were estimated using computing clusters at RIKEN-CCJ.

The large amount of data obtained in RHIC Year-4 has made it possible to identify  $\pi^0$  up to  $p_T \sim 20$  GeV/c for the central collisions. Figure 2 shows the fully corrected  $\pi^0$  invariant yield as a function of  $p_T$  for each centrality of collision.

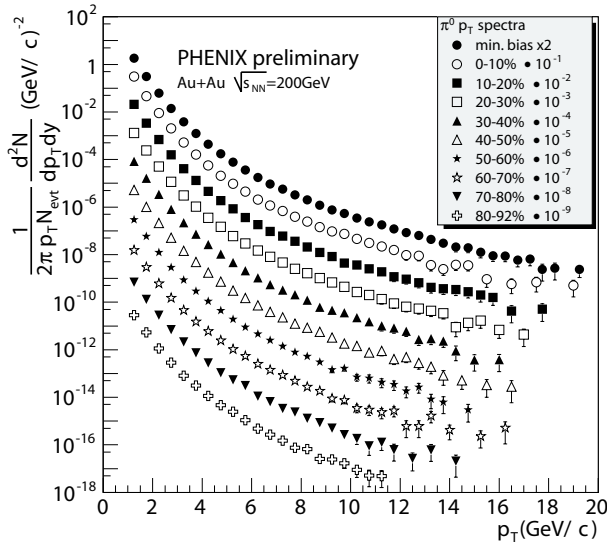


Figure 2. Invariant  $\pi^0$  yields at  $y=0$  versus  $p_T$  for minimum bias and 9 centralities in Au+Au at  $\sqrt{s_{NN}} = 200$  GeV

$R_{AA}$  as a function of  $p_T$  was obtained from corrected  $p_T$  spectra.  $\pi^0$  data obtained in PHENIX Year-3 run were used as the p+p reference. Figure 3 shows the preliminary Year-4 data of  $\pi^0 R_{AA}$  for most central events (0-10%) together with a theoretical prediction which employs the GLV model [8]. Strong  $\pi^0$  suppression by a factor of  $\sim 5$  is observed, and this suppression stays almost constant up to 20 GeV/c. The GLV model describes the strong suppression well and indicates an existence of bulk matter where the initial gluon density ( $dN^g/dy$ ) is more than 1100, which corresponds to an energy density of approximately 15 GeV/fm<sup>3</sup> in Au+Au collisions at  $\sqrt{s_{NN}} = 200$  GeV. The energy density is extremely larger than what is expected at RHIC.

#### 4. Summary

$\pi^0$  is measured in  $\sqrt{s_{NN}} = 200$  GeV Au+Au collisions in RHIC Year-4, and it is compared with GLV calculation. A strong  $\pi^0$  suppression by a factor of  $\sim 5$  is observed, and stays almost constant up to 20 GeV/c. It indicates that the dense matter with the energy density of much larger than  $\sim 1$  GeV/fm<sup>3</sup> is created at RHIC.

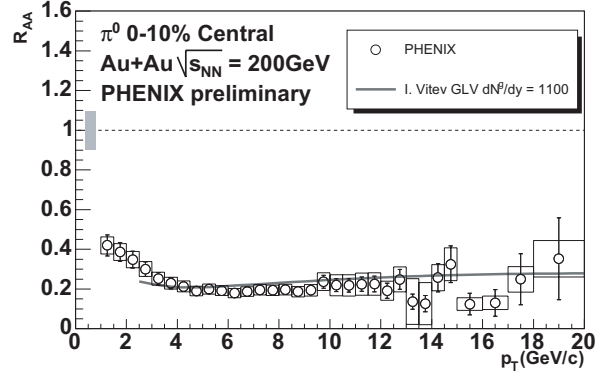


Figure 3. Comparison of  $\pi^0 R_{AA}$  with prediction of  $R_{AA}$  using GLV model in  $\sqrt{s_{NN}} = 200$  GeV Au+Au central (0-10%) collisions. In addition to the statistical and  $p_T$ -uncorrelated errors, point-to-point varying systematic errors are shown on the data points as boxes. An overall systematic error of  $T_{AA}$  normalization is shown on the dashed line drawn at 1.

#### References

- [1] K. Adcox *et al.*, Nucl. Instrum. Methods A **499** (2003) 469.
- [2] F. Karsch, Lect. Notes Phys. **583** (2002) 209.
- [3] S. S. Adler *et al.*, Phys. Rev. Lett. **91** (2003) 072301.
- [4] S. S. Adler *et al.*, Phys. Rev. Lett. **91** (2003) 072303.
- [5] S. S. Adler *et al.*, Phys. Rev. Lett. **94** (2005) 232301.
- [6] J. W. Cronin *et al.*, Phys. Rev. D **11** (1975) 3105.
- [7] L. Aphecetche *et al.*, Nucl. Instrum. Methods A **499** (2003) 521.
- [8] I. Vitev *et al.*: Phys. Rev. Lett. **89** (2002) 252301.

# **Accelerator and Instrumentation**



# Improvement of Magnet Power Supply for RIKEN AVF Cyclotron

S. Watanabe<sup>a</sup>, Y. Ohshiro<sup>a</sup>, S. Kubono<sup>a</sup>, M. Fukuda<sup>ab</sup>, M. Nagase<sup>c</sup>, A. Goto<sup>c</sup>, and M. Kase<sup>c</sup>

<sup>a</sup> Center for Nuclear Study, Graduate School of Science, University of Tokyo

<sup>b</sup> Takasaki Radiation Chemistry Research Establishment, JAERI

<sup>c</sup> RIKEN (The Institute of Physical and Chemical Research)

## 1. Introduction

Ion energy of the RIKEN AVF cyclotron is limited by maximum dee voltage of 50 kV for M/Q of 3 or less, and by maximum magnetic field of 1.74 T for M/Q of 3 or more. This base field limitation has been improved by increase of maximum output current of a main coil power supply from 1100 A to 1200 A [1]. Maximum magnetic rigidity of  $B\rho_{max} = 1.24$  Tm has thus been increased up to 1.30 Tm which enables to accelerate 9 MeV/u  $^{15}\text{N}^{5+}$  ions, required for nuclear astrophysics experiments. According to the increase of 5 for some of the trim coils have also upgraded. The maximum output currents of 5<sup>th</sup> (C5) and 6<sup>th</sup> trim coil (C6) power supplies have been upgraded from 70 A to 200 A and from 150 A to 250 A, respectively.

Name	Excitation current required for $^{15}\text{N}^{5+}$ 9MeV/u	Maximum output voltage and current of power supply
MAIN	1192.84 A	170 V 1100 A → 190 V 1200 A
Trim C1	128.65 A	6 V 151.9 A
Trim C2	225.9 A	11 V 303.9 A
Trim C3	43.07 A	10 V 151.8 A
Trim C4	-23.56 A	10 V 101.4 A
Trim C5	-131.94 A	8 V 70 A → 23 V 200 A
Trim C6	-171.40 A	13 V 150 A → 22 V 250 A
Trim C7	-253.00 A	21 V 253.0 A
Trim C8	-364.30 A	35 V 364.3 A
Trim C9	-231.39 A	13 V 253.4 A

Table 1. Maximum output voltage and current of the magnet power supplies

## 2. Modification of magnet power supply

The solution near an ideal magnetic field distribution where the divergence from an isochronous magnetic field becomes the minimum has been exercised. We found the best combination of the trim coil currents, it generates the ideal magnetic field distribution. Change of the coil power supplies, which should be improved, was planned based on the result. Modified maximum output voltage and current of the magnet power supplies are shown in Table 1. Maximum output power of the MAIN, C5, and C6 are enlarged for acceleration of  $^{15}\text{N}^{5+}$  ions by 8%, 180% and 64%, respectively. In the future, we should also reinforce the maximum output of the power supplies of C7 and C8; whereas other trims coil currents are within nominal maximum out-

put voltage and current of the present power supplies. Estimated coil resistances and required cable cross-sections of the AVF cyclotron magnet system are summarized in Table 2. Note that the maximum cable currents are estimated by multiplying a safety factor of 0.7 to acceptable cable currents at 60°C. Other physical conditions are at room temperature of 30°C, a hollow conductor of the main coil with a cross section of 17.7 x 17.7 mm<sup>2</sup> x  $\phi$ 6.5, and the hollow conductor of the trim coils with the cross section of 6 x mm<sup>2</sup> x  $\phi$ 4.

Name	Turn number	Coil resistances at estimated temp. ( $\Omega$ )
Main	160+160	0.1294 <sub>20°C</sub> / 0.1524 <sub>65°C</sub>
Trim C1	8	0.0148 <sub>20°C</sub> / 0.0156 <sub>30°C</sub>
Trim C2	9	0.0222 <sub>20°C</sub> / 0.0234 <sub>35°C</sub>
Trim C3	10	0.0316 <sub>20°C</sub> / 0.0342 <sub>40°C</sub>
Trim C4	11	0.046 <sub>20°C</sub> / 0.0496 <sub>40°C</sub>
Trim C5	9	0.046 <sub>20°C</sub> / 0.0488 <sub>35°C</sub>
Trim C6	10	0.0582 <sub>20°C</sub> / 0.064 <sub>45°C</sub>
Trim C7	10	0.0656 <sub>20°C</sub> / 0.0758 <sub>60°C</sub>
Trim C8	9	0.0686 <sub>20°C</sub> / 0.0942 <sub>115°C</sub>
Trim C9	4	0.0358 <sub>20°C</sub> / 0.04 <sub>50°C</sub>

Name	Required cable cross-section	Maximum cable current
Main	200 mm <sup>2</sup> x 4	1310 A
Trim C1	100 mm <sup>2</sup> x 1	170 A
Trim C2	100 mm <sup>2</sup> x 2	340 A
Trim C3	100 mm <sup>2</sup> x 1	170 A
Trim C4	60 mm <sup>2</sup> x 1	123 A
Trim C5	150 mm <sup>2</sup> x 1	226 A
Trim C6	200 mm <sup>2</sup> x 1	268 A
Trim C7	100 mm <sup>2</sup> x 1	170 A
Trim C8	100 mm <sup>2</sup> x 1	340 A
Trim C9	100 mm <sup>2</sup> x 1	170 A

Table 2. List of the AVF cyclotron magnet coil system

## 3. Main magnet power supply

The specifications of the AVF main coil power supply are listed in Table 3. The advancement is achieved basically by using a current control circuit with an error amplifier, a DC-CT, and a reference current source. The current control circuit in a thermal stabilization box has been installed in the main magnet power supply. The limited space of original power supply is offered for new main transformer, additional transistor bank, and new chalk transformer. This table shows that maximum power rating of an input AC line is to be modified. For example, a no fuse breaker

(NFB) of 500 A is required in the input AC line. A leakage flux around the main magnet has been measured. Due to the magnetic excitation power enlargement, leakage flux around the main coil became larger than former maximum current. n

<sup>7</sup>Li, <sup>14</sup>N, <sup>15</sup>N, <sup>18</sup>O, <sup>24</sup>Mg, <sup>40</sup>Ar for CRIB experiments.

## References

[1] M. Fukuda *et al.*, CNS Annual Report 2004(2005) 65.

Room Temperature	10sim40°C
Input AC voltage, phase, and frequency	400sim440 V, 3 phases, 50/60 Hz
Input voltage stability	+/- 10%
Input power rating	310 kVA, 35 kVA over than original type
Cooling water	30 +/- 2.5°C, 0.49 Mpa/cm <sup>2</sup> average, 15 L/min
Inductance and res istance as Output Load	500 mH, 0.158 Ω at 30°C
Output current (original / improved)	0~1100 A / 0~1200 A
Output voltage (original / improved)	0~170 V/ 0~190 V, Trip voltage is set at 195 V
Output Current range	0~100%
Current stability (original / improved)	+/-1x10 <sup>-5</sup> /8 hr / 1x10 <sup>-5</sup> /8 hr
Current ripple	1x10 <sup>-5</sup> Ap-p (obtained at inductance load)
Output DC power (original / improved)	187 kW / 228 kW
Output current detector (original / improved)	(Resister / DC-CT)
Width, Height, Dips	W 1600 mm, H 2000 mm, D 1300 mm
Main trans. (based on JEC-2200, JEM-1310)	Weight=930 kg, Water Cooling (12 L/min)

Table 3. Specifications of RIKEN AVF main coil PS. Note: flow rate of the main transformer at maximum output power. Total flow rate is not shown in this table.

## 4. Trim coil power supply system

The trim coil power supply system consists of 9 pairs of a transistor bank (C1~C9) with an isolation transformer with delta-delta connections. A new transistor bank for C5 and C6 has been constructed and replaced the former transistor bank; nevertheless former current control unit is used. Specifications of the replaced trim coil power supply system are summarized in Table 4.

Room Temperature	10~40°C
Input AC voltage, phase, and frequency	400~440 V, 3 phases, 50/60 Hz
Input voltage stability	+/- 10%
Input power rating (C5 / C6) and connections	7.4 kVA / 8.8 kVA, Star (in) -dDelta (out)
Cooling water (Temp, Pressure, Flow rate)	30 +/- 2.5 °C, 0.49 Mpa/cm <sup>2</sup> average, 15L/min
Output current (C5 / C6)	0~200 A / 0~250 A, Trip current is 220 A / 275 A
Output voltage (C5 / C6)	0~23 V * / 0~22 V **
Output Current range	0~100% /30 sec
Current stability	+/-5 x 10 <sup>-5</sup> /8 hr
Current ripple (L=1 mH, R=0.05 Ω)	1x10 <sup>-4</sup> Ap-p (obtained at inductance load)
Output DC power (C5 / C6)	2 kW / 3.75 kW
Output current measurement device	DC-CT
Width, Height, Dips, Weight	W 700 mm, H 2000 mm, D 1260 mm, 500 kg
Output Polarity (Plus or Minus)	By Manual Switch (2PDT300A)

Table 4. Specifications of replaced AVF trim coil power supply system (C5, C6). Note: output voltages are estimated by the cable resistances of 60 mm<sup>2</sup> (\*) and 100 mm<sup>2</sup> (\*\*), respectively.

## 5. Summary

After the improvement of the power supplies, a main coil and nine pairs of concentric trim coils wound on spiral sectors was generated an isochronous field for acceleration of

# Design of a CNS Charge Breeder ECR Ion Source

Y. Ohshiro, S. Yamaka, S. Watanabe, T. Nakagawa<sup>a</sup>, T. Hattori<sup>b</sup>, M. Oyaizu<sup>c</sup>, H. Miyatake<sup>c</sup>  
and S. Kubono

*Center for Nuclear Study, Graduate School of Sciences, University of Tokyo*

<sup>a</sup>*RIKEN (The Institute of Physical and Chemical Research)*

<sup>b</sup>*Research laboratory for Nuclear Reactors, Tokyo Institute of Technology*

<sup>c</sup>*High Energy Accelerator Research Organization*

## Introduction

A charge breeder ECR ion source (named CBECR) utilizes secondarily ionization of singly charged heavy ions by interactions with a high-energy electron shell generated by ECR plasma, in order to produce highly charged heavy ion beams [1]. Characteristic of a CBECR ion source is to have an ion source for generating singly charged heavy ions separate from an ECR plasma chamber [2]. It is advantageous to have this separate structure, since the ECR plasma chamber is free from deposition of evaporated metallic material from the ion source [3]. In this report, details of the CBECR design are described, with main emphasis on a charged breeding efficiency which is the ratio of the number of ions ejected from the heavy ion source and the number injected to the ECR plasma zone.

## 1. Structure

A cross-sectional view of the CBECR at CNS is shown in Fig. 1. At a heavy ion source, marked as ① in Fig. 1, high-intensity singly charged ions are produced. Two types of ion sources are planned to use; a volume type ion source [4] for generating intensive low-charged ion beams from gaseous material, and a sputtering type one for metallic material.

An existing HiECR ion source [5] is being used as CBECR, and improvement has been made so as to be able to operate with 14 GHz RF. Then, the singly ions extracted from the heavy ion source are injected into the 14 GHz CBECR through the beam transport system consisted of an Einzel lens triplet. For optimizing the transmission efficiency of the injection ions, voltage of the lenses, E1, E2 and E3 (in Fig. 1) is adjusted to be 8 kV, 10 kV and 11 kV, respectively. The final lens (E3) and a decelerator are set on a supporting bar movable along the beam axis in order to have capability of fine-tuning of beam optics.

Optimization of the incident beam will be carried out so as to maximize the number of secondarily ionization of injected ions in the CBECR (ionization efficiency). The singly charged ions are decelerated just before arriving at a plasma chamber. A decelerator, which consists of a pair of cylindrical electrodes with inner diameter of 2 cm and 3.4 cm, respectively, is located axially into the plasma chamber. The singly ions are decelerated by the potential difference on the tip surface

of two electrodes, (see a potential map in Fig. 1).

## 2. Beam simulation

Depending on the incident angles of singly ions entered in CBECR plasma, rebound of a certain fraction of ions from the plasma meniscus is anticipated. To investigate the geometrical beam acceptance of the CBECR, we have performed a beam optics calculation, by using SIMION7.

Ar<sup>1+</sup> ions of 10.005 keV starting from the position of the anode hole (0.1 cm in diameter) with different off-axis positions and angles enter the region for deceleration as shown in Fig. 1. The value of 5 eV is the potential difference to the two ion sources. The potential difference was chosen to trap optimally the ions in the ECR plasma.

The simulation results show that more than 80 % of singly charged ions ejected from the ion source are successfully injected into the ECR plasma zone. The specification of the components designed based on calculation is listed in the table 1.

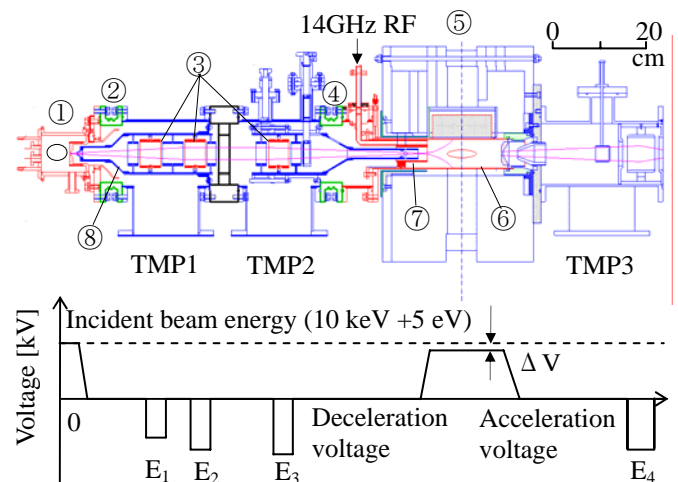


Fig. 1. A cross-sectional view of the CNS charges breeding system and potential map for injection of interest ions. ① Volume type ion source, ②④ Insulator (MC nylon), ③ Einzel lens (E<sub>1-4</sub>), ⑤ Charge breeder ECR ion source (CBECR), ⑥ Plasma chamber, ⑦ Decelerator, ⑧ Conical wall.

### 3. Specification of the CBECR

Differential pumping technique is used to keep the pressure difference between the heavy ion source and CBECR. The extraction region of heavy ions is pumped by TMP1, and the region with Einzel lenses is pumped by TMP2, and the two regions are completely separately by the conical wall to prevent inflow of the gas from ion source to CBECR. Vacuum pressure in the ion source, the extraction region and the lenses region is estimated to be  $10^{-3}$  Torr,  $10^{-5}$  Torr, and  $10^{-6}$  Torr, respectively, during  $\text{Ar}^+$  ion generation. As a result, the vacuum pressure in the plasma chamber of CBECR can be kept at  $10^{-7}$  Torr, and can produce the highly charged ions by the higher intensity.

Without A/Z analysis, the ions are directly injected into the CBECR. Although the ions are mainly singly ions, 2 or more charge state ions and residual gas ions are also extracted and injected into the CBECR, simultaneously. Effect of injection of these mixed ions to the generation of multi-charge ions is of interest.

A decelerator is inserted near the peak of the mirror magnetic field of the CBECR. In order to optimize the deceleration effect, the gap between the inner and outer cylindrical electrodes can change by moving the inner one along the beam axis. Slowing down the incident ions inside the plasma chamber will result in ion confinement for a longer time, which should contribute producing more intensive ions.

Table 1. Specification of each device designed.

First stage ion source (IS)	
• Volume type IS	E.g. $\text{Ar}^+$ , $^{15}\text{N}^+$ production
• Spattering type IS	E.g. $\text{Li}^+$ - $\text{Cu}^+$ production
• Extraction voltage	10 kV + 5 V
Beam transport system	
• Max. Einzel lens voltage	20 kV ( $E_1 - E_4$ )
• Deceleration voltage	10 kV
Charge breeder ECRIS	
• RF frequency	14 GHz
• Max. Mirror field	12 kG
• Surface field of sextupol	10.4 kG
• Correction coil	13500 AT ( $C_1 - C_3$ )
• Acceleration voltage	10 kV
Vacuum system	
• Pumping speed	500 l/s (TMP <sub>1</sub> - TMP <sub>3</sub> )

### 4. Conclusion

Design was made for the charge breeding system, and simulation was performed for the ion optics in order to optimize the system performance. The CBECR is currently under construction. It is the present target to inject the  $\text{Ar}^+$  ions of 20  $\mu\text{A}$  to CRECR, and to produce high intensity  $\text{Ar}^{11+}$ . Moreover, production of metal ion from Li to Cu with high intensity is planned.

### References

- [1] M Sekiguchi, T. Nakagawa, Proc. of the 12th Int. Workshop on ECR Ion Sources. INS-J-182 (1995).
- [2] M.Oyaizu *et al.*, Rev. Sci. Instrum. **73** (2002) 806.
- [3] Y. Ohshiro *et al.*, CNS. Annual Report 2005 (2006) 59.
- [4] S. Watanabe *et al.*, CNS. Annual Report 2004 (2005) 61.
- [5] D. Nagae *et al.*, CNS. Annual Report 2002 (2003) 69.

# Production of High Intensity $^{40}\text{Ca}^{11+}$ Ion Beam

Y. Ohshiro, S. Yamaka, S. Watanabe Y. Higurashi<sup>a</sup>, T. Kageyama<sup>a</sup>, and S. Kubono

Center for Nuclear Study, Graduate School of Sciences, University of Tokyo  
<sup>a</sup>RIKEN (The Institute of Physical and Chemical Research)

## 1. Introduction

At the AVF cyclotron facility of RIKEN, metallic ions have been developed by a Hyper ECR ion source and routinely used for nuclear physics experiments. The metallic ions have been stably produced by two methods: a crucible insertion method [1] and a rod insertion method [2] for the ECR source. The metallic ions developed include  $^7\text{Li}^{2+}$ ,  $^7\text{Li}^{3+}$ ,  $^{28}\text{Si}^{9+}$  and  $^{40}\text{Ca}^{11+}$ . Typical beam intensities are shown in Table 1. Here, we identified the optimum positions of the crucible and the rod that provide the maximum beam current.

## 2. ECR set up for Ca ion production

For ion production with a solid material, the Hyper ECR ion source was set up as shown in Fig. 1. An RF wall that intercepts a microwave was set at a distance of 12.5 cm from the sextupole magnet center. A rod of  $\text{CaF}_2$  which has a 6 cm in length on 0.4 cm squares was inserted into a plasma chamber through a hole of 1.4 cm in diameter on the RF wall.

The operating conditions for the maximum  $^{40}\text{Ca}^{11+}$  ion beam currents were obtained as follows: The peak mirror fields were enhanced to 13.2 kG and 12.0 kG with MC1 and MC2, respectively (See Fig.1). The length of a second stage ECR zone was approximately 6.3 cm in length. An RF (14.2 GHz) power of 320 W was fed into the ECR plasma. Oxygen was used as supporting gas. The vacuum pressure was in a range of  $10^{-7}$  Torr during  $^{40}\text{Ca}^{11+}$  ion production.

## 3. Search for optimum position for solid material

When the material rod was placed near the RF wall, high-intensity ion beams were extracted. As shown in Fig. 2, the maximum currents were obtained within 1.5 cm from the RF wall. A heat source, which evaporates the rod, will be in this area distant from the second stage ECR zone.

Table 1. Beam intensities of metallic ions obtained

Ion	Beam intensity ( $\mu\text{A}$ )	Charged material
$^7\text{Li}^{3+}$	75	Li pure metal (crucible)
$^7\text{Li}^{2+}$	200	Li pure metal (crucible)
$^{40}\text{Ca}^{11+}$	8.5	Ca pure metal (crucible)
$^{28}\text{Si}^{9+}$	32	$\text{SiO}_2$ rod
$^{40}\text{Ca}^{11+}$	50	$\text{CaF}_2$ rod

The maximum beam current of 50  $\mu\text{A}$  was obtained for  $^{40}\text{Ca}^{11+}$  at 0.32 cm place of the rod from the RF wall (mark ● shown in Fig. 2). The rod consumption rate was approximately 0.1 mm/h in length.

Note that, the position of the RF wall was close to the peak of the mirror field (MC1) and the rod locates in the same area as the first stage ECR zone (see Fig. 1). Thus, the surface of the rod can be heated by the electrons in the zone. The electron density in this zone will be measured later.

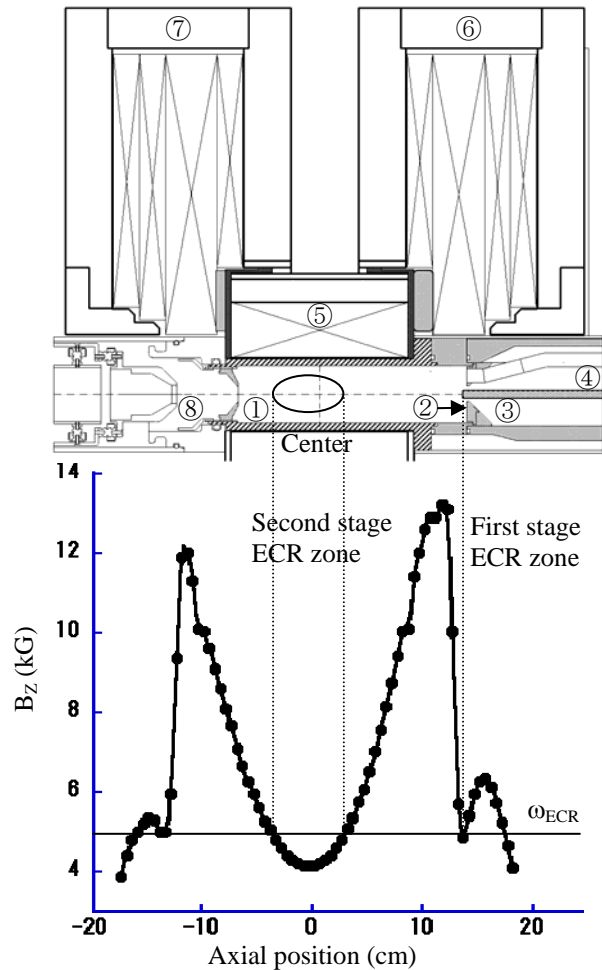


Fig. 1. Schematic drawing of Hyper ECR ion source together with mirror field distribution used for  $^{40}\text{Ca}^{11+}$  ions production. ① Plasma chamber, ② RF wall, ③ Solid material, ④ Movable rod, ⑤ Sextupole magnet, ⑥ MC1, ⑦ MC2, ⑧ Extractor.

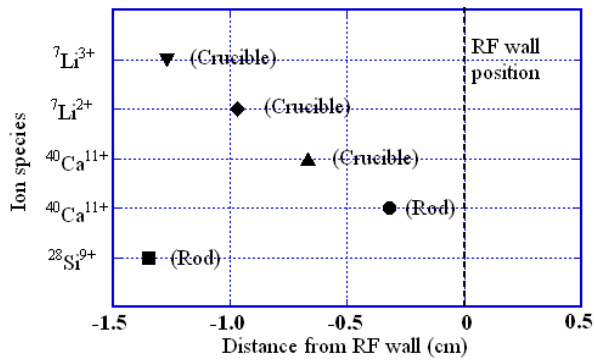


Fig. 2. The distance of the tips of the crucible and the rod placed in the plasma chamber.

#### 4. Conclusion

In the past year,  ${}^{40}\text{Ca}^{11+}$  ions have been successfully extracted from the Hyper ECR ion source with the intensity as high as 50 eμA. This value was obtained by placing the metallic material rod near the first stage ECR zone in the ion source. The physical conditions of the new area are under investigation.

#### References

- [1] Y. Ohshiro *et al.*, RIKEN Accel. Prog. Rep. 39 (2006) 231
- [2] Y. Ohshiro *et al.*, RIKEN Accel. Prog. Rep. 38 (2005) 253

# High Resolution SHARAQ Spectrometer

T. Uesaka, S. Shimoura, T. Kawabata, H. Sakai<sup>a</sup>, S. Kubono, E. Ideguchi, H. Yamaguchi, T. Kubo<sup>b</sup>,  
and G. P. Berg<sup>c</sup>

*Center for Nuclear Study, Graduate School of Science, University of Tokyo*

<sup>a</sup> *Department of Physics, Graduate School of Science, University of Tokyo*

<sup>b</sup> *RIKEN (the Institute for Physical and Chemical Research)*

<sup>c</sup> *Department of Physics, Notre Dame University*

## 1. Overview

The SHARAQ spectrometer is a high resolution magnetic spectrometer designed for radioactive isotope (RI) beam experiments at the RI Beam Factory (RIBF). It can analyze particles with magnetic rigidity of 1.8–6.8 Tm, which corresponds to an energy of 40–440 MeV/A for  $A/Z = 2$  particles. Momentum and angular resolutions are  $\delta p/p \sim 1/15000$  and  $\sim 1$  mrad, respectively. The spectrometer can rotate around its target position from  $-2^\circ$  to  $15^\circ$  for finite angle measurements. Figure 1 shows a view of the SHARAQ spectrometer.

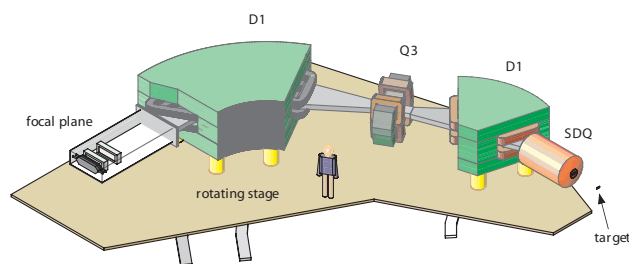


Figure 1. The SHARAQ spectrometer.

The SHARAQ spectrometer will be placed at E20 experimental area of the RIBF building. RI beams, produced at the primary target position (F0), are transported to the SHARAQ target position through the BigRIPS beam-line (F0–F6) [1] and the SHARAQ beam-line [2]. The beam-line as a whole is designed to fulfill dispersion-matching conditions when combined with the SHARAQ spectrometer. Simultaneous achievement of (lateral) dispersion matching and angular dispersion matching conditions are crucially important in the use of SHARAQ for RI beams which necessarily accompany a large momentum spread. The beam-line will be also operated in an achromatic mode to provide a small beam spot at the target position when necessary.

## 2. Magnets

The SHARAQ spectrometer consists of three quadrupole and two dipole magnets.

First doublet quadrupoles (Q1 and Q2) are superconducting magnets. Its design is, for the most part, inherited from that of superconducting triplet quadrupoles of BigRIPS [3]. Modification has been made in its warm bore shape which is  $\phi 240$  mm circle in the original triplet quadrupoles: Q1 and Q2 has a warm bore of horizontally-wide diamond shape, 340 mm in width and 230 mm in height to accept a horizontally extended beam enve-

lope. The subsequent normal-conducting dipole (D1) and quadrupole (Q3) magnets are recycled from the decommissioned spectrograph SMART [4]. The D1 magnet, which was used as a  $60^\circ$  bending magnet with a bending radius of  $\rho = 2.4$  m in SMART, is used as a  $32.7^\circ$  bending with a bending radius of  $\rho = 4.4$  m in SHARAQ. Both entrance and exit axes to the magnet are tilted by  $13.7^\circ$  in horizontally focusing direction.

The last dipole magnet, D2, will be newly constructed. Details of the design is described in other reports [5, 6]. The D2 magnet is a  $60^\circ$ -bending magnet with a pole gap of 200 mm. From ion-optical calculations shown below, it is required that the D2 magnet should have a good field region, in which  $\Delta B/B \sim 10^{-4}$  is achieved, of  $\pm 400$  mm from the central orbit. The entrance of the D2 pole will be curved to eliminate higher order aberrations, while the exit is tilted by  $30^\circ$  in horizontal focusing direction to reduce a distance from the D2 magnet to the focal plane.

Specifications of Q1, Q2, Q3, D1, and D2 are listed in Tables 1 and 2, respectively. It should be noted that the effective lengths of quadrupoles are dependent on the magnetic field strength and thus the values in the table represent typical ones.

Table 1. Specifications of Q1–3 magnets.

	Q1	Q2	Q3
bore [mm]	$340^W \times 230^H$	$\phi 270$	$\phi 270$
max. gradient [T/m]	14.1	14.1	7.4
effective length [mm]	530	1020	840

Table 2. Specifications of D1 and D2 magnets.

	D1	D2
bending radius [m]	4.4	4.4
bending angle [deg]	32.7	60
gap [mm]	230	200
max. field strength [T]	1.55	1.55
weight [t]	102	$\sim 280$

## 3. First order ion-optical calculation

First order ion-optical calculations by use of GIOS [7] are made to optimize magnetic field settings. Q1 and Q2 field strengths are tuned so that horizontal envelope after Q2 should be as wide as the Q2 bore width and vertical envelope at Q3 as much as the Q3 bore diameter. Q3 strength, in turn, is adjusted to achieve a zero vertical magnification

( $y|y$ ). The vanishing vertical magnification is essential in attaining a required level of the vertical angular resolution.

The resulting first-order transfer matrix is shown below. Here  $x$  (1st variable),  $y$  (3rd) are the positions in [m], while  $a$  (2nd) and  $b$  (4th) are  $p_x/p$  and  $p_y/p$  where  $p_x, p_y, p$  denote the  $x$ -,  $y$ -components, and the norm of particle momentum. The 6th variable  $\delta = (p - p_0)/p_0$  represents a momentum difference from that of a central-ray particle.

$$\begin{pmatrix} 0.397 & 0.000 & 0.000 & 0.000 & 0.000 & 5.858 \\ 0.773 & 2.516 & 0.000 & 0.000 & 0.000 & -0.661 \\ 0.000 & 0.000 & 0.000 & -2.304 & 0.000 & 0.000 \\ 0.000 & 0.000 & 0.434 & -0.197 & 0.000 & 0.000 \\ -0.295 & -0.907 & 0.000 & 0.000 & 1.000 & -0.028 \\ 0.000 & 0.000 & 0.000 & 0.000 & 0.000 & 1.000 \end{pmatrix}$$

A resolving power, obtained by dividing a dispersion [ $(x|\delta) = 5.858$  m] by a magnification in dispersive plane [ $(x|x) = 0.397$ ] is calculated to be 14.8 m. Assuming a beam image size measured at the target position (or at the beginning of the beam-line in the dispersion matching mode) is 1 mm, the resulting momentum resolution is evaluated to be  $\delta p/p=1/14800$ . A large value of ( $y|b$ ) and a vanishing vertical magnification ( $y|y) = 0.0$  lead a high angular resolution of  $\Delta b < 1$  mrad in the vertical direction, while the horizontal angular resolution  $\Delta a$  is comparable in size. Thus designed performance of the SHARAQ spectrometer is presented in Table 3.

Table 3. Designed performances of the SHARAQ spectrometer.

dispersion ( $D$ ) [m]	5.86
horizontal magnification ( $M_x$ )	0.40
$D/M_x$ [m]	14.7 m
momentum resolution (for image size of 1 mm)	1/14700
vertical magnification	0.0
angular resolution	<1 mrad
vertical acceptance [mrad]	$\pm 50$
horizontal acceptance [mrad]	
dispersion matching mode	$\pm 17$
beam focus mode	$\pm 30$
solid angle [msr]	
dispersion matching mode	2.7
beam focus mode	4.8

#### 4. Higher-order aberrations

Ion optical calculations with COSY INFINITY [10] are carried out to evaluate contributions from higher order aberrations. Fringing field distributions obtained from field map measurements [8,9] are used in the calculations. It is found that major aberrations ( $x|aa$ ) and ( $x|aaa$ ) originate from inhomogeneous field distribution of Q1 and Q2 in the region of  $r > 12$  cm. The entrance pole of D2 will be shaped in a 3rd order polynomial form to eliminate the aberrations. By this modification, the broadening of an image size at the focal plane can be as small as that obtained by the first order calculation.

#### 5. Schedule

The SHARAQ spectrometer will be put into operation in 2008: construction of the D2 magnet is planned to finish in March 2007. In the first half of FY2007, all the magnet together with a rotating stage will be installed at E20 experimental area of the RIBF building. Following the completion of the installation, field map measurements of the magnets will be made in the second half of FY2007. Design and construction of beam-line magnets, together with development of beam-line and focal plane detectors will be carried out in parallel by the end of FY2007.

#### References

- [1] T. Kubo, Nucl. Instrum. Methods Phys. Res. B **204** (2003) 97.
- [2] T. Kawabata *et al.*, CNS Annual Report 2005 (2006) 63.
- [3] K. Kusaka *et al.*, IEEE Trans. Appl. Supercond. **14** (2004) 310.
- [4] T. Ichihara *et al.*, Nucl. Phys. A **569** (1994) 287c.
- [5] T. Uesaka, G. P. Berg *et al.*, CNS Annual Report 2005 (2006) 65.
- [6] G. P. Berg, private communication.
- [7] H. Wollnik *et al.*, AIP Conf. Proc. **177** (1998) 74.
- [8] H. Suzuki, private communication.
- [9] Y. Tajima, private communication.
- [10] M. Berz *et al.* Phys. Rev. C **47** (1993) 537.

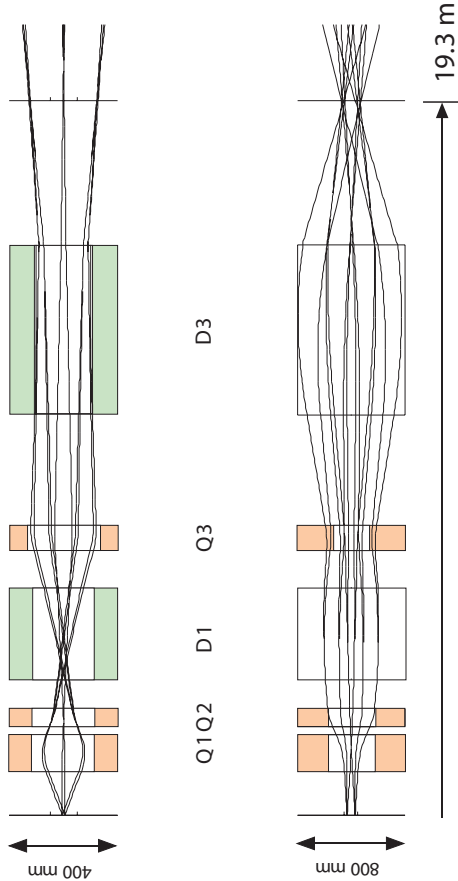


Figure 2. Results of the first order ion-optical calculation.

# High Resolution Beam Line for the SHARAQ Spectrometer

T. Kawabata<sup>a</sup>, T. Kubo<sup>b</sup>, H. Sakai<sup>c</sup>, S. Shimoura<sup>a</sup>, and T. Uesaka<sup>a</sup>

<sup>a</sup> Center for Nuclear Study, Graduate School of Science, University of Tokyo

<sup>b</sup> RIKEN (The Institute of Physical and Chemical Research)

<sup>c</sup> Department of Physics, Graduate School of Science, University of Tokyo

The construction of the SHARAQ spectrometer has started in 2005 by the Center for Nuclear Study [1]. The SHARAQ spectrometer is designed to achieve a high momentum resolution of  $\delta p/p \sim 1/15000$  for charged particles with a magnetic rigidity of  $B\rho = 6.8$  Tm. The SHARAQ spectrometer will be devoted to the nuclear spectroscopic study using RI beams produced by the RI beam factory (RIBF) at RIKEN. Since the RI beams have a variety of isospin, spin, and internal energy, the RI-beam induced reactions are expected to be useful tools to probe nuclear many body systems.

Since the RI beams generally have a large emittance, the dispersion matching technique [2, 3] must be introduced to perform high resolution measurements. If the dispersions of the SHARAQ spectrometer and its beam line are properly “matched”, the missing-mass resolution can be significantly improved better than the momentum spread of the RI beam.

Following the notation of the computer code TRANSPORT [4], the horizontal position  $x$  and angle  $\theta$  at the focal plane of the spectrometer are related to those at the starting point of the beam line by using the transfer matrix elements of the spectrometer ( $s_{ij}$ ) and beam line ( $b_{ij}$ ).

$$\begin{aligned} x = & (s_{11}b_{11} + s_{12}b_{21})x_0 \\ & + (s_{11}b_{12} + s_{12}b_{22})\theta_0 \\ & + (s_{11}b_{16} + s_{12}b_{26} + s_{16})\delta_0, \end{aligned} \quad (1)$$

$$\begin{aligned} \theta = & (s_{21}b_{11} + s_{22}b_{21})x_0 \\ & + (s_{21}b_{12} + s_{22}b_{22})\theta_0 \\ & + (s_{21}b_{16} + s_{22}b_{26} + s_{26})\delta_0. \end{aligned} \quad (2)$$

The  $x_0$ ,  $\theta_0$ , and  $\delta_0$  are the horizontal position, angle, and fractional momentum deviation from the central trajectory ( $\delta \equiv \Delta p/p$ ) at the starting point of the beam line. When the coefficients of the momentum dependent terms in Eqs. (1) and (2) are zero as

$$s_{11}b_{16} + s_{12}b_{26} + s_{16} = 0, \quad (3)$$

$$s_{21}b_{16} + s_{22}b_{26} + s_{26} = 0, \quad (4)$$

the horizontal position and angle at the focal plane are independent of the momentum spread of the beam. Eqs. (3) and (4) are commonly called as the momentum- and angular-dispersion matching conditions, respectively. It is necessary for the high-resolution spectroscopy with the secondary RI beam to construct the beam line satisfying those matching conditions. From Eqs. (3), (4), and the SHARAQ design values of  $s_{ij}$ , the dispersion matching conditions for the beam-line transfer matrix elements are determined to be  $b_{16} = -13.66$  m and  $b_{26} = 4.53$  rad.

The SHARAQ spectrometer will be installed in the E20 experimental room at RIBF as seen in Fig. 1. Since the RI

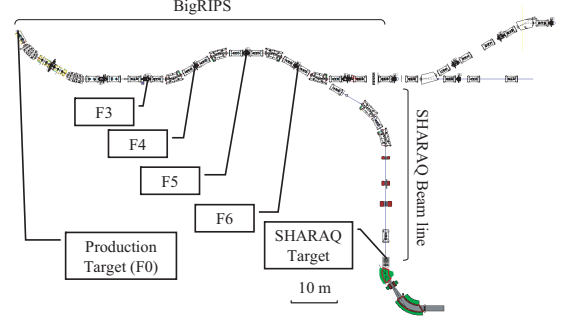


Figure 1. Layout of the SHARAQ spectrometer and the high-resolution beam line at RIBF.

beam emitted from the production target at F0 is achromatically focused at F3 in the normal beam transport procedure for the BigRIPS fragment separator [5], we determined F3 to be the starting point of the SHARAQ beam line.

The SHARAQ beam line shares the magnetic elements with the BigRIPS fragment separator up to F6. After F6, the SHARAQ beam line branches from BigRIPS and bends  $60^\circ$  toward the target. Since the layout of the magnetic elements of the BigRIPS fragment separator has been already determined, the layout between the branching point and the target can be optimized to satisfy the dispersion matching conditions using the computer code GIOS [6].

One realistic solution for the dispersive beam transport is shown in Fig. 2. The two  $30^\circ$  bending magnets (BM) are used with the several quadrupole magnets for the beam transport from F6 to the SHARAQ target. Although most of the quadrupole magnets are the superconducting triplet quadrupole magnets (STQ) with the warm bore radius of 14 cm [7], only the doublet (DQ) and singlet (SQ) quadrupole magnets are the normal conducting magnets with the maximum field gradient of 4.3 T/m and with the bore radius of 14 cm. DQ and SQ are located between BM-S2 and STQ-S3. The maximum magnetic rigidity of the beam line is 8.5 Tm, which is limited by the maximum field gradient of 15 T/m of STQ.

The magnetic-field gradients for the several couples of STQs are constrained to be symmetric. Namely, the field gradients of the three quadrupole magnets of STQ9 are equal to those in STQ12. Similarly, the field gradients of STQ10 and STQ13 are equal to those of STQ11 and STQ-S1, respectively. This symmetric constraint for the field gradients is helpful to simplify the beam line tuning and to minimize the higher order aberration.

The beam is focused both horizontally and vertically at SQ in the last straight section after BM-S2. At this point,

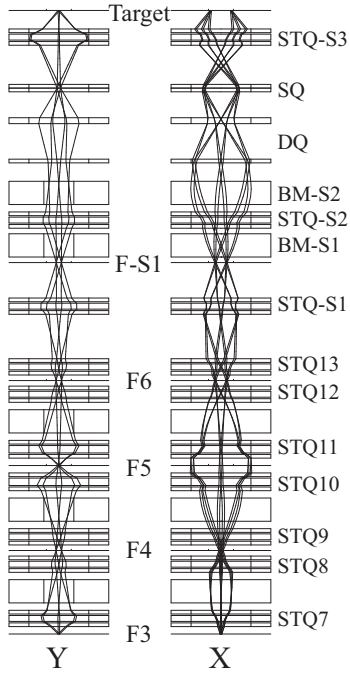


Figure 2. Envelopes of the dispersive beam transport from F3 to the SHARAQ target in the horizontal (right) and vertical (left) planes. Trajectories are drawn for particles with  $x = \pm 3$  mm,  $y = \pm 3$  mm,  $\theta = \pm 10$  and 0 mr,  $\phi = \pm 30$  and 0 mr, and  $\delta = \pm 0.3\%$ , respectively.

the horizontal size of the beam envelope is large while the vertical size is relatively small. The horizontal beam size is dominated by the momentum spread of the beam due to the large dispersion of 23 m. Thus, SQ can change the correlation between the momentum and the horizontal angle of the beam trajectory, which is presented by the  $b_{26}$  term in the transfer matrix, while the other ion optical properties such as the dispersion are nearly unchanged. The  $b_{16}$  term is easily changed by tuning STQ-S3 since there is only one STQ between SQ and the target. Thus, the double focusing point at SQ in the last straight section is useful to realize the dispersion matching conditions.

The transfer matrix of the SHARAQ beam line obtained by the first order ion optical calculation is tabulated in Table 1. The dispersion matching conditions are successfully satisfied, while the horizontal and vertical magnifications are almost unity. The off diagonal terms of  $b_{21}$  and  $b_{43}$  are kept small to reduce the angular spread caused by  $x_0$  and  $y_0$ .

In the present calculation, only the first order effects are taken into account, however, the higher order aberration is not negligible since the secondary RI beams have a large emittance. The hexapole and octupole magnets are useful to correct such higher order effects. In order to optimize the layout of those multipole magnets and their field strengths, it is necessary to perform the higher-order ion optical calculation. The higher-order calculation is still in progress, and the results will be reported elsewhere soon.

$(x x) (= b_{11})$	-0.92	$(x \theta) (= b_{12})$	0.00
$(\theta x) (= b_{21})$	0.11	$(\theta \theta) (= b_{22})$	-1.09
$(x \delta) (= b_{16})$	-13.66	$(\theta \delta) (= b_{26})$	4.53
$(y y) (= b_{33})$	1.16	$(y \phi) (= b_{34})$	0.00
$(\phi y) (= b_{43})$	0.55	$(\phi \phi) (= b_{44})$	0.86

Table 1. Beam transfer matrix of the SHARAQ beam line obtained by the first order ion optical calculation by GIOS. The units for the lengths and angles are m and radian, respectively.

## References

- [1] T. Uesaka *et al.*, CNS Annual Report 2005 (2006) 61.
- [2] B. L. Cohen, Rev. Sci. Instr. **30** (1959) 415.
- [3] T. Wakasa *et al.*, Nucl. Instrum. Methods A **482** (2002) 79, and references therein.
- [4] K. L. Brown *et al.*, SLAC Report No. 91 Rev. 1, 1974 (unpublished).
- [5] T. Kubo, Nucl. Instrum. Methods B **204** (2003) 97.
- [6] H. Wollnik *et al.*, Ion-optics code GIOS, University of Giessen, Germany.
- [7] K. Kusaka *et al.*, IEEE Trans. Appl. Supercond. **14** (2004) 310.

# Design of D2 Dipole Magnet for the SHARAQ Spectrometer

T. Uesaka, G. P. Berg<sup>a</sup>, S. Shimoura, T. Kawabata, and H. Sakai<sup>b</sup>

*Center for Nuclear Study, Graduate School of Science, University of Tokyo*

<sup>a</sup> *Department of Physics, Notre Dame University*

<sup>b</sup> *Department of Physics, Graduate School of Science, University of Tokyo*

## 1. Design goal

The high resolution SHARAQ spectrometer [1] consists of three quadrupole magnets and two dipole magnets. The third quadrupole and the first dipole magnets are recycled from the decommissioned spectrograph SMART [2]. The first doublet quadrupoles are currently under construction. The last dipole magnet, D2, will be newly constructed in FY2006. Since D2 is the largest magnet in SHARAQ providing 60°-bending, its design is the most critical part in the design of the spectrometer as a whole.

Ion optical calculations [1] place requirements on specifications of D2: it should have a pole gap wider than 200 mm and a good field region wider than  $\pm 400$  mm from the central orbit. In the good field region, field homogeneity  $\Delta B/B$  should be as small as  $10^{-4}$ , which should be achieved in the field range of 0.4–1.55 T. The entrance edge is required to be shaped in a 3rd-order polynomial curve for elimination of higher-order aberrations, while the exit edge should be inclined by 30° for horizontal focusing.

The goal of the present work is to find a design of the magnet to meet these requirements. For this purpose, magnetic field calculations has been made by use of a code based on a finite element method. The calculations was carried out in two dimensional axisymmetrical geometry [3].

## 2. Poles and Return Yokes

Cross section and top view of the optimized D2 dipole magnet are shown in Figs. 1 and 2, respectively.

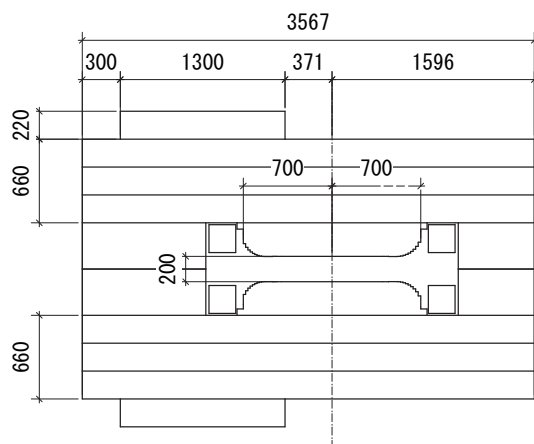


Figure 1. Cross section of the D2 dipole magnet. Numbers are in millimeter.

The bending radius of D2 is 4.4 m. Top and bottom yokes have a thickness of 660 mm. Auxiliary yokes with a thickness of 220 mm and a width of 1300 mm are added in the low-momentum side (left in the figure) to decrease saturation effects.

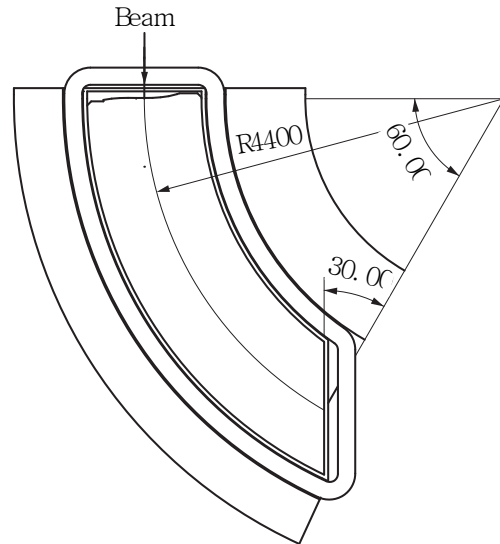


Figure 2. Top view of the D2 dipole magnet.

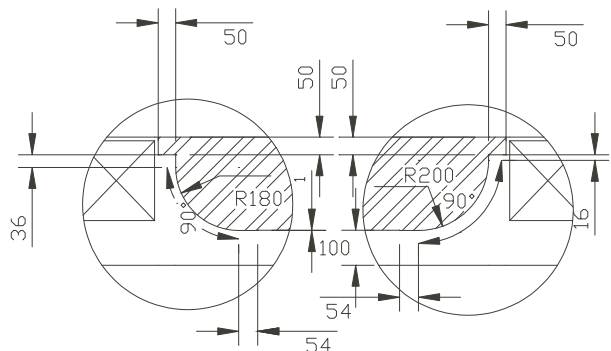


Figure 3. The side profile of D2 pole piece. For details, see the text.

Design of the pole pieces is the most important part of the present work. Figure 1 shows the cross section of the pole piece. The pole width of 1400 mm is needed to provide a good field region of  $\pm 400$  mm from the central orbit. In addition, Rose shims and rounded-shape fillets are introduced to both sides of the pole pieces. Radii of the fillets are 180 mm at the low-momentum side and 200 mm at the high-momentum side. The arcs of the fillets can be replaced with step functions with a sufficient number of steps, if necessary. Length of the Rose shims is 54 mm from the bottom end of the fillets and thickness is 1 mm. The pole piece should be made of one piece of low carbon magnetic iron.

Results of magnetic field calculations are shown in Figs. 4 and 5 for typical magnetic field strength of  $B=1.6$  T and  $B=0.38$  T, respectively. The ripples in the curves rep-

resent uncertainty in the finite element calculations and are smaller than  $10^{-4}$ .

The high-field calculation is made for a current of  $1.3 \times 10^5$  A·turns. Saturation effect at this magnetic field is 3%.

The homogeneity of the magnetic field is found to be as small as  $\Delta B/B = 2 \times 10^{-4}$  in the region of  $r = \rho \pm 400$  mm, where  $\rho = 4400$  mm.

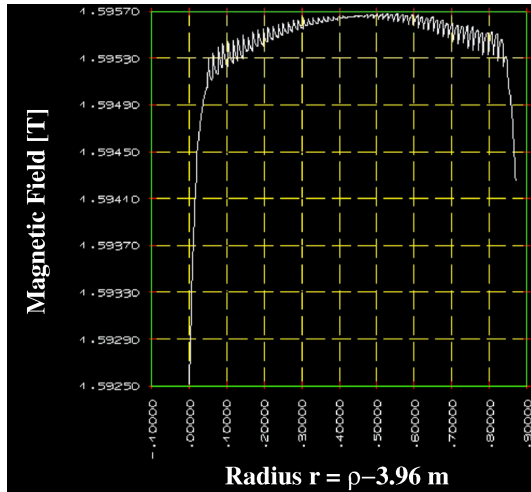


Figure 4. Results of magnetic field calculations for high-field of  $B=1.6$  T.

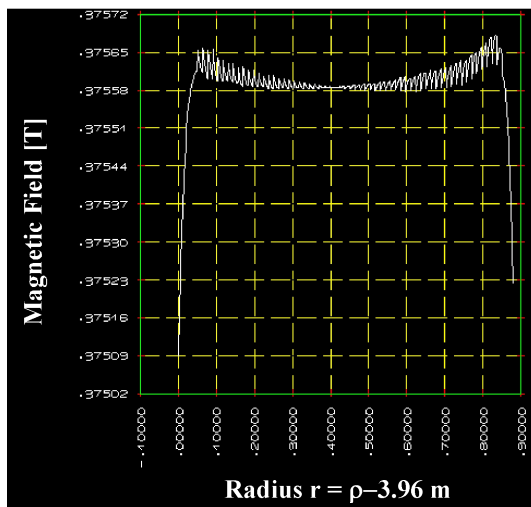


Figure 5. Results of magnetic field calculations for low field of  $B=0.38$  T.

The Rogowski profile is introduced to entrance and exit edges of the D2 magnet. Field clamps are also placed at both edges.

### 3. Coil design

Excitation of the magnet up to  $B = 1.55$  T requires magnetomotive force of  $\sim 2.6 \times 10^5$  A·turns. On the other hand, an expected pressure drop of the cooling water is 5 atm at the RIBF experimental hall. The temperature increase should be kept less than  $30^\circ\text{C}$  under this condition. A circumference of the coil winding is about 14 m. The coil

will be designed to fulfill these required specifications. The preliminary designed coil assumed in the above considerations is wound using a hollow conductor with a square cross section of  $26 \times 26$  mm<sup>2</sup> and a water cooling channel of 16 mm in diameter. The coil consists of four pancakes with 16 windings for each. The cross section of the whole coil unit is  $219 \times 228$  mm<sup>2</sup> including insulating materials.

### 4. Conclusions

We have studied the design of the dipole magnet D2. The design of the magnet will be completed by making small modifications proposed by a manufacturer. The construction of D2 will be completed in FY2006.

### References

- [1] T. Uesaka *et al.*, CNS Annual Report 2005 (2006) 61.
- [2] T. Ichihara *et al.*, Nucl. Phys. A **569** (1994) 287c.
- [3] , G. P. Berg, Design Study of a New Dipole Magnet D2 for the SHARAQ Spectrometer, *unpublished*, 2005.

## Status of CNS GRAPE

E. Ideguchi, S. Shimoura, H. Baba<sup>a</sup>, T. Fukuchi<sup>b</sup>, M. Kurokawa<sup>a</sup>, M. Liu, S. Michimasa<sup>a</sup>, M. Niikura, S. Ota, Y. Zheng, and H. Sakai<sup>c</sup>

*Center for Nuclear Study, Graduate School of Science, the University of Tokyo*

<sup>a</sup>*The Institute of Physical and Chemical Research (RIKEN)*

<sup>b</sup>*Department of Physics, Rikkyo University*

<sup>c</sup>*Department of Physics, the University of Tokyo*

Since year 2000, we have been developing a position sensitive germanium (Ge) detector array, CNS GRAPE (**G**amma-**R**ay detector **A**rray with **P**osition and **E**nergy sensitivity) for high-resolution in-beam gamma-ray spectroscopy using RI beams. In order to correct for the Doppler broadening effect from the fast moving reaction products, the array was designed to have position sensitivities in the Ge crystal by using the pulse shape analysis techniques. The total array consists of 18 detectors and each of which contains two Ge planar crystals with effective radius of 3 cm and thickness of 2 cm. The outer side of each crystal has  $3 \times 3$  electrodes [1]. The planar structure and the segmenting electrodes bring us different pulse shapes depending on the depth of interaction. The resolution of less than 1% for  $v/c = 0.3$  can be achieved after Doppler shift correction. The total efficiency of 5 % for 1 MeV gamma ray is expected.

In this year we have performed following physics experiments and developments.

- $\beta$  decay studies of neutron-rich nuclei ( $^{17}\text{B}$ ,  $^{19,20}\text{C}$ ,  $^{23,24}\text{O}$ ,  $^{21,22}\text{N}$ ) [2]. In the measurement CNS GRAPE was placed by turning  $90^\circ$  relative to the beam direction from the usual setting in order to cover the  $\pm 20^\circ$  and  $\pm 160^\circ$  relative to the beam direction. In front of each Ge detector of GRAPE, a plastic scintillator was placed to veto the  $\beta$ -ray signals. In addition to the GRAPE, two Clover Ge detectors [3] with BGO anti-Compton shield were placed at  $90^\circ$ .
- A lifetime measurement of first  $2^+$  state in  $^{32}\text{Mg}$  by using Recoil Distance Method [4]. In the measurement 6 Ge detectors of CNS GRAPE were used combining with 14 BGO detectors placed upstream and downstream of the GRAPE for the Compton suppression.
- An excitation function measurement by the  $^{19}\text{F} + ^{96}\text{Zr}$  reaction [5]. Two Ge detectors of CNS GRAPE and one coaxial Ge detector were placed at  $120^\circ$  and  $90^\circ$  relative to the beam direction, respectively. In the measurement a Si Ball, a  $4\pi$  array of Si detectors [6] was used in order to detect evaporated charged-particles in coincidence with  $\gamma$  rays.
- In-beam  $\gamma$ -ray measurement by the fusion reaction of neutron-rich beam  $^{46}\text{Ar}$  with  $^9\text{Be}$  target was performed in order to investigate high-spin states in neutron-rich Ca and Ti isotopes [7]. In this measure-

ment the full set of CNS GRAPE with 2 Clover Ge detectors and a coaxial Ge detector were used.

- Gamma-ray imaging capability by using CNS GRAPE was examined [8].
- R&D of CdTe detector was performed for a future  $\gamma$ -ray detector array [9].
- A Si-Barrel array was developed for the detection of evaporated charged particles in the fusion reaction of RI beam. The array consists of 15 Si detectors and the size of each Si detector is  $48 \text{ mm} \times 48 \text{ mm}$  with  $450 \mu\text{m}$  thickness as shown in Fig. 1. These detectors were arranged in 3 rings with forming pentagonal barrel shape. This auxiliary detector was used in the  $^{46}\text{Ar} + ^9\text{Be}$  experiment together with CNS GRAPE.

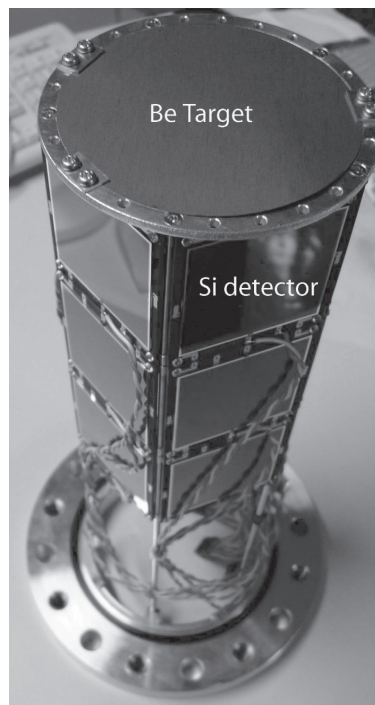


Figure 1. Si-Barrel array with  $^9\text{Be}$  target.

In 2006, we plan to perform the following physics experiments and detector developments.

- A measurement of Gamow-Teller transition strength by the  $(d, ^2\text{He})$  reaction.

- Multiple Coulomb excitation measurement to investigate oblate collective excitations.
- In-beam  $\gamma$ -ray spectroscopy in  $A\sim 100$ ,  $Z\sim 50$  region.
- Construction of a test bench for BGO shield and performance evaluation of the prototype BGO shield.
- R&D of the digital signal processing and analysis system for the three-dimensional position determination.

## References

- [1] S. Shimoura, Nucl. Instrum. Methods A **525** (2004) 188.
- [2] T.K. Onishi *et al.*, CNS Annual Report 2005 (2006) 39.
- [3] G. Duchene *et al.*, Nucl. Instrum. Methods A **432** (1999) 90.
- [4] M.K. Suzuki *et al.*, CNS Annual Report 2005 (2006) 35.
- [5] Y. Zheng *et al.*, CNS Annual Report 2005 (2006) 12.
- [6] T. Kuroyanagi *et al.*, Nucl. Instrum. Methods A **316** (1992) 289.
- [7] M. Niikura *et al.*, CNS Annual Report 2005 (2006) 29.
- [8] Y. Zheng *et al.*, CNS Annual Report 2005 (2006) 69.
- [9] T. Moriguchi *et al.*, CNS Annual Report 2005 (2006) 75.

# Gamma-Ray Imaging Analysis by Using CNS GRAPE

Y. Zheng, E. Ideguchi, H. Baba<sup>a</sup>, T. Fukuchi<sup>b</sup>, M. Kurokawa<sup>a</sup>, M. Liu, S. Michimasa<sup>a</sup>, M. Niikura, S. Ota, and S. Shimoura

Center for Nuclear Study, Graduate School of Science, University of Tokyo

<sup>a</sup>RIKEN(The Institute of Physical and Chemical Research)

<sup>b</sup>Department of Physics, Rikkyo University

## 1. Introduction

Gamma-ray imaging technique allows to locate the invisible radioactive material and has important applications in nuclear medicine [1] and astrophysics [2]. The technique requires detectors with high position sensitivity to determine the three-dimensional location of the gamma-ray interaction point in the detector. CNS GRAPE [3] consists of an array of segmented planar Ge detectors and the interaction point in the Ge crystal can be deduced based on the pulse shape analysis. This capability opens up the possibility of gamma-ray imaging.

In order to examine the imaging capability of GRAPE, we performed the gamma-ray measurement with a standard source of <sup>22</sup>Na to extract the source position by gamma-ray imaging analysis. The two 0.511 MeV annihilation gamma-rays emitted simultaneously in opposite directions from the <sup>22</sup>Na source may be both detected by GRAPE. The location of the <sup>22</sup>Na source is reconstructed, by combining the directional information of the detected positron annihilation lines. In this report, the preliminary result of the gamma-ray imaging analysis is presented.

## 2. Measurement

In the measurement, GRAPE was comprised of 17 Ge detectors, surrounding a target cell in which the source was located. Fig. 1 shows a schematic view of the GRAPE system together with the target cell. A coordinate system ( $x', y', z'$ ) is used to represent the position of the detectors and the <sup>22</sup>Na source. The  $x'$  and  $z'$  directions are shown in Fig. 1 and the  $y'$  direction is perpendicular to  $x'$  and  $z'$  and the origin is the center of the GRAPE system. The source was placed at two positions in the target cell as marked in Fig. 1 during the measurement. The distance of the two positions along the  $z'$  direction is 8 mm. (By taking the source thickness (2 mm) into consideration, the difference of the two positions of the <sup>22</sup>Na source along the  $z'$  direction is about 6 mm.)

A total of  $2 \times 10^5$  positron annihilation single-hit events was obtained and used for analysis. Here, single-hit means only one segment of the detector was fired.

## 3. Analysis and Result

Fig. 2 shows a schematic view of a segmented Ge detector of GRAPE. Here we use the coordinate system ( $x, y, z$ ) to represent interaction position within the detector. The rise times of the signals from different segments contain information on the interaction position. The net charge signal and the total signal are used for pulse shape analysis [4] to

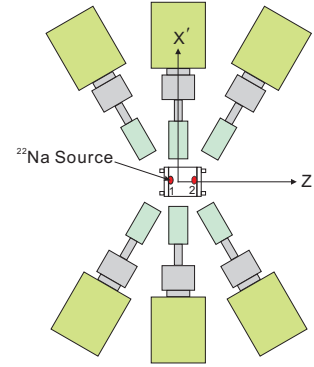


Figure 1. Schematic view of GRAPE together with the target cell. The two locations of the <sup>22</sup>Na source are marked in the figure.

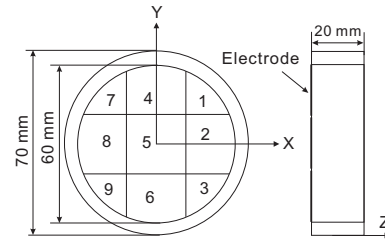


Figure 2. Schematic view of the GRAPE detector. Numbers are given to identify the segments.

extract the depth of the interaction point ( $z$ ). The net charge signal is the signal from the segment including the interaction point and the total signal is the analog summation of the signals from all the nine segments. The depth of interaction points can be extracted by using two kinds of zero-cross timings,  $T_{hit}$  and  $T_{sum}$  picked up after  $CR^2 - RC^4$  shaping of the net charge signal and total signal, respectively. Calculations have been performed for the center-, side-, and corner segment [5]. Fig. 3 shows the result of the simulations calculated in 1 mm steps from  $z = 0$  mm to  $z = 20$  mm for different interaction positions.

Experimentally obtained  $T_{sum} - (T_{hit} - T_{sum})$  values are also plotted in Fig. 4. By comparing these two plots, the depth of interaction of each event was extracted. The resolution for the  $z$  coordinate of the interaction point based on the pulse shape analysis is expected to be 1 – 2 mm. The other two coordinates ( $x$  and  $y$ ) of the interaction point was determined based on the size of each segment. The resolution for these two coordinates thus has the same order of magnitude of the size of the segment (20 mm). For each positron annihilation event, a pair of 3D interaction positions were obtained and the track line of the annihilation

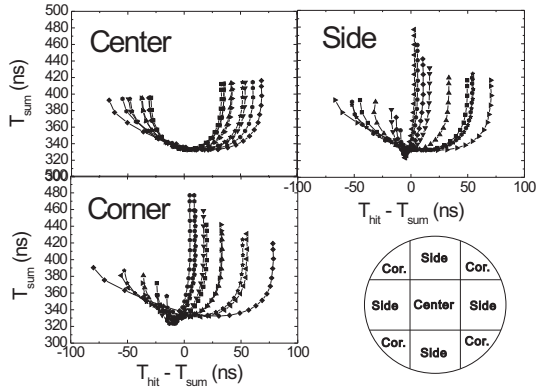


Figure 3. Simulation result for the zero-cross times of center-, side-, and corner segment for different interaction points. The dots in a line from the left to the right are related to  $z$  values from 0 to 20 mm in 1 mm steps.

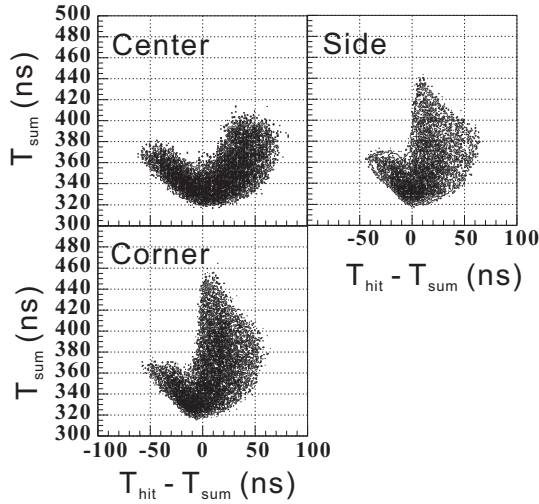


Figure 4. Zero-cross time of the total signal ( $T_{sum}$ ) is plotted against that of the net charge signal ( $T_{hit}$ ) minus  $T_{sum}$  for a center-, side-, and corner segment based on the data from pulse shape analysis.

gamma-rays was then reconstructed.

Ideally, track lines of the annihilation gamma-rays intersect each other at the source position. However, due to the resolution of the interaction position, these track lines reconstructed by GRAPE might not intersect each other spatially. In that case, we assume the source locate at the center of the distance between two of the track lines. Fig. 5 shows the  $z'$  projection of the result of the gamma-ray imaging analysis. We can clearly see two peaks at  $z' = 2.78$  mm with a  $\sigma$  value of 1.35 mm and  $z' = 8.55$  mm with a  $\sigma$  value of 1.21 mm respectively in the figure, indicating the two locations of the  $^{22}\text{Na}$  source along the  $z'$  direction. The difference of the two peak values is 5.77 mm. It is consistent with the expected value (about 6 mm). From the result, an average resolution of 1.28 mm is obtained for the  $z'$  coordinate of the source location. Here, we use only the detectors which are perpendicular to the  $z'$  direction. We have also obtained the result with all detectors. It gives the corresponding location value as 2.6 mm and 8.2 mm, respectively, with an average resolution of 2.8 mm. The

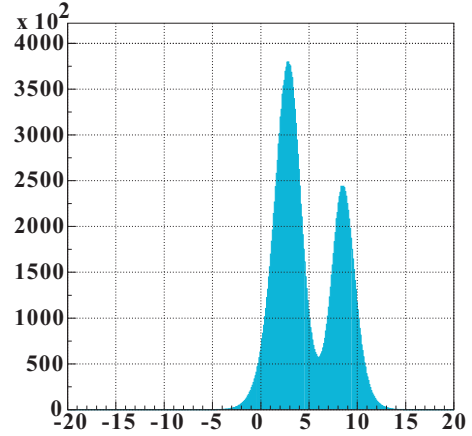


Figure 5. Projection of the gamma-ray imaging result on the  $z'$  direction (mm). Only the detectors perpendicular to the  $z'$  direction were used.

position resolution here is more than twice worse than the previous value (1.28 mm). This is because in this case the  $z'$  coordinate of the source position is more related to the  $x$  and  $y$  coordinates of the interaction point within the detector which have the resolution equivalent to the size of the segment.

In summary, we have extracted the  $z'$  coordinate of the source position with an average resolution of 1.28 mm using the detectors which are perpendicular to the  $z'$  direction. To determine the other two coordinates ( $x'$  and  $y'$ ), pulse shape analysis to gain a position sensitivity finer than the segment size is now in progress.

## References

- [1] C.M. Tempany *et al.*, Journal of the American Medical Association **285** (2001) 562.
- [2] G.F. Bignami, Science **22** **298** (November 2002) 1560.
- [3] S. Shimoura, Nucl. Instrum. Methods A **525** (2004) 188.
- [4] Th. Kröll *et al.*, Nucl. Instrum Methods A **463** (2001) 227.
- [5] M. Kurokawa *et al.*, IEEE Trans. Nucl. Sci. **50** (2003) 1309.

# Development of Liquid Nitrogen-Cooled Gas Target System

H. Yamaguchi, S. Kubono, G. Amadio, Y. Wakabayashi, A. Saito, J. J. He, and H. Fujikawa

*Center for Nuclear Study, Graduate School of Science, University of Tokyo*

## 1. Introduction

Light-ion gas targets ( $H_2$ ,  $D_2$ ,  $^3He$ ,  $^4He$  etc.) are often used for the RI beam production at CRIB (CNS Radio Isotope Beam separator) [2, 3, 4]. For holding the gas, water-cooled gas cells have been used at CRIB. The water-cooled gas cells are 20–80 mm long, and they have  $2.2 \mu\text{m}$ -thick Havar foils for the beam windows. To obtain a more intense RI beam for low-cross section measurements, it is desirable to make the gas target thicker. However, the gas cell cannot be elongated much more than the current length of 80 mm, since the edges of the target will be more distant from the focal position, which should make the collection efficiency significantly worse. We have also experienced that the foils of the water-cooled gas target were broken by high power beams. For example, an irradiation of  $^{40}\text{Ar}$  beam of 4.5 MeV of 200 pA, which deposited heat of about 16 W on the target, broke the foils immediately.

To solve these problems, we have constructed a low-temperature gas target system for CRIB. The design and preliminary beam test of the new gas target system are described below.

## 2. Design

The main features of the new gas target system are as the following.

### 1. Liquid-nitrogen cooling

The target gas is cooled by liquid nitrogen. If the target is ideally cooled to near the liquid nitrogen temperature (77K), it can be 3–4 times thicker compared to the room temperature target. Low temperature is also good for having a stability against high power beams. The new target is expected to be durable with the beams of 100 W order.

### 2. Forced gas flow

We made a flow of the target gas, so that the heated gas goes out of the target, while the cooled gas comes into the target again. We know there is an effect of the target pressure reduction depending on the beam intensity. That is, when the beam is intense (heat deposit is more than 10 mW/mm), the gas only around the beam track is heated up and effective thickness of the target decreases [5]. Although the velocity of the molecule is quite high (order of 1000 m/s for relatively light gases), we may avoid the pressure-reduction effect to some extent, by making the gas flow.

### 3. Oxygen concentration monitoring

As we circulate hydrogen gas in an enclosed system, we have to concern the possibility of the explosion, which may happen if the air leaks into the gas sys-

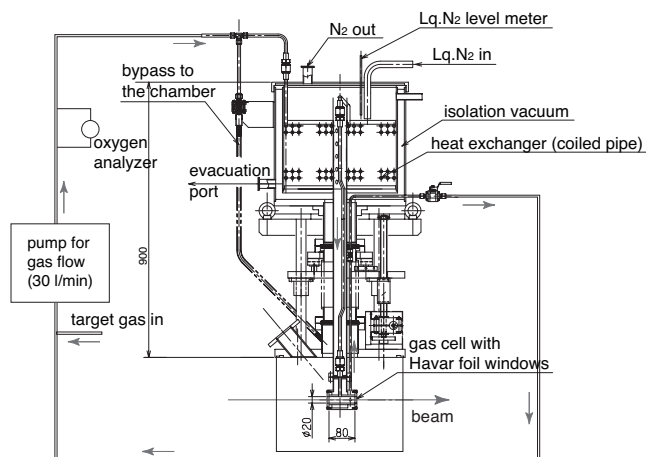


Figure 1. Design of the low-temperature gas target system.

tem. The lower and higher explosive limits of hydrogen are 4.1% and 74.8%, when expressed by the concentration by volume on air. Therefore, we have to keep the concentration of the hydrogen higher than 74.8%, or equivalently, the concentration of oxygen must be lower than 5%. We have installed an oxygen analyzer for monitoring the concentration during the run.

Fig. 1 shows the whole structure of our system. The target gas cell, shown at the bottom of the figure in a vacuum chamber, is similar to the water-cooled one. It is 80 mm-long, and it has a 20 mm-diameter cylindrical hole to keep the gas inside. On the beam direction sides of the cell, flanges with Havar foils were attached and sealed using indium wires.

Above the target cell, there is a dewar-type vessel (here we refer to it as “top dewar”) filled with liquid nitrogen, in order to cool the target gas. The liquid nitrogen is supplied from a 120-liter self-pressurized bottle, which can be easily disconnected from the system for refilling. There is a liquid-nitrogen level meter in the top dewar, and if the level goes down below a limit, an automatic valve lets the liquid nitrogen in, to keep the level almost constant. The liquid nitrogen also goes into the duct connected to the gas cell and cools the cell directly.

There is a gas circulation line through the target cell and the top dewar, most of which consists of 3/8-inch diameter pipes. The target gas can be injected to the circulation line using a gas system, having valves for controlling the injection speed, and a Baratron gauge for the gas pressure monitoring. A diaphragm pump (Iwaki APN-P450NST) was installed in the line for making a gas flow of 30 l/m (80 l/m was possible for hydrogen gas) There is a heat exchanger (coiled-pipe type) in the top dewar, and the injected room-

temperature gas is cooled down to 77K, as the gas passes through the heat exchanger. The cooled gas is transmitted along the vertical duct, and reaches at the cell. The gas is heated by the beam in the cell, and soon it goes out of the vacuum chamber. Since the pump cannot circulate low-temperature gas, the gas must be warmed up before entering the circulation pump again. To keep the gas temperature close to the room temperature, a heat bath was installed. In case the measured gas temperature is low (lower than 0 °C), the heater is turned on and it warms up the gas to the room temperature. However, when we used hydrogen gas at 600 Torr with the flow rate of 30 l/m or less, the gas was already warmed up to the room temperature in the long line from the vacuum chamber to the water bath.

An oxygen analyzer (GE sensing Japan Co. Ltd, O2X1 with OX-3) is installed in a sideline of the circulation system, and it monitors concentration of oxygen in the gas all during the run.

### 3. Test with the beam

We have performed two preliminary test experiments so far, and obtained the following results.

The consumption rate of the liquid nitrogen was about 200 l/day when there is no gas circulation and the beam current is much less than 1W. The consumption was several times higher than that when circulation was 40 l/min, however, the rate was not measured precisely. The theoretical consumption rate is 2.0 l/h (48 l/day) per flow rate of 10 l/min. The actual large consumption is supposed to be due to the heat loss from the top dewar, as the material of the cover is heat-conducting (SUS). We are planning to cover it with some thermal-insulating materials.

The primary beam used in the test runs is 3.4 MeV/u  ${}^7\text{Li}^{2+}$ , 3 e $\mu$ A at maximum. The cooled target worked stably with this maximum current, which proves that the target can accept the heat load of 5 W.

Gas thickness was evaluated by comparing the measured energy loss of the  ${}^7\text{Li}$  beam with a calculation, since the gas temperature inside the cell was not known precisely. At the first test, we used hydrogen gas of 300 Torr and the obtained gas thickness was 0.3 mg/cm<sup>2</sup>. The corresponding temperature calculated from this thickness was 200 K. In this first test, we could not make a good gas circulation, indicating that there was a problem in the gas system. For example, a choking of the pipe by some frozen materials might prevented the good circulation and cooling. In the second test, we used hydrogen gas of 600 Torr, and the gas thickness was 1.9 mg/cm<sup>2</sup>. The thickness was not changed for the different circulation rates of 0 l/min and 40 l/min. The corresponding temperature was 80K, which was fairly close to the liquid-nitrogen temperature.

The produced secondary beam was  ${}^7\text{Be}^{4+}$  of about 2.5 MeV/u. Beam separation was carried out by selecting the magnetic rigidity of the beam. When we adjusted the magnetic rigidity to the value of  ${}^7\text{Be}^{4+}$ , the contamination from the primary beam ( ${}^7\text{Li}^{3+}$ ) was still dominant, and the purity of  ${}^7\text{Be}^{4+}$  was 3–5%. To improve the beam purity, we put in degraders just after the momentum dispersive focal

Degrader	Purity	Beam width (mm)
no degrader	3%	6.0
2 $\mu$ m Mylar	90%	8.7
3 $\mu$ m Mylar	$\sim$ 100%	17

Table 1. Purity and width of the secondary beam,  ${}^7\text{Be}$ , with different degrader settings. The target thickness was 1.9 mg/cm<sup>2</sup>. Beam width is the horizontal width of the secondary beam at F2 focal plane, denoted as the root mean square width in mm.

plane (F1) of CRIB. The results are summarized in Table 1. Using the thin Mylar foils, we can separate the two beams, as the energy losses in the foil are different for the two.

A  ${}^7\text{Be}^{4+}$  beam of  $1 \times 10^6$  pps was obtained at the first test, when the primary beam current was 1.1 e $\mu$ A. At the second test, the beam rate was  $10^5$  pps order even with a higher primary beam current of 3 e $\mu$ A. The low rate was possibly due to a large momentum dispersion at F1, which might be caused by the energy straggling in the target. The expected momentum dispersion from the calculation was  $\pm$  9%, but our measurement shows the real dispersion was much more than 10%, and it could not be determined.

In a near future, we expect to have a  ${}^7\text{Be}$  beam of the order of  $10^7$  pps, by optimizing the beam and target condition.

### References

- [1] T. Teranishi *et al.*, CNS Annual Report 2003 (2004) 81.
- [2] S. Kubono *et al.*, Eur. Phys. J. A **13** (2002) 217.
- [3] Y. Yanagisawa *et al.*, Nucl. Instrum. Methods Phys. Res., Sect. A **539** (2005) 74.
- [4] T. Teranishi *et al.*, Phys. Lett. B **556** (2003) 27.
- [5] J. Goerres *et al.*, Nucl. Instrum. Methods **177** (1980) 295.
- [6] J. F. Ziegler, *et al.*, "The Stopping and Range of Ions in Solids" Pergamon Press, New York (1985)

# *d-p* Elastic Scattering Measurement at Internal Target Station of Nuclotron

K. Suda, T. Uesaka, V. P. Ladygin<sup>a</sup>, T. Kawabata, Y. Maeda, K. Itoh<sup>b</sup>, S. Sakaguchi, Y. Sasamoto, H. Sakai<sup>c</sup>, K. Sekiguchi<sup>d</sup>, P. K. Kurilkin<sup>a</sup>, Yu. V. Gurchin<sup>a</sup>, A. Yu. Isupov<sup>a</sup>, M. Janek<sup>a,e</sup>, J. T. Karachuk<sup>a,f</sup>, A. N. Khrenov<sup>a</sup>, A. S. Kiselev<sup>a</sup>, V. A. Kizka<sup>a</sup>, J. Kliman<sup>a,g</sup>, V. A. Krasnov<sup>a</sup>, A. N. Livanov<sup>a</sup>, A. I. Malakhov<sup>a</sup>, V. Matoucek<sup>g</sup>, M. Morhac<sup>g</sup>, S. M. Piyadin<sup>a</sup>, S. G. Reznikov<sup>a</sup>, I. Turzo<sup>g</sup>, and T. A. Vasiliev<sup>a</sup>

*Center for Nuclear Study, Graduate School of Science, University of Tokyo*

<sup>a</sup>*Joint Institute for Nuclear Research, Russia*

<sup>b</sup>*Department of Physics, Saitama University*

<sup>c</sup>*Department of Physics, University of Tokyo*

<sup>d</sup>*RIKEN (The Institute of Physical and Chemical Research)*

<sup>e</sup>*P. J. Šafárik University, Slovakia*

<sup>f</sup>*Advanced Research Institute for Electrical Engineering, Romania*

<sup>g</sup>*Institute of Physics Slovak Academy of Sciences, Slovakia*

<sup>h</sup>*University of Chemical Technology and Metallurgy, Bulgaria*

## 1. Introduction

The high-energy deuteron beam polarimeter based on the *d-p* elastic scattering was constructed at the internal target station (ITS) of the superconducting synchrotron Nuclotron at JINR [1]. The ITS polarimeter will be used for the spin physics programs with polarized deuteron beams at 1.0 – 2.0 GeV. It will also provide the data at 880 MeV, which corresponds to the maximum deuteron beam energy at RIBF in Japan. Therefore, it is useful for a development of the deuteron beam polarimeter at RIBF. The ITS polarimeter will also be a unique tool to study the three-nucleon forces at 300 – 800 MeV emphasizing the energy dependence of the reaction.

At the energy region 0.88 – 2.0 GeV, analyzing powers for the *d-p* elastic scattering are expected to be large at backward angles ( $\theta_{c.m.} > 70^\circ$ ). The expectation is based on the similarity in the analyzing power distributions expressed by the mandelstam variable  $t$  from the existing data at 1.2, 1.6, and 2.0 GeV [2, 3, 4, 5], which is called  $t$ -scaling. The calibration measurement of analyzing powers was necessary in order to determine precise beam polarizations at these energies. In this report, we describe the calibration measurement with polarized beams performed in June, 2005.

## 2. Experiment

Measurement of the analyzing powers for the *d-p* elastic scattering by using the ITS polarimeter was performed at 880 MeV and 2 GeV at JINR. The beam polarizations were measured using the polarimeter at 270 MeV, where the absolute calibration of the analyzing powers was performed at RIKEN [6]. The vector and tensor polarized deuteron beams were provided by the cryogenic atomic beam source POLARIS. Two modes of vector and tensor polarizations were used as well as unpolarized mode,  $(P_Z, P_{ZZ}) = (+1/3, 1)$ ,  $(+1/3, -1)$ , and  $(0, 0)$ , where the values are theoretical maxima. Typical beam intensity was  $3 \times 10^7$  particles/spill, and the spill duration was 8 seconds.

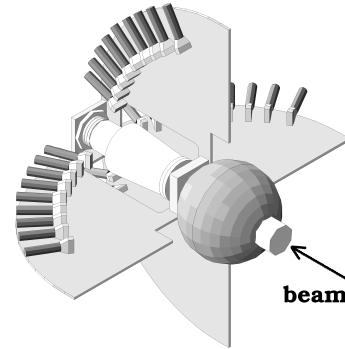


Figure 1. Schematic view of the detector setup.

Figure 1 shows the schematic view of the ITS polarimeter. The ITS is composed of a spherical hull, a beam duct and the target stage where the target holder carrying up 6 different targets is located [7]. A polyethylene sheet of 10  $\mu\text{m}$  thickness was used as a target as well as carbon wires for the background measurement. The scattered deuterons and recoiled protons were detected in kinematical coincidence. Detectors were placed on the detector stage at the downstream of the target. Each detector consisted of a plastic scintillation counter coupled to a photomultiplier tube through a light guide. Nine proton detectors were placed in the directions of left, right, and up, at c.m.s. scattering angles ranging from  $60^\circ$  –  $140^\circ$ , while only four detectors in the down direction ranging from  $110^\circ$  –  $140^\circ$  because the lower flange of the hull limited the acceptance. Corresponding to the proton detectors, three segmented deuteron detectors were placed in the directions of left, right, and down, and one detector in the up direction only for the backward angles, except that the down detector at the most forward angle was not placed due to the conflict of the PMTs. Instead of it, one of the proton detectors were used to detect deuterons.

The quasi-elastic *p-p* scattering was used to monitor relative luminosity. Two detectors were placed in the directions of left and right at  $\theta_{c.m.} = 90^\circ$ , where the vector analyzing

power vanishes.

At each spill, the target was swept from the high- to low momentum sides of the Nuclotron. When the beams pass through the target, its energy decreases, and its orbital radius in the Nuclotron ring decreases. Consequently, the interaction point shifts along the target position by about 4–7 mm, which causes a false asymmetry of the scattering. In order to estimate this effect, the target position was monitored by counting the number of pulses transmitted to the step motor attached to the target holder.

### 3. Analysis

The data at 880 MeV were analyzed. The events of the  $d$ - $p$  elastic scattering were clearly identified by energy losses and a difference of time of flights of deuterons and protons. Figure 2 shows a spectrum of time difference between deuteron and proton detectors obtained for the polyethylene target. A peak corresponding to the  $d$ - $p$  elastic scattering was clearly observed. The carbon contribution was found to be not negligible at this energy. Therefore, the yield for the carbon was subtracted from that for the polyethylene. The events were selected by a narrow gate indicated in Fig. 2 in order to increase the S/N ratio. Figure 3 shows an energy loss correlation between deuteron and proton, gated by the time difference. A clear locus corresponding to the  $d$ - $p$  elastic scattering was observed, and the region indicated by a dashed line was selected. No cuts of the target position were applied for the present analysis. The analyzing powers at 880 MeV were obtained from the asymmetries of yields and the beam polarizations obtained at 270 MeV.

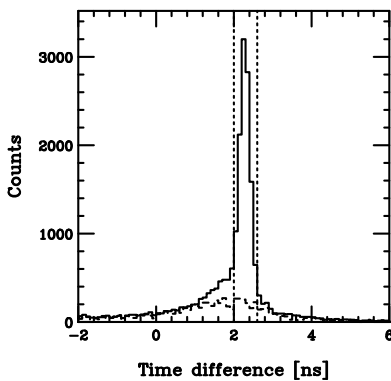


Figure 2. Time difference between deuteron and proton detectors. The solid line shows a spectrum for the polyethylene target, and dashed line for the carbon. The  $d$ - $p$  elastic scattering events are selected by dotted lines.

### 4. Results

The preliminary results of the analyzing powers for the  $d$ - $p$  elastic scattering at 880 MeV are shown in Fig. 4. Only statistical errors are shown. The  $A_y$  has moderately large values ( $\sim -0.3$ ) at the wide angular range  $\theta_{c.m.} = 70^\circ$ – $140^\circ$ , and follows the  $t$  scaling. However, the  $A_{yy}$  is large only at  $\theta_{c.m.} = 60^\circ$ , and deviates from the  $t$  scaling. This indicates that the vector and tensor polarizations should be measured at two different angles.

The obtained data at 880 MeV will be useful to con-

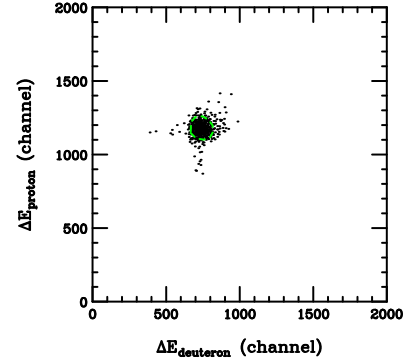


Figure 3. Energy loss correlation of deuteron and proton detectors gated by the time difference. A locus corresponding to the  $d$ - $p$  elastic scattering can be seen clearly.

struct a new polarimeter at RIBF. Analysis for 2 GeV is in progress.

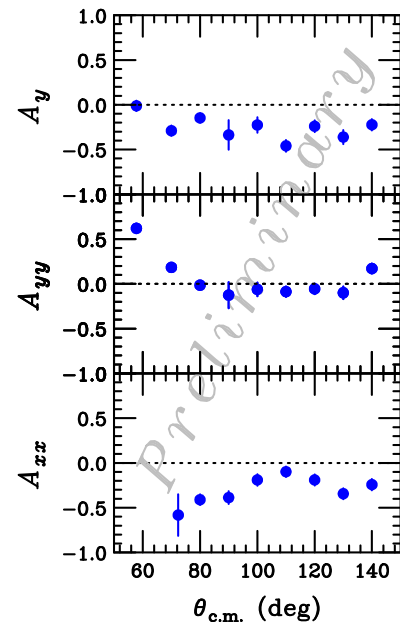


Figure 4. The analyzing powers for the  $d$ - $p$  elastic scattering at  $E_d = 880$  MeV. Only statistical errors are shown.

### References

- [1] T. Uesaka *et al.*, CNS Annual Report (2004) 81.
- [2] M. Bleszynski *et al.*, Phys. Lett. B **87** (1979) 178.
- [3] M. Bleszynski *et al.*, Phys. Lett. B **106** (1981) 42.
- [4] M. Haji-Saied *et al.*, Phys. Rev. C **36** (1987) 2010.
- [5] V. Ghazikhanian *et al.*, Phys. Rev. C **43** (1991) 1532.
- [6] K. Suda *et al.*, RIKEN Accel. Prog. Rep. **35** (2002) 174.
- [7] A. I. Malakhov *et al.*, Nucl. Instrum. Methods A **440** (2000) 320.

# Digital Pulse Shape Analysis of Thick CdTe Detectors

T. Moriguchi<sup>a</sup>, T. Hoya<sup>a</sup>, M. Niikura, S. Ota, H. Baba<sup>b</sup>, T. Fukuchi<sup>c</sup>, E. Ideguchi and S. Shimoura

Center for Nuclear Study, Graduate School of Science, University of Tokyo

<sup>a</sup>Institute of Physics, University of Tsukuba

<sup>b</sup>RIKEN (The Institute of Physical and Chemical Research)

<sup>c</sup>Department of Physics, Osaka University

## 1. Introduction

We have been developing planar-type gamma-ray detectors with Cadmium Telluride (CdTe). CdTe has high efficiency for photo-electric absorption of gamma-rays because of the large atomic number ( $Z_{\text{Cd}} = 48$ ,  $Z_{\text{Te}} = 52$ ). It is also possible for the CdTe detectors to use without cooling because of a large band-gap (1.52 eV) which is larger than Silicon (see Table. 1). Since the mobility of charge carriers is small especially for holes, however, charge collection is very sensitive to the trapping effect due to the defects in a crystal. Since the trapping effects result characteristic pulse shapes, pulse shape analysis may be used for their correction. Actually, fast-slow analog pulse shape method provided a possible correction [2]. As an alternative and quantitative method, we performed digital pulse shape analysis of pulse-shape data recorded using flash ADCs.

	CdTe	Ge	Si
Atomic number $Z$	48/52	32	14
Density [g/cm <sup>3</sup> ]	6.02	5.33	2.33
Energy gap [eV]	1.52	0.72	1.12
Average energy per electron-hole pair [eV]	4.43	2.98	3.61
Electron mobility [cm <sup>2</sup> /Vs]	800~1100	3900	1350
Hole mobility [cm <sup>2</sup> /Vs]	50~100	1900	480

Table 1. Some physical properties of CdTe, Ge and Si. [1]

## 2. Model

The shape of charge pulse ( $Q(t)$ ) induced in the electrode depends on the initial charge ( $Q_0$ ), drift velocities of charge carriers ( $v_e$ ,  $v_h$ ), and amounts of trapping effects which may be characterized by life time ( $\tau_e, \tau_h$ ) [3]. The drift velocity is determined by the mobility and the electric field. For a planar-type detector of infinite size of electrodes, explicit expression is:

$$Q(t) = \frac{Q_0}{D} \left( v_e \tau_e \left( 1 - \exp\left(-\frac{t}{\tau_e}\right) \right) + v_h \tau_h \left( 1 - \exp\left(-\frac{t}{\tau_h}\right) \right) \right) \quad (1)$$

$$t_e = \min(t, x/v_e)$$

$$t_h = \min(t, (D-x)/v_h)$$

where  $x$  and  $D$  are the interaction position from the cathode and the thickness of the detector, respectively. The following discussion, we assume  $\tau_e = \tau_h = \tau$ , because of  $\mu_e \tau_e / \mu_h \tau_h \sim \mu_e / \mu_h \sim 10$ , where  $\mu_e$  and  $\mu_h$  are mobility of electrons and holes, respectively [4]. Figure. 1 shows pulse shapes of

CdTe calculated by Eq. (1) under the assumption that thickness of crystal is 5-mm and the bias voltage is 700 V. In Fig. 1, the pulse in case A has a fast rise time determined by the electrons with high mobility. On the other hand, the pulse in case D has a slow rise time determined by the holes with low mobility. In general, pulse shapes from the CdTe detectors are a composition of the two extremes, such as pulse shapes in case B and C. The initial charge  $Q_0$  and the interaction position  $x$  can be obtained by the analyzing pulse shapes.

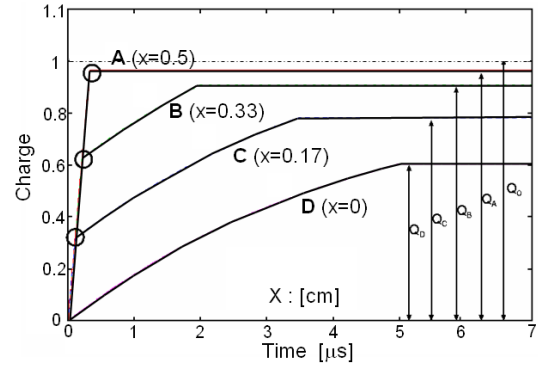


Figure 1. Pulse shape of CdTe by Eq. (1). The open circles are the times that the electrons arrive at anode ( $=x/v_e$ ). A~D correspond to the pulse shapes which have the different  $x$  (see the text in detail).

## 3. Experiment

A planar-type CdTe detectors of 5-mm thick having double-sided strips with guard rings were used (see Fig. 2). In order to identify charge pulses from the central and the edge regions, four strips and three guardrings were connected to extract central and edge pulses, respectively. As shown in Fig. 3, the charge pulse obtained through charge-sensitive preamplifiers (CP-528A) were recorded by flash ADC (XIA Pixie-4). This flash ADC has performances of 75 MHz/14-bit digitizing of input signal. The amplifier (ORTEC 571), the timing SCA (ORTEC 420A), the gate generator (ORTEC 416A) and the attenuator are used for making the trigger pulses. Shapping time of the amplifier was set 6  $\mu\text{s}$  corresponding to the slow rise time for 700-V bias voltage. <sup>137</sup>Cs source was used for the gamma-rays to be detected. About 4500 events were collected which have non-zero induced charge in the strip sums.

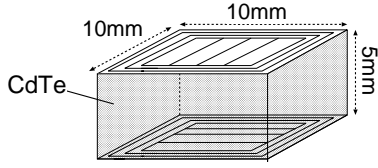


Figure 2. The CdTe detectors (Acrorad Co., Ltd) and the structure of electrodes. There are four strips and three guard rings each of the electrodes.

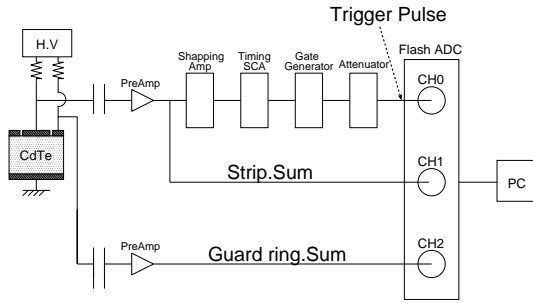


Figure 3. The experimental setup to record pulse shapes from the CdTe detector.

#### 4. Result and Analysis

Figure 4 shows obtained typical pulse shapes. The label “total” denotes the sum of the “central” and “edge” signals, which simulates the pulse shape of planar detector with infinite area corresponding to the model function (Eq. (1)). By  $\chi^2$ -fittings for obtained pulse-shapes, the common parameters were determined to be  $v_e = 1.4 \text{ cm}/\mu\text{s}$ ,  $v_h = 0.15 \text{ cm}/\mu\text{s}$ , and  $\tau = 4.5 \mu\text{s}$ . The parameters  $Q_0$  and  $x$  was obtained event-by-event by the fitting. Figure 5 shows: (a)  $x$  versus non-corrected charge  $Q(t = \infty)$ , and (b)  $x$  versus  $Q_0$ . It is shown that  $Q_0$  are almost constant for the full-energy peak (662 keV) independent of  $x$ . The projection spectra for the two are shown in Fig. 6, where the low-energy tail of the full-energy peak in (b) is remarkably smaller than that of (a).

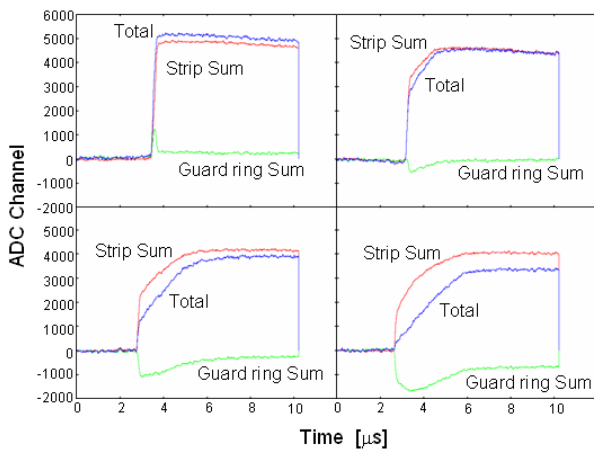


Figure 4. Typical pulse shapes which are an output from the preamplifier.

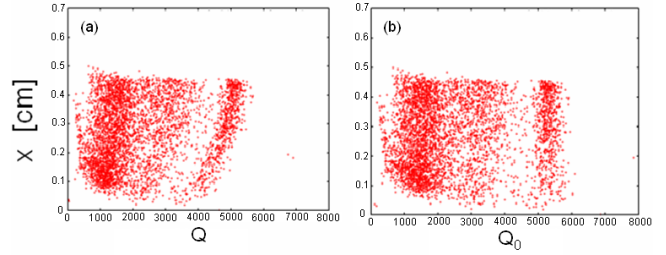


Figure 5. The interaction position  $x$  versus the initial charge  $Q_0$  (a) without correction and (b) with correction.

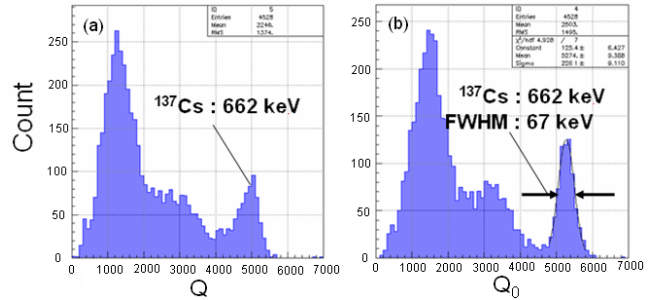


Figure 6. The energy spectrum with a  $^{137}\text{Cs}$  source (a) without correction and (b) with correction.

#### 5. Summary

We have analyzed shapes of charge pulses of a planer-type CdTe detector recorded using 75 MHz/14 bit flash ADCs. The pulse-shape data were fitted by a model function taking into account the differences of the drift velocities of electron and hole and the trapping effects. The results indicate the possibility of using thick CdTe as a position sensitive photon detector. Further quantitative analysis especially for each of “central” and “edge” pulses is in progress in order to evaluate the capability of three dimensional position determination.

#### References

- [1] I. Strzalkowski., S. Joshi and C. R. Crowell, Appl. Phys. Rev. Lett. **28** (1976) 350.
- [2] T. Tamaki *et al.*, CNS Annual Report 2004 (2005) 75.
- [3] K. Hecht, Z. Phys. **77** (1932) 235.
- [4] T. Takahashi *et al.*, SPIE. **3446** (1998) 29.

# Polarized Proton Target Performance During Scattering Experiment

T. Wakui, S. Sakaguchi<sup>a</sup>, T. Kawahara<sup>b</sup>, M. Hatano<sup>c,1</sup>, T. Uesaka<sup>a</sup>, and H. Sakai<sup>c</sup>

*Cyclotron and Radioisotope Center, Tohoku University*

<sup>a</sup> *Center for Nuclear Study, Graduate School of Science, University of Tokyo*

<sup>b</sup> *Department of Physics, Toho University*

<sup>c</sup> *Department of Physics, University of Tokyo*

## 1. Introduction

A polarized solid proton target using a crystal of naphthalene doped with pentacene has been developed for  $\vec{p}$ -RI scattering experiments [1]. The target is unique in that protons can be polarized at a low magnetic field of 0.1 T and a higher temperature of 100 K. This feature enables the target to be used in  $\vec{p}$ -RI scattering experiments under the inverse kinematic condition.

The polarized proton target has been used in scattering experiments with  $^6\text{He}$  beams in July 2003 and in July 2005 at the RIKEN projectile fragment separator (RIPS). In both experiments, the vector analyzing power for the elastic scattering of polarized proton and  $^6\text{He}$  at the energy of 71 MeV/u was measured [2, 3]. In this report, we describe the polarized proton target system and its performance during the scattering experiment in 2005.

## 2. Target system

Protons in the target crystal is polarized by combining methods called “microwave-induced optical nuclear polarization” and “integrated solid effect” [4]. This method requires for the target system to have a magnet for a polarization holding field, a laser for optical excitation, a microwave system and a field sweep system for polarization transfer, and an NMR system for measuring relative value of proton polarization. Figure 1 shows a schematic of the polarized proton target system.

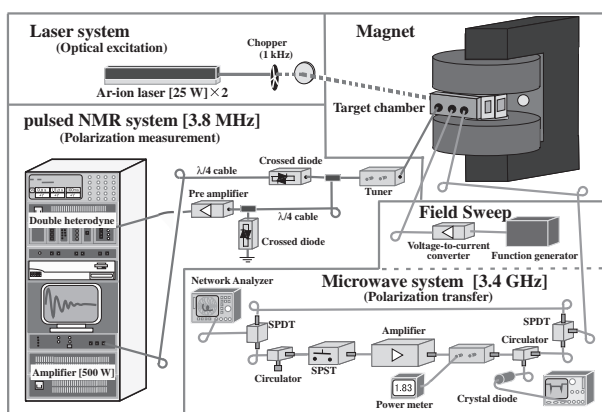


Figure 1. A schematic view of the polarized proton target system.

The system consists of a target chamber, a C-type magnet, two Ar-ion lasers, a microwave system and an NMR spectrometer.

A target crystal is placed in a target chamber which is mounted in a C-type magnet. The magnet produces the

maximum field of 700 mT and a typical operating field during the experiment is 90 mT. The field uniformity is better than 0.2 mT over the target volume. The uniformity is sufficiently smaller than the internal field of 4 mT in the target crystal.

Two Ar-ion lasers are used to excite pentacene molecules in the target crystal. Both lasers have the maximum power of 25 W in the multiline operation mode. The laser beams are pulsed by an optical chopper. Typical repetition rate and pulse width for the optical excitation are 2 kHz and 13  $\mu\text{s}$ , respectively. The resulting average power is 650 mW. The pulsed laser beams are transmitted by using optical fibers to the target system. Typical transmission efficiency is 50%.

The polarization transfer is carried out with the microwave and field sweep systems. The frequency of microwave is 3.4 GHz which corresponds to an ESR frequency of the lowest triplet state of pentacene at 90 mT. The microwaves are pulsed by a SPST switch and amplified by a solid-state amplifier having the maximum output power of 10 W. The amplified microwaves reach the target through a directional coupler and a circulator. The transmitted power to the target is monitored by a power meter attached to the directional coupler with a directivity of 30 dB. The reflected microwaves from the target are detected by a crystal diode connected to the circulator. The detected signal is used to tune the microwave frequency.

The relative value of proton polarization during the scattering experiments is monitored with a pulsed NMR spectrometer. The NMR frequency in 90 mT is 3.8 MHz. RF pulses from the NMR spectrometer pass through a crossed diode and a tuner for impedance matching, and then reach a 35-turn NMR coil. An NMR signal induced in the same NMR coil by RF pulses is passed through the tuner and is amplified with a preamplifier that has a 30 dB gain. The amplified NMR signal is processed with a receiver of double-heterodyne type. Absolute value of proton polarization is calibrated by measuring the analyzing power for  $\vec{p} + ^4\text{He}$  elastic scattering at 80 MeV/u.

## 3. Target performance

The proton polarization history during the experiment in 2005 is shown in Fig. 2. The polarization build-up was started at 0 days without  $^6\text{He}$  beam irradiation. Adjustments for the polarization condition cause a fluctuation of the build-up curve. The maximum proton polarization of 20.4(58)% was obtained just before starting  $^6\text{He}$  beam irradiation at 1.8 days. The average proton polarization during the beam irradiation was 13.8(39)%.

The direction of the proton polarization vector should be

<sup>1</sup>Present address: Central Research Laboratory, Hitachi Ltd.

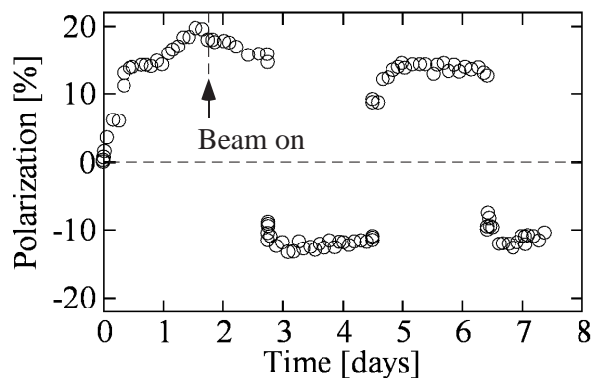


Figure 2. Proton polarization history during the scattering experiment performed in July 2005. The maximum polarization was 20.4(58)%. The polarization decreased due to radiation damage after the  ${}^6\text{He}$  beam irradiation was started at 1.8 days. The polarization direction was reversed three times by using a pulsed NMR method.

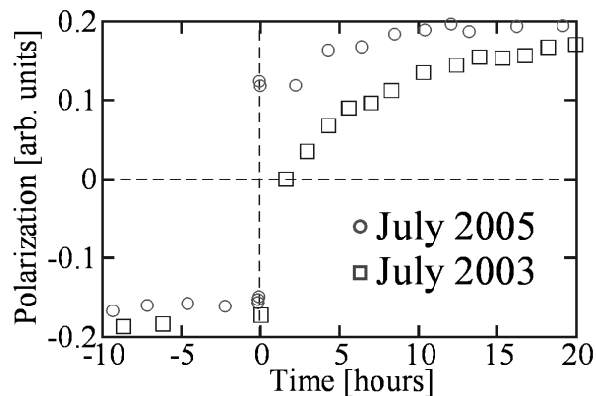


Figure 3. An example of the polarization reversal by using a pulsed NMR method (open circles). The polarization direction was reversed in  $2.2 \mu\text{s}$  with the reversal efficiency of 70%. A result of the polarization reversal by a build-up method is also plotted for comparison (open squares).

reversed to reduce the systematic uncertainties in scattering experiments. In the scattering experiment in 2003, the polarization direction was reversed by build-up to the opposite direction after polarization destruction. This method took approximately 10 hours to recover the polarization. To save the time, we have introduced a new polarization reversal method, the pulsed NMR method [5]. In this method, the polarization vector rotates around the oscillating field applied perpendicular to the external field. The rotation angle depends on the length of time the oscillating field is on,  $t$ , and the strength of the oscillating field. A result of the polarization reversal by the pulsed NMR method in the scattering experiment is shown in Fig. 3. We achieved the polarization reversal in  $t=2.2 \mu\text{s}$  with the reversal efficiency of approximately 70%. By using this method, a scattering experiment can be performed without a long interruption for the polarization build-up.

As can be seen from Fig. 2, the proton polarization de-

creases gradually due to radiation damage after the beam irradiation was started. To estimate the contribution from the radiation damage to the relaxation rate, we measured the relaxation rate before and after the scattering experiment. The relaxation rate measured before the experiment, which corresponds to the intrinsic relaxation rate of the target crystal, was  $0.127(6) \text{ h}^{-1}$  and that measured after the experiment was  $0.295(4) \text{ h}^{-1}$ . Thus, an increase in the relaxation rate was  $0.168(7) \text{ h}^{-1}$ . To deduce the contribution from the radiation damage, we assume that the increase in the relaxation rate took place by laser irradiation and  ${}^6\text{He}$  beam irradiation. The relaxation rate caused by laser irradiation is linearly increased with the laser power and with time for laser irradiation. The proportionality constant obtained from an independent study is  $(1.1 \pm 0.5) \times 10^{-3} \text{ W}^{-1} \text{ h}^{-2}$  [6]. For the scattering experiment, the relaxation rate due to the laser irradiation was estimated to be  $0.036(16) \text{ h}^{-1}$  using the proportionality constant. The relaxation rate due to the  ${}^6\text{He}$  beam irradiation was then obtained as  $0.132(17) \text{ h}^{-1}$ .

For a higher beam intensity or a longer experimental run, the contribution from radiation damage will increase. Since the proton polarization decreases with increasing relaxation rate, the relaxation rate due to radiation damage should be reduced periodically by changing the target crystal.

#### 4. Summary

A polarized solid proton target for RI beam experiments has been developed and successfully used in the scattering experiments with  ${}^6\text{He}$  beams. In the experiment in 2005, the maximum and average proton polarization were 20.4(58)% and 13.8(39)%, respectively. The decrease in proton polarization during beam irradiation was mainly due to radiation damage, whose contribution to the relaxation rate was 45% for the scattering experiment in 2005.

#### References

- [1] T. Wakui *et al.*, RIKEN Accel. Prog. Rep. **34** (2001) 149.
- [2] M. Hatano, *et al.*, Eur. Phys. J. A **25** (2005) 255.
- [3] S. Sakaguchi *et al.*, CNS Annual Report 2005 (2006) 27.
- [4] A. Henstra, T.-S. Lin, J. Schmidt, W.Th. Wenckebach, Chem. Phys. Lett. **165**, 6 (1990).
- [5] T. Kawahara *et al.*, CNS Annual Report 2005 (2006) 81.
- [6] T. Wakui *et al.*, CNS Annual Report 2003 (2004) 84.

# Polarization Relaxation Time of Polarized $^3\text{He}$ in Target Cell with Ti Windows

K. Itoh and T. Uesaka<sup>a</sup>.

*Graduate School of Science and Engineering, Saitama University.*

<sup>a</sup> *Center for Nuclear Study, Graduate School of Science, University of Tokyo.*

## 1. Polarized $^3\text{He}$ target for RI beam experiments.

A spin-exchange type polarized  $^3\text{He}$  target has been developing at CNS. Main motivation of developing it is to use the target in RI-beam experiments. In the spin-exchange method [1] [2], the  $^3\text{He}$  gas in a glass cell is polarized via the spin-exchange reaction with Rb atoms. We employ this method because it enables us to make a high density  $^3\text{He}$  target rather easily. From the viewpoint of the count rate, high density target is favorable for RI-beam experiments.

When we use this polarized  $^3\text{He}$  target in the RI-beam experiments, one of serious problems is the thick cell material. Not only the thick cell material causes background events, but also it makes difficult to detect low energy recoil particles. As a result, thick cell material makes reaction channel identification difficult. Therefore, we started to develop the target cells in which thin metal foils are partly used.

## 2. Development of new target cell in which thin metal foil is partly used.

There are some requirements for the foil materials. Firstly, the foil materials have to be tolerant to the nitric acid. It is known that the interaction between polarized  $^3\text{He}$  and paramagnetic impurities (in particular iron ions) on the cell wall is one of the main causes of the spin relaxation. In order to remove paramagnetic impurities, the inner wall of the target cell has to be cleaned using the nitric acid. Secondly, foil materials must be strong enough to keep high pressure gases with several atms. We usually fill the  $^3\text{He}$  gas with a high pressure of about 3-8 atms in the target cell. Thirdly, spin relaxation time of the foil material must be long to achieve high target polarization. We chose Ti for the foil material by considering the first and second requirement. We prepare the cell in which Ti foils are partly used and measure the relaxation time.

Figure 1 shows the schematic view of the target cell in which the Ti foils are partly used. The most part of the cell is made of borosilicate glass (Corning7056). The cell has a so-called “double cell” structure which consists of a target cell and an optically pumping cell. Those two cells are connected to each other through a pipe with an inner diameter of 10 mm.

The target cell has cylindrical shape ( $\phi$  50 mm  $\times$  100 mm). The entrance and exit windows which the RI beams pass through are covered by the 50- $\mu\text{m}^t$  Ti foils instead of the glass. The foils are glued to the glass by using STYCAST 1266 (epoxy). The pumping cell has also cylindrical shape ( $\phi$  60 mm  $\times$  70 mm). The volume of target cell and pumping cell are both  $\sim 200 \text{ cm}^3$ . The pressure of  $^3\text{He}$  gas in the “Ti-cell” is kept at about 1 atm for the easy treatment in the present study.

In the cold relaxation process where the cell temperature

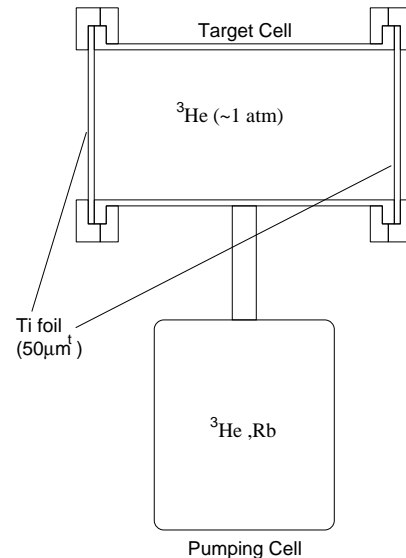


Figure 1. Schematic view of a cell with Ti foil.

is room temperature, the polarization depends only on the spin relaxation time  $\tau$ . The relaxation time was deduced by measuring the  $^3\text{He}$  polarization as a function of time. The measured result are fitted with the curve:

$$P(t) = P(0) \exp(-t/\tau) \quad (1)$$

The time dependence of the polarization was measured by the AFP-NMR technique and the cold relaxation time of the “Ti-cell” was deduced. The result is shown in Fig 2 with the closed circles and solid line. The measured cold relaxation time for the “Ti-cell” was  $\sim 3.7$  hours. It was about 4 times shorter than the relaxation time of normal cell which is made from glass only. It is also shorter than the relaxation times of cells used by the Mainz group in which metal foil is partly used. [3]

## 3. Demagnetization of target cell.

The increase of spin relaxation rate in the “Ti-cell” compared with the normal cell was mainly attributed to the paramagnetic impurities of the Ti foil [4]. The purity of the Ti in the foil is  $\sim 99\%$  and the main impurities of the titanium foil are iron. To reduce the spin relaxation effect attributed to the paramagnetic impurities, demagnetization of the “Ti-cell” was performed.

The Ti foil is demagnetized by using the C-type magnet. The magnetic field was repeatedly applied to the Ti foil in the demagnetization process. The direction of the magnetic field was periodically changed to the opposite direction, and the field was gradually decreased.

After demagnetizing the cell, the cold relaxation time

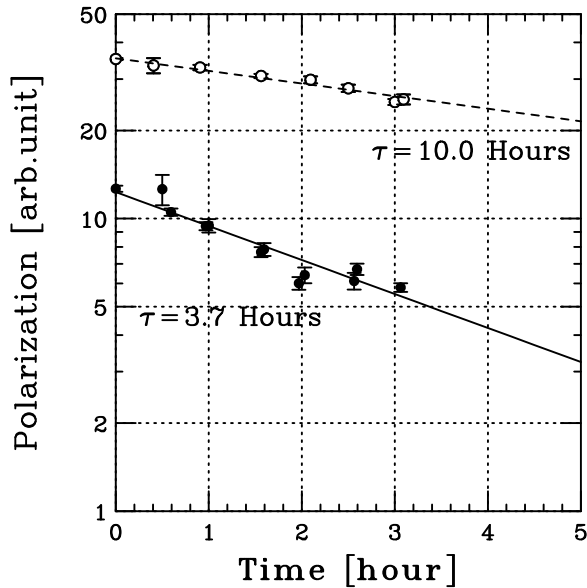


Figure 2. Time dependence of  $^3\text{He}$  polarization in a cold relaxation process. The measured polarization is plotted as a function of the time. The closed circles and solid line show the result of relaxation measurement before demagnetizing the target cell. The open circles and dashed line show the result of relaxation measurement after demagnetizing the target cell. The solid, and dashed lines show the fitting result with the Eq. 1.

was measured again. The result is shown in Fig 2 with the open circles and dashed line. The measured cold relaxation time after demagnetizing the cell was  $\sim 10.0$  hours.

#### 4. Conclusion.

The target cell with the Ti windows has been developed. Before demagnetizing, the measured relaxation time of the “Ti-cell” was about 4 times shorter than normal cell which is made from glass only. After demagnetizing the cell, the spin relaxation time is considerably improved.

#### References

- [1] M. A. Bouchiat *et al*, Phys. Rev. Lett. **5** (1960) 373.
- [2] T.E.Chupp *et al.*, Phys. Rev. C **36** (1987) 6.
- [3] J.Krimmer, XIth International Workshop on Polarized Sources and Targets, Tokyo, 2005 (to be published).
- [4] J.Krimmer, private communication.

# New Method of Polarization Reversal by means of 180-Degree Pulse Nuclear Magnetic Resonance

T. Kawahara, T. Wakui<sup>a</sup>, T. Uesaka<sup>b</sup>, and S. Sakaguchi<sup>b</sup>

*Department of Physics, Toho University*

<sup>a</sup>*Cyclotron and Radioisotope Center, Tohoku University*

<sup>b</sup>*Center for Nuclear Study, Graduate School of Science, University of Tokyo*

## 1. Introduction

The polarized proton target for RI beam experiment should be operated in a low magnetic field (0.01–0.3T) and at high temperature (77–300K) in order to detect low energy recoil proton. One possible method to achieve the polarization is to make use of a population difference of electrons in Zeeman sublevels in photo excited triplet state of aromatic molecules [1]. Because this population difference is independent of temperature or magnetic field, proton can be polarized in a low magnetic field of 0.3T and at high temperature of 100K, by transferring the population difference of electrons. The polarized proton target by the method has been successfully constructed and applied to RI beam experiments [3,4].

In the measurement of polarization observables, it is indispensable to reverse the direction of polarization in order to reduce the systematic uncertainties. In the previous measurement [4], no efficient polarization reversal method was available and the polarization was built up in the opposite direction, which costs time loss of more than several hours. Surely a new method to flip the polarization axis is needed for more efficient use of machine time. We have applied a pulse NMR method for the purpose.

## 2. Pulse NMR method

In the pulse NMR, the spin is flipped by applying the transverse magnetic field  $B_1$  which is perpendicular to a static magnetic field  $B_0$ . Here the flip angle of the spin can be written as

$$\theta = \gamma_I B_1 \Delta t \quad (1)$$

where  $\gamma_1 = 2.68 \times 10^8 s^{-1} T^{-1}$  is the gyromagnetic ratio of proton, and  $\Delta t$  is pulse width. After turning off the  $B_1$  pulse, the spin precesses around the static magnetic field  $B_0$ , which causes an induced current in the NMR coil. The induced signal is called “free induction decay” (FID) signal. Its amplitude, FID amplitude, is proportional to the degree of polarization. For the reversal of the spin, the flip angle  $\theta$  must be 180-deg. It can be easily understood that a flip angle of 180-deg can be achieved by a long pulse duration  $\Delta t$  and/or strong perpendicular magnetic field  $B_1$ . Long pulse duration, however, leads to decrease of polarization due to the spin–lattice relaxation during the reversal.

To avoid the loss of polarization, we tried to make stronger  $B_1$  field keeping the pulse duration as short as a few microseconds. An NMR coil was modified for this.

## 3. Upgrade of the NMR coil

The spin flip angle  $\theta$  is directly related to the FID signal amplitude  $V_{\text{FID}}$ , as  $V_{\text{FID}} \propto \sin \theta$ .  $V_{\text{FID}}$  for the original

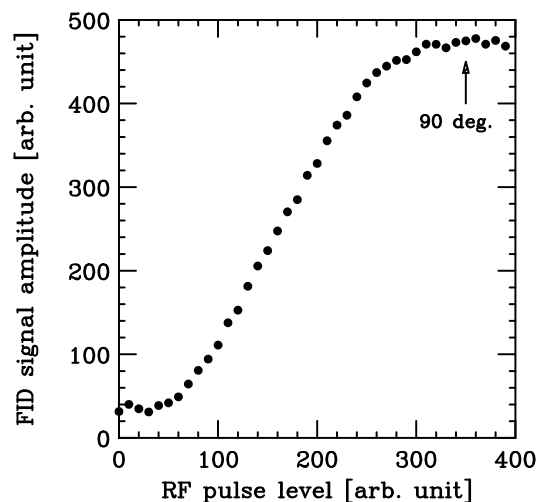


Figure 1. FID signal amplitude for the original NMR coil is shown as a function of the strength of transverse magnetic field.

NMR coil, which is 10-turn of 0.35-mm $\phi$  copper wire, is shown in Fig. 1 as a function of the strength of perpendicular field  $B_1$ . It is clearly seen that the spin is rotated by only 90-deg ( $\sin \theta \sim 1$ ) even for the strongest  $B_1$  which is limited by a maximum power of a RF amplifier. Various combinations of a wire diameter and a turn number were tried to produce stronger  $B_1$ . It should be noted that, not only a turn number but also a wire diameter affects the  $B_1$  strength. This is because the wire diameter changes impedance of the coil and thus is related to matching between the coil and the RF circuit. Whenever a new NMR coil was made, its impedance matching to the circuit was adjusted using a tuner, made of variable capacitances, at an appropriate frequency that is determined by the magnetic field strength. Finally, a coil of 35-turns of a 0.35 mm $\phi$  copper wire was found to be the best one in the current conditions. Using this NMR coil, we succeeded in rotating the polarization of a water sample by 180-deg. The result is shown in Fig. 2.

## 4. The optimization of pulse width

After the NMR coil was upgraded, we optimized the RF pulse width. Since spin relaxation is fast during the rotation procedure, a shorter pulse width is preferable. On the other hand, the rotation angle can be smaller than 180 $^\circ$  when the pulse width is too short. The efficiency of the polarization reversal was evaluated by measuring the polarization loss in repeated reversals. The results for pulse widths of between 1.0 $\mu$ sec and 4.0 $\mu$ sec are shown in Fig. 3. From the results, the pulse width is determined to 2.2 $\mu$ sec.

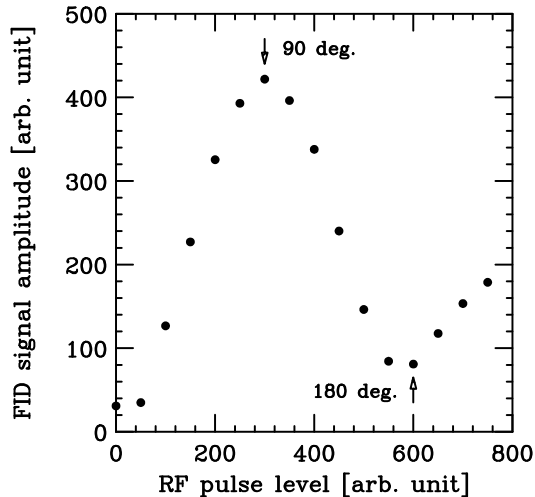


Figure 2. FID signal amplitude for the upgrade NMR coil is shown as a function of the strength of transverse magnetic field.

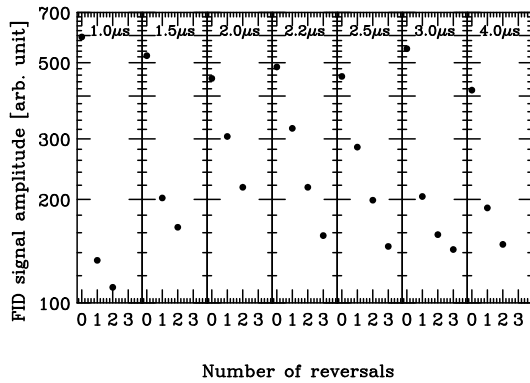


Figure 3. Efficiency of polarization reversal is shown. The polarization was reversed three times. The RF pulse width was changed between  $1.0\mu\text{sec}$  and  $4.0\mu\text{sec}$ . An optimum pulse width was found at  $\Delta t = 2.2\mu\text{sec}$ .

## 5. Results

We applied this polarization reversal technique to the actual polarized proton target made of naphthalene doped with a small amount of pentacene. Since the efficiency of the reversal depends line width of NMR spectrum, it can be different depending on materials. Thus the efficiency for protons in naphthalene is in general, different from that in water. In Fig. 4, the result of polarization measurement during  $\vec{p} + {}^6\text{He}$  scattering experiment [2, 3] is shown. Closed circles denote the results taken in 2005, where our new technique was applied, while open circles represent data for 2003 measurement. At  $t = 0$  hour, the polarization was reversed in both cases. It is found that the efficiency of the polarization reversal by the new technique is about 70% in naphthalene.

## 6. Summary

By using the 180-deg pulse NMR method, we have succeeded in the reversal of the direction of polarization. The NMR coil was upgraded by changing the turn number from

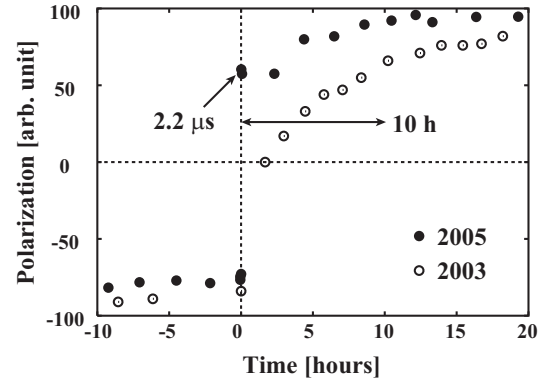


Figure 4. Time development of proton polarization. Closed circles and open circles indicate data in 2005 and 2003, respectively. The polarization is reversed at  $T=0$ .

10 times to 35 times. In addition we optimized the RF pulse width to achieve high efficiency of the polarization reversal. The RF pulse width was determined to  $2.2\mu\text{sec}$ . The new method was used for the polarization reversal during the  $\vec{p} + {}^6\text{He}$  scattering experiment. The efficiency of the polarization reversal was about 70% in naphthalene, and this time was  $2.2\mu\text{sec}$ , which was dramatically shortened from 10 hours in 2003 experiment [4].

## References

- [1] T. Wakui *et al.*, Nucl. Instrum. Methods A **550** (2005) 521.
- [2] T. Wakui *et al.*, CNS Annual Report 2005 (2006) 77.
- [3] S. Sakaguchi *et al.*, CNS Annual Report 2005 (2006) 27.
- [4] M. Hatano *et al.*, Eur. Phys. J. A **25** (2005) 255.

# Performance of Gas Electron Multiplier (GEM) Developed at CNS

Y. L. Yamaguchi, H. Hamagaki, K. Ozawa, S. X. Oda, Y. Aramaki and S. Sano<sup>a</sup>

Center for Nuclear Study, Graduate School of Science, University of Tokyo

<sup>a</sup> Advanced Research Institute for Science and Engineering, Waseda University

## 1. Introduction

The Gas Electron Multiplier (GEM) is a micro pattern gas detector which has an application possibility. The GEM is a metalized polymer foil with holes [1]. Mechanism of signal amplification in the GEM is as follows. The metal layers play a role of electrodes and a high voltage is applied between them. This voltage applied between the GEM electrodes is called as  $V_{\text{GEM}}$ . When a drift electron passes through the hole in the GEM, a strong electric field inside a hole induces a cascade of electrons.

The holes of the GEM made at CERN (CERN-GEM) is fabricated by the wet etching method and has holes with a double-conical shape. It was reported that CERN-GEM could not maintain its gain stable [2].

A new type of a GEM by the dry etching method (CNS-GEM) was successfully developed at CNS [3], [4]. CNS-GEM has holes with a cylindrical shape.

In this report, the performance of CNS-GEM is reported in comparison with that of CERN-GEM.

## 2. Fabrication of GEM

### 2.1. Fabrication by the dry etching method

The standard GEM consists of a 50  $\mu\text{m}$ -thick Kapton coated with 5  $\mu\text{m}$ -thick copper, and the pitch and diameter of the holes are 140  $\mu\text{m}$  and 70  $\mu\text{m}$ , respectively. CERN-GEM has holes with a double-conical shape which is characteristic of the wet etching of the polymer (the left panel in Fig. 1).

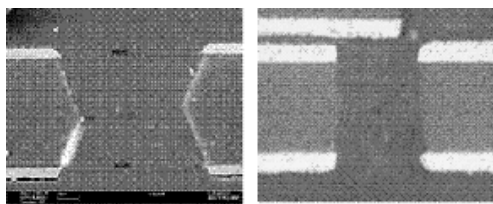


Figure 1. The cross section of a hole of CERN-GEM (left panel) and CNS-GEM (right panel).

On the other hand, CNS-GEM is fabricated by the dry etching method at Scienergy CO., Ltd. CNS-GEM has holes with a cylindrical shape (the right panel in Fig. 1). The main difference between CNS-GEM and CERN-GEM is a shape inside the holes.

### 2.2. Advantage of CNS-GEM

Compared with CERN-GEM, CNS-GEM is expected to have two main advantages.

One is that CNS-GEM is expected to have better gain stability than CERN-GEM. It has been reported that CERN-GEM could not maintain its gain stable. One possible reason for this is that the Kapton insulator inside the holes charges up. The charging-up can be stronger due to a double-conical shape inside the holes of CERN-GEM.

CNS-GEM has a less probability of charging-up because of a cylindrical shape inside the holes.

Another advantage is that CNS-GEM is expected to have higher gain than CERN-GEM. CNS-GEM has larger effective area in which electrons induce ionization than CERN-GEM because CNS-GEM has no bulge of Kapton inside the hole.

## 3. Measurements

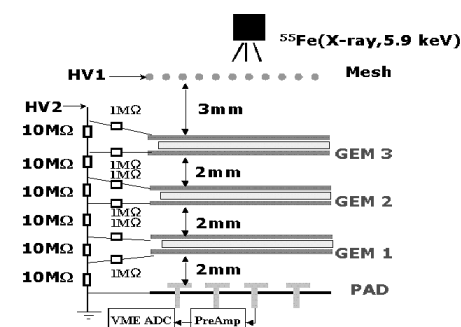


Figure 2. A schematic view of the GEM test setup.

### 3.1. Setup

Figure 2 shows a schematic view of the GEM setup. Measurements were carried out with three GEM foils mounted in a chamber [5]. The distance between neighboring GEMs is 2 mm. The high voltages to the GEM electrodes are supplied from a single HV source to 'HV2' in Fig. 2. The HV2 is equally divided using a chain of 10 M $\Omega$  resistors and sub-divided voltages are provided to individual electrodes. A drift plane, which is a metallic mesh, is mounted 3 mm above the uppermost GEM. The high voltage 'HV1' is given to the drift plane. HV1 is 200 V higher than HV2 during our measurements. When electrons produced in the GEM holes approach copper readout pads, positive charges are induced on the readout pads and negative charges flow into a charge-sensitive pre-amplifier and are recorded using a VME ADC module.

A thermocouple sensor and a barometer are placed in the chamber for the purpose of monitoring the temperature and pressure.

### 3.2. How to measure the properties of GEM

The  $P/T$ , time and  $V_{\text{GEM}}$  dependences of gain are measured. The  $P$  and  $T$  is the pressure and the temperature in the chamber. In our measurements, an  $^{55}\text{Fe}$  (X-ray, 5.9 keV) standard source with an intensity of 370 kBq is used. The chamber is filled with Ar(70%)–CO<sub>2</sub>(30%) or Ar(90%)–CH<sub>4</sub>(10%). The flow rate of the gas is adjusted to about 200 cc/min at the atmospheric pressure.

During measurements of  $P/T$  dependence and time dependence of the gain,  $V_{\text{GEM}}$  is kept constant.

## 4. Results

The ADC spectra around the 5.9 keV peak are fitted with a Gaussian. From the mean value ( $S_{\text{mean}}$ ), the gain ( $G$ ) is calculated as  $G = (S_{\text{mean}}/C) \cdot (1/q_e n_e)$ , where  $q_e$  is the electron charge. The  $n_e$  is the number of electron-ion pairs created by the absorption of 5.9 keV X ray: 212 for Ar(70%)–CO<sub>2</sub>(30%) and 225 for Ar(90%)–CH<sub>4</sub>(10%) [6]. The constant,  $C$ , is obtained to be 2.976 fC<sup>-1</sup> from the calibration of the pre-amplifier and the ADC.

### 4.1. $P/T$ dependence of the gain

Figure 3 shows the  $P/T$  dependence of the gain in the case of Ar–CH<sub>4</sub>. The left and the right panels in Fig. 3 show the measured gain of CNS-GEM and of CERN-GEM as a function of  $P/T$ , respectively. The symbols represent the experimental results and the solid lines represent the exponential functions which are obtained from fitting of the experimental results. It is found that the gain is very sensitive to the gas density. A change of 1% in the  $P/T$  value causes a gain variation of about 10% in Ar–CH<sub>4</sub>.

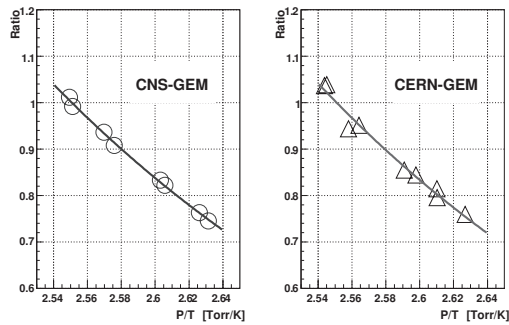


Figure 3. The  $P/T$  dependence of the gain of CNS-GEM (left panel) and CERN-GEM (right panel) for Ar–CH<sub>4</sub>.

### 4.2. Time dependence of the gain

Figure 4 shows the measured gain as a function of the il-

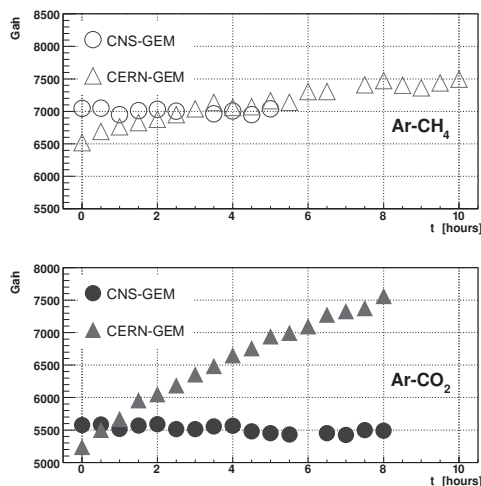


Figure 4. The time dependence of the gain for Ar–CH<sub>4</sub> (top panel) and for Ar–CO<sub>2</sub> (bottom panel).

lumination time which means a time while the voltage is applied to GEM electrodes. The top panel shows the results for Ar–CH<sub>4</sub> and the bottom panel shows the results for Ar–CO<sub>2</sub>. The circle and the triangle symbols represent

the results of CNS-GEM and of CERN-GEM, respectively. These results are normalised to SATP condition by the obtained relation between the gain and  $P/T$ , where SATP means Standard Ambient Temperature and Pressure as  $P = 760$  Torr,  $T = 298$  K i.e.  $P/T \approx 2.55$  Torr/K. The gain of CNS-GEM is stable within a few percents for more than 5 hours, while that of CERN-GEM increases more than 10% over 6 hours.

### 4.3. $V_{\text{GEM}}$ dependence of the gain

The gain as a function of the  $V_{\text{GEM}}$  for Ar–CO<sub>2</sub> was measured as shown in Fig. 5. An increase of 10 V in  $V_{\text{GEM}}$  causes an increase of the gain by a factor of 2. The gain of CNS-GEM is higher than that of CERN-GEM by a factor of  $\sim 1.2$ .

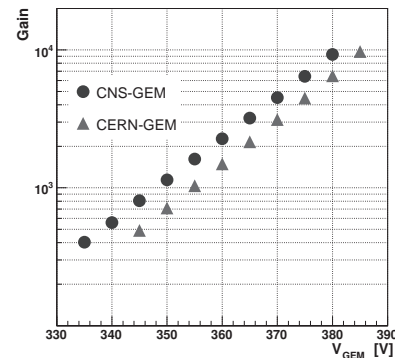


Figure 5. Comparison of the  $V_{\text{GEM}}$  dependence of the gain of CNS-GEM with that of CERN-GEM for Ar–CO<sub>2</sub>.

## 5. Summary and Outlook

The  $P/T$ , time, and  $V_{\text{GEM}}$  dependence of the gain were measured. CNS-GEM is found to have higher gain and better gain stability than CERN-GEM. Gain instability might depend on other factor, such as surface conditions and gas purity. It is need to measure a gain stability using different lots of CNS-GEM and of CERN-GEM.

Efforts are on going to search for optimum GEM structure, such as thickness, hole diameters, materials and so on.

## References

- [1] F. Sauli, Nucl. Instrum. Methods A **386** (1997) 531.
- [2] S. Bachmann, *et al.*, Nucl. Instrum. Methods A **438** (1999) 376.
- [3] M. Inuzuka *et al.*, CNS Annual Report (2003) **35**.
- [4] T. Tamagawa *et al.*, Nucl. Instrum. Methods A **560**(2006) 418-424.
- [5] M. Inuzuka *et al.*, Nucl. Instrum. Methods A **525** (2004) 529.
- [6] F. Sauli, CERN Yellow Report 77-09 (1977).

# Development of a CsI-coated Gas Electron Multiplier

Y. Aramaki, H. Hamagaki, K. Ozawa, S. Yokkaichi<sup>a</sup>, S. X. Oda, Y. Morino, Y. L. Yamaguchi, M. Inuzuka<sup>b</sup>, S. Sano<sup>c</sup>, and S. Maki<sup>d</sup>

Center for Nuclear Study, Graduate School of Science, University of Tokyo

<sup>a</sup>RIKEN (The Institute of Physical and Chemical Research)

<sup>b</sup>National Research Institute for Cultural Properties, Tokyo

<sup>c</sup>Department of Physics, Waseda University

<sup>d</sup>Department of Physics, Tokyo University of Science

## 1. Introduction

In the PHENIX experiment, a Hadron Blind Detector (HBD) which is a threshold-type Cherenkov counter using  $\text{CF}_4$  gas as a radiator is installed in 2006 [1]. Its main role is to identify and reject electron pairs from  $\pi^0$  Dalitz decays and  $\gamma$  external conversions which are major backgrounds for measurement of the low mass vector mesons. The HBD detector consists of a Cherenkov gas radiator, photocathode for UV photons, and a triple-Gas Electron Multiplier (a triple-GEM). Since the same gas material is used as a Cherenkov radiator as well as for electron multiplication, no windows are needed between a radiator part and a GEM part.

Caesium iodine (CsI) is chosen as a photocathode for UV Cherenkov photons. CsI is sensitive to the photons in the ultraviolet region ( $\lambda=115\text{--}320$  nm). CsI is evaporated on the surface of the front GEM foil. The thickness is 200 nm. Including the CsI-coated GEM, a triple-GEM serves for electron multiplication.

The GEM is a  $50\ \mu\text{m}$  thick polyimide sheet which is covered with  $5\ \mu\text{m}$  thick copper foils at both sides, with regularly placed penetrating holes, as is shown in Fig. 1. The typical diameter and pitch of the holes are  $70\ \mu\text{m}$  and  $140\ \mu\text{m}$ , respectively. High electric fields are realized inside the holes with low voltage difference between the both sides of the GEM and the charge multiplication is induced inside the holes. Relatively high gain can be achieved with the triple-GEM, while maintaining low discharge probability.

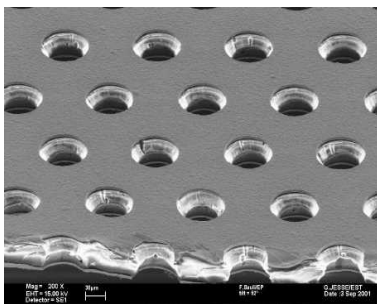


Figure 1. A micrograph of a GEM foil.

## 2. Structure of a CsI coated GEM

There are two possible modes to collect photoelectrons, i.e., reflective photocathode mode and transmissive photo-

cathode mode. Since a reflective photocathode mode has relatively high quantum efficiency and it can suppress photon feedback [3], the reflective photocathode mode was chosen for our development. With ultraviolet (UV) photons impinged on the CsI coated on a GEM, photoelectrons are produced and are emitted back from the CsI surface. The photoelectrons are attracted inside the holes, and the charge multiplication is induced inside the holes.

Before CsI evaporation, the GEM is plated with nickel and gold to avoid the chemical reaction between copper and CsI. The evaporation of CsI is carried out by Hamamatsu Photonics.

## 3. Setup

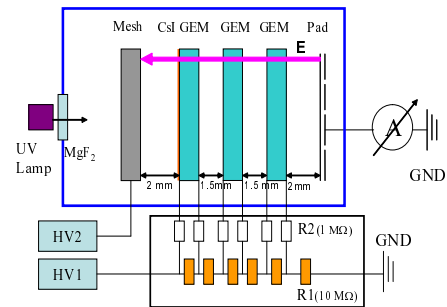


Figure 2. Setup of a triple-GEM detector and the resistive chain to divide the voltage.

Figure 2 shows a schematic view of the test setup. The GEMs, the readout pad and the mesh were mounted inside the box made of stainless steel (the stainless box), the diameter and the height of which are 24 cm and 10 cm, respectively. In order to keep CsI from being exposed to the air, the mounting was performed inside a glove-box with constantly flowing dry nitrogen gas. The humidity was 1000 ppm after a flow rate was 480 cc per minute a whole day.

The GEMs have  $10\ \text{cm} \times 10\ \text{cm}$  sensitive area. The distance between the mesh and the CsI-coated GEM is 1.5 mm. The distance between GEMs is 1.5 mm and the distance between the bottom GEM (GEM 3) and the readout pad is 2 mm. For readout signals, 5 by 5 array of pads with  $1\ \text{cm} \times 1\ \text{cm}$  square shape are used. All pads are connected to a current meter via feedthroughs. Two high voltage power supplies, HV1 and HV2 are used to apply high voltage to the GEMs and the mesh, respectively. As shown in Fig. 2, R1 and R2 are  $10\ \text{M}\Omega$  and  $1\ \text{M}\Omega$ , respectively. These

resistors are in the shield box outside the stainless box. The voltage supplied to the mesh is set lower than that for the CsI-coated GEM, so as to reject electrons produced in the area between the MgF<sub>2</sub> window and the mesh. A deuterium lamp (the wave length is 115–400 nm) is set in front of the MgF<sub>2</sub> (the cutoff wave length is 110 nm.) window.

The stainless box is pumped down to 10<sup>-6</sup> Torr (10<sup>-4</sup> Pa) to reduce the water content, and a mixed gas of Ar/CH<sub>4</sub> (90%/10%) is flushed into the stainless box. The humidity in the stainless box was 50 ppm. UV photons from the deuterium lamp are irradiated the CsI-coated GEM.

#### 4. Result

The photocurrent from the CsI-coated GEM was measured using the current meter with UV light irradiation. Figure 3 shows the photocurrent as a function of the voltage across the GEM. As higher voltage was applied to the GEMs, the value of the photocurrent became larger. Background leak current was in the order of 10 pA, and it was negligible compared to the current when UV light was irradiated. This result means that the CsI photocathode converts UV light into photoelectrons and the photoelectrons are multiplied.

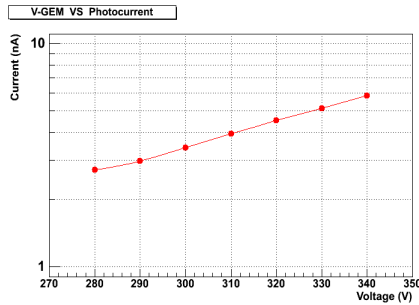


Figure 3. The photocurrent from GEMs is shown as a function of the voltage across GEMs.

#### 5. Summary and Outlook

CsI-coated GEMs were developed for using as UV photon detectors for using as photocathodes of threshold-type. CsI is sensitive to UV light ( $\lambda=115\text{--}320$  nm). We confirmed that the CsI-coated GEM reacts to UV light.

The quantum efficiency (QE) of the CsI-coated GEM will be measured as a function of the wave length. The setup for the QE measurement is shown in Figure 4. The QE of the CsI-coated GEM at a given wavelength  $\lambda$  is given by the following formula.

$$QE_{CsI}(\lambda) = QE_{PMT}(\lambda) \frac{R(\lambda) G_{PMT}}{T(\lambda) G_{GEM}} \frac{I_{CsI}(\lambda)}{I_{PMT}(\lambda) \cdot C_1 \cdot C_2}$$

where R and T are the indexes of reflection ( $R$ ) and transmission ( $T$ ) of the half mirror which provides a part of UV photons to a reference counter and the ratio of  $R$  to  $T$  will be determined using two PhotoMultiplier Tubes (PMTs),  $I_{PMT}$  is the photocurrent from the reference PMT,  $I_{CsI}$  is the photocurrent from the CsI photocathode,  $G_{GEM}$  is the

gain of the triple-GEM, which will be measured with a radioactive source,  $C_1$  is the mesh transparency ( $C_1 = 0.81$ ), and  $C_2$  is the opacity of the CsI layer due to the GEM holes ( $C_2 = 0.833$ ).  $G_{PMT}$  and  $QE_{PMT}$  are the gain and the quantum efficiency of the reference PMT, respectively.

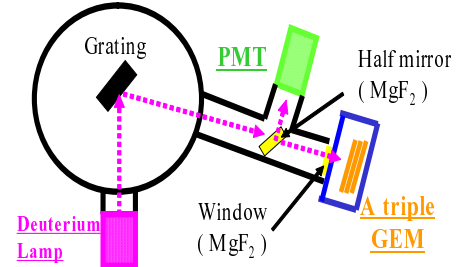


Figure 4. Setup for measuring the QE of the CsI photocathode.

There are two problems to be solved for using as a threshold-type Cherenkov counter. Firstly, there is a degradation of the QE of the CsI photocathode during long-term operation because of the nature of deliquescence which CsI has and the ion-feedback produced in multiplication. Secondly choice of a proper gas is to be made. The high refractive index of the gas is demanded to obtain the large number of photons. The gas is also required to have sufficiently large gain by the GEM multiplication. For example, CF<sub>4</sub> gas has high refractive index, but it needs high voltage to realize a reasonable gain, which may cause frequent discharge and instability of GEM operation.

We will carry out an electron beam test to check the performance of the threshold-type Cherenkov counter.

#### References

- [1] Z. Fraenkel *et al.*, Nucl. Instrum. Methods A **546** (2005) 466.
- [2] F. Sauli, Nucl. Instrum. Methods A **386** (1997) 531.
- [3] D. Mörmann *et al.*, Nucl. Instrum Methods A **471** (2001) 333.

# Simulation Study of Gas Electron Multiplier

S. Sano, H. Hamagaki, K. Ozawa, S. Yokkaichi<sup>a</sup>, T. Isobe, S. X. Oda, and Y. L. Yamaguchi

Center for Nuclear Study, Graduate School of Science, University of Tokyo

<sup>a</sup>RIKEN (The Institute of Physical and Chemical Research)

## 1. Introduction

The Gas Electron Multiplier (GEM) is used for signal amplification by the avalanche process. GEM is a metal-coated polyimide foil with circular holes in a closed packed geometry. The both side metals are used as electrodes.[1]. The typical thickness of the GEM foil is 50  $\mu\text{m}$ , and the typical pitch and diameter of the holes are 140  $\mu\text{m}$  and 70  $\mu\text{m}$ , respectively [2]. With a few hundreds volts applied between the two electrodes, electron multiplication due to the avalanche process becomes active inside the holes.

The GEM fabricated by the chemical etching method at CERN (CERN-GEM) has double-conical holes. A new type of GEM was developed at CNS (CNS-GEM) by the dry etching method, and it has cylindrical holes. It was reported that CNS-GEM has higher gain and better gain stability compared with CERN-GEM [3]. It is thought that these differences are due to the difference in the hole shape.

Quantitative understanding of GEM characteristics is needed for further GEM development. As the first step, we simulated the electron multiplication with GEM.

## 2. Simulation

### 2.1. Simulation method

The procedure of the simulation is as follows. The electric field around a GEM is calculated by Maxwell 3D which is a software to analyze a three dimensional electric field. The calculated electric field data is imported into Garfield which simulates motion of electrons and ions in gas.

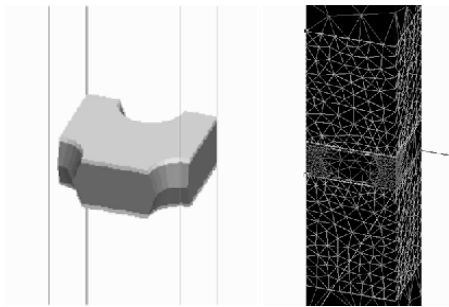


Figure 1. The left panel is a unit cell of GEM structure. The right panel is mesh (tetrahedrons). Smaller mesh gives a more accurate solution of the electric field.

Maxwell 3D carries out the calculation with the finite element method where the electric field is obtained for each mesh engraved on objects. The structure of GEM is described by a unit cell in two directions (the left panel of Fig. 1). An accurate solution of a strong electric field inside of holes of the GEM is obtained by downsizing of the mesh inside of holes as shown in Fig. 1.

### 2.2. Condition for simulation

The voltage condition for this simulation is shown below.

$$V_d = V_{\text{GEM}} = V_i$$

where  $V_d$ ,  $V_{\text{GEM}}$ , and  $V_i$  is the potential between the uppermost boundary of the unit cell and the upper electrode of the GEM (2 mm-thick drift region), between the electrodes, and between lower electrode and the lowermost boundary of the unit cell (2 mm-thick induction region), respectively. Ar(70%)+CO<sub>2</sub>(30%) at atmospheric pressure is used.

### 2.3. Avalanche simulation

Figure 2 shows an avalanche with CNS-GEM. An electron which comes from the drift region triggers an avalanche inside the hole and multiplied electrons come out from the hole. The zigzag lines and straight lines indicate the drift lines of electrons and ions, respectively. Approximately 80% of created electrons are absorbed at the lower GEM copper electrode and the rest drift to readout pads (lowermost boundary of Fig. 2). Twenty percents of created ions also reach the drift plane (the uppermost boundary of Fig. 2). The gain of the GEM is defined as the number of electrons which reached the readout pads.

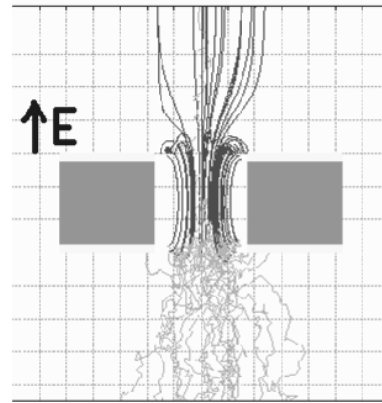


Figure 2. Avalanche with CNS-GEM.

### 2.4. $V_{\text{GEM}}$ dependence of gain

Figure 3 shows the distribution of the number of multiplied electrons which reaches the readout pads. One event is simulated with 100 seed electrons, and the gain is obtained from the average of this histogram.

Figure 4 shows the number of the electrons created by avalanche, the gain, and the measured gain of single CNS-GEM and CERN-GEM as a function of  $V_{\text{GEM}}$ . The measured gain of single GEM is obtained as the cubic root of the measured gain of triple GEM with assumption that each GEM layer works independently in triple GEM structure. The gain obtained by the simulation exponentially increases as  $V_{\text{GEM}}$  increases, and this behavior is consistent with the

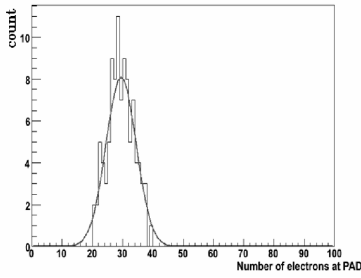


Figure 3. The Multiplication distribution fit with a Gaussian, of which the mean corresponds to the gain of GEM.

measured gain.

But absolute gain appears to have big differences between simulation and measurement. The simulated gain of CNS-GEM attains to 60 at  $V_{GEM} = 350$  V, while the measured gain is 10. The reason for this disagreement is not well understood yet.

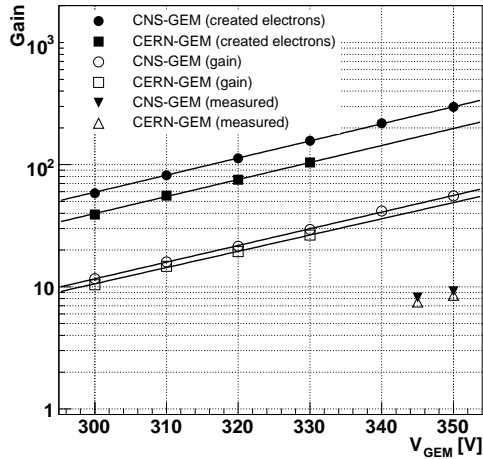


Figure 4.  $V_{GEM}$  dependence of created electrons, gain, and measured gain.

### 2.5. Extraction efficiency

Figure 5 (left) shows the electric field along the center axis of a GEM hole for several values of  $V_{GEM}$ . The electric field inside a hole of CNS-GEM is slightly stronger than that of CERN-GEM. But it is not enough to explain the difference in the gain. Figure 5 (right) shows the radial distribution of the point of creation of secondary electrons in the hole. It is found from Fig. 5 that CNS-GEM creates larger number of electrons near the edge of a hole than CERN-GEM. This will be ascribed to the difference in the shape of the holes.

The extraction efficiency is the probability that electrons created by an avalanche reach the pads. As shown in Fig. 4, the number of the secondary electrons created by CNS-GEM is higher than that by CERN-GEM by a factor of about 1.5 and the gain of CNS-GEM is also higher than that of CERN-GEM by a factor of 1.1. This means the extraction efficiency of CNS-GEM is lower than that of CERN-GEM. The reason for the difference in the extraction efficiency appears to be as follows. Almost electrons created at

near the edge of a hole drift to the lower electrode of GEM and are absorbed. So the gain of each GEM is determined by the number of electrons created at the inner region of the hole. Consequently, there is not a so big difference in each gain as the difference in each total number of created electrons.

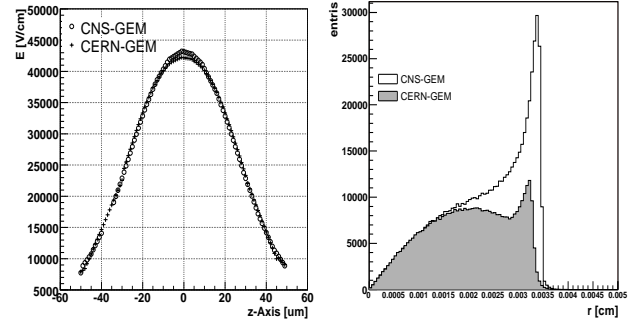


Figure 5. left: electric field on the center axis of each GEM holes. right: distribution of the creation place of electrons in holes.

### 3. Summary

Electron multiplication by GEM was simulated using Maxwell 3D and Garfield. Some qualitative features,  $V_{GEM}$  dependence of gain, the ratio of gains of CNS-GEM and CERN-GEM, comparable with measurement result, except for the absolute gain. This simulation could be used to the optimization of the GEM structure.

### References

- [1] F. Sauli, Nucl. Instrum. Methods A **386** (1997) 531.
- [2] S. Bachmann *et al.*, Nucl. Instrum. Methods A **438** (1999) 376.
- [3] Y. L. Yamaguchi *et al.*, CNS Annual Report 2004 (2005) 93.

# Measurements of Ion Feedback in the Gas Electron Multiplier (GEM)

S. Maki, H. Hamagaki<sup>a</sup>, K. Ozawa<sup>a</sup>, S.X. Oda<sup>a</sup>, Y. Morino<sup>a</sup>, Y. Aramaki<sup>a</sup>, Y.L. Yamaguchi<sup>a</sup>,  
S. Sano<sup>b</sup>, S. Yokkaichi<sup>c</sup>, and J. Chiba

*Faculty of Science and Technology, Tokyo University of Science*

<sup>a</sup>*Center for Nuclear Study, Graduate School of Science, University of Tokyo*

<sup>b</sup>*School of Science and Engineering, Waseda University*

<sup>c</sup>*RIKEN (The Institute of Physical and Chemical Research)*

## 1. Introduction

The gas electron multiplier (GEM) is produced with plasma and laser etching for piercing a metalized polymer foil in Japan [1, 2]. Main difference in the GEMs made in Japan and at CERN is the shapes of those holes which are cylindrical and double-conical, respectively.

## 2. Ion feedback

Figure 1 shows a schematic view of the multiplication mechanism in the GEM. Radiation ionizes a gas molecule in the drift region and the created electrons induce an avalanche in a hole. The multiplied electrons are collected by the readout pads through the induction region. The applied voltage between the electrodes on both sides of the polymer foil,  $V_{GEM}$ , determines the electric fields inside the holes.

This electron multiplication process generates the same numbers of electrons and positive ions simultaneously. Part of positive ions drift to the cathode mesh which is located at the opposite side of the anode pads, and this drift of positive ions to the cathode is often called as ion feedback or ion backflow. Since ion feedback distorts the electric field and recombines with electrons in the drift region, it worsens the detector performance, in particular, in case of the time projection chamber (TPC) which has a large drift region [3, 4].

The GEM is expected to well suppress the ion feedback compared to the multi-wire proportional chamber (MWPC), which is usually used in the TPC. Therefore better detector performance could be achieved by using the GEM. To understand the ion feedback suppression quantitatively, the ion feedback in the GEM was measured.

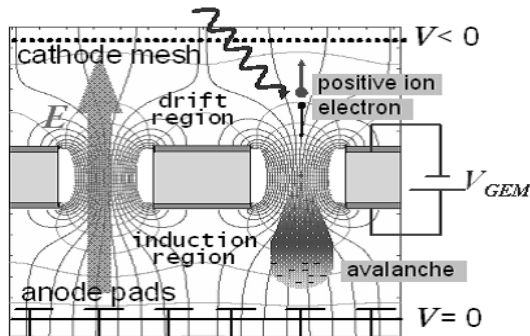


Figure 1. A schematic view of the multiplication mechanism by the GEM foil.

## 3. Measurements

The measurement setup is shown in Fig. 2. The chamber was filled with a gas mixture of Ar-CH<sub>4</sub> (in the volume proportions of 90:10) and used for all measurements. The continuous X-ray whose mean energy is 17 keV was irradiated to the chamber to create electron-ion pairs. The sensitive area of each GEM, which was made in Japan, is 10 cm × 10 cm. The electric field in the drift region is defined as  $E_d$ . Likewise, the electric fields in the transfer region and the induction region are defined as  $E_t$  and  $E_i$ , respectively.

Voltages supplied to the cathode mesh and the electrodes on the GEM foils were collectively controlled by a high voltage (HV) module (REPIC RPH-042). The voltage to the cathode mesh was directly supplied from the HV module, while the supplied voltage to the GEM electrodes was divided into 6 equal parts by a resistor chain, as shown in Fig. 2.

Two picoammeters A1 and A2 (ADVANTEST R8240 and R8340A, respectively) are used to measure currents. A1 measured the cathode current,  $I_c$ , which represents feedback ions from the GEMs, and A2 measured the anode current,  $I_a$ , which represents multiplied electrons. Finally, the fraction of ion feedback  $F$  is defined as the ratio of the ion-caused current  $I_c$  to the electron-caused current  $I_a$ , i.e.  $F = I_c/I_a$ . To eliminate the background contribution, the values of these currents at  $V_{GEM} \sim 50$  V were subtracted.

We focused on the dependence of ion feedback  $F$  on the parameters of  $V_{GEM}$ ,  $E_d$ ,  $E_t/E_i$  and the number of GEM foils.

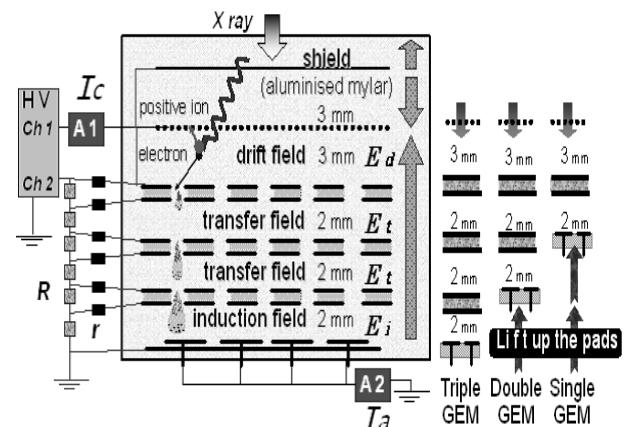


Figure 2. A schematic view of the ion feedback measurement.

## 4. Results

### 4.1. $V_{GEM}$ dependence

Figure 3 shows the cathode current  $I_c$  and the anode current  $I_a$  as a function of  $V_{GEM}$ , with the single, double and triple GEMs. As  $V_{GEM}$  increases, both the currents  $I_c$  and  $I_a$  increase exponentially. In the measurements, the  $E_d$  and  $E_t/E_i$  are fixed to 0.33 kV/cm and 1, respectively.

The ion feedback  $F(= I_c/I_a)$  is shown in Fig. 4 as a function of  $V_{GEM}$ . It decreases as  $V_{GEM}$  increases. Although the ion feedback is larger in the triple GEM compared to the double and single GEMs in the low  $V_{GEM}$ , it decreased rapidly and comparable at  $V_{GEM} \sim 330$  V.

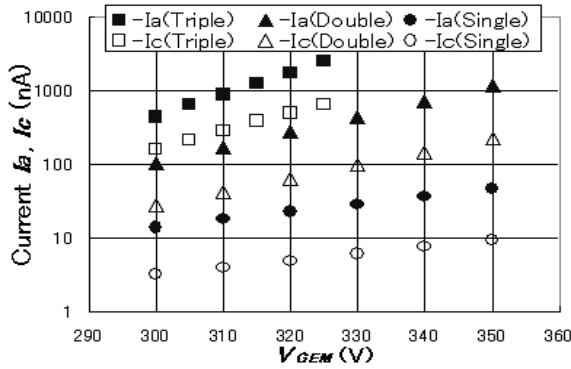


Figure 3. The measured currents  $I_c$  and  $I_a$  as a function of  $V_{GEM}$  at  $E_d = 0.33$  kV/cm.

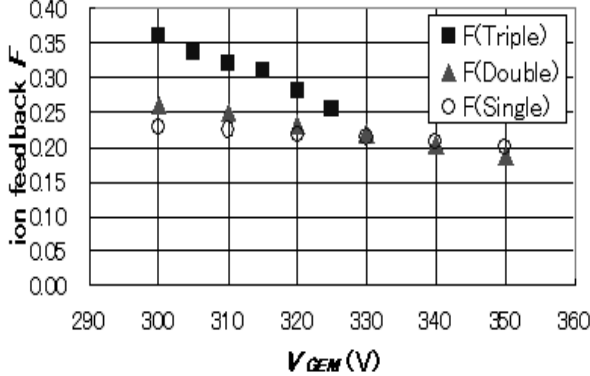


Figure 4. The ion feedback  $F$  as a function of  $V_{GEM}$  at  $E_d = 0.33$  kV/cm.

### 4.2. $E_d$ dependence

Dependence of the ion feedback  $F$  on the drift field  $E_d$  is shown in Fig. 5. In the measurements, the  $V_{GEM}$  and  $E_t/E_i$  are fixed to 320 V and 1, respectively. The ion feedback increases in proportion to  $E_d$  and is suppressed to less than 5% with the low drift field of  $E_d < 0.05$  kV/cm.

### 4.3. $E_t/E_i$ dependence

The ion feedback was measured with three values of the ratio,  $E_t/E_i = 0.5, 1$  and  $2$  using the double GEM. The  $E_t/E_i$  dependence of the ion feedback is shown in Fig. 6 as a function of  $V_{GEM}$ . As the ratio  $E_t/E_i$  increases, the ion feedback decreases. The variation of  $E_t/E_i$  less affects the ion feedback than the variation of  $E_d$ .

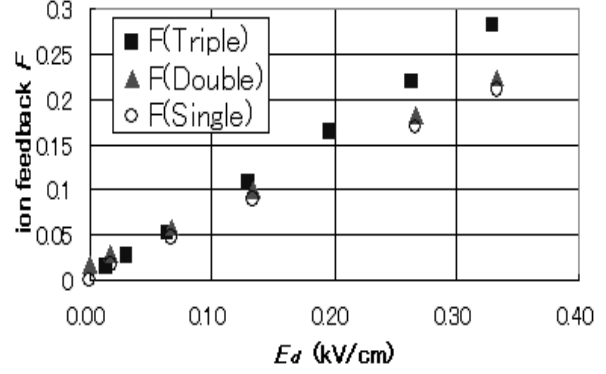


Figure 5. The ion feedback as a function of the drift field  $E_d$  at  $V_{GEM} = 320$  V with the parameter of the number of GEMs.

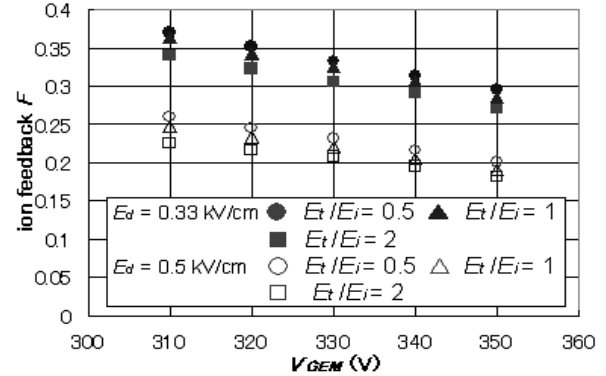


Figure 6. The electric field  $E_t/E_i$  dependence of the ion feedback with the double GEM.

## 5. Conclusion

The ion feedback suppression is one of expected advantages of the GEM. Dependence of the ion feedback  $F$  on various parameters, such as  $V_{GEM}$ ,  $E_d$  and  $E_t/E_i$ , was investigated. We achieved the ion feedback of less than 5% in the GEM. The ion feedback decreases when the voltage supplied to the GEM  $V_{GEM}$  increases. The ion feedback is more dependent on the drift field  $E_d$  than the transfer field  $E_t$ . To minimize the ion feedback, to decrease the drift field  $E_d$  is effective.

## References

- [1] M. Inuzuka *et al.*, Nucl. Instrum. Methods A **525** (2004) 529.
- [2] T. Tamagawa, *et al.*, Nucl. Instrum. Methods A **560** (2006) 418.
- [3] S. Bachmann, *et al.*, Nucl. Instrum. Methods A **438** (1999) 376.
- [4] A. Bonder, *et al.*, Nucl. Instrum. Methods A **496** (2003) 325.

# Electron Identification Capability of Real Size, Six Layer Transition Radiation Detector for ALICE

Y. Morino, S. Saito, T. Gunji, H. Hamagaki, and K. Ozawa,  
for the ALICE TRD Collaboration

Center for Nuclear Study, Graduate School of Science, University of Tokyo

## 1. Introduction

It is predicted from lattice Quantum Chromo Dynamics (QCD) calculations that a phase transition from hadronic matter to a plasma of deconfined quarks and gluons, called quark-gluon plasma (QGP) occurs at high energy density. The ALICE experiment is one of the experiments at Large Hadron Collider (LHC) at CERN, planned to start operation in 2008. The physics goal of the ALICE experiment is to study such a QCD phase transition in heavy ion collisions at center of mass energy of  $\sqrt{s_{NN}} = 5.5$  TeV [1].

For studying properties of QGP, measurement of quarkonia ( $J/\psi$ ,  $\Upsilon$ ) is important because quarkonia are the promising probes of QGP formation. Since a di-electron decay channel is convenient to measure the quarkonia, the identification of electron is important at the ALICE.

The Transition Radiation Detector (TRD) of the ALICE is designed to provide electron identification. For measuring quarkonia, it is required for the ALICE TRD to achieve the pion misidentification probability of less than 1% at 90% electron efficiency at momenta in excess of 3 GeV/c [2].

## 2. Real size TRD and test experiment

Transition radiation (TR) is emitted when a charged particle crosses the boundary between two media with different dielectric constants [3]. More than one TR photon, typically soft X-rays, is produced if Lorentz factor  $\gamma$  of the charged particle is larger than about 2000, which corresponds to about 1 GeV/c for electrons and about 280 GeV/c for pions. Therefore in the momentum range between 1 and 280 GeV/c, electrons are uniquely identified by detecting TR photon.

The ALICE TRD consists of six detector layers, and each layer is composed of a radiator and a drift chamber. The radiator consists of polypropylene fiber mats (fiber diameter is about  $15\mu\text{m}$ ), sandwiched between two Rohacell HF71 sheets. The total thickness of the radiator is 4.8 cm. The drift chamber has a drift region of 30 mm and an amplification region of 7 mm, and is operated with Xe-CO<sub>2</sub> (85%-15%) gas mixture.

After several test experiments with small prototypes and prototype Front End Electronics (FEE) [4], the design of TRD and FEE were fixed and the real size TRDs and prototype FEE were developed and constructed. The first beam test of six layered TRDs with production size ( $939 \times 1070 \times 105$  and  $981 \times 1070 \times 105$  mm<sup>3</sup>) was performed at the CERN PS accelerator in October 2004. One readout board (ROB), which was mounted on the back-end of the TRD, was used for each detector layer to read out the signals from 288 cathode pads. ROB includes 16 Multi

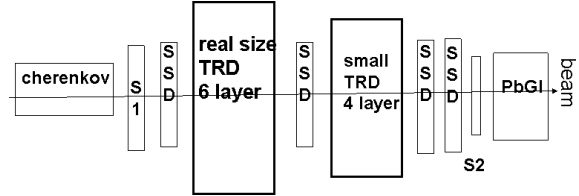


Figure 1. A schematic view of the beam test setup. TRD, two scintillators (S1,S2), Cherenkov detector, Pb-glass calorimeter (PbGI) and four Si-strip detectors (SSD).

Chip Modules (MCMs). A Pre-amplifier/Shaper (PASA) is mounted on each MCM, and signal digitization (10-bit, 10 MHz sample frequency) is also performed on the board [2].

Measurements were carried out with electron-pion mixed beam with momentum variable from 1 to 10 GeV/c. Figure 1 shows a schematic view of the test experimental setup. Scintillators provided beam triggers. The Cherenkov detector and the Pb-glass calorimeter were used for separating electron events and pion events. Four Si-strip detectors were used for precise beam position measurements.

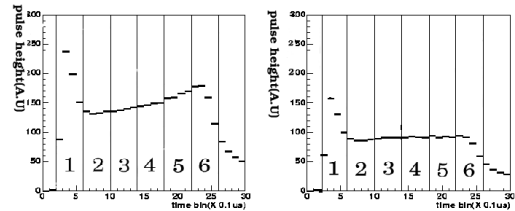


Figure 2. Average pulse height in one detector layer as a function of drift time at the beam momentum of 4 GeV/c. Left panel shows electron events and right one shows pion events.

## 3. Analysis

Figure 2 shows the average pulse height for pions and electrons as a function of drift time in one layer at the beam momentum of 4 GeV/c. The peak at the small drift time, marked as “1” in Fig.2, originates from the amplification region, and the plateau after the peak is from the drift region. In the case of electron events, TR photons are absorbed at the entrance of the drift chamber, and these contributions are clearly seen around the end of drift time. For exploiting TR contribution for electron identification, the drift region was split into six sections, as indicated in Fig.2.

A bi-dimensional likelihood analysis method was used for evaluating electron identification capability [5]. The likelihood ratio is defined for each event as the ratio of electron probability to pion probability. These probability is determined from energy deposit distribution at each drift

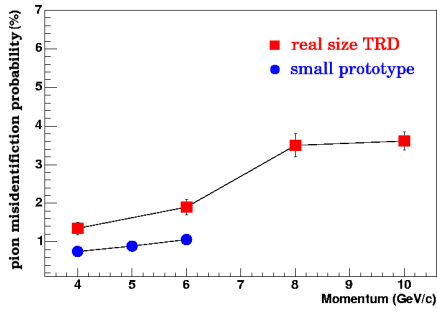


Figure 3. The pion misidentification probability by bi-dimensional likelihood method as a function of a beam momentum and the result of small prototype.

region in each TRD layer.

Figure 3 shows pion misidentification probability as a function of beam momentum, with earlier results from small prototype TRDs [4]. Squares show the result from real size TRDs and circles show from small prototype. The result for real size TRD is slightly worse than that for small prototype. Since FEE, which consists of MCMs and ROB, was newly installed on the back of the real size TRD, the real size TRD has larger material budget than small prototype. Due to larger material budget, the amount of knockout electrons should increase in the case of the real size TRD. To study the effect of increased material budget, the simulation study was performed. Figure 4 shows the pion misidentification probability obtained from the simulation and real data as a function of the number of TRD layers used for analysis at 4 GeV/c. In this figure, the circles show the result from real size TRD, the triangles show the result from small prototype. The reverse triangles show the results from the simulation with FEE and the closed squares show the results from the simulation without FEE. The difference of the pion misidentification probability between the real size TRD and small prototype is comparable with the difference of the simulation result between the two cases with and without FEE. Since the ALICE TRD will be operated

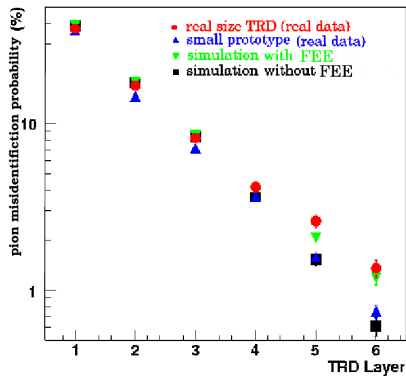


Figure 4. The pion misidentification probability of the simulation and real data as a function of the number of TRD layers used for analysis at 4 GeV/c. The simulations are two case, with FEE and without FEE.

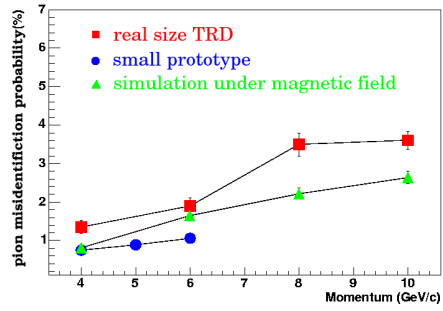


Figure 5. Pion misidentification probability of the simulation and real data as a function of momentum. The simulation is under magnetic field.

under 0.4 T magnetic field at the ALICE experiment, the effect of magnetic field was also studied by the simulation. It is expected that under magnetic field the pion misidentification probability gets near the extrapolated value of the small prototype, because the most of knockout electrons will go away from the parent track. Figure 5 shows misidentification probability of pions from the simulation under the magnetic field as a function of momentum, with the result from real size TRD and small prototype. The squares show the results from the real size TRD, the circles show the result from the small prototype and the triangles show the results of the simulation under the magnetic field. The pion misidentification probability at the simulation with magnetic field becomes 0.80% at 4 GeV/c. This result satisfies the requirement of the ALICE TRD.

#### 4. Summary

The first beam test of real size TRD of the ALICE detector system at LHC was performed successfully. Electron identification capability and the effect of knockout electron were studied using the simulation study. From the simulation study, it is expected that the ALICE TRD will satisfy the requirement at 4 GeV/c under magnetic field.

#### References

- [1] ALICE Collaboration Technical Proposal, CERN/LHCC,95-71.
- [2] ALICE TRD Technical Design Report, CERN/LHCC,2001-021; <http://www-alice.gsi.de/trd>
- [3] M.L.Cherry *et al.*, Phys. Rev. **D10** (1974) 3594.
- [4] T. Gunji *et al.*, CNS-REP-61 (2004) 65.
- [5] A. Andronic *et al.*, Nucl. Instrum. Methods A **522** (2004) 40.

# **Theoretical Nuclear Physics**



# Large Scale Nuclear Structure Calculations in CNS

N. Shimizu<sup>a</sup>, T. Otsuka<sup>a,b,c</sup>, N. Itagaki<sup>a,d</sup>, T. Mizusaki<sup>b,e</sup>, M. Honma<sup>f</sup>, and Y. Utsuno<sup>g</sup>

<sup>a</sup>Department of Physics, University of Tokyo

<sup>b</sup>Center for Nuclear Study, Graduate School of Science, University of Tokyo

<sup>c</sup>RIKEN (The Institute of Physical and Chemical Research)

<sup>d</sup>Hahn-Meitner-Institut

<sup>e</sup>Institute of Natural Sciences, Senshu University

<sup>f</sup>Center for Mathematical Sciences, University of Aizu

<sup>g</sup>Japan Atomic Energy Agency

## 1. Introduction

Our group has developed theoretical methods to solve quantum many-body problem and performed nuclear structure calculations to discuss various nuclear structure. These theoretical works have been supported by the CNS, RIKEN Accelerator Research Facility (RARF), and the Department of Physics, University of Tokyo [1, 2]. We summarize the achievements of our works in Sects.2-7 individually.

## 2. Evolution of Nuclear Shells due to the Tensor Force

We showed that the monopole effect of the tensor force is presented in the shell structure, exhibiting how spherical single-particle energies are shifted as protons or neutrons occupy certain orbits [3]. An analytic relation for such shifts exhibited their general features clearly and explained intuitively. Single-particle levels were shown to change in a systematic and robust way, by using the  $\pi+\rho$  meson exchange tensor potential, consistently with the chiral perturbation idea.

## 3. Cluster-Shell Competition in Light Nuclei

We proposed a simple model to describe cluster-shell competition [4]. Introducing only one parameter ( $\Lambda$ ) to the wave function makes it possible to describe the asymptotic transition of two valence neutrons in  $^{10}\text{Be}$  ( $\alpha + \alpha + n + n$ ) from a di-neutron to independent particles when the contribution of the spin-orbit interaction is taken into account. Similarly in  $^{12}\text{C}$ , a transition from a  $3\alpha$  configuration to a  $2\alpha + 4N$  configuration was represented, and we showed a strong contribution of the spin-orbit interaction in the ground state. We investigated further this transition from the cluster state ( $\alpha + ^{16}\text{O}$ ) to the shell-model state ( $^{16}\text{O} + \text{four nucleons}$ ) in  $^{20}\text{Ne}$ .

We modified the alpha-cluster model by including the contribution of the tensor interaction for light nuclei [5]. In  $^8\text{Be}$ , the energy curve with respect to the relative distance between the two  $^4\text{He}$  clusters suggests that the cluster structure persists even though the tensor interaction contributes strongly. In addition to the tensor interaction, a simplified method to take into account the strong spin-orbit contribution was introduced and the coupling effects of these two models was shown to be important in  $^{12}\text{C}$ , in contrast to  $^8\text{Be}$ .

## 4. Shell-Model Calculation of Nuclei around $N \sim 20, 28$

For the structure of exotic nuclei, we have performed systematic shell-model calculations [6, 7, 8, 9, 10, 11, 12, 13] in the  $N \sim 20$  region using the SDPF-M interaction [14]. While we have mainly studied the so-called "island of inversion" region until the last year, we have been extending the region including stable nuclei recently. The  $N = 20$  isotones around  $Z = 20$  are known to have a spherical-deformed shape coexistence: the former and the latter are dominated by the normal and intruder states, respectively. Thus, the description of that region is highly related to the appropriateness of the shell gap given by the Hamiltonian adopted. Figure 1 shows the energy levels of  $^{36}\text{S}$  compared between experiment and shell model, showing a good agreement with experiment including the deformed states by MCSM calculation with SDPF-M. This agreement strongly supports the varying  $N = 20$  shell gap as  $Z$  moves, dominated by the spin-isospin dependence [15] or the tensor force [3] in the effective interaction.

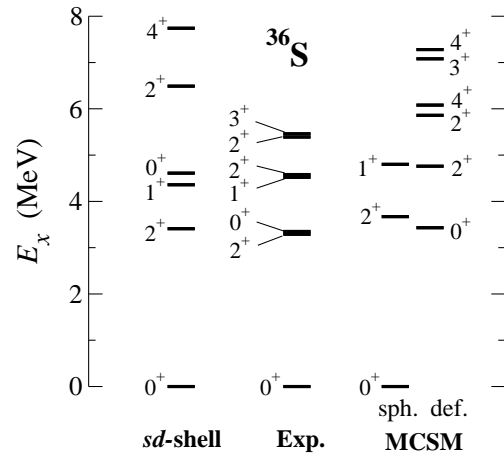


Figure 1. Experimental energy levels of  $^{36}\text{S}$  compared to shell-model calculations performed by the  $sd$  shell model with USD and by the MCSM calculation with SDPF-M.

Since the SDPF-M interaction is not designed to calculate the nuclear structure in the  $N \sim 28$  region due to the limitation of the model space, we have started to make a new effective interaction for the full  $sd$ - $pf$  shell model space to give a unified nuclear structure and a shell evolution over this region. We have developed a code to calculate the two-

body matrix elements of any potential form of interaction. Comparing the  $T = 0$  tensor part among interactions on the market, we have found that that of the GXPF1 interaction for the  $pf$  shell is rather close to the  $\pi + \rho$  tensor force whereas that of USD for the  $sd$  shell is much weaker than  $\pi + \rho$ . That seems to justify a modification to USD in the monopole interaction taken in SDPF-M from a microscopic point of view. We have adopted  $\pi + \rho$  as the  $T = 0$  tensor part of the cross shell interaction, making a shell-model calculation for  $N = 28$  isotones. As a result, the tensor interaction plays an essential role in the magic structure of  $^{42}\text{Si}$  which is a candidate for a new magic nucleus. The new interaction predicts it containing a large oblate deformed component, whereas an interaction based on the Millener-Kurath interaction results in a nearly spherical nucleus due to the difference of both the proton and the neutron shell gaps caused by the tensor interaction.

### 5. Structure of Neutron-Rich $pf$ -Shell Nuclei

The structure of neutron-rich  $pf$ -shell nuclei has been investigated on the basis of the large scale shell-model calculations with the effective interaction GXPF1 [16]. The energy levels of the  $N=31$  isotope  $^{53}\text{Ti}$  [17] was measured, which are in good agreement with the shell-model prediction [18]. On the other hand, the measured E2 transition strengths deviate from the predicted values at  $N=32$  for both Ti and Cr isotopes [19, 20]. These results suggest a need of large neutron polarization charge, consistently with the study of the systematics in the ratio of the E2 transition matrix elements  $M_n/M_p$  for the  $N=28$  isotopes [21, 22]. Also, the property of Gamow-Teller transitions has been investigated [22, 23] by using the same effective interaction.

### 6. Quadrupole collective states

The nuclear structure of ground states and low-lying excited states of even-even isotopes around  $^{134}\text{Ba}$  was described using the nuclear shell model microscopically [24]. In terms of the collective model, the structure of Ba isotopes is known to vary from spherical shape to axially symmetric deformed rotor and triaxially deformed shape depending on the neutron numbers. Moreover, it shows the realization of the critical point symmetry,  $E(5)$ , which is considered to be appeared at  $^{134}\text{Ba}$ . By using the microscopic description using the nuclear shell model, our study provided microscopic evidence to support these views, and showed that the structures of  $^{126-130}\text{Ba}$  are well described by the axially symmetric rotor with  $\gamma$ -vibration.

### 7. Extrapolation Method with Projected Deformed Basis

We showed that the exact solution of large-scale shell model calculations can be obtained by the energy variance extrapolation method with spherical and deformed bases [25]. The extrapolation formula including  $\hat{H}^3$  matrix element was presented in shell model calculations, and its feasibility was also shown in  $pf$ -shell calculation.

### 8. Summary

We have carried out various nuclear structure calculations and produced a lot of achievements during fiscal year 2005 [3, 4, 5, 6, 7, 8, 9, 10, 11, 12, 13, 17, 18, 19, 20, 21, 22, 23, 24, 25].

### References

- [1] Grant-in-Aid for Specially Promoted Research (13002001) from the Ministry of Education, Science, Sport, Culture and Technology.
- [2] N. Shimizu, T. Otsuka, N. Itagaki, T. Mizusaki, M. Honma, and Y. Utsuno, CNS Annual Report 2004 (2004) 95.
- [3] T. Otsuka, T. Suzuki, R. Fujimoto, H. Grawe, and Y. Akaishi, Phys. Rev. Lett. **95** (2005) 232502.
- [4] N. Itagaki, H. Masui, M. Ito, and S. Aoyama, Phys. Rev. C **71** (2005) 064307.
- [5] N. Itagaki, H. Masui, M. Ito, S. Aoyama, and K. Ikeda, Phys. Rev. C **73** (2006) 034310.
- [6] V. Tripathi *et al.*, Phys. Rev. Lett. **94** (2005) 162501.
- [7] Y. Utsuno, Euro. Phys. J. A **25** Suppl. (2005) 209.
- [8] P. Mason *et al.*, Phys. Rev. C **71** (2005) 014316.
- [9] T. K. Onishi *et al.*, Phys. Rev. C **72** (2005) 024308.
- [10] M. Belleguic *et al.*, Phys. Rev. C **72** (2005) 054316.
- [11] Y. Utsuno *et al.*, J. Phys.: Conf. Ser. **20** (2005) 167.
- [12] M. Ionescu-Bujor *et al.*, Phys. Rev. C **73** (2006) 024310.
- [13] Y. Utsuno *et al.*, *Proceedings of the 5th Italy-Japan Symposium on Recent Achievements and Perspectives in Nuclear Physics*, (World Scientific, Singapore, 2005) p. 19.
- [14] Y. Utsuno *et al.*, Phys. Rev. C **60** (1999) 054315; *ibid.* **70** (2004) 044307.
- [15] T. Otsuka *et al.*, Phys. Rev. Lett. **87** (2001) 082502.
- [16] M. Honma, T. Otsuka, B. A. Brown, and T. Mizusaki, Phys. Rev. C **69** (2004) 034335.
- [17] B. Fornal *et al.*, Phys. Rev. C **72** (2005) 044315.
- [18] M. Honma *et al.*, Eur. Phys. Jour. A **25** Suppl. 1 (2005) 499.
- [19] D.-C. Dinca *et al.*, Phys. Rev. C **71** (2005) 041302(R).
- [20] A. Bürger *et al.*, Phys. Lett. B **622** (2005) 29.
- [21] L. A. Riley *et al.*, Phys. Rev. C **72** (2005) 024311.
- [22] M. Honma *et al.*, Jour. Phys. Conf. Ser. **20** (2005) 7.
- [23] T. Adachi *et al.*, Phys. Rev. C **73** (2006) 024311.
- [24] N. Shimizu, T. Otsuka, T. Mizusaki, and M. Honma, Jour. Phys. Conf. Ser. **20** (2005) 65.
- [25] T. Mizusaki, AIP Conference Proceedings **831** (2005) 235.

# Large-Scale Shell-Model Description of $^{16}\text{C}$ with Microscopic Effective Interactions

S. Fujii<sup>a</sup>, T. Mizusaki<sup>a,b</sup>, T. Otsuka<sup>a,c,d</sup>, T. Sebe<sup>e</sup>, and A. Arima<sup>f</sup>

<sup>a</sup>*Center for Nuclear Study, Graduate School of Science, University of Tokyo*

<sup>b</sup>*Institute of Natural Sciences, Senshu University*

<sup>c</sup>*Department of Physics, University of Tokyo*

<sup>d</sup>*RIKEN (The Institute of Physical and Chemical Research)*

<sup>e</sup>*Faculty of Engineering, Hosei University*

<sup>f</sup>*Science Museum, Japan Science Foundation*

In the shell-model calculation for nuclei, the dimension of the matrix to be diagonalized has been increasing with the progress of the computer performance. This allows one to study nuclei more microscopically without arbitrary assumptions or restrictions. The no-core shell model (NCSM) is representative of this kind of study, and its application to nuclei with the mass number up to  $A \simeq 12$  has been extensively performed in recent years [1, 2]. In the NCSM, the effective interaction is derived from a bare nuclear force in free space, and the model space is taken as large as possible until the calculated result does not depend on the model-space size. Thus, the NCSM is fully microscopic and would have a predictive power. As the mass number is larger, however, it becomes more difficult to obtain the converged result with increasing the model-space size due to a huge computation size. Therefore, it is still of much importance to construct a model for describing light nuclei even if one starts with the bare nuclear force.

In a recent experiment at RIKEN, it has been found that the  $E2$  transition strength between the first  $2^+$  and the ground  $0^+$  states in  $^{16}\text{C}$  is anomalously hindered as  $B(E2; 2_1^+ \rightarrow 0_1^+) = 0.63_{\pm 0.16(\text{syst})}^{\pm 0.11(\text{stat})} e^2\text{fm}^4$  [3], while the  $B(E2; 2_1^+ \rightarrow 0_1^+)$  in other even-even nuclei is known to be rather strong. The dominance of neutron excitation is also suggested for the same transition [4]. In order to theoretically investigate such interesting properties, several calculations have been performed. For neutron-rich carbon isotopes with the mass number  $A \geq 15$ , neutrons begin to fill the  $1s_{1/2}$  and  $0d_{5/2}$  states, while the protons occupy mainly up to the  $0p_{3/2}$  state. Low-lying energy levels of such systems can be well described by the conventional shell model using effective interactions for the  $0p1s0d$  shell [5, 6, 7, 8]. However, the  $B(E2; 2_1^+ \rightarrow 0_1^+)$  values calculated by the shell model using the usual effective charges are significantly larger than the experiments. A similar tendency of  $B(E2; 2_1^+ \rightarrow 0_1^+)$  is seen in the calculations using the bare charges within the anti-symmetrized molecular dynamics (AMD) framework [9]. The discrepancies between the calculations and the experiments may be due to the fact that those models do not include certain exotic features of unstable nuclei because of their bases with some assumptions or adjustments in and near stable nuclei.

In order to deal with this problem, we have recently proposed a new microscopic shell model of no-core type [10]. The model space is composed of the  $0s$ ,  $0p$ ,  $1s0d$  and  $1p0f$

shells. Since the model space is of no-core type and is rather large as compared to that of the conventional shell model, we do not employ the effective charges but use the bare charges. The effective two-body interaction is microscopically derived from a bare nucleon-nucleon potential through a unitary transformation which is used in the unitary-model-operator approach (UMOA) [11, 12]. In the actual shell-model diagonalization, some truncations are needed due to the limited computer power though the calculation is still large scale. The nucleon excitations from the hole states of  $^{14}\text{C}$  are restricted up to two nucleons, and the excitations to the  $1p0f$  shell are also up to two nucleons. The three-or-more-body effective interactions are not taken into account for simplicity though the many-body effective interactions can be generated through the unitary transformation. As for the treatment of the spurious center-of-mass (c.m.) motion, we follow the Gloeckner-Lawson prescription as has been done in many of the shell-model calculations in which a multi- $\hbar\Omega$  model space is considered. Thus, the present shell-model Hamiltonian is composed of the transformed Hamiltonian which contains the sums of the kinetic energy and the two-body effective interaction, and the c.m. Hamiltonian which is multiplied by a large value  $\beta_{\text{c.m.}}$ .

In the following calculations, the CD-Bonn potential [13] is employed as the two-body bare interaction, and the Coulomb force is also included for the proton-proton channel. Since we adopt the above-mentioned approximations, our calculated results may have a  $\hbar\Omega$  dependence. We have confirmed that the  $\hbar\Omega$  dependences of the calculated energy levels of  $^{14-18}\text{C}$  become weak in the range between  $\hbar\Omega = 14$  and  $16$  MeV, and there appear energy minima in this region. Thus, in this study, we use the value of  $\hbar\Omega = 15$  MeV in all the calculations. Since we introduce a minimal refinement of one-body energies in a simple way which will be explained later, we need to use a common value of  $\hbar\Omega$ .

In Fig. 1, calculated and experimental low-lying energy levels of  $^{16}\text{C}$  are shown. The first column in Fig. 1, denoted by ‘‘original’’, represents the results obtained directly from the present method without any adjustable parameters. It is seen that the calculated  $2_1^+$ ,  $2_2^+$  and  $4_1^+$  states are in good agreement with the experiment though the  $0_2^+$  and  $3_1^+$  states appear somewhat higher than the experiment.

We note here that, in the present shell-model calculation for  $^{15}\text{C}$ , the  $1/2_1^+$  state appears above the  $5/2_1^+$  state, contrary to the experiment. This wrong ordering may be one of

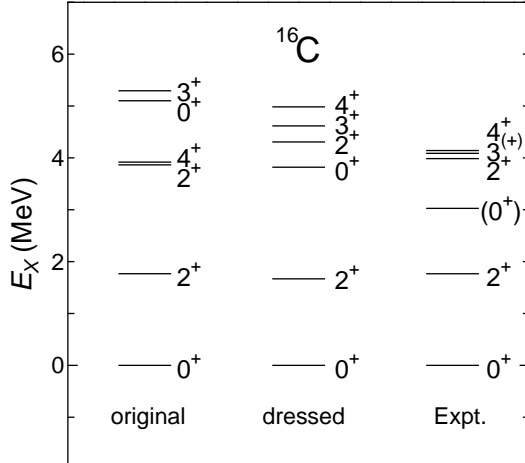


Figure 1. Low-lying energy levels of  $^{16}\text{C}$ .

the reasons for the discrepancy between the results and the experiments in the excited states of  $^{16}\text{C}$  for the case “original” in Fig. 1. If we consider a sufficiently large model space and calculate these energy levels using the same CD-Bonn potential within the UMOA framework, which is fully microscopic and appropriate for the description of the single-particle state, we can reproduce the correct ordering in  $^{15}\text{C}$  as has been shown in Ref. [14]. In order to obtain the correct ordering in  $^{15}\text{C}$  in the present shell model, we introduce a minimal refinement of neutron one-body energies on top of  $^{14}\text{C}$  so as to reproduce the UMOA results for  $^{15}\text{C}$ . In this way, we treat complex correlations coupled to a single-particle-like state within a rather simple framework. Thus, the present approach is a hybrid method combining a no-core type of shell model with single-particle information by the UMOA. Hereafter, we refer to the calculated results with the minimal refinement as “dressed”. As seen in the results for “dressed” in Fig. 1, the calculated results become better by introducing the dressed one-body energies. Namely, the correct ordering of the low-lying energy levels is obtained.

In Table 1, the calculated and experimental values of  $B(E2; 2_1^+ \rightarrow 0_1^+)$  for  $^{16}\text{C}$  are tabulated together with the values for  $^{14}\text{C}$  and  $^{18}\text{C}$  to investigate the isotope dependence. For  $^{16}\text{C}$ , the calculated  $B(E2)$  value becomes closer to the anomalously hindered experimental value by introducing the dressed one-body energies. As we have explained before, in the present calculation, we do not employ the effective charges for the neutron and proton but use the bare charges.

For  $^{14}\text{C}$ , the calculated results of  $B(E2; 2_1^+ \rightarrow 0_1^+)$  for “original” and “dressed” are identical, and show a good agreement with the experiment. We note, however, that the calculated energy spacings between the  $0_1^+$  and  $2_1^+$  states for the cases “original” and “dressed” are identically 5.39 MeV, whereas the experimental value is 7.01 MeV. Thus, the calculated energy spacings are somewhat smaller than the experiment.

For  $^{18}\text{C}$ , the calculated energy spacings between the  $0_1^+$  and  $2_1^+$  states for “original” and “dressed” are 1.44 and 1.73 MeV, respectively. Since the experimental value is 1.62

Isotopes	original	dressed	Expt.
$^{14}\text{C}$	3.42	3.42	$3.74 \pm 0.50$
$^{16}\text{C}$	1.30	0.84	$0.63^{+0.11(\text{stat})}_{-0.16(\text{syst})}$
$^{18}\text{C}$	1.19	2.10	

Table 1. The calculated and experimental  $B(E2; 2_1^+ \rightarrow 0_1^+)$  values in units of  $e^2\text{fm}^4$  for  $^{14,16,18}\text{C}$ . The experimental value for  $^{16}\text{C}$  is taken from Ref. [3].

MeV, our calculated results are not so different from the experiment. As for the  $B(E2; 2_1^+ \rightarrow 0_1^+)$ , as shown in Table 1, the result for “dressed” is larger than that for “original”. Furthermore, the result for  $^{18}\text{C}$  for “dressed” is about three times larger than the experimental value for  $^{16}\text{C}$ . A similar tendency is seen in the  $0p1s0d$  shell-model calculations [7,8]. Thus, it is of great interest that the  $B(E2)$  value for  $^{18}\text{C}$  is experimentally established.

In summary, we have investigated low-lying energy levels and  $B(E2; 2_1^+ \rightarrow 0_1^+)$  of  $^{16}\text{C}$  by introducing a new shell-model method of no-core type with the model space up to the  $1p0f$  shell. We have also calculated the  $B(E2; 2_1^+ \rightarrow 0_1^+)$  values for  $^{14}\text{C}$  and  $^{18}\text{C}$  to see the isotope dependence. The present work is the first study which can successfully describe the structure of  $^{16}\text{C}$  including its anomalously hindered  $B(E2; 2_1^+ \rightarrow 0_1^+)$  value based on the microscopic effective interaction with the bare charges. More detailed analyses for neutron-rich carbon isotopes are in progress.

## References

- [1] P. Navrátil, J. P. Vary, W. E. Ormand and B. R. Barrett, Phys. Rev. Lett. **87** (2001) 172502.
- [2] C. Forssén, P. Navrátil, W. E. Ormand and E. Caurier, Phys. Rev. C **71** (2005) 044312.
- [3] N. Imai *et al.*, Phys. Rev. Lett. **92** (2004) 062501.
- [4] Z. Elekes *et al.*, Phys. Lett. B **586** (2004) 34.
- [5] E. K. Warburton, B. A. Brown, Phys. Rev. C **46** (1992) 923.
- [6] V. Maddalena *et al.*, Phys. Rev. C **63** (2001) 024613.
- [7] R. Fujimoto, Ph. D. thesis, University of Tokyo, 2003.
- [8] H. Sagawa, X. R. Zhou, X. Z. Zhang and T. Suzuki, Phys. Rev. C **70** (2004) 054316.
- [9] Y. Kanada-En’yo, Phys. Rev. C **71** (2005) 014310.
- [10] S. Fujii, T. Mizusaki, T. Otsuka, T. Sebe and A. Arima, nucl-th/060131.
- [11] K. Suzuki and R. Okamoto, Prog. Theor. Phys. **92** (1994) 1045.
- [12] S. Fujii, R. Okamoto and K. Suzuki, Phys. Rev. C **69** (2004) 034328.
- [13] R. Machleidt, F. Sammarruca and Y. Song, Phys. Rev. C **53** (1996) R1483.
- [14] S. Fujii, R. Okamoto and K. Suzuki, J. Phys. Conf. Ser. **20** (2005) 83; nucl-th/0505076.

## **Other Activities**



## The Fourth CNS International Summer School (CISS05)

S. Shimoura, T. Otsuka<sup>a</sup>, T. Mizusaki<sup>b</sup>, and H. Sakai<sup>a</sup>

*Center for Nuclear Study (CNS), Graduate School of Science, University of Tokyo*

<sup>a</sup> *Department of Physics, Graduate School of Science, University of Tokyo*

<sup>b</sup> *Senshu University*

The 4th CNS International Summer School (CISS05) was held at the Wako branch of the Center for Nuclear Study (CNS), the University of Tokyo, in the period of August 18–23, 2005.

This summer school is the fourth one in the series which aimed at providing graduate students and Post Docs with basic knowledge and perspectives of nuclear physics. Topics of this year were “Nuclear forces”, “Mean field calculation”, and “Collective modes studied by direct reactions”. Short lectures on recent progress in physics with unstable nuclei were also presented. Additionally, physics performed in the SHARQA project was introduced.

The list of lecturers and the titles of lectures are shown below.

G.F. Bertsch (Washington, USA)	“Nuclear structure in mean-field theory and its extensions”
M.N. Harakeh (KVI, the Netherlands)	“Collective modes investigated by inelastic scattering and charge-exchange reactions with magnetic spectrometers”
R. Machleidt (Idaho, USA)	“Nuclear Forces”
T. Kajino (NAO)	“Nucleosynthesis in Supernovae and the Big-Bang”
K. Yabana (Tsukuba)	“Novel computational approaches for nuclear reactions”
N. Aoi (RIKEN)	“Exotic structure of unstable nuclei revealed through a gamma-ray spectroscopy technique”
E. Ideguchi (CNS)	“Study of high-spin states by using stable and unstable nuclear beams”
T. Mizusaki (Senshu/CNS)	“Shell model calculation – from basics to the latest methods –”
T. Teranishi (Kyushu)	“Low-energy radioactive beam experiments for nuclear astrophysics”
T. Uesaka (CNS)	“Studies of new excitation modes in nuclei via exothermic nuclear reactions”

This year, 111 attendances were gathered together from 6 countries: Among them, 22 attendances were from Asian countries, China, Korea, Malaysia, Vietnam, and Myanmar. Domestic attendances were from 15 universities and 2 institutes over the country.

The lectures were given from 10:00 in the morning to 18:00 in the evening. This year, the student and Post Doc sessions and Question Time were provided within the lecture time. Ten talks were given by graduate students and Post Docs. The attendances also communicated each other in the Free Discussion time after dinner with a relaxed atmosphere.

All the information concerning the summer school, including lecture notes, is open for access at the following URL:

<http://www.cns.s.u-tokyo.ac.jp/summerschool/>

The organizers thank all the attendances and all the members of the CNS who supported the summer school. They are also grateful to RIKEN for their supports in the preparation of the school. This school was supported in part by the International Exchange Program of Graduate School of Science, the University of Tokyo.

# Nuclear Scattering Experiments for Education of Undergraduate Students

T. Kawabata<sup>a</sup>, K. Yako<sup>b</sup>, Y. Sasamoto<sup>a</sup>, H. Sakai<sup>b</sup>, and S. Shimoura<sup>a</sup>

<sup>a</sup>Center for Nuclear Study, Graduate School of Science, University of Tokyo

<sup>b</sup>Department of Physics, University of Tokyo, Tokyo

Nuclear scattering experiments were performed for education of undergraduate students of the University of Tokyo as a part of the curriculum of experimental physics. This program was aiming at providing undergraduate students with an opportunity to learn how to study the world of  $< 10^{-14}$  m by using an ion beam from an accelerator. In this year, 32 students joined this program.

The four beam times were scheduled in the second semester for juniors, and 8 students participated in each beam time. The experiment was performed at the RIKEN accelerator research facility (RARF) using a 26-MeV alpha beam accelerated by the AVF cyclotron. The alpha beam extracted from the AVF cyclotron was transported to the CRIB beam line in the E7 experimental room. In each beam time, the students were divided into two groups and took one of the following two subjects;

1. Measurement of gamma rays emitted in the cascade decay of the rotational bands in  $^{154}\text{Gd}$  and  $^{184}\text{Os}$ .
2. Measurement of elastic scattering of  $\alpha$  particles from  $^{197}\text{Au}$ .

Before the experiment, the students learned the basic handling of the semiconductor detectors and electronic circuits at the Hongo campus, and attended a radiation safety lecture at RIKEN. They also joined a tour to the RI beam facility, which was under construction at RIKEN.

In the measurement of the rotational bands, excited states in  $^{154}\text{Gd}$  and  $^{184}\text{Os}$  nuclei were populated by the  $^{152}\text{Sm}(\alpha, 2n)$  and  $^{182}\text{W}(\alpha, 2n)$  reactions, respectively. The gamma rays emitted from the cascade decay of the rotational bands were measured by a high purity germanium detector located 50 cm away from the target. The energies of the gamma rays were recorded by a multi-channel analyzer (MCA) system. The gain and the efficiency of the detector system had been calibrated with standard gamma-ray sources of  $^{22}\text{Na}$ ,  $^{60}\text{Co}$ ,  $^{133}\text{Ba}$ , and  $^{137}\text{Cs}$ . The typical spectrum of the gamma rays from the cascade decay of the rotational band in  $^{154}\text{Gd}$  is shown in Fig. 1. The gamma rays from the  $10^+ \rightarrow 8^+$  decay were successfully measured. Based on the energies of the gamma rays, the moment of inertia and the deformation parameters of the excited states were discussed by using a classical rigid rotor model and a irrotational fluid model. The students found that the reality lies between the two extreme models. The initial population among the levels in the rotational band was also discussed by taking the effect of internal conversion into account.

In the  $\alpha + ^{197}\text{Au}$  measurement,  $\alpha$  particles scattered from the Au target with a thickness of  $1.42 \text{ mg/cm}^2$  were detected by a silicon PIN-diode located 11 cm away from the target.

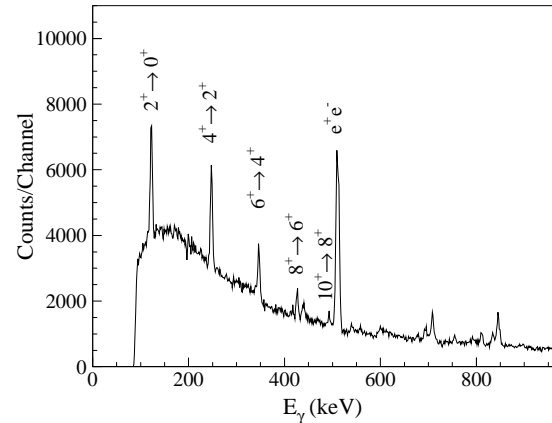


Figure 1. Typical spectrum of the gamma rays from the cascade decay of the rotational band in  $^{154}\text{Gd}$ .

A plastic collimator with a diameter of 6 mm was attached on the silicon detector. The energy spectrum of the scattered  $\alpha$  particles was recorded by the MCA system. The beam was stopped by a Faraday cup in the scattering chamber. The cross section for the alpha elastic scattering was measured in the angular range of  $\theta_{\text{lab}} = 25\text{--}150^\circ$ . The measured cross section was compared with the calculated cross section for the Rutherford scattering. The cross section was also analyzed by the potential-model calculation, and the radius of the gold nucleus was discussed. Some students obtained the radius of  $\sim 10$  fm by using a classical model where the trajectory of the  $\alpha$  particle in the nuclear potential is obtained by the Runge-Kutta method. Others tried to understand the scattering process by calculating the angular distribution by the distorted wave Born approximation with a Coulomb wave function and a realistic nuclear potential.

We believe this experiment is very impressive for the students. It was the first time for most of the students to use large experimental equipments. They learned basic things about the experimental nuclear physics and how to extract physics from the data.

The authors would like to thank Dr. Y. Uwamino, Prof. Y. Sakurai, and the RARF cyclotron crew for their helpful effort in the present program.

## **Appendices**

**Symposium, Workshop, Seminar, Colloquium, and PAC**

**CNS Reports**

**Publication List**

**Talks and Presentations**

**Personnel**



# Symposium, Workshop, Seminar, Colloquium, and PAC

## A. Symposium

1. The International Symposium on “Origin of Matter and Evolution of Galaxies 2005 - New Horizon of Nuclear Astrophysics and Cosmology -”  
November 8-11, 2005, Koshiba Hall, University of Tokyo, Tokyo, Japan.

This is a series of nuclear astrophysics international symposium being held roughly every other year since 1988 by CNS together with other institutions. The first meeting was very much promoted by the strong interest of radioactive nuclear beams in nuclear physics under a title of Heavy Ion Physics and Nuclear Astrophysical Problems.

It was hosted this time by five institutions; National Astronomical Observatory (NAO), The Graduate University for Advanced Studies (GUAS), Department of Astronomy, Graduate School of Science, University of Tokyo (Tokyo), Center for Nuclear Study, University of Tokyo (CNS), and RIKEN Accelerator Research Facility (RIKEN). The symposium was participated by about 150 people, including about 50 people from outside of Japan. Because of the special fund provided from GAUS under the conference name of “SUBARU Astronomy for the Establishment of Cosmo-Nuclear Astrophysics”, we placed an emphasis this time on observational works and cosmology. As for nuclear physics, it also was a good occasion. The third-generation RI Beam facility RIBF is just about to deliver the first beam, and low energy RI beams have become available at the CNS RI Beam in-flight separator CRIB at the University of Tokyo and also at Tokai RI ACcelerator facility TRIAC by the KEK-JAEA collaboration.

The symposium proceedings will be published soon as one of the conference reports of the American Institute of Physics.

The organizing committee was comprised of W. Aoki (NAO/GUAS: Co-chair), M. Y. Fujimoto (Hokkaido), S. Honda (NAO), T. Kajino (NAO/GUAS/Tokyo: Chair), S. Kawanomoto (NAO), S. Kubono (Tokyo: Co-chair), T. Motobayashi (RIKEN/Tokyo: Co-chair), K. Noguchi (NAO/GUAS), K. Nomoto (Tokyo: Co-chair), T. Shigeyama, (Big Bang Center, Tokyo), Y. Takeda (NAO/GUAS), and K. Yoneda (RIKEN).

2. The International Symposium on “Structure of exotic nuclei and nuclear forces”  
March 9-12, 2006, Koshiba Hall, University of Tokyo, Tokyo, Japan.

The purpose of the symposium was to discuss on theoretical and experimental developments and future prospects in physics of structure of exotic nuclei, and its relation to the nucleon-nucleon interaction, mainly from the viewpoint of the shell model. The related issues, for instance, the double beta decay, were discussed.

This symposium was organized mainly as an activity of the research project, “Monte Carlo Shell Model”, funded by Grant-in-Aid for Specially Promoted Research from the Ministry of Education, Culture, Sports, Science and Technology. It was supported by CNS as well as by RIKEN.

We enjoyed excellent and lively 26 invited talks and 34 oral presentations in the symposium with 78 participants. The participants are from Japan, United States, France, Germany, Italy, Great Britain and Hungary.

The proceedings will be published by the Institute of Physics.

The organizing committee was comprised of B.A. Brown (MSU), S. Fujii (CNS), M. Honma (Aizu), T. Kajino (NAO), T. Mizusaki (Senshu), T. Motobayashi (RIKEN), K. Muto (TIT), T. Otsuka, chair (Tokyo/CNS/RIKEN), P. Ring (TMU), N. Shimizu, scientific secretary (Tokyo), S. Shimoura (CNS), and Y. Utsuno, scientific secretary (JAEA).

## B. Workshop

1. 11th International Workshop on Polarized Sources and Targets (PST05)  
November 14–17, 2005, Yayoi Auditorium Ichijo Hall, the University of Tokyo, Japan.

The workshop is a traditional one to discuss physics and technologies related to the polarized gas/solid targets, polarized electron/ion/neutron sources, and polarimetry. Its 11th meeting was co-hosted by CNS and RIKEN. 82 scientists including 29 from abroad participated and joined active discussions on various aspects of polarization techniques and its applications.

The organizers are K. Asahi (co-chair, RIKEN/TITech), H. En'yo (RIKEN), K. Hatanaka (RCNP), N. Horikawa (Chubu), K. Imai (Kyoto), T. Iwata (Yamagata), T. Kawabata (CNS), Y. Miyachi (TITech), Y. Mori (Kyoto), T. Nakanishi (Nagoya), H. Okamura (CYRIC), H. Sakai (co-chair, Tokyo), N. Sakamoto (RIKEN), Y. Sakemi (RCNP), T. Shibata (TITech), T. Shimoda (Osaka), T. Tamae (LNS, Tohoku), A. Tamii (RCNP), M. Uchida (TITech), T. Uesaka (CNS, secretary), K. Yako (Tokyo), and A. Yoshimi (RIKEN, secretary).

2. Workshop on “Technical Aspects of SHARAQ Spectrometer”  
November 20, 2005, CNS Wako Campus, Saitama, Japan//

The purpose of this workshop was to discuss technical aspects of the design and construction of the SHARAQ spectrometer, the beamline with a large dispersion, and the detector system. Three professors. J.A. Nolen (ANL), H. Geissel (GSI) and W. Mittig (GANIL), were invited and made valuable suggestion and discussion with about 20 participant.

The organizers are S. Shimoura (CNS), T. Uesaka (CNS), and H. Sakai (Tokyo).

3. RIKEN-CNS RIBF International Workshop: “Correlation and Condensation: New Features in Loosely Bound and Unbound Nuclear States”  
December 8–10, 2005, Conference room, RIBF Building 2F, RIKEN

The scope of the workshop covered new features in loosely bound and unbound nuclear states such as di-neutron correlation and clustering phenomena. Recent theoretical and experimental results were presented and discussed with the 50 participants including the 5 speakers from abroad.

The organizers are S. Aoyama (Niigata), Y. Funaki (Kyoto), H. Horiuchi (Kyoto), T. Kawabata (CNS), M. Matsuo (Niigata), T. Motobayashi (RIKEN), T. Nakamura (TIT), and M. Takashina (RIKEN).

4. CNS Workshop on “Past, Present and Future of Shell Model (with a course of shell model code)”  
Jan 26-28, 2006, CNS Wako Campus, Saitama, Japan.

In this workshop, experimental and theoretical studies related to the shell model were presented, including some reviews and histories. Current problems and future directions were also indicated. The major discussions were on the issues such as recent progress on the Monte Carlo shell model, nuclear structure calculations from the first principle, properties of chiral band, recent results on random interactions, roles of nuclear shell model for astrophysics, and recent experimental developments. In addition to the ordinary talks and discussions, one-hour training course was offered so that participants can master how to run a state-of-the-art shell-model code.

The presentation file of each talk is now accessible on-line at the CNS WEB cite.

The organizers are T. Mizusaki (Senshu, CNS), S. Kubono (CNS), T. Shimoura (CNS), and S. Fujii (CNS).

5. International Workshop on “Physics of Quark Gluon Plasma”  
February 16-17, 2006, RIKEN, Saitama, Japan

The purpose of this workshop was to achieve further understanding for the property of QGP. We discussed on the hot results from RHIC with enough time slots. The RHIC operation was started to study Quark-Gluon-Plasma and we obtained various new results from RHIC data in 5 years. We realized that the hadronic matter with high

temperature and density has very rich phases, such as color glass condensate. Three professors, G. Baym(Illinois), J. Ruppert(Duke), and S. Midouszewski (Texas A&M) were invited and gave valuable talks. About 60 scientists participated and 17 talks were presented.

The presentation file of each talk is now accessible on-line at  
[http://phenix.cns.s.u-tokyo.ac.jp/ws06/index\\_e.html](http://phenix.cns.s.u-tokyo.ac.jp/ws06/index_e.html)

The organizers are H. Hamagaki(CNS), T. Hatsuda(Tokyo), H. En'yo(RIKEN), M. Asakawa(Osaka), S. Yokkaichi(RIKEN), K. Ozawa(CNS), and H. Torii(RIKEN).

6. International Workshop on "Nuclear Physics with RIBF"  
March 13-17, 2006, RIKEN, Saitama, Japan

This workshop organized by RIKEN and CNS on the occasion that the RI Beam Factory (RIBF) will be constructed in 2006. The aim of this workshop was to discuss various research programs in RIBF and to point out problems to be solved by exchanging ideas and interests. This workshop also gave a trigger to form collaborations and networks for both coming experimental and theoretical works. About 150 scientists including 30 from abroad participated and 90 talks were presented.

Workshop web site: <http://rarfaxp.riken.go.jp/RIBF2006/>

The organizers are T. Kubo (RIKEN), N. Aoi (RIKEN), H. Ueno(RIKEN), S. Shimoura (CNS), K. Asahi (RIKEN), T. Kobayashi (Tohoku), M. Wada (RIKEN), A. Ozawa (Tsukuba), M. Wakasugi (RIKEN), K. Morita (RIKEN), T. Kubono (CNS), T. Otsuka (Tokyo), A. Ono (Tohoku), K. Hagino (Tohoku), M. Matsuo (Niigata), T. Motobayashi (RIKEN), Y. Enyo (YIFP), H. Sagawa (Aizu), K. Ogata (Kyushu), A. Kohama (RIKEN), K. Yabana (Tsukuba), and H. Sakurai (RIKEN).

### C. CNS Seminar

1. "Indirect techniques in nuclear astrophysics",  
Prof. Akram M. Mukhamedzhanov(Cyclotron Institute, Texas A&M University), April 28th, 2005.
2. "High-Spin Level Structures of N=81 Near-Spherical Nuclei  $^{142}\text{Pm}$  and  $^{141}\text{Nd}$ ",  
Dr. Minliang Liu (CNS, University of Tokyo), October 13th, 2005.
3. "Study of the High-Spin States in  $^{145}\text{Tb}$  and  $^{157}\text{Yb}$ ",  
Dr. Yong Zheng(CNS, University of Tokyo), October 13th, 2005.
4. "超新星爆発と原子核物理について",  
Dr. Chikako Ishizuka (Hokkaido University), February 10th, 2006.

### D. CNS Colloquium

1. "Global aspects of hot and dense matter created at RHIC",  
Prof. Hideki Hamagaki (CNS, University of Tokyo), July 7th, 2005.
2. "Recent results from mass measurements at GANIL, odd even staggering and global energy problems",  
Prof. Wolfgang Mitting (Grand Accelérateur National D'Ions Lourds(GANIL)), December 5th, 2005.
3. "材料・バイオ・医学分野を切り拓く加速器テクノロジーの高度化研究",  
Prof. Mitsuhiro Fukuda (Japan Atomic Energy Agency), February 20th, 2006.
4. "Experimental studies for the rp process",  
Prof. Georg P. Berg(University of Notre Dame), February 20th, 2006.

## E. CNS Program Advisory Committee

The 6th CNS PAC meeting  
December 7th, 2005.

The CNS Program Advisory Committee examined 7 experimental proposals and evaluated research activities of each project at CNS.

### Approved Proposals

1. K.I. Hahn: The  $^{14}\text{O}(\alpha,p)^{17}\text{F}$  reaction at energies around the 6.15 MeV resonance in  $^{18}\text{Ne}$
2. S. Cherubini: Study of the  $^{18}\text{F}+p \rightarrow ^{15}\text{O}+\alpha$  reaction at astrophysical energies
3. A.A. Chen: On the Waiting Point at A=30 in X-ray Bursts:  $^{30}\text{S}(\alpha,p)^{33}\text{Cl}$  with CRIB
4. Lo.H. Khiem: Direct measurement of  $(\alpha,p)$  reaction with  $^{21}\text{Na}$  radioactive beam
5. T. Teranishi: Study of T=3/2 resonance levels in A=9 nuclei
6. K. Asahi: Production of polarized radioactive beams via the inverse-kinematics reactions and their application

## CNS Reports

#66 “CNS Annual Report 2004”,  
edited by T. Kawabata and H. Ayabe, Aug. 2005.

#67 “Low-Energy Radioisotope Beam Separator CRIB”,  
S. Michimasa, S. Shimoura, H. Iwasaki, M. Tamaki, S. Ota, N. Aoi, H. Baba, N. Iwasa, S. Kanno, S. Kubono,  
K. Kurita, M. Kurokawa, T. Minemura, T. Motobayashi, M. Notani, H. J. Ong, A. Saito, H. Sakurai, E. Takeshita,  
S. Takeuchi, Y. Yanagisawa, and A. Yoshida, Oct. 2005.

# Publication List

## A. Original Papers

1. K. Adcox *et al.* (PHENIX Collaboration): “Formation of dense partonic matter in relativistic nucleus nucleus collisions at RHIC: Experimental evaluation by the PHENIX collaboration”, Nucl. Phys. A **757** (2005) 184–283.
2. S. S. Adler *et al.* (PHENIX Collaboration): “Deuteron and antideuteron production in Au+Au collisions at  $\sqrt{s_{NN}} = 200$  GeV”, Phys. Rev. Lett. **94** (2005) 122302 (6 pages).
3. S. S. Adler *et al.* (PHENIX Collaboration): “Jet structure of baryon excess in Au+Au collisions at  $\sqrt{s_{NN}} = 200$  GeV”, Phys. Rev. C **71** (2005) 051902 (6 pages).
4. S. S. Adler *et al.* (PHENIX Collaboration): “Systematic studies of the centrality and  $\sqrt{s_{NN}}$  dependence of  $dE_T/d\eta$  and  $dN_{ch}/d\eta$  in heavy ion collisions at mid-rapidity”, Phys. Rev. C **71** (2005) 034908 (25 pages) [Erratum-ibid. C **71** (2005) 049901 (1 page)].
5. S. S. Adler *et al.* (PHENIX Collaboration): “Production of  $\phi$  mesons at mid-rapidity in  $\sqrt{s_{NN}} = 200$  GeV Au+Au collisions at RHIC”, Phys. Rev. C **72** (2005) 014903 (23 pages).
6. S. S. Adler *et al.* (PHENIX Collaboration): “Saturation of azimuthal anisotropy in Au+Au collisions at  $\sqrt{s_{NN}} = 62$ -200 GeV”, Phys. Rev. Lett. **94** (2005) 232302 (6 pages).
7. S. S. Adler *et al.* (PHENIX Collaboration): “Mid-rapidity direct-photon production in  $p + p$  collisions at  $\sqrt{s} = 200$  GeV”, Phys. Rev. D **71** (2005) 071102 (7pages).
8. S. S. Adler *et al.* (PHENIX Collaboration): “Measurement of single electron event anisotropy in Au+Au collisions at  $\sqrt{s_{NN}} = 200$  GeV”, Phys. Rev. C **72** (2005) 024901 (10 pages).
9. S. S. Adler *et al.* (PHENIX Collaboration): “Centrality dependence of direct photon production in  $\sqrt{s_{NN}} = 200$  GeV Au+Au collisions”, Phys. Rev. Lett. **94** (2005) 232301 (6 pages).
10. S. S. Adler *et al.* (PHENIX Collaboration): “Measurement of transverse single-spin asymmetries for mid-rapidity production of neutral pions and charged hadrons in polarized  $p + p$  collisions at  $\sqrt{s} = 200$  GeV”, Phys. Rev. Lett. **95** (2005) 202001 (6 pages).
11. S. S. Adler *et al.* (PHENIX Collaboration): “ $J/\psi$  production and nuclear effects for  $d$ +Au and  $p + p$  collisions at  $\sqrt{s_{NN}} = 200$  GeV”, Phys. Rev. Lett. **96** (2006) 012304 (6 pages).
12. S. S. Adler *et al.* (PHENIX Collaboration): “Single electrons from heavy flavor decays in  $p + p$  collisions at  $\sqrt{s} = 200$  GeV”, Phys. Rev. Lett. **96** (2006) 032001 (6 pages).
13. S. S. Adler *et al.* (PHENIX Collaboration): “Measurement of identified  $\pi^0$  and inclusive photon second-harmonic parameter  $v_2$  and implication for direct photon production in  $\sqrt{s_{NN}} = 200$  GeV Au+Au”, Phys. Rev. Lett. **96** (2006) 032302 (6 pages).
14. S. S. Adler *et al.* (PHENIX Collaboration): “Nuclear modification of electron spectra and implications for heavy quark energy loss in Au+Au collisions at  $\sqrt{s_{NN}} = 200$  GeV”, Phys. Rev. Lett. **96** (2006) 032301 (6 pages).
15. Z. Fraenkel, T. Gunji, H. Hamagaki, M. Inuzuka, T. Isobe, Y. Morino, S.X. Oda, K. Ozawa, S. Saito, T. Sakaguchi *et al.*: “A hadron blind detector for the PHENIX experiment at RHIC”, Nucl. Instrum. Methods A **546** (2005) 466–480.
16. C. Adler, T. Gunji, H. Hamagaki, M. Inuzuka *et al.* (ALICE Collaboration): “Electron/pion identification with ALICE TRD prototypes using a neural network algorithm”, Nucl. Instrum. Methods A **552** (2005) 364–371.
17. C. Adler, T. Gunji, H. Hamagaki *et al.* (ALICE Collaboration): “Position reconstruction in drift chambers operated with Xe, CO<sub>2</sub> (15%).”, Nucl. Instrum. Methods A **540** (2005) 140–157.
18. A. Andronic, T. Gunji, H. Hamagaki, Y. Morino, S. Saito *et al.* (ALICE Collaboration): “Transition radiation spectra of electrons from 1 GeV/c to 10 GeV/c in regular and irregular radiators”, Nucl. Instrum. Methods A **558** (2006) 516–525.

19. M. Naruki, H. Hamagaki, K. Ozawa *et al.*: “Experimental signature of the medium modification for  $\rho$  and  $\omega$  mesons in 12GeV  $p$ +A reactions”, *Phys. Rev. Lett.* **96** (2006) 092301 (4 pages).
20. J.K. Ahn, K. Ozawa *et al.*: “ $\Sigma^+p$  elastic scattering cross section in the region of  $350 \leq P_{\Sigma^+} \leq 750$  MeV/c with a scintillating fiber active target, *Nucl. Phys. A* **761** (2005) 41–66.
21. Y. Kondo, T. Nakamura, N. Aoi, H. Baba, D. Bazin, N. Fukuda, T. Gomi, H. Hasegawa, N. Imai, M. Ishihara, T. Kobayashi, T. Kubo, M. Miura, T. Motobayashi, A. Saito, H. Sakurai, S. Shimoura, T. Sugimoto, K. Watanabe, Y.X. Watanabe, T. Yakushiji, Y. Yanagisawa, and K. Yoneda: “In-beam  $\gamma$ -ray spectroscopy of neutron-rich boron isotopes  $^{15,17}\text{B}$  via inelastic scattering on  $^{12}\text{C}$ ”, *Phys. Rev. C* **71** (2005) 044611 (9 pages).
22. Z. Elekes, Zs. Dombrádi, R. Kanungo, H. Baba, Zs. Fülöp, J. Gibelin, Á. Horváth, E. Ideguchi, Y. Ichikawa, N. Iwasa, H. Iwasaki, S. Kanno, S. Kawai, Y. Kondo, T. Motobayashi, M. Notani, T. Ohnishi, A. Ozawa, H. Sakurai, S. Shimoura, E. Takeshita, S. Takeuchi, I. Tanihata, Y. Togano, C. Wu, Y. Yamaguchi, Y. Yanagisawa, A. Yoshida, and K. Yoshida: “Low-lying excited states in  $^{17,19}\text{C}$ ”, *Phys. Lett. B* **614** (2005) 174–180.
23. H. Iwasaki, T. Motobayashi, H. Sakurai, K. Yoneda, T. Gomi, N. Aoi, N. Fukuda, Zs. Fülöp, U. Futakami, Z. Gacsi, Y. Higurashi, N. Imai, N. Iwasa, T. Kubo, M. Kunibu, M. Kurokawa, Z. Liu, T. Minemura, A. Saito, M. Serata, S. Shimoura, S. Takeuchi, Y.X. Watanabe, K. Yamada, Y. Yanagisawa, and M. Ishihara: “Quadrupole collectivity of  $^{28}\text{Ne}$  and the boundary of the island of inversion”, *Phys. Lett. B* **620** (2005) 118–124.
24. R. Kanungo, Z. Elekes, H. Baba, Zs. Dombrádi, Zs. Fülöp, J. Gibelin, Á. Horváth, Y. Ichikawa, E. Ideguchi, N. Iwasa, H. Iwasaki, S. Kawai, Y. Kondo, T. Motobayashi, M. Notani, T. Ohnishi, A. Ozawa, H. Sakurai, S. Shimoura, E. Takeshita, and S. Takeuchi, I. Tanihata, Y. Togano, C. Wu, Y. Yamaguchi, Y. Yanagisawa, A. Yoshida, K. Yoshida: “Search for an isomeric state in  $^{19}\text{C}$ ”, *Nucl. Phys. A* **757** (2005) 315–328.
25. Zs. Dombrádi, Z. Elekes, R. Kanungo, H. Baba, Zs. Fülöp, J. Gibelin, Á. Horváth, E. Ideguchi, Y. Ichikawa, N. Iwasa, H. Iwasaki, S. Kanno, S. Kawai, Y. Kondo, T. Motobayashi, M. Notani, T. Ohnishi, A. Ozawa, H. Sakurai, S. Shimoura, E. Takeshita, S. Takeuchi, I. Tanihata, Y. Togano, C. Wu, Y. Yamaguchi, Y. Yanagisawa, A. Yoshida, and K. Yoshida: “Decoupling of valence neutrons from the core in  $^{17}\text{B}$ ”, *Phys. Lett. B* **621** (2005) 81–88.
26. H.J. Ong, N. Imai, N. Aoi, H. Sakurai, Zs. Dombrádi, A. Saito, Z. Elekes, H. Baba, K. Demichi, Zs. Fülöp, J. Gibelin, T. Gomi, H. Hasegawa, M. Ishihara, H. Iwasaki, S. Kanno, S. Kawai, T. Kubo, K. Kurita, Y.U. Matsuyama, S. Michimasa, T. Minemura, T. Motobayashi, M. Notani, S. Ota, H.K. Sakai, S. Shimoura, E. Takeshita, S. Takeuchi, M. Tamaki, Y. Togano, K. Yamada, Y. Yanagisawa, and K. Yoneda: “Neutron-dominant quadrupole collective motion in  $^{16}\text{C}$ ”, *Phys. Rev. C* **73** (2006) 024610 (5 pages).
27. R. du Rietz, S.J. Williams, D. Rudolph, J. Ekman, C. Fahlander, C. Andreoiu, M. Axiotis, M.A. Bentley, M.P. Carpenter, C. Chandler, R.J. Charity, R.M. Clark, M. Cromaz, A. Dewald, G. de Angelis, F. Della Vedova, P. Fallon, A. Gadea, G. Hammond, E. Ideguchi, S.M. Lenzi, A.O. Macchiavelli, N. Mărginean, M.N. Mineva, O. Möller, D.R. Napoli, M. Nespolo, W. Reviol, C. Rusu, B. Saha, D.G. Sarantites, D. Seweryniak, D. Tonev, and C.A. Ur: “Investigation of high-spin states in  $^{53}\text{Fe}$ ”, *Phys. Rev. C* **72** (2005) 014307 (10 pages).
28. B. Hadinia, B. Cederwall, J. Blomqvist, E. Ganioglu, P.T. Greenlees, K. Andgren, I.G. Darby, S. Eeckhaudt, E. Ideguchi, P.M. Jones, D.T. Joss, R. Julin, S. Juutinen, S. Ketelhut, K. Lagergren, A.-P. Leppänen, M. Leino, M. Nyman, J. Pakarinen, E.S. Paul, M. Petri, P. Rahkila, M. Sandzelius, J. Sarén, C. Scholey, J. Uusitalo, R. Wadsworth, and R. Wyss: “First identification of excited states in  $^{106}\text{Te}$  and evidence for isoscalar-enhanced vibrational collectivity”, *Phys. Rev. C* **72** (2005) 041303(R) (5 pages).
29. D. Rudolph, B.G. Carlsson, I. Ragnarsson, S. Åberg, C. Andreoiu, M.A. Bentley, M.P. Carpenter, R.J. Charity, R.M. Clark, M. Cromaz, J. Ekman, C. Fahlander, P. Fallon, E. Ideguchi, A.O. Macchiavelli, M.N. Mineva, W. Reviol, D.G. Sarantites, D. Seweryniak, and S.J. Williams: “ $^{58}\text{Ni}$ : An Unpaired Band Crossing at New Heights of Angular Momentum for Rotating Nuclei”, *Phys. Rev. Lett.* **96** (2006) 092501 (4 pages).
30. H. Ryuto, M. Kunibu, T. Minemura, T. Motobayashi, K. Sagara, S. Shimoura, M. Tamaki, Y. Yanagisawa, and Y. Yano: “Liquid hydrogen and helium targets for radioisotope beams at RIKEN”, *Nucl. Instrum. Methods A* **555** (2005) 1–5.
31. T. Fukuchi, Y. Gono, A. Odahara, S. Tanaka, M. Inoue, Y. Wakabayashi, T. Sasaki, M. Kibe, N. Hokoïwa, T. Shinozuka, M. Fujita, A. Yamasaki, T. Sonoda, C.S. Lee, Y.K. Kwon, J.Y. Moon, and J.H. Lee: “High-spin Isomer in  $^{93}\text{Mo}$ ”, *Eur. Phys. J. A* **24** (2005) 249–257.

32. A. Odahara, Y. Gono, T. Fukuchi, Y. Wakabayashi, H. Sagawa, W. Satula, and W. Nazarewicz: “Paring correlations in high-spin isomers”, *Phys. Rev. C* **72** (2005) 061303(R) (4 pages).
33. Y. Yanagisawa, S. Kubono, T. Teranishi, K. Ue, S. Michimasa, M. Notani, J.J. He, Y. Ohshiro, S. Shimoura, S. Watanabe, N. Yamazaki, H. Iwasaki, S. Kato, T. Kishida, T. Morikawa, and Y. Mizoi: ”Low-Energy Radioisotope Beam Separator CRIB”, *Nucl. Instrum. Methods A* **539** (2005) 74-83.
34. K. Yako, H. Sakai, M. B. Greenfield, K. Hatanaka, M. Hatano, J. Kamiya, H. Kato, Y. Kitamura, Y. Maeda, C. L. Morris, H. Okamura, J. Rapaport, T. Saito, Y. Sakemi, K. Sekiguchi, Y. Shimizu, K. Suda, A. Tamii, N. Uchi-gashima and T. Wakasa: ”Determination of the Gamow-Teller quenching factor from charge exchange reactions on  $^{90}\text{Zr}$ ”, *Phys. Lett. B* **615** (2005) 193-199.
35. K. Sekiguchi, H. Sakai, H. Witała, W. Glöckle, J. Golak, K. Hatanaka, M. Hatano, K. Itoh, H. Kamada, H. Kuboki, Y. Maeda, A. Nogga, H. Okamura, T. Saito, N. Sakamoto, Y. Sakemi, M. Sasano, Y. Shimizu, K. Suda, A. Tamii, T. Uesaka, T. Wakasa and K. Yako: “Resolving the Discrepancy of 135 MeV  $pd$  Elastic Scattering Cross Sections and Relativistic Effects”, *Phys. Rev. Lett.* **95** (2005) 162301 (4 pages).
36. P. Mermod, J. Blomgren, A. Hildebrand, C. Johansson, J. Klug, M. Osterlund, S. Pomp, U. Tippawan, B. Bergengwall, L. Nilsson, N. Olsson, O. Jonsson, A. Prokofiev, P. -U. Renberg, P. Nadel-Turonski, Y. Maeda, H. Sakai and A. Tamii: “Evidence of three-body force effects in neutron-deuteron scattering at 95 MeV”, *Phys. Rev. C* **72** (2005) 061002(R) (5 pages).
37. T. Wakasa, G. P. A. Berg, H. Fujimura, K. Fujita, K. Hatanaka, M. Ichimura, M. Itoh, J. Kamiya, T. Kawabata, Y. Kitamura, E. Obayashi, H. Sakaguchi, N. Sakamoto, Y. Sakemi, Y. Shimizu, H. Takeda, M. Uchida, Y. Yasuda, H. P. Yoshida and M. Yosoi: ”Study of the pionic enhancement in  $^{16}\text{O}(p, p')^{16}\text{O}(0^-, T = 1)$  at 295 MeV”, *Phys. Lett. B* **632** (2006) 485-489.
38. T. Wakui, M. Hatano, H. Sakai, T. Uesaka and A. Tamii: ”Proton polarizing system with Ar-ion laser for  $\bar{p}$ -RI scattering experiments”, *Nucl. Instrum. Methods A* **550** (2005) 521-534.
39. G. Neyens, M. Kowalska, D. Yordanov, K. Blaum, P. Himpe, P. Lievens, S. Mallion, R. Neugart, N. Vermeulen, Y. Utsuno, and T. Otsuka : “Measurement of the Spin and Magnetic Moment of  $^{31}\text{Mg}$ : Evidence for a Strongly Deformed Intruder Ground State”, *Phys. Rev. Lett.* **94** (2005) 022501 (4 pages).
40. M. Serra, T. Otsuka, Y. Akaishi, P. Ring and S. Hirose : “Relativistic Mean Field Models and Nucleon-Nucleon Interactions”, *Prog. Theor. Phys.* **113** (2005) 1009-1046.
41. Vandana Tripathi, S. L. Tabor, P. F. Mantica, C. R. Hoffman, M. Wiedeking, A. D. Davies, S. N. Liddick, W. F. Mueller, T. Otsuka, A. Stolz, B. E. Tomlin, Y. Utsuno, and A. Volya : “ $^{29}\text{Na}$ : Defining the edge of the island of inversion for  $Z=11$ ”, *Phys. Rev. Lett.* **94** (2005) 162501 (4 pages).
42. P. Mason, N. Mrginean, S.M. Lenzi, M. Ionescu-Bujor, F. Della Vedova, D. R. Napoli, T. Otsuka, Y. Utsuno, F. Nowacki, M. Axiotis, D. Bazzacco, P. G. Bizzeti, A. Bizzeti-Sona, F. Brandolini, M. Cardona, G. de Angelis E. Farnea, A. Gadea, D. Hojman, A. Iordachescu, C. Kalfas, Th. Kroll, S. Lunardi, T. Martinez, C. M. Petrache, B. Quintana, R. V. Ribas, C. Rossi Alvarez, C. A. Ur, R. Vlastou, and S. Zilio : “High spin structure of  $^{34}\text{S}$  and the proton-neutron coupling of intruder states”, *Phys. Rev. C* **71** (2005) 014316 (8 pages).
43. D.-C. Dinca, R.V.F. Janssens, A. Gade, D. Bazin, R. Broda, B.A. Brown, M. Campbell, M.P. Carpenter, P. Chowdhury, J.M. Cook, A.N. Deacon, B. Fornal, S.J. Freeman, T. Glasmacher, M. Honma, F. G. Kondev, J.-L. Lecouey, S.N. Liddick, P.F. Mantica, W.F. Mueller, H. Olliver, T. Otsuka, J.R. Terry, B.A. Tomlin, and K. Yoneda : “Reduced transition probabilities to the first  $2+$  state in  $^{52,54,56}\text{Ti}$  and development of shell closures at  $N=32,34$ ”, *Phys. Rev. C* **71** (2005) 041302 (4 pages).
44. A. Burger, T.R. Saito, H. Grawe, H. Hobel, P. Reiter, J. Gerl, M. Gorska, H.J. Wollersheim, A. Al-Khatib, A. Banu, T. Beck, F. Becker, P. Bednarczyk, G. Benzoni, A. Bracco, S. Brambilla, P. Bringel, F. Camera, E. Clement, P. Doornenbal, H. Geissel, A. Gorgen, J. Grebosz, G. Hammond, M. Hellstrom, M. Honma, M. Kavatsyuk, O. Kavatsyuk, M. Kmiecik, I. Kojouharov, W. Korten, N. Kurz, R. Lozeva, A. Maj, S. Mandal, B. Million, S. Muralithar, A. Neusser, F. Nowacki, T. Otsuka, Zs. Podolyak, N. Saito, A.K. Singh, H. Weick, C. Wheldon, O. Wieland, M. Winkler and RISING Collaboration : “Relativistic Coulomb excitation of neutron-rich  $^{54,56,58}\text{Cr}$ : On the pathway of magicity from  $N=40$  to  $N=32$ ”, *Phys. Lett. B* **622** (2005) 29-34.

45. T. Otsuka, T. Suzuki, R. Fujimoto, H. Grawe, and Y. Akaishi: “Evolution of Nuclear Shells due to the Tensor Force”, *Phys. Rev. Lett.* **95** (2005) 232502 (4 pages).
46. Y. Nagai, Y. Nagai, M. Igashira, T. Takaoka, T. Kikuchi, T. Shima, A. Tomyo, A. Mengoni, and T. Otsuka : “Li-7(n, $\gamma$ )Li-8 reaction and the S-17 factor at E-cm  $\leq$  500 keV”, *Phys. Rev. C* **71** (2005) 055803 (8 pages).
47. T.K. Ohnishi, A. Gelberg, H. Sakurai, K. Yoneda, N. Aoi, N. Imai, H. Baba, P. von Brentano, N. Fukuda, Y. Ichikawa, M. Ishihara, H. Iwasaki, D. Kameda, T. Kishida, A.F. Lisetskiy, H.J. Ong, M. Osada, T. Otsuka, M.K. Suzuki, K. Ue, Y. Utsuno, and H. Watanabe: “Gamow-Teller decay of the T=1 nucleus Cr-46”, *Phys. Rev. C* **72** (2005) 024308 (7 pages).
48. L.A. Riley, M.A. Abdelqader, D. Bazin, M.J. Bojazi, B.A. Brown, C.M. Campbell, J.A. Church, P.D. Cottle, D.C. Dinca, J. Enders, A. Gade, T. Glasmacher, M. Honma, S. Horibe, Z. Hu, K.W. Kemper, W.F. Mueller, H. Olliver, T. Otsuka, B.C. Perry, B.T. Roeder, B.M. Sherrill, T.P. Spencer, and J.R. Terry : “Thick-target inverse-kinematics proton scattering from Ar-46 and the N=28 shell below Ca-48”, *Phys. Rev. C* **72** (2005) 024311 (7 pages).
49. B. Fornal, S. Zhu, R.V.F. Janssens, M. Honma, R. Broda, B.A. Brown, M.P. Carpenter, S.J. Freeman, N. Hammond, F.G. Kondev, W. Krolas, T. Lauritsen, S.N. Liddick, C.J. Lister, S. Lunardi, P.F. Mantica, N. Marginean, T. Mizusaki, E.F. Moore, T. Otsuka, T. Pawlat, D. Seweryniak, B.E. Tomlin, C.A. Ur, I. Wiedenhover, and J. Wrzesinski : “Yrast structure of neutron-rich Ti-53”, *Phys. Rev. C* **72** (2005) 044315 (8 pages).
50. M. Bellegruic, F. Azaiez, Z. Dombradi, D. Sohler, M.J. Lopez-Jimenez, T. Otsuka, M.G. Saint-Laurent, O. Sorlin, M. Stanoiu, Y. Utsuno, Y.E. Penionzhkevich, N.L. Achouri, J.C. Angeli, C. Borcea, C. Bourgeois, J.M. Daugas, F. De Oliveira-Santos, Z. Dlouhy, C. Donzaud, J. Duprat, Z. Elekes, S. Grevy, D. Guillemaud-Mueller, S. Leenhardt, M. Lewitowicz, S.M. Lukyanov, W. Mittig, M.G. Porquet, F. Pougheon, P. Roussel-Chomaz, H. Savajols, Y. Sobolev, C. Stodel, and J. Timar : “Search for neutron excitation across the N=20 shell gap in 25-29Ne”, *Phys. Rev. C* **72** (2005) 054316 (7 pages).
51. M. Ionescu-Bujor, A. Iordachescu, D.R. Napoli, S.M. Lenzi, N. Marginean, T. Otsuka, Y. Utsuno, R.V. Ribas, M. Axiotis, D. Bazzacco, A.M. Bizzeti-Sona, P.G. Bizzeti, F. Brandolini, D. Bucurescu, M.A. Cardona, G. de Angelis, F. De Poli M, Della Vedova, E. Farnea, A. Gadea, D. Hojman, C.A. Kalfas, T. Kroll, S. Lunardi, T. Martinez, P. Mason, P. Pavan, B. Quintana, C.R. Alvarez, C.A. Ur, R. Vlastou, and S. Zilio : “High spin structure and intruder configurations in P-31”, *Phys. Rev. C* **73** (2006) 024310 (12 pages).
52. T. Adachi, Y. Fujita, P. von Brentano, A.F. Lisetskiy, G.P.A. Berg, C. Fransen, D. De Frenne, H. Fujita, K. Fujita, K. Hatanaka, M. Honma, E. Jacobs, J. Kamiya, K. Kawase, T. Mizusaki, K. Nakanishi, A. Negret, T. Otsuka, N. Pietralla, L. Popescu, Y. Sakemi, Y. Shimbara, Y. Shimizu, Y. Tameshige, A. Tamii, M. Uchida, T. Wakasa, M. Yosoi, and K.O. Zell : “High-resolution study of Gamow-Teller transitions from the T-z=1 nucleus Ti-46 to the T-z=0 nucleus V-46”, *Phys. Rev. C* **73** (2006) 024311 (10 pages).

## B. Proceedings

1. K. Ozawa for the PHENIX Collaboration: “Low mass dilepton production at RHIC energies”, Proceedings of International Conference on Hard and Electromagnetic Probes of High Energy Nuclear Collisions (HP 2004), Ericeira, Portugal, Nov. 4-10, 2004, *Eur. Phys. J. C* **43** (2005) 421–426.
2. J. Velkovska for the PHENIX Collaboration: “Can phi mesons give an answer to the baryon puzzle at RHIC?”, Proceedings of International Conference on Hard and Electromagnetic Probes of High Energy Nuclear Collisions (HP 2004), Ericeira, Portugal, Nov. 4-10, 2004, *Eur. Phys. J. C* **43** (2005) 317–322.
3. H. Busching for the PHENIX Collaboration: “Medium effects on high particle production measured with the PHENIX experiment”, Proceedings of International Conference on Hard and Electromagnetic Probes of High Energy Nuclear Collisions (HP 2004), Ericeira, Portugal, Nov. 4-10, 2004, *Eur. Phys. J. C* **43** (2005) 303–310.
4. B.A. Cole for the PHENIX Collaboration: “Differential probes of medium-induced energy loss”, Proceedings of International Conference on Hard and Electromagnetic Probes of High Energy Nuclear Collisions (HP 2004), Ericeira, Portugal, Nov. 4-10, 2004, *Eur. Phys. J. C* **43** 271–280.

5. O. Drapier for the PHENIX Collaboration: “Heavy flavor production in PHENIX”, Proceedings of International Conference on Hard and Electromagnetic Probes of High Energy Nuclear Collisions (HP 2004), Ericeira, Portugal, Nov. 4-10, 2004, *Eur. Phys. J. C* **43** (2005) 201–208.
6. M. Rosati for the PHENIX Collaboration: “Quarkonium production from d + Au to Au + Au collisions”, Proceedings of International Conference on Hard and Electromagnetic Probes of High Energy Nuclear Collisions (HP 2004), Ericeira, Portugal, Nov. 4-10, 2004, *Eur. Phys. J. C* **43** (2005) 173–178.  
 F. Kajihara: “PHENIX heavy flavor measurement by single leptons in p-p, d-Au and Au-Au”, Proc. of Heavy Flavor Productions & Hot/Dense Quark Matter, Dec. 12–14, 2005, Upton, NY, USA.  
 T. Gunji: “PHENIX Charmonium Measurement in p-p, d-Au and Au-Au”, Proc. of Heavy Flavor Productions & Hot/Dense Quark Matter, Dec. 12–14, 2005, Upton, NY, USA.
7. S.X. Oda, H. Hamagakim K. Ozawa, M. Inuzuka, T. Sakaguchi, T. Isobe, T. Gunji, S. Saito, Y. Morino, Y.L. Yamaguchi, S. Sawada and S. Yokkaichi: “Development of a Time Projection Chamber Using Gas Electron Multipliers (GEM-TPC)”, 2005 IEEE Nuclear Science Symposium, Oct. 23–29, 2005, Fajardo, Puerto Rico, 2005 IEEE Nuclear Science Symposium Conference Record (2005) 940–944.
8. S. Shimoura: “In-beam spectroscopy of exotic nuclei using direct reactions”, Proceedings of 5th Italy-Japan Symposium on Recent Achievements and Perspectives in Nuclear Physics, Naples, Italy, Nov. 3-7, 2004, eds. G. La Rana, C. Signorini, S. Shimoura, World Scientific ISBN 981-256-523-X (2005) pp. 3–7.
9. H. Hamagaki: “IS QGP FOUND AT RHIC?”, Proceedings of the 5th Italy-Japan Symposium on Recent Achievements and Perspectives in Nuclear Physics, Naples, Italy, Nov. 3-7, 2004, eds. G. La Rana, C. Signorini, S. Shimoura, World Scientific ISBN 981-256-523-X (2005) pp 275–282.
10. S. Kubono, T. Teranishi, M. Notani, H. Yamaguchi, A. Saito, J. J. He, Y. Wakabayashi, H. Fujikawa, G. Amadio, H. Baba, T. Fukuchi, S. Shimoura, S. Michimasa, S. Nishimura, M. Nishimura, Y. Gono, A. Odahara, S. Kato, J. Y. Moon, J. H. Lee, Y. K. Kwon, C. S. Lee, J. C. Kim, K. I. Hahn, T. Ishikawa, T. Hashimoto, H. Ishiyama, Y. X. Watanabe, M. H. Tanaka, H. Miyatake, Zs. Fülöp, V. Guimarães, and R. Lichtenthaler: “Direct Approach to Explosive Hydrogen Burning Process with CRIB”, Proceedings of 5th Italy-Japan Symposium on Recent Achievements and Perspectives in Nuclear Physics, Naples, Italy, Nov. 3-7, 2004, eds. G. La Rana, C. Signorini, S. Shimoura, World Scientific ISBN 981-256-523-X (2005) pp. 361–368.
11. T. Fukuchi, S. Shimoura, E. Ideguchi, H. Baba, M. Tamaki, M. Niikura, S. Ota, and M. Kurokawa: “Development of position sensitive Ge detector”, Proceedings of 5th Italy-Japan Symposium on Recent Achievements and Perspectives in Nuclear Physics, Naples, Italy, Nov. 3-7, 2004, eds. G. La Rana, C. Signorini, S. Shimoura, World Scientific ISBN 981-256-523-X (2005) pp. 449–453.
12. J.Y. Moon, C.S. Lee, J.H. Lee, C.C. Yun, J.C. Kim, M. Youn, S. Kubono, T. Teranishi, J.J. He, M. Notani, S. Nishimura, M. Nishimura, V. Guimaãres, R.F. Lichtenthale, and S. Kato: “Study of Proton Resonances in  $^{26}\text{Si}$  and  $^{27}\text{P}$  by Using the  $^{25}\text{Al}$  and  $^{26}\text{Si}$  Radioactive Ion Beams”, Proc. 8th Int. Symposium on Nuclei in the Cosmos, Vancouver, British Columbia, Canada, Jul. 19-23, 2004, *Nucl. Phys. A* **758** (2005) 158-161.
13. M. Kurata-Nishimura, S. Nishimura, S. Kubono, T. Teranishi, J.J. He and T. Motobayashi: “A New Approach for Cross Section Measurements at Low Energies Using a Monolithic Silicon Telescope”, Proc. 8th Int. Symposium on Nuclei in the Cosmos, Vancouver, British Columbia, Canada, Jul. 19-23, 2004, *Nucl. Phys. A* **758** (2005) 162-165.
14. Y. Togano, T. Gomi, T. Motobayashi, Y. Ando, N. Aoi, H. Baba, K. Demichi, Z. Elekes, N. Fukuda, Zs. Fülöp, U. Futakami, H. Hasegawa, Y. Higurashi, K. Ieki, N. Imai, M. Ishihara, K. Ishikawa, N. Iwasa, H. Iwasaki, S. Kanno, Y. Kondo, T. Kubo, S. Kubono, M. Kunibu, K. Kurita, Y.U. Matsuyama, S. Michimasa, T. Mine-mura, M. Miura, H. Murakami, T. Nakamura, M. Notani, S. Ota, A. Saito, H. Sakurai, M. Serata, S. Shimoura, T. Sugimoto, E. Takeshita, S. Takeuchi, K. Ue, K. Yamada, Y. Yanagisawa, K. Yoneda, and A. Yoshida: “Study of  $^{26}\text{Si}(p,\gamma)^{27}\text{P}$  reaction using Coulomb dissociation method”, Proc. 8th Int. Symposium on Nuclei in the Cosmos, Vancouver, British Columbia, Canada, Jul. 19-23, 2004, *Nucl. Phys. A* **758** (2005) 182c–185c.
15. S. Kubono, T. Teranishi, M. Notani, H. Yamaguchi, A. Saito, J.J. He, M. Wakabayashi, H. Fujikawa, G. Amadio, H. Baba, T. Fukuchi, S. Shimoura, S. Michimasa, S. Nishimura, M. Nishimura, Y. Gono, A. Odahara, S. Kato, J.Y. Moon, J.H. Lee, C.S. Lee, J.C. Kim, K.I. Hahn, T. Ishikawa, T. Hashimoto, H. Ishiyama, Y.X. Watanabe,

- M.H. Tanaka, H. Miyatake, Zs. Fülöp, V. Guimarães, and R. Lichtenthale: “Study of Stellar Reactions in Explosive Hydrogen Burning with CRIB”, Proc. 8th Int. Symposium on Nuclei in the Cosmos, Vancouver, British Columbia, Canada, Jul. 19-23, 2004, Nucl. Phys. A **758** (2005) 733c–736c.
16. T. Gomi, T. Motobayashi, Y. Ando, N. Aoi, H. Baba, K. Demichi, Z. Elekes, N. Fukuda, Zs. Fülöp, U. Futakami, H. Hasegawa, Y. Higurashi, K. Ieki, N. Imai, M. Ishihara, K. Ishikawa, N. Iwasa, H. Iwasaki, S. Kanno, Y. Kondo, T. Kubo, S. Kubono, M. Kunibu, K. Kurita, Y.U. Matsuyama, S. Michimasa, T. Minemura, M. Miura, H. Murakami, T. Nakamura, M. Notani, S. Ota, A. Saito, H. Sakurai, M. Serata, S. Shimoura, T. Sugimoto, E. Takeshita, S. Takeuchi, Y. Togano, K. Ue, K. Yamada, Y. Yanagisawa, and K. Yoneda: “Coulomb Dissociation of  $^{23}\text{Al}$  for the stellar  $^{22}\text{Mg}(p,\gamma)^{23}\text{Al}$  reaction”, Proc. 8th Int. Symposium on Nuclei in the Cosmos, Vancouver, British Columbia, Canada, Jul. 19-23, 2004, Nucl. Phys. A **758** (2005) 761c–764c.
  17. T. Gomi, T. Motobayashi, Y. Ando, N. Aoi, H. Baba, K. Demichi, Z. Elekes, N. Fukuda, Zs. Fülöp, U. Futakami, H. Hasegawa, Y. Higurashi, K. Ieki, N. Imai, M. Ishihara, K. Ishikawa, N. Iwasa, H. Iwasaki, S. Kanno, Y. Kondo, T. Kubo, S. Kubono, M. Kunibu, K. Kurita, Y.U. Matsuyama, S. Michimasa, T. Minemura, M. Miura, H. Murakami, T. Nakamura, M. Notani, S. Ota, A. Saito, H. Sakurai, M. Serata, S. Shimoura, T. Sugimoto, E. Takeshita, S. Takeuchi, Y. Togano, K. Ue, K. Yamada, Y. Yanagisawa, K. Yoneda, and A. Yoshida: “Coulomb dissociation experiment for explosive hydrogen burning: study of the  $^{22}\text{Mg}(p,\gamma)^{23}\text{Al}$  reaction”, Proc. Int. Conf. on the interface between NUClear STructure, Astrophysics and Reactions (NUSTAR05), Guildford, UK, Jan. 5-8, (2005), J. Phys. G **31** (2005) S1517–S1521.
  18. S. Shimoura: “Single particle states in exotic nuclei via nucleon transfer reactions at 30–60 A MeV”, Proc. Int. Conf. on the interface between NUClear STructure, Astrophysics and Reactions (NUSTAR05), Guildford, UK, Jan. 5-8, (2005), J. Phys. G **31** (2005) S1759–S1764.
  19. M. Hatano, H. Sakai, T. Wakui, T. Uesaka, N. Aoi, Y. Ichikawa, T. Ikeda, K. Itoh, H. Iwasaki, T. Kawabata, H. Kuboki, Y. Maeda, N. Matsui, T. Ohnishi, T. K. Onishi, T. Saito, N. Sakamoto, M. Sasano, Y. Satou, K. Sekiguchi, K. Suda, A. Tamii, Y. Yanagisawa and K. Yako: “First experiment of  $^6\text{He}$  with a polarized proton target”, Proc. Fourth Int. Conf. on Exotic Nuclei and Atomic Masses (ENAM04), Pine Mountain, Georgia, USA, Sep. 12–16, 2004, Eur. Phys. J. A **25** (2005) 255–258.
  20. H.J. Ong, N. Imai, N. Aoi, H. Sakurai, Zs. Dombrádi, A. Saito, Z. Elekes, H. Baba, K. Demichi, Zs. Fülöp, J. Gibelin, T. Gomi, H. Hasegawa, M. Ishihara, H. Iwasaki, S. Kanno, T. Kubo, K. Kurita, Y.U. Matsuyama, S. Michimasa, T. Minemura, T. Motobayashi, M. Notani, S. Ota, H.K. Sakai, S. Shimoura, E. Takeshita, S. Takeuchi, M. Tamaki, Y. Togano, K. Yamada, Y. Yanagisawa, and K. Yoneda: “Inelastic proton scattering on  $^{16}\text{C}$ ”, Proc. Fourth Int. Conf. on Exotic Nuclei and Atomic Masses (ENAM 04), Pine Mountain, Georgia, USA, Sep. 12-16, 2004, Eur. Phys. J. A **25** Suppl.1 (2005) 347–348.
  21. S. Michimasa, S. Shimoura, H. Iwasaki, M. Tamaki, S. Ota, N. Aoi, H. Baba, N. Iwasa, S. Kanno, S. Kubono, K. Kurita, M. Kurokawa, T. Minemura, T. Motobayashi, M. Notani, H.J. Ong, A. Saito, H. Sakurai, E. Takeshita, S. Takeuchi, Y. Yanagisawa, and A. Yoshida: “Study of single-particle states in  $^{23}\text{F}$  using a proton transfer reaction”, Proc. Fourth Int. Conf. on Exotic Nuclei and Atomic Masses (ENAM 04), Pine Mountain, Georgia, USA, Sep. 12-16, 2004, Eur. Phys. J. A **25** Suppl.1 (2005) 367–370.
  22. A. Odahara, Y. Wakabayashi, T. Fukuchi, Y. Gono, and H. Sagawa: “High-spin shape isomers and the nuclear Jahn-Teller effect”, Proc. Fourth Int. Conf. on Exotic Nuclei and Atomic Masses (ENAM 04), Pine Mountain, Georgia, USA, Sep. 12-16, 2004, Eur. Phys. J. A **25**, Suppl.1 (2005) 375–376
  23. K. Yamada, T. Motobayashi, N. Aoi, H. Baba, K. Demichi, Z. Elekes, J. Gibelin, T. Gomi, H. Hasegawa, N. Imai, H. Iwasaki, S. Kanno, T. Kubo, K. Kurita, Y.U. Matsuyama, S. Michimasa, T. Minemura, M. Notani, T. Onishi, H.J. Ong, S. Ota, A. Ozawa, A. Saito, H. Sakurai, S. Shimoura, E. Takeshita, S. Takeuchi, M. Tamaki, Y. Togano, Y. Yanagisawa, K. Yoneda, and I. Tanihata: “Reduced transition probabilities for the first  $2^+$  excited state in  $^{46}\text{Cr}$ ,  $^{50}\text{Fe}$ , and  $^{54}\text{Ni}$ ”, Proc. Fourth Int. Conf. on Exotic Nuclei and Atomic Masses (ENAM 04), Pine Mountain, Georgia, USA, Sep. 12-16, 2004, Eur. Phys. J. A **25** Suppl.1 (2005) 409–413.
  24. H. Iwasaki, N. Aoi, S. Takeuchi, S. Ota, H. Sakurai, M. Tamaki, T.K. Onishi, E. Takeshita, H.J. Ong, N. Iwasa, H. Baba, Z. Elekes, T. Fukuchi, Y. Ichikawa, M. Ishihara, S. Kanno, R. Kanungo, S. Kawai, T. Kubo, K. Kurita, S. Michimasa, M. Niikura, A. Saito, Y. Satou, S. Shimoura, H. Suzuki, M.K. Suzuki, Y. Togano, Y. Yanagisawa, and T. Motobayashi: “Intermediate-energy Coulomb excitation of the neutron-rich Ge isotopes around  $N=50$ ”, Proc. Fourth Int. Conf. on Exotic Nuclei and Atomic Masses (ENAM 04), Pine Mountain, Georgia, USA, Sep. 12-16, 2004, Eur. Phys. J. A **25** Suppl.1 (2005) 415–417.

25. E. Ideguchi, M. Niikura, C. Ishida, T. Fukuchi, H. Baba, N. Hokoïwa, H. Iwasaki, T. Koike, T. Komatsubara, T. Kubo, M. Kurokawa, S. Michimasa, K. Miyakawa, K. Morimoto, T. Ohnishi, S. Ota, A. Ozawa, S. Shimoura, T. Suda, M. Tamaki, I. Tanihata, Y. Wakabayashi, K. Yoshida, and B. Cederwall: "Study of high-spin states in the  $^{48}\text{Ca}$  region by using secondary fusion reactions", Proc. Fourth Int. Conf. on Exotic Nuclei and Atomic Masses (ENAM 04), Pine Mountain, Georgia, USA, Sep. 12-16, 2004, Eur. Phys. J. A **25** Suppl.1 (2005) 429-430.
26. S. Kubono, T. Teranishi, M. Notani, H. Yamaguchi, A. Saito, J. J. He, Y. Wakabayashi, H. Fujikawa, G. Amadio, H. Baba, T. Fukuchi, S. Shimoura, S. Michimasa, S. Nishimura, M. Nishimura, Y. Gono, A. Odahara, S. Kato, J. Y. Moon, J. H. Lee, Y. K. Kwon, C. S. Lee, K. I. Hahn, Zs. Fülöp, V. Guimarães, and R. Lichtenthaler "Nuclear astrophysics at the east drip line", Proc. of the 2nd Int. Conf. on Nuclear Physics in Astrophysics, Debrecen, Hungary, May 16-20, 2005, Eur. Phys. J. A **27** (2006) 327-332.
27. Y. Togano, T. Gomi, T. Motobayashi, Y. Ando, N. Aoi, H. Baba, K. Demichi, Z. Elekes, N. Fukuda, Zs. Fülöp, U. Futakami, H. Hasegawa, Y. Higurashi, K. Ieki, N. Imai, M. Ishihara, K. Ishikawa, N. Iwasa, H. Iwasaki, S. Kanno, Y. Kondo, T. Kubo, S. Kubono, M. Kunibu, K. Kurita, Y. U. Matsuyama, S. Michimasa, T. Minemura, M. Miura, H. Murakami, T. Nakamura, M. Notani, S. Ota, A. Saito, H. Sakurai, M. Serata, S. Shimoura, T. Sugimoto, E. Takeshita, S. Takeuchi, K. Ue, K. Yamada, Y. Yanagisawa, K. Yoneda, and A. Yoshida: "Study of the  $^{26}\text{Si}(p,\gamma)^{27}\text{P}$  reaction through Coulomb dissociation of  $^{27}\text{P}$ ", Proc. of the 2nd Int. Conf. on Nuclear Physics in Astrophysics, Debrecen, Hungary, May 16-20, 2005, Eur. Phys. J. A **27** (2006) 233-236.
28. Y. Maeda, H. Sakai, T. Kawabata, K. Suda, K. Yako, M. Hatano, T. Saito, H. Kuboki, M. Sasano, K. Hatanaka, Y. Sakemi, A. Tamii, J. Kamiya, Y. Shimizu, K. Fujita, H. Okamura, T. Wakasa, T. Kudoh, Y. Hagiwara, Y. Nagasue, K. Sekiguchi, K. Itoh, M. B. Greenfield and H. Kamada: "Measurements of the  $n + d$  elastic scattering at 250 MeV and the three-nucleon forces", Proc. the 16th International Spin Physics Symposium (SPIN2004), Trieste, Italy, Oct. 10-16, 2004, ed. by K. Aulenbacher, F. Bradamante, A. Bressan and A. Martin., World Scientific ISBN 981-256-315-6 (2005) pp. 631-634.
29. T. Kawabata: "Isovector and isoscalar spin-flip  $M1$  strengths in  $^{11}\text{B}$ ", Proc. the 16th International Spin Physics Symposium (SPIN2004), Trieste, Italy, Oct. 10-16, 2004, ed. by K. Aulenbacher, F. Bradamante, A. Bressan and A. Martin, World Scientific ISBN 981-256-315-6 (2005) pp. 645-648.
30. K. Suda, H. Okamura, T. Uesaka, R. Suzuki, H. Kumasaka, T. Ikeda, K. Itoh, H. Sakai, A. Tamii, K. Sekiguchi, K. Yako, Y. Maeda, M. Hatano, T. Saito, H. Kuboki, N. Sakamoto and Y. Satou: "Tensor analyzing power of the  $^{16}\text{O}(d, ^2\text{He})$  reaction at 0 degrees and structure of the spin-dipole resonances", Proc. the 16th International Spin Physics Symposium (SPIN2004), Trieste, Italy, Oct. 10-16, 2004, ed. by K. Aulenbacher, F. Bradamante, A. Bressan and A. Martin., World Scientific ISBN 981-256-315-6 (2005) pp. 649-652.
31. M. Hatano, H. Sakai, T. Wakui, T. Uesaka, N. Aoi, Y. Ichikawa, T. Ikeda, K. Itoh, H. Iwasaki, T. Kawabata, H. Kuboki, Y. Maeda, N. Matsui, T. Ohnishi, T. K. Onishi, T. Saito, N. Sakamoto, M. Sasano, Y. Satou, K. Sekiguchi, K. Suda, A. Tamii, Y. Yanagisawa and K. Yako: " $^6\text{He}$  Scattering With Polarized Proton Target", Proc. International Conference on Nuclei at the Limits, Argonne, Illinois, USA, Jul. 26-30, 2004, AIP Conf. Proc. **764** (2005) 360-364.
32. T. Uesaka, T. Wakui, T. Kawabata, M. Hatano, H. Sakai, K. Yako, Y. Maeda, T. Saito, M. Sasano, H. Iwasaki, T. Ohnishi, Y. Ichikawa, K. Sekiguchi, N. Aoi, T. Ohnishi, Y. Yanagisawa, A. Tamii, Y. Satou and N. Matsui: "Polarized Proton Target to probe Unstable Nuclei", Proc. Workshop on light ion beams and polarization phenomena, Tsukuba, Ibaragi, Japan, Nov. 26, 2004, GENSHIKAKU Kenkyu **49** (2005) 45-51.
33. T. Uesaka: "Spin-dependent momentum distribution of  $\vec{d}-\vec{p}$  cluster in  $^3\text{He}$  studied via the proton induced exclusive knockout reactions", Proc. Recent Progress and Future Perspective in Few-Body Physics, Research Center for Nuclear Physics, Osaka, Japan, Dec. 23-25, 2004, GENSHIKAKU Kenkyu **49**-No.6 (2005) 239-243.
34. T. Kawabata for the RCNP E114, E137, and E207 Collaborations: "Isoscalar and isovector spin-flip  $M1$  strengths in  $^{11}\text{B}$ ", Proc. International Symposium on Correlation Dynamics in Nuclei (CDN05), Tokyo, Japan, Jan. 31-Feb. 4, 2005, J. Phys. Conf. Ser. **20** (2005) 175-176.
35. S. Fujii, R. Okamoto and K. Suzuki: "The unitary-model-operator approach to nuclear many-body problems", Proc. of the International Symposium on Correlation Dynamics in Nuclei (CDN05), Tokyo, Japan, Jan. 31-Feb. 4, 2005, J. Phys. Conf. Ser. **20**, (2005) 83-88.

36. T. Otsuka, T. Suzuki, R. Fujimoto, T. Matsuo, D. Abe, H. Grawe, and Y. Akaishi: “Shell Structure of Exotic Nuclei and Nuclear Force”, Proc. of Int. Symp. on Exotic Nuclei (EXON2004), Peterhof, Russia, Jul. 5–12, 2004, ed. by Yu.E. Penionzhkevich and E.A. Cherepanov, World Scientific ISBN 981-256-392-X (2005) pp. 467–478.
37. T. Otsuka and N. Shimizu: “Quantum Chaos Generates Regularities”, Proc. of Workshop on Nuclei and Mesoscopic Physics (WNMP2004), East Lansing, USA, Oct. 23–26, 2004, AIP Conf. Proc. **777** (2005) pp. 135–139.
38. T. Otsuka : “Varying Shell Structure of sd-pf Nuclei”, Proc. of 12th Int. Symp. on Capture Gamma-Ray Spectroscopy and Related Topics, Notre Dame, USA, Sep. 4–9, 2005, AIP Conf. Proc. **819** (2006) pp. 65–70.
39. S. Fujii, R. Okamoto and K. Suzuki: “Ground-state energies and single-particle levels from microscopic effective interactions”, Proc. of the YITP Workshop on New Developments in Nuclear Self-Consistent Mean-Field Theories, Kyoto, Japan, May 30–Jun. 1, 2005, Soryushiron Kenkyu **111** (2005) B11–B13.

### C. Theses

1. A. Saito: “Exotic Cluster States in  $^{12}\text{Be}$  via  $\alpha$ -inelastic Scattering”, Ph.D. Thesis, Rikkyo University, November 2005.
2. Y. Morino: “Study of Electron Identification Capability of ALICE TRD”, Master Thesis, University of Tokyo, March 2006.
3. Y. Sasamoto: “Study of cluster states in  $^{11}\text{B}$  and  $^{13}\text{C}$  via alpha inelastic scattering”, Master Thesis, University of Tokyo, March 2006.
4. S. Sakaguchi: “Analyzing Power Measurement for the  $\vec{p}+^6\text{He}$  Elastic Scattering at 71 MeV/u with Upgraded Solid Polarized Proton Target”, Master Thesis, University of Tokyo, March 2006.
5. H. Fujikawa: “Development of a High-Efficiency Method for a Resonant Scattering with the Thick Target Method”, Master thesis, University of Tokyo, March 2005.

### D. Other Publications

1. 上坂友洋 : 「元素の地平、原子核の地平」, 物理学会誌 9月号 (2005) 697 .

## Talks and Presentations

### A. Conferences

1. F. Kajihara (invited): “PHENIX heavy flavor measurement by single leptons in p-p, d-Au and Au-Au”, Workshop on Heavy Flavor Productions & Hot/Dense Quark Matter, Dec. 12–14, 2005, Brookhaven National Laboratory, Upton, New York, USA.
2. T. Gunji (invited): “PHENIX Charmonium Measurement in p+p, d+Au, Au+Au and Cu+Cu collisions”, Workshop on Heavy Flavor Productions & Hot/Dense Quark Matter, Dec. 12–14, 2005, Brookhaven National Laboratory, Upton, New York, U.S.A
3. F. Kajihara (invited): “Heavy quark measurement by single leptons in the PHENIX experiment”, CNS-RIKEN Joint Workshop on Physics of Quark Gluon Plasma, Feb. 16–17, 2006, RIKEN, Wako, Saitama, Japan.
4. T. Gunji (invited): “Charmonium Measurement in Heavy Ion Collisions at RHIC”, CNS-RIKEN Joint Workshop on Physics of Quark-Gluon-Plasma, Feb. 16–17, 2006, RIKEN, Wako, Saitama, Japan
5. T. Isobe (invited): “Measurement of high-pT hadrons as probes of dense matter at RHIC-PHENIX”, CNS-RIKEN Joint Workshop on Physics of Quark-Gluon-Plasma, Feb. 16–17, 2006, RIKEN, Wako, Saitama, Japan
6. T. Isobe for the PHENIX Collaboration (invited): “Measurement of high-pT hadrons at RHIC-PHENIX”, XLI<sup>st</sup> Rencontres de Moriond QCD and Hadronic interactions, Mar. 18–25, 2006, La Thuile, Vallée d’Aoste, Italy.
7. T. Gunji for the PHENIX Collaboration (poster): “ $J/\psi \rightarrow e^+e^-$  Measurements in  $\sqrt{s_{NN}}=200$  GeV Au+Au collisions by PHENIX at RHIC”, 18th International Conference on Ultra Relativistic Nucleus-Nucleus Collisions (Quark Matter 2005), Aug. 4–9, 2005, Eötvös University, Budapest, Hungary.
8. T. Isobe for the PHENIX Collaboration (poster): “Measurement of neutral pions in  $\sqrt{s_{NN}}=200$  GeV and 62.4 GeV Au+Au collisions at RHIC-PHENIX”, 18th International Conference on Ultra Relativistic Nucleus-Nucleus Collisions (Quark Matter 2005), Aug. 4–9, 2005, Eötvös University, Budapest, Hungary.
9. F. Kajihara for the PHENIX Collaboration (poster): “Measurement of single electrons from heavy flavor decays in  $\sqrt{s_{NN}}=200$  GeV d+Au and Au+Au collisions by PHENIX”, 18th International Conference on Ultra Relativistic Nucleus-Nucleus Collisions (Quark Matter 2005), Aug. 4–9, 2005, Eötvös University, Budapest, Hungary.
10. K. Ozawa for the PHENIX Collaboration (poster): “Measurements of  $\phi \rightarrow e^+e^-$  in Au-Au collisions at  $\sqrt{s_{NN}}=200$  GeV”, 18th International Conference on Ultra Relativistic Nucleus-Nucleus Collisions (Quark Matter 2005), Aug. 4–9, 2005, Eötvös University, Budapest, Hungary.
11. T. Gunji for the PHENIX Collaboration: “Measurements of  $J/\psi$  yields at Forward-Rapidity and Mid-Rapidity in Au+Au collisions at  $\sqrt{s_{NN}}=200$  GeV by PHENIX at RHIC”, Particles and Nuclei International Conference 2005 (PANIC05), Oct. 24–28, 2005, Santa Fe, New Mexico, U.S.A
12. T. Isobe for the PHENIX Collaboration: “Measurement of neutral mesons in  $\sqrt{s_{NN}}=200$  GeV Au+Au and Cu+Cu collisions at RHIC-PHENIX”, Particles and Nuclei International Conference 2005 (PANIC05), Oct. 24–28, 2005, Santa Fe, New Mexico, U.S.A
13. H. Hamagaki: “RICH in the PHENIX Experiment at RHIC”, International RICH-Workshop of the CBM Experiment at FAIR, Mar. 6–7, 2006, Gesellschaft für Schwerionenforschung (GSI), Darmstadt, Germany.
14. K. Ozawa (invited): “Status of GEM development at CNS”, Workshop on Micro Pattern Gas Detector, Jan. 26–27, 2006, RCNP, Osaka, Japan.
15. K. Ozawa (invited): “Development of photon detector using CsI photo-cathode and GEM at PHENIX”, Workshop on Next Generation Photon Sensor, Dec. 26–27, 2005, KEK, Tsukuba, Ibaraki, Japan.
16. S.X. Oda, H. Hamagakim K. Ozawa, M. Inuzuka, T. Sakaguchi, T. Isobe, T. Gunji, S. Saito, Y. Morino, Y.L. Yamaguchi, S. Sawada and S. Yokkaichi: “Development of a Time Projection Chamber Using Gas Electron Multipliers (GEM-TPC)”, 2005 IEEE Nuclear Science Symposium, Oct. 23–29, 2005, Fajardo, Puerto Rico.

17. S. Kubono (invited): “Study of Stellar Reactions Relevant to Explosive Hydrogen Burning with CRIB”, Annual Meeting of the Canadian Physical Society Meeting, Jun. 6-9, 2005, Vancouver, Canada.
18. S. Kubono (invited): “Experimental Approach to Explosive Hydrogen Burning with Low-Energy RI Beams”, GSI workshop on Astrophysics and Nuclear Structure (Hirshegg 2006), January 16-20, 2006, Hirshegg, Austria.
19. S. Kubono (invited): “CRIB and PA for Nuclear Physics and Nuclear Astrophysics”, Japan-China Collaboration Meeting, Feb. 6-7, 2006, RIKEN, Wako, Saitama, Japan.
20. H. Yamaguchi, A. Saito, J.J. He, Y. Wakabayashi, G. Amadio, H. Fujikawa, S. Kubono, L.H. Kiem, Y.K. Kwon, M. Niikura, T. Teranishi, S. Nishimura, Y. Togano, N. Iwasa and K. Inafuku: “Proton resonance scattering of  $^7\text{Be}$ ”, Origin of Matter and Evolution of Galaxies (OMEG05), Nov. 8–11, 2005, University of Tokyo, Tokyo, Japan.
21. H. Yamaguchi: “Current development of low-energy RI beam separator CRIB RI Beam Experiments”, Second workshop of nuclear spectroscopy study using stopped or slow RI beam, Mar. 7–8, 2005, JAERI, Tokai, Japan.
22. S. Shimoura (invited): “In-beam spectroscopy of exotic nuclei via direct reactions at intermediate energy”, RIKEN RIBF international workshop on Collective motions in unstable nuclei –experiments vs. theories–, May 24–26, 2005 RIKEN, Wako, Saitama, Japan.
23. S. Shimoura: “Single-particle states in exotic nuclei via  $(\alpha, t)$  and  $(\alpha, ^3\text{He})$  reaction at 30-60 A MeV”, 2005 Summer Meeting on Direct Reactions with Exotic Beams (DREB2005), Jun. 22-25, 2005, MSU, East Lansing, Michigan, USA.
24. T. Uesaka: “Polarization Measurement for the  $p$ - $^6\text{He}$  Elastic Scattering”, 2005 Summer Meeting on Direct Reactions with Exotic Beams (DREB2005), Jun. 22-25, 2005, MSU, East Lansing, Michigan, USA.
25. H. Baba: “Isoscalar monopole and dipole responses in unstable nucleus  $^{14}\text{O}$ ”, 2005 Summer Meeting on Direct Reactions with Exotic Beams (DREB2005), Jun. 22-25, 2005MSU, East Lansing, Michigan, USA.
26. A. Saito: “ $^6\text{He} + ^6\text{He}$  cluster states in  $^{12}\text{Be}$  via alpha inelastic scattering”, 2005 Summer Meeting on Direct Reactions with Exotic Beams (DREB2005), Jun. 22-25, 2005, MSU, East Lansing, Michigan, USA.
27. M. Niikura: “Study of High-Spin States in Neutron-rich Ti Isotopes”, 4th CNS International Summer School (CISS05), Aug. 18–23, 2005, CNS, Wako, Saitama, Japan.
28. A. Saito: “ $^6\text{He} + ^6\text{He}$  cluster states in  $^{12}\text{Be}$  via  $\alpha$ -inelastic scattering”, RIKEN-CNS RIBF International Workshop on “Correlation and Condensation: New Features in Loosely Bound and Unbound Nuclear States”, Dec. 8–10, 2005, RIKEN, Wako, Saitama, Japan.
29. T. Kawabata, H. Akimune, H. Fujimura, H. Fujita, Y. Fujita, M. Fujiwara, K. Hara, K. Y. Hara, K. Hatanaka, T. Ishikawa, M. Itoh, J. Kamiya, S. Kishi, M. Nakamura, K. Nakanishi, T. Noro, H. Sakaguchi, Y. Shimbara, H. Takeda, A. Tamii, S. Terashima, H. Toyokawa, M. Uchida, H. Ueno, T. Wakasa, Y. Yasuda, H. P. Yoshida and M. Yosoi: “Excitation strengths and cluster structures in  $^{11}\text{B}$  and  $^{13}\text{C}$ ”, RIKEN-CNS RIBF International Workshop on “Correlation and Condensation: New Features in Loosely Bound and Unbound Nuclear States”, Dec. 8–10, 2005, RIKEN, Wako, Saitama, Japan.
30. S. Fujii, T. Mizusaki, T. Otsuka, T. Sebe and A. Arima: “Shell-model description of  $^{16}\text{C}$  with microscopic effective interactions”, RIKEN-CNS RIBF International Workshop on “Correlation and Condensation: New Features in Loosely Bound and Unbound Nuclear States”, Dec. 8–10, 2005, RIKEN, Wako, Saitama, Japan.
31. S. Shimoura: “Structure change in light neutron-rich nuclei via nucleon transfer reactions”, CNS Workshop on Past, Present and Future of Shell Model, Jan. 26–28, 2006, CNS, Wako, Saitama, Japan.
32. S. Fujii, T. Mizusaki, T. Otsuka, T. Sebe and A. Arima: “Shell-model description of  $^{16}\text{C}$  with modern NN forces” (in Japanese), CNS Workshop on Past, Present and Future of Shell Model (with a Course of Shell Model Code), Jan. 26–28, 2006, CNS, Wako, Saitama, Japan.
33. S. Shimoura: “High resolution magnetic spectrometer SHARAQ in RIBF”, Annual FRS-NUSTAR meeting, Feb. 22–24, 2006, GSI, Darmstadt, Germany.
34. S. Shimoura (invited): “In-beam spectroscopy of exotic nuclei probed by  $\alpha$ -induced direct reactions”, International Symposium on Structure of Exotic Nuclei and Nuclear Forces (SENUF 06), Mar. 9–12, 2006, University of Tokyo, Tokyo, Japan.

35. T. Uesaka: “Experimental studies of spin-dependent interactions in unstable nuclei with a polarized proton solid target”, International Symposium on Structure of Exotic Nuclei and Nuclear Forces (SENUF 06), Mar. 9–12, 2006, University of Tokyo, Tokyo, Japan.
36. S. Fujii (Invited): “Shell-model description of  $^{16}\text{C}$  with modern NN forces”, International Symposium on Structure of Exotic Nuclei and Nuclear Forces (SENUF 06), Mar. 9–12, 2006, University of Tokyo, Tokyo, Japan.
37. T. Kawabata, H. Akimune, H. Fujita, Y. Fujita, M. Fujiwara, K. Hara, K. Hatanaka, M. Itoh, Y. Kanada-En’yo, S. Kishi, K. Nakanishi, H. Sakaguchi, Y. Shimbara, A. Tamii, S. Terashima, M. Uchida, T. Wakasa, Y. Yasuda, H. P. Yoshida and M. Yosoi: “Dilute cluster structure in  $^{11}\text{B}$ ”, International Symposium on Structure of Exotic Nuclei and Nuclear Forces (SENUF06), Mar. 9–12, 2006, University of Tokyo, Tokyo, Japan.
38. T. Kawabata, H. Akimune, H. Fujimura, H. Fujita, Y. Fujita, M. Fujiwara, K. Hara, K. Y. Hara, K. Hatanaka, T. Ishikawa, M. Itoh, J. Kamiya, S. Kishi, M. Nakamura, K. Nakanishi, T. Noro, H. Sakaguchi, Y. Shimbara, H. Takeda, A. Tamii, S. Terashima, H. Toyokawa, M. Uchida, H. Ueno, T. Wakasa, Y. Yasuda, H. P. Yoshida and M. Yosoi: “Excitation strengths and cluster structures in  $^{11}\text{B}$ ”, International Workshop on “Alpha-particle Condensation in Nuclei”, August 19–20, 2005, Rostock University, Rostock, Germany.
39. T. Wakui (Invited): “Polarized Proton Solid Target for Exotic Nuclear Beam Experiment”, 11th International Workshop on Polarized Sources and Targets (PST05), Nov. 14–17, 2005, University of Tokyo, Tokyo, Japan.
40. K. Suda, H. Okamura, T. Uesaka, J. Nishikawa, H. Kumasaka, R. Suzuki, H. Sakai, A. Tamii, T. Ohnishi, K. Sekiguchi, K. Yako, S. Sakoda, H. Kato, M. Hatano, Y. Maeda, T. Saito, T. Ishida, N. Sakamoto, Y. Satou, K. Hatanaka, T. Wakasa and J. Kamiya (poster): “A new tool to calibrate deuteron beam polarization at intermediate energies”, 11th International Workshop on Polarized Sources and Targets (PST05), Nov. 14–17, 2005, University of Tokyo, Tokyo, Japan.
41. K. Itoh and T. Uesaka (poster): “Development of spin-exchange type polarized  $^3\text{He}$  target for RI-beam experiments”, 11th International Workshop on Polarized Sources and Targets (PST05), Nov. 14–17, 2005, University of Tokyo, Tokyo, Japan.
42. S. Sakaguchi, T. Uesaka, T. Wakui, T. Kawabata, N. Aoi, Y. Hashimoto, M. Ichikawa, Y. Ichikawa, K. Itoh, M. Itoh, H. Iwasaki, T. Kawahara, H. Kuboki, Y. Maeda, R. Matsuo, T. Nakao, H. Okamura, H. Sakai, N. Sakamoto, Y. Sasamoto, M. Sasano, Y. Satou, K. Sekiguchi, M. Shinohara, K. Suda, D. Suzuki, Y. Takahashi, A. Tamii, K. Yako and M. Yamaguchi (poster): “Polarization Measurement of Polarized Proton Solid Target via the  $\vec{p}+^4\text{He}$  Elastic Scattering”, 11th International Workshop on Polarized Sources and Targets (PST05), Nov. 14–17, 2005, University of Tokyo, Tokyo, Japan.
43. T. Uesaka: “SHARAQ Project”, International Symposium on the 15 Years of Spectrometer SMART and New Turn to RIBF, November 11–12, 2005, Wako, Saitama, Japan.
44. T. Uesaka: “SHARAQ Spectrometer”, Workshop on technical aspects of SHARAQ spectrometer, November 20, 2005, Wako, Saitama, Japan.
45. T. Kawabata: “SHARAQ Beam Line”, Workshop on technical aspects of SHARAQ spectrometer, November 20, 2005, Wako, Saitama, Japan.
46. S. Shimoura: “Physics Program with the SHARAQ Spectrometer”, International Workshop on “Nuclear Physics with RIBF”, Mar. 13–17, 2006, RIKEN, Wako, Saitama, Japan.
47. T. Uesaka: “Polarization Phenomena in Nucleon Knockout Reactions and  $j_>$  and  $j_<$  distributions in nuclei”, International Workshop on “Nuclear Physics with RIBF”, Mar. 13–17, 2006, RIKEN, Wako, Saitama, Japan.
48. S. Kubono: “Low-Energy RIB Separator CRIB - Another RIB Facility at RIKEN -”, International Workshop on “Nuclear Physics with RIBF”, Mar. 13–17, 2006, RIKEN, Wako, Saitama, Japan.
49. T. Otsuka: “Exploring variations of single-particle motions in RIBF nuclei”, International Workshop on “Nuclear Physics with RIBF”, Mar. 13–17, 2006, RIKEN, Wako, Saitama, Japan.
50. S. Fujii: “Structures of unstable nuclei from modern NN forces”, International Workshop on “Nuclear Physics with RIBF”, Mar. 13–17, 2006, RIKEN, Wako, Japan.

51. T. Otsuka: “New aspect of nuclear mean field theory; Spin-isospin interaction and shell evolution”, YITP Workshop on New Developments in Nuclear Self-Consistent Mean-Field Theories, May 30 - Jun. 1, 2005, Kyoto, Japan.
52. S. Fujii: “The unitary-model-operator approach to nuclear many-body problems”, YITP workshop on New Developments in Nuclear Self-Consistent Mean-Field Theories, May 30–Jun. 1, 2005, Kyoto, Japan.
53. T. Otsuka: “TDHF calculations on nuclear reactions”, Symposium en l’honneur de Paul Bonche, Jun. 27, 2005, Saclay, France.
54. T. Otsuka: “Spin-isospin NN interaction in nuclear mean field”, Workshop ESNT Recent developments in mean-field methods and treatment of pairing, Jun. 28 – Jul. 8, 2005, Saclay, France.
55. T. Otsuka: “Varying Shell Structure of sd-pf Nuclei”, 12th Int. Symp. on Capture Gamma-Ray Spectroscopy and Related Topics, Sep. 4–9, 2005, Notre Dame, USA.
56. T. Otsuka: “Neutrino reaction and double beta decay in medium-heavy nuclei”, Workshop on Neutrino Nuclear Responses in Double Beta Decays and Low-energy Astro-neutrinos, Dec. 2–4, 2005, Harima Science Park, Japan.
57. S. Fujii (Invited): “Recent developments of the nuclear structure study with microscopic effective interactions” (in Japanese), YITP Workshop on Tensor Force and Many-Nucleon Correlations, Sep. 1–6, 2005, Kyoto, Japan.

## B. JPS Meetings

1. F. Kajihara for the PHENIX Collaboration: “Single electron measurement from heavy flavor decays in d+Au and Au+Au collisions at  $\sqrt{s_{NN}} = 200$  GeV”, 2nd Joint Meeting of the Nuclear Physics Divisions of the APS and The Physical Society of Japan, Sep. 18–22, 2005, Ritz Carlton Hotel, Maui, Hawaii, USA.
2. T. Gunji for the PHENIX Collaboration: “Measurement of  $J/\psi \rightarrow e^+e^-$  in Au+Au Collisions at  $\sqrt{s_{NN}} = 200$  GeV by PHENIX at RHIC”, 2nd Joint Meeting of the Nuclear Physics Divisions of the APS and The Physical Society of Japan, Sep. 18–22, 2005, Ritz Carlton Hotel, Maui, Hawaii, USA.
3. T. Isobe for the PHENIX Collaboration: “Neutral pion production in  $\sqrt{s_{NN}} = 200$  GeV Au+Au collisions at RHIC-PHENIX”, 2nd Joint Meeting of the Nuclear Physics Divisions of the APS and The Physical Society of Japan, Sep. 18–22, 2005, Ritz Carlton Hotel, Maui, Hawaii, USA.
4. S.X. Oda for the PHENIX Collaboration: “Measurement of vector mesons via di-electrons in Cu+Cu collisions at  $\sqrt{s_{NN}} = 200$  GeV at RHIC-PHENIX”, 2nd Joint Meeting of the Nuclear Physics Divisions of the APS and The Physical Society of Japan, Sep. 18–22, 2005, Ritz Carlton Hotel, Maui, Hawaii, USA.
5. Y. Morino, S. Shota, T. Gunji, H. Hamagaki, and K. Ozawa for the ALICE TRD Collaboration: “Electron identification capability of real size Transition Radiation Detector for ALICE using neural network method”, 2nd Joint Meeting of the Nuclear Physics Divisions of the APS and The Physical Society of Japan, Sep. 18–22, 2005, Ritz Carlton Hotel, Maui, Hawaii, USA.
6. K. Ozawa for the PHENIX Collaboration (invited): “Measurements of J/psi and photon at RHIC”, DNP/JPS Joint meeting workshop “Strongly interacting matter probed at RHIC”, 2nd Joint Meeting of the Nuclear Physics Divisions of the APS and The Physical Society of Japan, Sep. 18–22, 2005, Ritz Carlton Hotel, Maui, Hawaii, USA.
7. Y.L. Yamaguchi, H. Hamagaki, K. Ozawa, S.X. Oda, M. Inuzuka, and S. Sano: “Measurements of Stability of Gas Electron Multiplier (GEM)”, 2nd Joint Meeting of the Nuclear Physics Divisions of the APS and The Physical Society of Japan, Sep. 18–22, 2005, Ritz Carlton Hotel, Maui, Hawaii, USA.
8. S. Shimoura : “Properties of Excited States in Exotic Nuclei Probed by Direct Reactions”, Mini-symposium on Structure Changes of Asymmetric Nuclear Systems I, 2nd Joint Meeting of the Nuclear Physics Divisions of the APS and The Physical Society of Japan, Sep. 18–22, 2005, Ritz Carlton Hotel, Maui, Hawaii, USA.
9. S. Ota for R337n Collaboration : “Gamma Spectroscopy of  $^{13}\text{B}$  via Proton Transfer Reaction at 50 MeV/nucleon”, Mini-symposium on Structure Changes of Asymmetric Nuclear Systems I, 2nd Joint Meeting of the Nuclear Physics Divisions of the APS and The Physical Society of Japan, Sep. 18–22, 2005, Maui, Hawaii, USA.

10. S. Michimasa, N. Aoi, H. Baba, M. Kurokawa, T. Minemura, T. Motobayashi, S. Takeuchi, Y. Yanagisawa, A. Yoshida, S. Shimoura, M. Tamaki, S. Kubono, A. Saito, H. Iwasaki, H.J. Ong, H. Sakurai, S. Ota, N. Iwasa, S. Kanno, K. Kurita, and E. Takeshita : “Measurement of Proton Transfer Reaction for Single-Particle States in  $^{23}\text{F}$ ”, Mini-symposium on Structure Changes of Asymmetric Nuclear Systems I, 2nd Joint Meeting of the Nuclear Physics Divisions of the APS and The Physical Society of Japan, Sep. 18–22, 2005, Ritz Carlton Hotel, Maui, Hawaii, USA.
11. T. Fukui for R373n Collaboration : “In beam  $\gamma$ -ray spectroscopy via  $^{32}\text{Mg}(\alpha,\alpha')$  reaction”, Mini-symposium on Structure Changes of Asymmetric Nuclear Systems I, 2nd Joint Meeting of the Nuclear Physics Divisions of the APS and The Physical Society of Japan, Sep. 18–22, 2005, Maui, Hawaii, USA.
12. M. Niikura, E. Ideguchi, H. Iwasaki, S. Shimoura, M. Tamaki, T. Fukuchi, H. Baba, T. Kubo, M. Kurokawa, S. Michimasa, K. Morimoto, T. Ohnishi, T. Suda, K. Yoshida, S. Ota, N. Hokoiva, Y. Wakabayashi, C. Ishida, T. Koike, T. Komatsubara, K. Miyakawa, A. Ozawa, and I. Tanihata : “Study of High-Spin States in neutron-rich Ti Isotopes”, Mini-symposium on Structure Changes of Asymmetric Nuclear Systems II, 2nd Joint Meeting of the Nuclear Physics Divisions of the APS and The Physical Society of Japan, Sep. 18–22, 2005, Maui, Hawaii, USA.
13. E. Ideguchi, S. Shimoura, M. Niikura, M. Tamaki, H. Iwasaki, H. Sakai, T. Fukuchi, H. Baba, M. Kurokawa, S. Michimasa, and S. Ota : “Gamma-Ray detector Array with Position and Energy sensitivity (GRAPE)”, Mini-symposium on New Technology in Gamma Ray Detection, 2nd Joint Meeting of the Nuclear Physics Divisions of the APS and The Physical Society of Japan, Sep. 18–22, 2005, Ritz Carlton Hotel, Maui, Hawaii, USA.
14. T. Fukuchi, S. Shimoura, E. Ideguchi, M. Kurokawa, H. Baba, S. Ota, M. Tamaki, and M. Niikura : “Development of Position Sensitive Germanium Detector”, Mini-symposium on New Technology in Gamma Ray Detection, 2nd Joint Meeting of the Nuclear Physics Divisions of the APS and The Physical Society of Japan, Sep. 18–22, 2005, Ritz Carlton Hotel, Maui, Hawaii, USA.
15. H. Yamaguchi, A. Saito, J.J. He, Y. Wakabayashi, G. Amadio, H. Fujikawa, S. Kubono, N. Yamazaki, T. Teranishi, M. Niikura, Y. Yanagisawa, S. Michimasa, S. Nishimura, M. Nishimura, Z. Fulop and Z. Elekes: “Wien filter for the enhancement of the RI beam separator CRIB”, 2nd Joint Meeting of the Nuclear Physics Divisions of the APS and The Physical Society of Japan, Sep. 18–22, 2005, Ritz Carlton Hotel, Maui, Hawaii, USA.
16. Y. Wakabayashi, A. Odahara, Y. Gono, T. Fukuchi, S. Kubono, T. Teranishi, H. Yamaguchi, E. Ideguchi, J.J. He, H. Fujikawa, G. Amadio, A. Saitoh, S. Shimoura, S. Ota, H. Baba, S. Nishimura, S. Michimasa, M. Nishimura, H. Watanabe, T. Kishida, J.Y. Moon, and T. Ishi: “Search for high-spin isomers using radioactive-isotope  $^{17}\text{N}$  beam”, 2nd Joint Meeting of the Nuclear Physics Divisions of the APS and The Physical Society of Japan, Sep. 18–22, 2005, Ritz Carlton Hotel, Maui, Hawaii, USA.
17. T. Kawabata, H. Akimune, H. Fujimura, H. Fujita, Y. Fujita, M. Fujiwara, K. Hara, K. Y. Hara, K. Hatanaka, T. Ishikawa, M. Itoh, J. Kamiya, S. Kishi, M. Nakamura, K. Nakanishi, T. Noro, H. Sakaguchi, Y. Shimbara, H. Takeda, A. Tamii, S. Terashima, H. Toyokawa, M. Uchida, H. Ueno, T. Wakasa, Y. Yasuda, H. P. Yoshida and M. Yosoi: “Excitation strengths and cluster structures in  $^{11}\text{B}$ ”, 2nd Joint Meeting of the Nuclear Physics Divisions of the APS and The Physical Society of Japan, Sep. 18–22, 2005, Ritz Carlton Hotel, Maui, Hawaii, USA.
18. Y. Sasamoto, T. Kawabata, I. Sugai, Y. Takeda and M. Hamagaki: “Preparation of Self-supporting  $^{11}\text{B}$  target”, 2nd Joint Meeting of the Nuclear Physics Divisions of the APS and The Physical Society of Japan, Sep. 18–22, 2005, Ritz Carlton Hotel, Maui, Hawaii, USA.
19. S. Sakaguchi, T. Wakui, T. Uesaka, T. Kawabata, K. Itoh, H. Kuboki, Y. Maeda, H. Sakai, Y. Sasamoto, M. Sasano, K. Sekiguchi, K. Suda, Y. Takahashi and K. Yako: “Polarized proton solid target and its application to RI beam experiments”, 2nd Joint Meeting of the Nuclear Physics Divisions of the APS and The Physical Society of Japan, Sep. 18–22, 2005, Ritz Carlton Hotel, Maui, Hawaii, USA.
20. Y. Maeda, H. Sakai, T. Kawabata, K. Yako, K. Suda, M. Hatano, T. Saito, H. Kuboki, M. Sasano, K. Hatanaka, Y. Sakemi, A. Tamii, Y. Shimizu, Y. Tameshige, J. Blomgren, P. Mermod, H. Witala, M. B. Greenfield, K. Itoh, H. Kamada, H. Okamura, Y. Satou, K. Sekiguchi, T. Wakasa and J. Kamiya: “Measurements of the n+d elastic scattering and the three-nucleon force effects”, 2nd Joint Meeting of the Nuclear Physics Divisions of the APS and The Physical Society of Japan, Sep. 18–22, 2005, Ritz Carlton Hotel, Maui, Hawaii, USA.

21. T. Uesaka, V. Ladygin, K. Suda, Y. Maeda, L. S. Azhgirey, Yu. V. Gurchin, A. Yu. Isupov, K. Itoh, M. Janek, J.-T. Karachuk, T. Kawabata, A. N. Khrenov, A. S. Kiselev, V. Kizka, J. Kliman, V. A. Krasnov, A. N. Livanov, A. I. Malakhov, V. Matoucek, M. Morhac, S. Nedeov, S. Rangelov, S. G. Reznikov, S. Sakaguchi, H. Sakai, Y. Sasamoto, K. Sekiguchi, I. Turzo and T. A. Vasiliev: “*d-p* Elastic Scattering Measurement at Internal Target Station of Nuclotron”, 2nd Joint Meeting of the Nuclear Physics Divisions of the APS and The Physical Society of Japan, Sep. 18–22, 2005, Ritz Carlton Hotel, Maui, Hawaii, USA.
22. T. Otsuka: “Nuclear structure, nuclear force and spin-isospin excitations in stellar processes”, Workshop on Neutrino Astrophysics, 2nd Joint Meeting of the Nuclear Physics Divisions of the APS and The Physical Society of Japan, Sep 18–22, 2005, Ritz Carlton Hotel, Maui, Hawaii, USA.
23. S. Fujii, R. Okamoto and K. Suzuki: “Microscopic description of single-particle levels with modern NN interactions”, 2nd Joint Meeting of the Nuclear Physics Divisions of the APS and The Physical Society of Japan, Sep. 18–22, 2005, Ritz Carlton Hotel, Maui, Hawaii, USA.
24. T. Isobe for the PHENIX Collaboration: “Measurement of direct photon in  $\sqrt{s_{NN}}=200$  GeV Au+Au collisions at RHIC-PHENIX”, JPS Spring meeting, Mar. 27–30, 2006, Ehime University and Matsuyama University, Matsuyama, Japan.
25. S.X. Oda for the PHENIX Collaboration: “ $J/\psi \rightarrow e^+e^-$  Measurement in Cu+Cu collisions at RHIC-PHENIX”, JPS Spring meeting, Mar. 27–30, 2006, Ehime University and Matsuyama University, Matsuyama, Japan.
26. S. Shimoura : “Nuclear spectroscopy via direct reactions probed by RI beams”, JPS Spring Meeting, Mar. 27–30, 2006, Matsuyama, Japan.
27. E. Ideguchi, B. Cederwall, E. Ganioglu, B. Hadinia, K. Lagergren, T. Back, S. Eeckhaudt, T. Grahn, P. Greenlees, A. Johnson, D.T. Joss, R. Julin, S. Juutinen, H. Kettunen, M. Leino, A.-P. Leppanen, P. Nieminen, M. Nyman, J. Pakarinen, E. S. Paul, P. Rahkila, C. Scholey, J. Uusitalo, R. Wadsworth, D. R. Wiseman, and R. Wyss : “High-spin collective rotational states in  $^{107}\text{In}$ ”, JPS Spring Meeting, Mar. 27–30, 2006, Matsuyama, Japan.
28. M. Liu, Y.H. Zhang, X.H. Zhou, Y.X. Guo, X.G. Lei, Z. Liu, and J. He: “High-Spin Level Structure of N=81 Near-Spherical Nucleus  $^{142}\text{Pm}$ ”, JPS Spring Meeting, Mar. 27–30, 2006, Matsuyama, Japan.
29. Y. Zheng. X.H. Zhou. Y.H. Zhang. X.Y. Guo. X.G. Lei. Z Liu, T. Hayakawa, M. Oshima, Y. Toh, T. Shizuma, J. Katakura, Y. Hatsukawa, M. Matsuda, H. Kusakari, M. Sugawara, K. Furuno, T. Komatsubara, S.X. Wen, L.H. Zhu, and C.X. Yang: “Study of the High-Spin States in  $^{145}\text{Tb}$  and  $^{157}\text{Yb}$ ”, JPS Spring Meeting, Mar. 27–30, 2006, Matsuyama, Japan.
30. A. Saito, S. Shimoura, T. Minemura, Y.U. Matsuyama, H. Baba, N. Aoi, T. Gomi, Y. Higurashi, K. Ieki, N. Imai, N. Iwasa, H. Iwasaki, S. Kanno, S. Kubono, M. Kunibu, S. Michimasa, T. Motobayashi, T. Nakamura, H. Ryuto, H. Sakurai, M. Serata, E. Takeshita, S. Takeuchi, T. Teranishi, K. Ue, K. Yamada, and Y. Yanagisawa : “Cluster structure in  $^{12}\text{Be}$  via  $\alpha$  inelastic scattering”, JPS Spring Meeting, Mar. 27–30, 2006, Ehime University and Matsuyama University, Matsuyama, Japan.
31. K. Suda, T. Uesaka, V.P. Ladygin, Y. Maeda, L. S. Azhgirey, Y. V. Gurchin, A. Y. Isupov, K. Itoh, M. Janek, J. -T. Karachuk, T. Kawabata, A. N. Khrenov, A. S. Kiselev, V. Kizka, J. Kliman, V. A. Krasnov, A. N. Livanov, A. I. Malakov, S. G. Reznikov, S. Sakaguchi, H. Sakai, Y. Sasamoto, K. Sekiguchi, T. A. Vasiliev and S. Nedeov: ”*d-p* Elastic Scattering Measurement at Internal Target Station of Nuclotron”, JPS Spring Meeting, Mar. 27–30, 2006, Ehime University and Matsuyama University, Matsuyama, Japan.
32. Y. Sasamoto, T. Kawabata, T. Uesaka, K. Suda, Y. Maeda, K. Itoh, S. Sakaguchi, K. Hatanaka, M. Fujiwara, A. Tamii, Y. Shimizu, K. Nakanishi, K. Kawase, H. Hashimoto, Y. Tameshige, H. Matsubara, M. Itoh, H. P. Yoshida and M. Uchida: “Cluster states in  $^{11}\text{B}$ ”, JPS Spring Meeting, Mar. 27–30, 2006, Ehime University and Matsuyama University, Matsuyama, Japan.
33. S. Sakaguchi, T. Uesaka, T. Wakui, T. Kawabata, N. Aoi, Y. Hashimoto, M. Ichikawa, Y. Ichikawa, K. Itoh, M. Itoh, H. Iwasaki, T. Kawahara, H. Kuboki, Y. Maeda, R. Matsuo, T. Nakao, H. Okamura, H. Sakai, N. Sakamoto, Y. Sasamoto, M. Sasano, Y. Satou, K. Sekiguchi, M. Shinohara, K. Suda, D. Suzuki, Y. Takahashi, A. Tamii, K. Yako, and M. Yamaguchi: “Analyzing Power Measurement for the  $\bar{p}+^6\text{He}$  Elastic Scattering at 71 MeV/u”, JPS Spring Meeting, Mar. 27–30, 2006, Ehime University and Matsuyama University, Matsuyama, Japan.

34. T. Kawahara, T. Wakui, T. Uesaka and S. Sakaguchi: “New method of polarization reversal by means of 180-deg pulse nuclear magnetic resonance”, JPS Spring Meeting, Mar. 27–30, 2006, Ehime University and Matsuyama University, Matsuyama, Japan.
35. T. Uesaka: “Polarization in Proton Scattering from Unstable Nuclei”, JPS Spring Meeting, Mar. 27–30, 2006, Ehime University and Matsuyama University, Matsuyama, Japan.
36. S. Fujii, T. Mizusaki, T. Otsuka, T. Sebe and A. Arima: “Shell-model description of  $^{16}\text{C}$  with microscopic effective interactions”, JPS Spring meeting, Mar. 27–30, 2006, Ehime University and Matsuyama University, Matsuyama, Japan.
37. Y. Aramaki, H. Hamagaki, K. Ozawa, S. Yokkaichi, S.X. Oda, Y. Morino, Y.L. Yamaguchi, M. Inuzuka, S. Sano, and S. Maki: “Development of a CsI-coated Gas Electron Multiplier”, JPS Spring meeting, Mar. 27–30, 2006, Ehime University and Matsuyama University, Matsuyama, Japan.
38. Y.L. Yamaguchi, H. Hamagaki, K. Ozawa, S.X. Oda, Y. Aramaki, S. Sano, and S. Maki: “Simulation study for the behavior of GEM detector”, JPS Spring meeting, Mar. 27–30, 2006, Ehime University and Matsuyama University, Matsuyama, Japan.
39. S. Maki, H. Hamagaki, K. Ozawa, S.X. Oda, Y. Morino, Y.L. Yamaguchi, Y. Aramaki, S. Sano, S. Yokkaichi, and J. Chiba: “Measurements of ion feedback in gas electron multipliers (GEM)”, JPS Spring meeting, Mar. 27–30, 2006, Ehime University and Matsuyama University, Matsuyama, Japan.

### C. Lectures

1. S. Kubono: “Lecture series on Nuclear Astrophysics”, INST(The Institute for Nuclear Science and Technology) Summer School on Nuclear Physics and Astrophysics, August 28 - 31, 2005, Hanoi, Vietnam.
2. S. Kubono: “Lecture on Experimental Nuclear Astrophysics with Low Energy RI Beams”, Nuclear Astrophysics Summer School, October 3 - 7, 2005, Santa Tecla, Italy.
3. E. Ideguchi : “Study of high-spin states by using stable and unstable nuclear beams”, 4th CNS International Summer School (CISS05), Aug.18–23, 2005, CNS, Wako, Saitama, Japan.
4. T. Uesaka: “Studies of New Excitation Modes in Nuclei via Exothermic Nuclear Reactions —Physics of SHARAQ—”, 4th CNS International Summer School (CISS05), Aug.18–23, 2005, CNS, Wako, Saitama, Japan.

### D. Seminars

1. H. Hamagaki: “Global Aspects of Hot and Dense Matter Created at RHIC”, Jul. 7, 2005, CNS Colloquium, Wako, Saitama, Japan.
2. H. Hamagaki: “Frontier in the study of Quark Gluon Plasma”, Nov. 11, 2005, A special seminar series on Frontier in Physics, Tohoku University, Miyagi, Japan.
3. M. Liu : “High-Spin Level Structures of N=81 Near-Spherical Nuclei  $^{142}\text{Pm}$  and  $^{141}\text{Nd}$ ”, Oct. 13, 2005, CNS Seminar, Wako, Saitama, Japan.
4. Y. Zheng : “Study of the High-Spin States in  $^{145}\text{Tb}$  and  $^{157}\text{Yb}$ ”, Oct. 13, 2005, CNS Seminar, Wako, Saitama, Japan.
5. S. Sakaguchi: “Analyzing Power Measurement for the  $\vec{p}+^6\text{He}$  Elastic Scattering”, Dec. 8, 2005, Nuclear Theory Seminar at Hosei University, Tokyo, Japan.
6. T. Uesaka: “Proton polarization in aromatic molecules and its application”, Dec. 14, 2005, Seminar at Toho University, Chiba, Japan.  
A. Saito: “Studies of resonance states in proton-rich nuclei with low-energy RI beams”, Jun. 1, 2006, Seminar at the University of Tsukuba Tandem Accelerator Center (UTTAC), Tsukuba, Japan.

7. T. Kawabata: "Dilute cluster state in  $^{11}\text{B}$ ", Mar. 21, 2006, NSL Seminar at Notre Dame University, South Bend, Indiana, USA.
8. S. Fujii: "Recent developments of the nuclear structure study with microscopic effective interactions", Jan. 13, 2006, Nuclear Theory Seminar, Saitama University, Saitama, Japan.

## Personnel

### Director

SAKAI, Hideyuki ( ~ May 2005)	<i>Professor, Department of Physics, Graduate School of Science</i>
OTSUKA, Takaharu (June 2005 ~)	<i>Professor, Department of Physics, Graduate School of Science</i>

### Scientific Staff

#### 1. Accelerator Research

WATANABE, Shin-ichi	<i>Research Associate</i>
---------------------	---------------------------

#### 2. Heavy-Ion Collisions

SHIMOURA, Susumu	<i>Professor</i>
UESAKA, Tomohiro (June 2005 ~)	<i>Associate Professor</i>
UESAKA, Tomohiro ( ~ May 2005)	<i>Lecturer</i>
IDEGUCHI, Eiji	<i>Lecturer</i>
IWASAKI, Hironori	<i>Research Associate</i>
KAWABATA, Takahiro	<i>Research Associate</i>
WAKUI, Takashi ( ~ August 2005)	<i>Research Associate</i>

#### 3. Nuclear Structure in Extreme States

KUBONO, Shigeru	<i>Professor</i>
HAMAGAKI, Hideki	<i>Associate Professor</i>
YAMAGUCHI, Hidetoshi	<i>Research Associate</i>
OZAWA, Kyoichiro	<i>Research Associate</i>

### Guest Professors

FUKUDA, Mitsuhiro	<i>Japan Atomic Energy Research Institute</i>
MIZUSAKI, Takahiro	<i>Senshu University</i>

### Technical Staff

OHSHIRO, Yukimitsu	YAMAZAKI, Norio
--------------------	-----------------

### **Technical Assistants**

YAMAKA, Shoichi  
SUZUKI, Masaharu

NAGATA, Takeshi (February 2006 ~ )  
MARUNO, Tomohiro ( ~ January 2006)

### **Post Doctoral Associates**

SUDA, Kenji  
SAITO, Akito  
MAEDA, Yukie  
LIU, Minlang  
LE, Khiem H. ( ~ January 2006)

FUJII, Shinichiro  
KINO, Koichi  
HE, Jianjun  
ZHENG, Yong

### **Graduate Students**

KAJIHARA, Fukutaro  
GUNJI, Taku  
KURIHARA, Narumi ( ~ August 2005)  
NIIKURA, Megumi  
FUJIKAWA, Hisashi  
SAKAGUCHI, Satoshi  
SASAMOTO, Yoshiko  
YAMAGUCHI, Yorito

WAKABAYASHI, Yasuo  
ISOBE, Tadaaki  
TAMAKI, Mitsuru  
ODA, Susumu  
MORINO, Yuhei  
SAITO, Shota  
AMADIO, Guilherme  
ARAMAKI, Youki

### **Administration Staff**

HIRANO, Midori  
YAMAMOTO, Ikuko  
YAMAGUCHI, Miwa  
AYABE, Hiroko ( ~ Sep. 2005)

TAKEUCHI, Kazuko  
ITAGAKI, Toshiko  
ENDO, Takako

## Committees

### Council

IWASAWA, Yasuhiro (chair)	<i>Dean, Graduate School of Science</i>
YAMAMOTO, Masayuki	<i>Department of Biophysics and Biochemistry, Graduate School of Science</i>
EGUCHI, Tohru	<i>Department of Physics, Graduate School of Science</i>
SAKAI, Hideyuki	<i>Department of Physics, Graduate School of Science</i>
OTSUKA, Takaharu	<i>Department of Physics, Graduate School of Science</i>
Hayano, Ryugo (June 2005 ~ )	<i>Department of Physics, Graduate School of Science</i>
KUBONO, Shigeru	<i>Center for Nuclear Study, Graduate School of Science</i>
SHIMOURA, Susumu	<i>Center for Nuclear Study, Graduate School of Science</i>
NAGAMIYA, Shoji	<i>J-PARC Project Office, High Energy Accelerator Research Organization</i>

### Steering Committee

SAKAI, Hideyuki	<i>Department of Physics, Graduate School of Science</i>
OTSUKA, Takaharu (chair: ~ May 2005)	<i>Department of Physics, Graduate School of Science</i>
SHIMOURA, Susumu	<i>Center for Nuclear Study, Graduate School of Science</i>
KUBONO, Shigeru	<i>Center for Nuclear Study, Graduate School of Science</i>
HAMAGAKI, Hideki	<i>Center for Nuclear Study, Graduate School of Science</i>
AIHARA, Hiroaki	<i>Department of Physics, Graduate School of Science</i>
HAYANO, Ryugo (chair: June 2005 ~ )	<i>Department of Physics, Graduate School of Science</i>
Hamaguchi, Hiroo	<i>Department of Chemistry, Graduate School of Science</i>
KOBAYASHI, Tomio	<i>International Center for Elementary Particle Physics</i>
YAMAZAKI, Yasunori	<i>Institute of Physics, Graduate School of Arts and Sciences</i>
NAKAZAWA, Masaharu	<i>Department of Quantum Engineering and Systems Science, Graduate School of Engineering</i>

### Program Advisory Committee

NAKAMURA, Takashi (chair)	<i>Tokyo Institute of Technology</i>
HAMAMOTO, Ikuko	<i>University of Lund, Sweden</i>
ISHII, Tetsuo	<i>Japan Atomic Energy Research Institute</i>
SHIMODA, Tadashi	<i>Osaka University</i>
MITTING, Wolfgang	<i>Grand Accelérateur National D'Ions Lourds</i>
KAJINO, Toshitaka	<i>Univeristy of Tokyo</i>
NORO, Tetsuo	<i>Kyushu Univeristy</i>
prof. T. Kajino (NAO),	



